APPLIED
COMPUTATIONAL
ELECTROMAGNETICS
SOCIETY
JOURNAL

APRIL 2024 REVIEWERS

Jawad K. Ali

Sami Barmada

Behrokh Beiranvand

Bhattacharya

Malcolm M. Bibby

Yuanxi Cao

Mehmet Onur Kok

Koushick

Anubhav Kumar

Wang-Sang Lee

Bai Lei

Yaqeen Mezaal

Jafar Mohammed

Sathishkumar N.

Leszek Nowosielski

Mahdi Oliaei

Saeed Reza Ostadzadeh

Andrew Peterson

S. Ramesh

Jalil Rashed

C. J. Reddy

Ayman Ayd R. Saad

Suganthi Santhanam

Varun Singh

Marsellas Waller

Jun Wang

Dariusz Wojcik

Tao Yuan

TABLE OF CONTENTS

Prediction of Antenna Performance based on Scalable Data-informed Machine Learning Methods

Yiming Chen[1], Veysel Demir[2], Srirama Bhupatiraju[3], Atef Z. Elsherbeni[1], Joselito Gavilan[3], and Kiril Stoynov[3]

[1]Department of Electrical Engineering
Colorado School of Mines, Golden 80401, USA
yimingchen@mines.edu, aelsherb@mines.edu

[2]Department of Electrical Engineering
Northern Illinois University, Dekalb 60115, USA vdemir@niu.edu

[3]Antenna Group
Nvidia, Santa Clara 95050, USA
sbhupatiraju@nvidia.com, lito.gavilan@gmail.com, kstoynov@nvidia.com

Abstract – This paper proposes a scalable architecture for predicting antenna performance using various data-informed machine learning (DIML) methods. By utilizing the computation power of graphics processing units (GPUs), the architecture takes advantage of hardware (HW) acceleration from the beginning of electromagnetic (EM) full-wave simulation to the final machine learning (ML) validation. A total of 49152 full-wave simulations of a classical microwave patch antenna forms the ML dataset. The dataset contains the performance of patch antenna on six commonly used materials and two standard thicknesses in a wide frequency range from 0.1 to 20 GHz. A total of 13 base ML models are stacked and ensembled in a tabular workflow with performance as 0.970 and 0.933 F_1 scores for two classification models, as well as 0.912 and 0.819 R_2 scores for two regression models. Moreover, an image-based workflow is proposed. The image-based workflow yields the 0.823 R_2 score, indicating a near real-time prediction for all S_{11} values from 0.1 to 20 GHz. The proposed architecture requires neither the fine-tuned hyperparameters in the ML-assisted optimization (MLAO) model for specified antenna design nor the pre-knowledge required in the physics-informed models. The fully automated process with data collection and the customized ML pipeline provides the architecture with robust scalability in future work where more antenna types, materials, and performance requirements can be involved. Also, it could be wrapped as a pre-trained ML model as a reference for other antenna designs.

Index Terms – Data informed, ensemble, full-wave simulation, machine learning, scalability, stacking, wide frequency range.

I. INTRODUCTION

With the unlocking of computing power, machine learning (ML) brings new prospects for non-linear and non-convex problems in higher dimensions or deeper networks. By regarding the weighting parameters as constants or a prior distribution, the Frequentist aspect [1] and Bayesian aspect [2] establish two separate systems to interpret the black-box behaviors of ML. Even though the mechanisms are different, both aspects set up similar representable matrices linking the input and output as the shared goal. Electromagnetic (EM) problems always suffer from complex input combinations, time-consuming simulations, multiple local bests, and rapid design changes. All these hindrances are exactly in line with the goal to overcome using ML. Hence, ML is undoubtedly the new perspective to explore EM problems [3, 4], and well-trained ML models could provide real-time prediction of the EM responses.

ML has been getting attention in various EM applications. For instance, at the RF system level [5–8], a customized statistical ML model combined with entropy weight theory [5] was trained by 2001 samples to predict the path loss of RF wave propagation in the very high frequency (VHF) band. ML was implemented to speed up near-field RF measurements [6] or calibrate stochastic radio propagation [7]. In [8], ML was applied to device scheduling in an over-the-air (OTA) system with lower computational loads.

From the ML point of view, as for the ML-assisted optimization (MLAO) for antenna and array designs, the traditional ML methods [9–11] demonstrated outstanding performance. For instance, the Gaussian process regression (GPR) provided the pre-knowledge guidance

to optimize array mutual coupling with low side-lobe level (SLL) [9]. The support vector regressor (SVR) was utilized to predict the magnitude and the phase of periodic units' EM response for reflectarrays [10]. SVR also assisted in converting the polarization and reshaping the beam with an isoflux pattern [11]. Moreover, advanced deep learning (DL) and reinforcement learning (RL) were integrated into the antenna design processes [12–16]. For instance, the Bayesian neural networks (NNs) wrapping as surrogate models assisted antenna optimization with varying performance metrics [12, 13]. In [14], a computer-vision (CV) DL model combined with a traditional global optimization method, the genetic algorithm (GA), tuned the array elements for beam steering. Relying on human-like decisions with reward or penalty, RL realized automation learning in array decoupling optimization [15]. The variational autoencoders (AEs) in [16] encoded the optimum physical structure for the transmitarray design as a generative model.

From the antenna applications aspect, ML methods were also widely used in many antenna designs [17–20]. For example, in [17] the multiple-input multiple-output (MIMO) antenna in ultra-wideband (UWB) took advantage of the hybrid ML model to optimize the envelope correlation coefficient (ECC), diversity gain (DG), and total active reflection coefficient (TARC). This hybrid ML model was composed of SVR, GPR, and NN. Also related to the MIMO, the intelligent antenna switching, and massive MIMO in [18] achieved 18.5% higher energy efficiency over the traditional optimization methods. The RL scheme provided the optimized mapping between user elements (UE) positions and the number of active antennas during the switching in MIMO. Categorizing the information radiated from radio-frequency identification (RFID) chipless tags by utilizing ML was also a research topic. Over 99.3% accuracy was accomplished in chipless RFID measurement with five classification models [19]. Four regression models were evaluated to detect the sensing information of the 8-bit ID tag [20]. ML models also extracted high-dimensional meta-features from EM responses of on-body or implanted antennas [21–25]. For example, 1500 images in [21] were fed into convolutional neural networks (CNNs) for cancer detection.

Unlike various MLAO methods wrapped with surrogate models summarized in [26–28], data-informed machine learning (DIML) methods are explored in this paper, benefitting from a large dataset and simplicity of input/output (I/O) pairs. Data informing means all data are generated and packaged in customized formats in the first stage and then fed into the ML models in the second stage. In other words, DIMLs are regarded as "offline learning" compared to "online learning" of MLAO as a one-stage process [26]. DIML leverages generalization and scalability to include more antenna configurations with a unified format into a general model. It eliminates the consideration for the uncertain number of trials to find the local-best priori conditions in surrogate models [13, 27]. However, as a trade-off, there would be more variables from various antenna configurations to form the I/O datasets. DIML takes the fine-tuning ability of a single antenna configuration in exchange for pursuing the generalization and scalability of multiple configurations [28].

Compared with the data-informed concept, physics-informed machine learning (PIML) methods require much less data but more pre-knowledge physics. It solves the unknowns in partial differential equations (PDEs) at the high-dimensional expansions of classical EM algorithms. For example, PIMLs were applied with the Method of Moments (MoM) [29], Finite Element Method (FEM) [30], and Finite-Difference Time-Domain (FDTD) method [31, 32]. PIML mimics the behavior of numerical full-wave simulation solvers, which brings EM theoretical support to black-box prediction with the online learning surrogate. In [33], the application of PDEs transforms the classic NNs into PIML, and the proposed integral error function bypassed the pre-calculated training set with the self-learning ability. Nvidia's "Modulus" platform provides end-to-end ML solutions for various physics problems by linking the gap between DIML and PIML methods [34].

This paper presents an automated architecture utilizing the graphics processing unit (GPU) with the scalability of predicting antenna performance using DIML methods. The DIML methods are integrated with antenna design and will be necessary for our future works with PIML architecture. The general DIML architecture is presented in Fig. 1, containing two workflows utilizing a massive dataset of 49152 samples.

This paper is organized as follows. A dataset with 49152 full-wave simulations is described in Section II. The tabular workflow is demonstrated in Section III. Two classification models and two regression models based on ensemble learning are implemented to automate the predictions of antenna performance. In Section IV, the image-based workflow implements a DL NN with the Fourier Neural Operator (FNO) [35] to predict the input reflection coefficients (S_{11}) on the wide frequency range from 0.1 to 20 GHz. This neural operator is carefully designed to fit the EM frequency response with fine-tuned prediction accuracy. The conclusions and further work are presented in Section V.
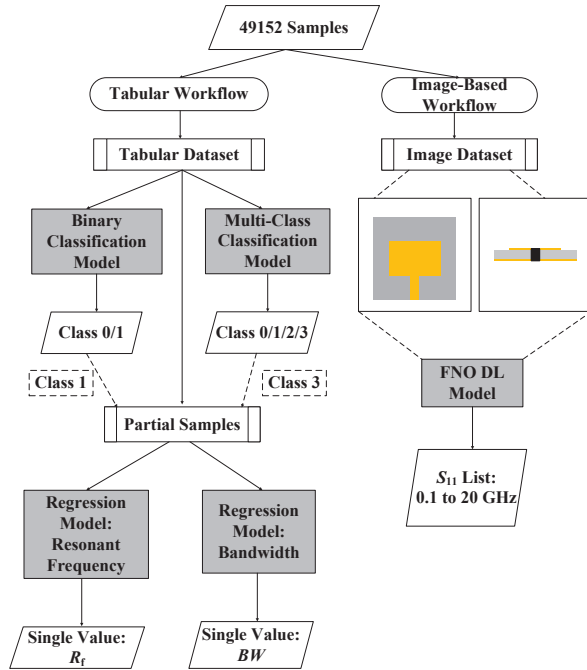
Fig. 1. The general architecture for the tabular and image-based workflow.

Fig. 2. Geometry of classical patch antenna on six different substrate materials (ε_{rj}) with two commercial thicknesses (h_i), 12 combinations constitute the total dataset.

II. DATASETS

As one of the most critical parts of DIML, it is essential to construct corresponding datasets feeding into the ML models with varying prediction targets. In this paper, a classical microstrip patch antenna fed by a transmission line (TL) on various substrates is used, as shown in Fig. 2. Since the proposed architecture is for generalization purposes and not for the specific antenna fine-tuning at a pre-defined narrow band, the scalability for this architecture will be discussed in the tabular and image-based workflows in Section III and Section IV, respectively.

In Fig. 2, six materials are listed with the relative permittivity (ε_r) covering a relatively wide range with discrete samplings as 2.2, 3.38, 4.0, 4.2, 4.4, and 6.12. These RF materials are often commercially available as RO5880C, RO4003C, FR4 type 1, FR4 type 2, FR4 type 3, and RO4360G2 in the order mentioned. It is apparent that the ε_r sampling is denser around 4.2 because FR4 is the most commonly used material for both EM research and industry mass production by compromising material loss tangents for the low cost.

Moreover, the FR4 ε_r values 4.0, 4.2, and 4.4 are the top three values appearing in various manufacturing datasheets, considering frequency dependency, temperature dependency, material variations, and testing methods. Similarly, the thickness values 0.8 mm and 1.6 mm are two typical thicknesses on the datasheets for all six mentioned materials without extra costs of customized

thickness. Six materials with two thicknesses form 12 combinations. In each combination, antenna dimensions sweep in the same way on the fixed 50 mm × 50 mm footprint size of the substrate with fully covered ground. In Fig. 2, when RO5880C is selected as the substrate (gray color) with ε_{r1}=2.2 and h_2=1.6 mm, the 50-Ω TL connects the radiating patch and the substrate edge for RF port excitation. The width W_{TL} is adaptively adjusted by the substrate thickness and permittivity to achieve the 50-Ω characteristic impedance. Hence, there are 12 different W_{TL} values for 12 combinations of substrate. The length L_{TL} is a dependent variable, making sure the TL connects the patch and the port at the substrate edge.

The radiating patch width W and length L vary from 5 mm to 36.5 mm with 0.5-mm increments, creating a 64×64 uniform grid-search space. Hence, there are 4096 antenna configurations in each substrate combination so, for the total dataset with 12 combinations, there are 49152 antenna configurations and, to rephrase, 49152 data samples for ML models to train and test with.

EM full-wave simulator CEMS based on FDTD method integrated with GPU acceleration [36] is used to obtain the full-wave responses for those 49152 antenna configurations at the frequency range from 0.1 to 20 GHz with 20 MHz frequency step (996 frequency points in total). Under the listed HW platform - Intel(R) Core (TM) i9-13900K; NVIDIA 4090 GPU with 24 GB memory; 128-GB DDR5 RAM at 4800 MHz - each antenna simulation takes 0.26 minutes. The time-domain (TD) solver is preset as 2000 time-steps and uniform cuboid cell sizes with increments of 0.1 mm, 0.25 mm, and 0.2 mm along x, y, and z directions, respectively. This cell
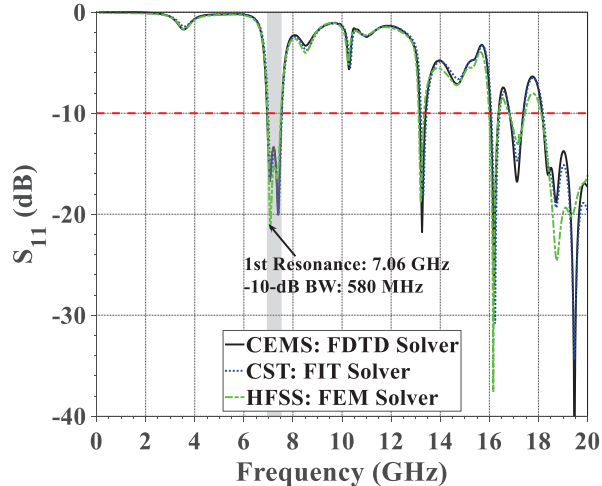
Fig. 3. Simulated S_{11} comparison among three full-wave simulation software with different solvers.

size will be regarded as the image-resolution limitation in the following image-based workflow.

CEMS simulations are repeated for each of the 49152 configurations, and the input reflection coefficients are obtained as S_{11} in decibel scale. For example, the result of one simulation is shown in Fig. 3. To check the consistency, simulation results from two other commercial full-wave simulation software, CST 2023 S_2 [37] and HFSS 2023 R_1 [38], are obtained to compare the simulated S_{11} values as the blue dotted curve and the green dash-dotted curve in Fig. 3, respectively. As CEMS uses the TD solver (FDTD), CST also uses a TD solver but with Finite Integration Technique (FIT), while HFSS utilizes an FD solver with FEM method. The S_{11} results from three simulators match with each other. Some deviations in the HFSS curve at the range higher than 18 GHz are caused by the inherent limitation of FD solvers for wide-band simulation [39].

A customized application programming interface (API) called CEMSPy is developed to automate the pipeline, from the massive generation of antenna models to the data post-processing of simulated results. Consequently, both inputs (antenna configurations) and outputs (S_{11} values) are ready to feed into the black boxes to establish the I/O relationship mapping for ML models. The tabular and image-based workflows use the same dataset of 49152 samples for single value prediction in Section III and the whole S_{11} curve regression in Section IV, respectively.

III. TABULAR WORKFLOW
A. Tabular datasets

For ML training based on the tabular dataset, all input features and output labels are arranged in the column-based table. The configuration information of

the 49152 classical patch antenna mentioned in Fig. 2 forms 49152 rows of the tabular dataset. Five configurations, W, L, h_i, ε_{rj}, and W_{TL}, are regarded as five input features for the tabular workflow. This research considers S_{11} values at 996 discrete points in the frequency range from 0.1 to 20 GHz as the ground-true outputs for each data sample. The output labels are the extracted observations from these simulated S_{11} values. These observations could be the discrete values as the classification labels or the continuous values as the regression labels. There are two classification labels and two regression labels in the tabular workflow, which will be discussed in detail.

In a previous work related to the tabular workflow, authors have shown that more data produces higher prediction accuracy by increasing the number of samples from 256 to 4209 [40]. The authors also inspected the binary classification (BC) and single-value regression models with 20480 antenna configurations on a single substrate [41]. As a continuation of the previous work, the tabular workflow in this work extends the prediction range from 0.1 to 20 GHz to show the generalization and combines 12 different material settings to show the scalability. First, two classification models will be introduced using the 1st and 2nd labels in Part B of this section. Two regression models will be presented using the 3rd and 4th labels stored in the tabular dataset in Part C. After that, the prediction of all S_{11} values at all frequencies will be discussed in Section IV.

B. Binary and multi-class classifications

As the 1st output label, the BC model is trying to predict if there is a valid resonance (R_f) in a valid bandwidth (BW). The valid R_f means 10% or less power reflects back to the excitation port, while the valid BW means the head and tail of -10-dB bandwidth are inside the frequency range from 0.1 to 20 GHz. The label assignments of valid R_f and BW are packaged in CEMSPy API and can be tailored to any frequency range for specified design requirements.

Figure 4 shows the label assignments for both the 1st label of BC and 2nd label of multi-class classification (MC). The same set of curves is applied to demonstrate the classification representations for both BC and 4-class MC, so there are four curves in Fig. 4.

For BC, the output at 996 frequency points having at least one valid R_f in a valid BW can be categorized as Class 1, like the black solid curve in Fig. 4. The S_{11} values in the valid band from 6.76 to 7.5 GHz are below -10 dB with two valid resonances at 6.88 and 7.36 GHz. Any other scenarios are categorized as Class 0 for BC. Under such binary strategies, 88.36% of samples in all 49152 antenna outputs are assigned in Binary Class 1 (BC: 1). The rest are assigned in Binary Class 0 (BC:
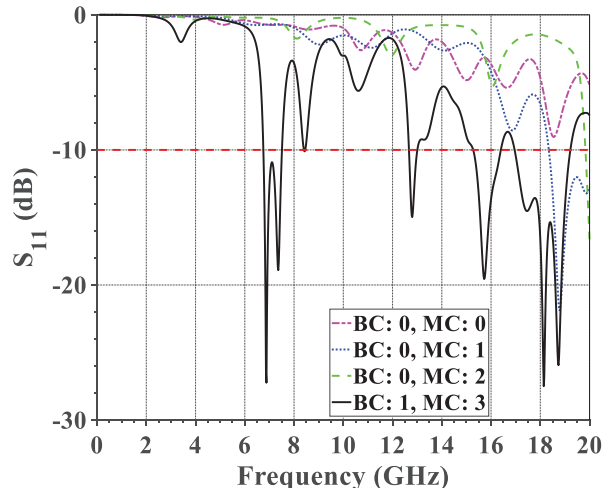
Fig. 4. Four S_{11} simulation results as the classing representatives of binary classification (BC) and multi-class classification (MC).

0). The definition of class assignment is demonstrated in Table 1. All 49152 samples are processed by CEMSPy and assigned the corresponding Class 0 or Class 1 for BC. The assigned binary information is stored in the tabular dataset as the 1st output label. Hence, five columns as five input features (W, L, h_i, ε_{rj}, and W_{TL}) and one column as the output label is poised for binary ML training and validation.

Table 1: Binary and multi-class definitions

(R_f, BW)	BC	MC	Ratio of Total (%)
(0, 0)	0	0	10.38
(Valid, Invalid)	0	1	0.76
(Invalid, Invalid)	0	2	0.50
(Valid, Valid)	1	3	88.36

An automatic ML tool called "AutoGluon" builds a platform for ensemble learning on tabular datasets for both classification and regression problems [42]. Ensemble learning is a weighted strategy that combines all well-trained models as a weighted ML model to make the best predictions. Many APIs in AutoGluon provide the flexibility to customize the ensembling structure, like the selection of ML base models, the distribution of weights, etc. Associated with a customized CEMSPy script, Auto-Gluon is integrated into the tabular workflow to process the tabular data automatically with scalable presetting.

For BC, all 49152 samples in the total dataset are split stochastically into train/test datasets with the ratio r_s: 80/20 under random seed 2. The same random strategy is carried through all the following work to maintain consistency and reproducibility. Those 20% samples as the test set only work for the well-trained model's over-

all performance on new data after training. During the training/validation iterations, 13 base models are listed in Table 2 that are trained on 36821 samples and validated simultaneously on the remaining 2500 samples in the 39321 train dataset. Two classification metrics, F_1 score and Log loss, are used for the quantitative evaluation during the iteration of training/validation process. A total of 13 base models are updated independently towards the perfect prediction score of 1.0 and loss of 0.0 as the ideal goals. The training/validation process of 13 models will terminate when the F_1 score does not increase or Log loss no longer decreases significantly. For each sample, the F_1 score is calculated as:

$$F_1 = \frac{2TP}{2TP + FP + FN}, \quad (1)$$

where TP, often called "True Positive", stands for the correct prediction of Class 1. Similarly, in statistical analysis, FP (False Positive) and FN (False Negative) stand for overestimation and underestimation. However, it can be noticed that TN (True Negative) is missed in the F_1 score. In other words, the scenario for the correct rejection is not counted. That is the reason why another metric Log loss is used as:

$$L_{\log}(y, p) = -[y \log(p) + (1 - y) \log(1 - p)], \quad (2)$$

where, p is the probability estimating label $y=1$ for a single sample. The averaged value F_1 score and Log loss on all test samples evaluate the general reliability of the BC model.

Table 2: Ensemble model for binary classification

Index	Model	F_1 Score	Log Loss
0	Stacked Model	0.970272	0.171912
1	KNeighborsUnif	0.968224	0.389549
2	CatBoost	0.967822	0.185379
3	KNeighborsDist	0.967149	0.386027
4	XGBoost	0.965579	0.188325
5	LightGBMLarge	0.965428	0.181846
6	ExtraTreesEntr	0.964930	0.290892
7	ExtraTreesGini	0.964856	0.286748
8	LightGBM	0.964516	0.190572
9	RandomForestEntr	0.963731	0.301912
10	RandomForestGini	0.963173	0.315406
11	NeuralNetFastAI	0.962329	0.205084
12	NeuralNetTorch	0.961868	0.185094
13	LightGBMXT	0.961072	0.197700

The final F_1 score and Log loss average on the test datasets are displayed in Table 2. The stacked model at index 0 is the weighted combination of all 13 base models from 1 to 13. As a result, when the new/unseen antenna configuration is characterized by five features, W, L, h_i, ε_{rj}, and W_{TL}, the stacked model can make the

real-time prediction of whether there is a resonance point in a valid BW (BC: 1) or not (BC: 0). The F_1 score 0.97027 and Log loss 0.171912 indicates the ensemble model can achieve relatively reasonable prediction in the frequency range from 0.1 to 20 GHz.

For the 2nd output label, the MC aims to refine the binary classes to four classes. The data categories for MC are also summarized in Table 1. For example, invalid BW means either the head or tail is out of the preset frequency range. For the blue-dotted and green-dashed curves in Fig. 4, both tails are out of 20 GHz, so these two antenna configurations are regarded as having invalid BW.

The invalid R_f is only triggered when there is an invalid BW. According to the definition, if a valid -10-dB BW exists, at least one peak value must be inside the range. The green-dashed curve in Fig. 4 presents the antenna configuration with both invalid R_f and BW because of the S_{11} values' monotonical decrease at the tail of the frequency range. Mirror symmetrically, if the S_{11} values increase monotonically at the head range, that configuration also has invalid R_f and BW.

An automatic pipeline has already been established for BC prediction using CEMSPy as mentioned previously. With its scalability, MC can also be implemented similarly with the slight modification of BC models. The prediction of 20% of test data achieves 0.93323 weighted F_1 and 0.2004 Log loss. However, it can also be noted in the last column of Table 1 that Class 1 (MC: 1) and Class 2 (MC: 2) have a relatively small number of samples compared to the total number of samples. As a result, it is an unbalanced MC problem in the whole frequency range, and it causes the MC model to be unbalanced and gives it an inherently high F_1 score of 0.93323. Therefore, for the unbalanced MC, an additional term called 'balanced Acc' is a more convincing metric to evaluate the quality of the unbalanced model:

$$Acc_{balanced} = \frac{TP}{2(TP+FN)} + \frac{TN}{2(TN+FP)}, \quad (3)$$

where TP, TN, FN, and FP follow the exact definition in (1). It gives a value of 0.55790, which is not a good score but in line with expectations due to the imbalance.

MC is not applicable for prediction in such a wide frequency range from 0.1 to 20 GHz. The application scenario would be more suitable to classify with clear objectives in narrower bands, like limiting the range to around 5.8 GHz for Wi-Fi design or around 10 GHz for space communication. In such narrow bands, the four reallocated classes will be more balanced, and the prediction will be more accurate. The CEMSPy API provides scalable functions to automate the general pipeline with the required objectives. For example, to optimize an antenna at 5.8 GHz for Wi-Fi applications, CEMSPy APIs will only simulate the models in the frequency range from 5 to 7 GHz and make the multiple-class

assignment accordingly. In addition to balancing the MC, it will save significant time and computational resources to generate the I/O dataset with auto-assigned classes.

C. Single-value regressions

Unlike classification problems, single-value regression focuses on predicting a continuous value extracted from all S_{11} values at 996 frequency points. In this section, the 1st valid R_f and its BW will be predicted by two regression models with similar automatic pipelines as mentioned before, but for the regression scenarios. Following the 1st and 2nd labels in the tabular dataset of all 49152 samples, the 3rd label and 4th label are assigned to the 1st valid R_f and its valid BW, respectively. Hence, the first single-value regression model could predict the 1st valid R_f for a given input set of W, L, h_i, ε_{rj}, and W_{TL}, and the second model for the associated BW. There is an assumption that the input antenna configuration should have a valid R_f and valid BW. A data filter follows the class definition in Table 1. Only BC: 1 (same as MC: 3) are considered as valid samples for the two regression models. The samples in these classes are also described as "Partial Samples" in the general architecture shown in Fig. 1.

By taking 88.36% of the total 49152 samples, a truncated tabular dataset with 43431 antenna configurations is selected for two regression models. Each configuration extracts the 3rd output label, R_f in GHz, and the 4th label, BW in MHz, from the corresponding S_{11} values at 996 frequency points. For comparison, the 1st and 2nd labels are assigned as binary and multiple classes in BC and MC problems. Before the train/test splitting, 10 samples as the observers from each substrate combination (12 combinations) are dropped out randomly and stitched together as an observation dataset with 120 samples. Those samples will not be involved in any training/validation or testing process. Eventually, there are 34648, 8663, and 120 samples for training/validation, testing, and observation. The deeper reason for the observation dataset with 120 samples is that they can evenly observe the final model performance on different substrate combinations. If the model performance has a noticeable degradation in one of the 12 substrate combinations, the hyperparameters can be fine-tuned and prioritized for the respective combination separately.

Like the BC and MC pipelines, the ensemble learning method is also applied to the two single-value regression models but with deeper stacking. In the 1st stacking layer, 11 base ML models produce 10 outputs as 10 new features for the 2nd layer. Those 10 features are imported as the input in the 2nd stacking level to predict the targeted single-value output, which is R_f and BW, respectively. Compared with a one-layer structure with 13 flattened base models for BC and MC, each single-value

regression model is weighted by 21 stacked models. One score metric called R^2 score:

$$R^2 = 1 - \frac{\sum_{i=1}^{N}(y_i - \hat{y}_i)}{\sum_{i=1}^{N}\left(y_i - \frac{1}{N}\sum_{i=1}^{N}y_i\right)}, \qquad (4)$$

and another loss metric called root-mean-squared error (*RMSE*):

$$RMSE = \sqrt{\frac{1}{N}\sum_{i=1}^{N}(y_i - \hat{y}_i)^2} \qquad (5)$$

are enforced to increase the score and reduce the loss during each training/validation iteration. After training, (4) and (5) are applied again to evaluate the final model performance as two averaged values.

In both (4) and (5), y_i represents the simulated value as ground true and $\hat{y}_i$ as the corresponding predicted value by regression. Theoretically, perfect regression always has a maximum score of 1.0 and a minimum loss of 0.0, like the F_1 score and *Log* loss for the ideal classification. The final performances for the R_f and *BW* regressions are listed in Table 3. The R^2/*RMSE* values for the test dataset with 8663 samples are the global representation of the well-trained models. The R^2/*RMSE* ones for 120 observers are used to mimic the behavior of well-trained models when seeing new data from 12 substrate combinations evenly. The "new" here means 10 sets of (W, L, h_i, ε_{rj}, and W_{TL}) from each 12 combinations that are generated randomly to observe their predicted R_f and *BW*.

Table 3: Single-value regression performance

Prediction	Dataset	Samples	R^2 Score	*RMSE*
R_f	Test	8663	0.912440	1.171061
R_f	User	120	0.932543	1.119442
BW	Test	8663	0.818673	135.9358
BW	User	120	0.770934	162.6399

To better visualize the offset between the true value from simulation and the prediction from ML, the absolute relative error (*ARE*) in percentage

$$ARE = \left|\frac{y_i - \hat{y}_i}{y_i}\right| \times 100\%, \qquad (6)$$

is used, where y_i and $\hat{y}_i$ follow the same definition as in (4) and (5).

For both single-value regressions of R_f and BW, both prediction/true offsets for 8663 samples can be calculated and stored in two *ARE* lists: ARE_{Rf} and ARE_{BW}. The cumulative distribution function (CDF) is implemented to observe the error distribution for both regressions as shown in Fig. 5. Two markers are printed based on the cumulative probabilities of two threshold values on the solid red and the blue-dashed curves, respectively. Since the R_2 score value is a bounded value in the range

[0.0, 1.0], it can be regarded as a threshold representative of the cumulative probability. The first threshold is the same as the cumulative probability 0.5 for both curves. The second threshold is the R_2 score but different for R_f (solid red curve) and *BW* (blue-dashed curve). As the first vertical dashed threshold on the solid red curve, 50% of samples in total 8663 have *ARE* equal to or less than 3.17% for R_f. The second threshold indicates that 91% have *ARE* equal to or less than 18.87%. Also, as the two thresholds on the blue-dashed curve, 50% of samples have *ARE* equal to or less than 17.75% for *BW*, and 82% have *ARE* equal to or less than 64.62%.
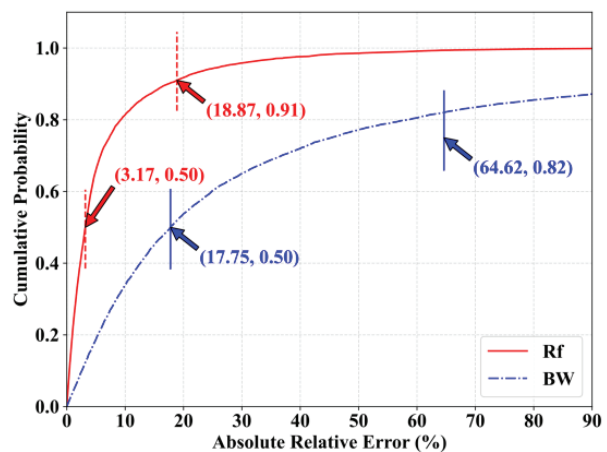
Fig. 5. Cumulative distribution of absolute relative error between true and prediction for Rf and BW on 8663 test samples.

Comparing the *ARE* curve for *BW* with that for R_f in Fig. 5, there is a dramatic degradation in *BW* prediction due to the resolution preset for frequency points. For the purpose of generalization, a very wide frequency range from 0.1 to 20 GHz with an incremental step of 20 MHz is utilized to show the performance on those 996 frequency points. The minimum -10 dB *BW* is 40 MHz because at least two values equal to or less than -10 dB could form a band. For better visualization of the value distribution, both the 3rd and 4th labels of all 43311 samples are normalized to the same range from 0.0 to 1.0 range based on the min-max normalization, as shown in Fig. 6. The normalized *BW* on the right has a much more compact distribution than that for normalized R_f on the left. It can be expected that many antenna configurations with lower *BW* performance will share the same BW values (4th label) under such frequency resolution.

Further uniqueness analysis in Table 4 shows the extreme cases with the top-3 and bottom-3 unique counts for the 3rd and 4th labels of all 43311 samples. There are 839 unique R_f values as the 3rd label and 145 unique *BW* values as the 4th label for all 43311 samples. The
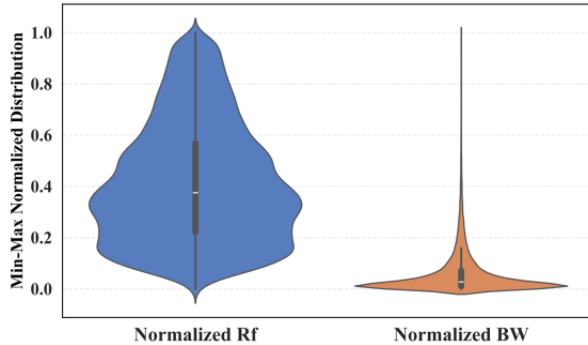
Fig. 6. Min-Max normalized distribution for both valid R_f and valid BW on 43311 samples.

Table 4: Unique counts for R_f and BW

Index	R_f (GHz)	Counts	BW (MHz)	Counts
Top 1	8.34	118	40.0	5509
Top 2	5.80	116	60.0	4935
Top 3	7.16	111	80.0	3796
Bottom 3	19.94	1	3120.0	1
Bottom 2	3.18	1	3060.0	1
Bottom 1	3.12	1	3340.0	1

top-3 and bottom-3 unique counts are listed in Table 4 after sorting from largest to smallest. For example, 5509 samples of a total of 43311 have the same 40-MHz *BW*, which is highly concentrated compared to 118 samples with 8.34-GHz R_f as the maximum unique counts.

From Table 4 and Fig. 6, it can be concluded that for a wide band range with such frequency resolution, the *BW* prediction cannot perform well due to the concentrated distribution with large identical values. As mentioned previously in the MC part, it is also a limitation of generalization, even though the BC and R_f regression performances are reasonably good.

D. Limitation of tabular workflow

When considering generalization and scalability as the purposes, the limitation of tabular workflow is raised from two aspects. First, from the local point of view, even though the predictions are relatively good for BC and R_f regression, the wide frequency range brings imbalance for the class definition in MC. Also, the frequency resolution limits the output uniqueness and distribution in BW regression. The first limitation can be broken by setting the narrow range for specific design requirements mentioned as the 5 to 7 GHz range for 5.8 GHz Wi-Fi antenna design in the MC part. The second limitation can be eliminated with a smaller sweeping step in the narrow range. Both concerns can be solved by utilizing the scalable CEMSPy APIs. However, it will push the model to fall into the specific local optimum and defeat

the purpose of generalization. Second, from the global aspect, the tabular workflow is based on tabular datasets. Ideally, when more antenna configurations are included, users can extend the feature space along the column and the number of samples along the row to achieve scalability. However, various configurations share different parameters, and these parameters increase the complexity of constructing the tabular dataset. More configurations cause much more extensive and sparser feature space with the majority number of NaN values. Defining and unifying the variable names in tabular datasets will also be problematic. As a result, an image-based workflow is introduced in the following section. No parameter needs to be defined in the input tabular dataset; all antenna configurations will be described by the images of slice cuts from different observation planes, like magnetic resonance imaging (MRI) scanning for human tissues.

IV. IMAGE-BASED WORKFLOW

There is always a principle of DIML that post-processed data should be easy to expand at high-dimensional mapping space as the bridge connecting inputs and outputs. Inevitably, some information will be lost in the feature-extraction period from original data to post-processed data, like from the full-wave simulation model to the tabular dataset. The more information is retained from the original data, the more complicated and accurate outputs can be predicted [2]. In the tabular workflow, the original data from 49152 full-wave simulations are extracted and stored in the tabular dataset. Five input features (W, L, h_i, ε_{rj}, and W_{TL}) in the five columns are applied to predict four single-value labels column by column as BC, MC, R_f, and *BW* regression.

For each label in the tabular workflow, the single value is extracted from all S_{11} values at 996 frequency points with presupposed conditions and assumptions. Hence, all four labels highly summarize the S_{11} responses but discard lots of information in the original 996 values. It restricts the tabular workflow from achieving the purpose of generalization and scalability.

This section presents the details of the image-based workflow, showing that images carry much more input information than the tabular dataset, and the workflow will predict all the S_{11} values in the whole frequency range. The same patch antenna in Fig. 2 demonstrates the image-based workflow. Two images with 600×600 resolutions are encoded and shown in Fig. 7. They represent two cross-sectional views of a 60 mm × 60 mm × 60 mm EM problem space. The antenna is placed at the center of the problem space based on proportional dimensions. Two cross-sectional views are selected as the observation of the patch antenna at the x-y and x-z planes in Fig. 2. All pixels in the two images are assigned the encoded
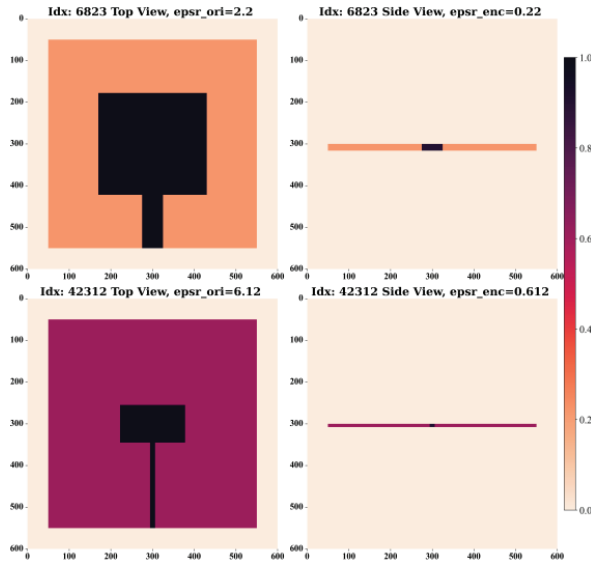
Fig. 7. Encoded images of top and side views of two random samples at the index of 6823 and 42312 in total 49152 samples.

values in Table 5, to represent the materials considered with EM characteristics. For instance, the pixels with values of 0.22 represent substrate material RO5880 in these pixels.

Table 5: Encoding card

Materials	Info	Encoded Value	Encoded Range
Free Space	Lossless Transmission	0.0	[0.0, 0.1]
Buffer 1	Boundary	NaN	(0.1, 0.2)
RO5880	ε_r=2.2	0.220	[0.2, 0.8]
RO4003C	ε_r=3.38	0.338	[0.2, 0.8]
FR4 Type 1	ε_r=4.0	0.400	[0.2, 0.8]
FR4 Type 2	ε_r=4.2	0.420	[0.2, 0.8]
FR4 Type 3	ε_r=4.4	0.440	[0.2, 0.8]
RO4360G	ε_r=6.12	0.612	[0.2, 0.8]
Buffer 2	Boundary	NaN	(0.8, 0.9)
Port	SMA Feed	0.9	[0.9, 1.0]
Perfect Conductor	Lossless Reflection	1.0	[0.9, 1.0]

Encoded values in the range [0.0, 1.0] are assigned to distinguish components by filling in the image pixels to represent antenna configurations with material information. Table 5 lists the encoding information for all corresponding components. There are two boundaries to split all components into three sections with enough buffering. In the middle-encoded range [0.2, 0.8], all dielectric materials are normalized in this range. Cur-

rently, the normalization factor 10 is applied on all dielectric materials, and it can be modified for scalability if the dielectric materials have relative permittivity less than 2 or larger than 8.

The two terminal values, 0.0 and 1.0, represent the free space and perfect conductor (PEC) as the lossless transmission and lossless reflection, respectively. The values can be assigned in the range [0.0, 0.1] for any lossy propagating environment. Any conducting materials with losses can be placed in the range [0.9, 1.0]. For example, the Subminiature Version A (SMA) port is assigned as 0.9. When new materials are involved, they can be designated as new values in the encoded card as new rows in Table 5. Then, new antenna configurations can pick up the values to form the images accordingly. Thus, the image-based workflow can be extended to any antenna configurations with the scalable card in Table 5.

Two encoded images for the demo configurations are displayed in Fig. 7, and they exemplify all configurations through shapes and colors. Instead of defining the variables in the tabular dataset, images carry all information in pixels, even for the different antenna types. In Fig. 7, two antenna configurations with the indices of 6823 and 42312 are selected from the total 49182 antenna samples. In the left column of Fig. 7, two top-view images embody the difference in three aspects: substrate materials, radiating patch dimensions, and width of TL. From the right column, the difference is presented in substrate thickness, width of TL, and substrate materials. Applying this encoding strategy using the integrated CEMSPy scripts, all 49152 antenna samples can be encoded and stored in a high-dimensional matrix with shape (49152, 600, 600, 2) as the ML inputs.

In the input matrix, the 1st dimension shows the number of samples N_{sam}, the 2nd and 3rd dimensions are the resolution of R_x and R_y, and the 4th dimension is the number of the plane-cut views N_{cp}. As the target of image-based workflow, all S_{11} values at 996 frequency points from 0.1 to 20 GHz are predicted. Hence, the output matrix is formed in the shape (49152, 996). In the output matrix, the first dimension is the same as N_{sam} for inputs, and the second dimension is the number of S_{11} values at N_{freq} frequency points.

So far, the I/O matrices are ready for the image-based DIML workflow. However, the I/O here is much more complicated than that for the tabular dataset. Furthermore, as the S_{11} curves manifested in Figs. 3 and 4, there are correlations among adjacent points on the curves. In other words, the S_{11} curve could be regarded as sequential data. Theoretically, it means for the EM response of the conjugated impedance matching at the excitation port, there should be a continuous EM response along with frequency [39]. This EM property makes the traditional ML architecture not suitable for the

image-based workflow since the independent and identical distribution (i.i.d.) is often assumed in many ML models [2]. Therefore, FNO is raised as a succinct and efficient solution using an eight-layer structure with relatively faster convergence for the S_{11} curve regression. It involves the EM I/O characteristics in the spectral convolutional transformations [35].

For the training/validation splitting, 152 samples are dropped out randomly only for observation purposes, as the observers mentioned in the tabular regression workflow. Then, an 80/20 splitting ratio is applied to the remaining 49000 samples. So, there are 39200 samples for training and, during the training iterations, 9800 samples are monitored to provide the performance feedback simultaneously. The model performance is optimized by evaluating the R^2 score and L_2 loss on the training and validating sets correspondingly. The R^2 score is illustrated in (4) and L_2 loss is the squared value of *RMSE* mentioned in (5). Second, after the training/validation process, all 152 samples are used to "observe" the well-trained models and provide the evaluation since those 152 samples are new and unseen by the well-trained model.

The brief NN architecture with matrix shape information is portrayed in Fig. 8, based on a single data batch with five samples. Four fully connected (FC) layers and four Fourier layers alternately construct the main skeleton of this NN used in the image-based workflow.

In the dashed zoom-in box of Fig. 8, each input $v(x)$ processes the Fourier layers shown in the gray shadow area. The Fourier operator starts from the Fourier transform F, to the linear transform $\mathfrak{R}$ with a low-pass filter, then applies the inverse Fourier transform F^{-1}. During the backpropagation, the operator adjusts weights w to maximize the R^2 score and minimize L_2 loss.

By superimposing the transform and weights, the activation function Gaussian Error Linear Unit (GELU) introduces non-linearity into the model. The FNO learns the complex patterns from the images with 600×600 pixels. GELU provides a smooth curve, making it computationally beneficial for optimization with faster convergence during training. The same activation function is also applied to link the FC layers. Taking five samples as the batch size B_s of a 4-D input, the variation of batch shape between NN layers is described in the intermediate flow of Fig. 8. The batch shape starts from the initial inputs with shape (B_s, R_x, R_y, N_{cp}) to the final output with shape (B_s, N_{freq}). The smoothness and nonmonotonicity of GELU bring the possibility of predicting the continuous S_{11} curves at N_{freq} points.

The hyperparameters in the NN architecture are fine-tuned to achieve the trade-off between the best performance of the R^2 score and L_2 loss. This workflow optimizes eight hyperparameters: learning rate L_r,
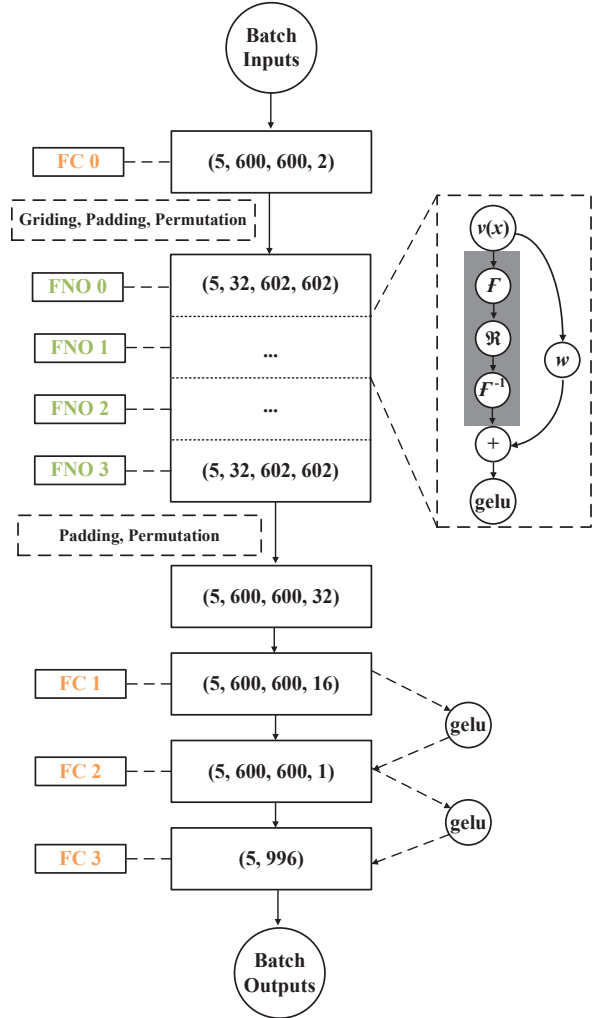
Fig. 8. Neural network architecture with four Fourier and four fully connected layers takes five samples as a batch during optimizing the R^2 score and L_2 loss.

batch size B_s, step size S_s, gamma Γ, modes N_{mod}, widths W_d, number of FC layers N_{FC}, and number of FNO layers N_{FNO}. By grid searching the hyperparameter space, eight hyperparameters are selected as L_r=0.001, B_s=S_s=5, Γ=0.5, N_{mod}=W_d=32, and N_{FC}=N_{FNO}=4. The L_2 loss and R^2 scores are achieved as 0.0742 and 0.9091 on 39200 training samples after 160 epochs and corresponding 0.0871 and 0.8728 on 9800 validation samples.

The L_2 loss and R^2 score variations with epochs are shown in Fig. 9. Both loss and score values for training and validation remain stable after 60 epochs, which indicates that the DIML model can converge and catch the prediction properly without underfitting or overfitting issues.

After the training/validation process with 160 epochs, 152 random samples are fed into the well-trained
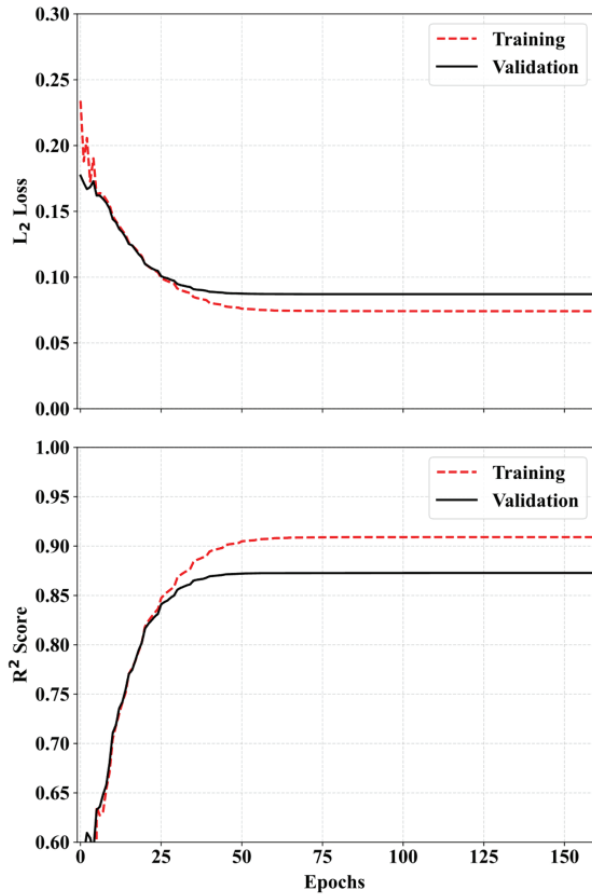
Fig. 9. Training/validation L_2 loss and R^2 score variations with epochs.

Fig. 10. Representative comparison of prediction and full-wave simulation at three indexes in all 152 samples: 34, 137 and 59.

model to review the prediction performance on random antenna configurations. A total of 152 samples perform 0.0877 and 0.8725 for the averaged L_2 loss and R^2 score, respectively. Figure 10 compares the simulated S_{11} results as ground truth and the predicted S_{11} results by the FNO model on three representative antenna configurations. In each subplot of Fig. 10, the floating textbox shows the sample index in 152 total observation samples. The red-dashed curves represent the simulated S_{11} results as true values. The solid black curves show the predicted S_{11} when two encoded images are fed into the well-trained NNs without simulation. Moreover, for the input matrix with shape (152, 600, 600, 2), the model can make the prediction for all 152 samples in near real-time and produce an output matrix with shape (152, 996).

In the top subplot of Fig. 10, when the S_{11} curve transits smoothly with less resonance along the full frequency range from 0.1 to 20 GHz, the fluctuations are relatively small. The FNO model can predict the S_{11} values on all 996 frequency points very well. This case is classified as MC 0 in Table 1 with both zero R_f and BW.

In the middle subplot, this kind of S_{11} response is a typical performance requirement of an alternative antenna design. The EM response has several resonances with S_{11} values below -10 dB, and the impedance matching at the excitation port is conjugated harmoniously without glitches. But, in the higher frequency range, the FNO model could not predict the bands with two nearby resonances, like around 15 and 17.5 GHz. It is one topic of the authors' following work to fine-tune the FNO model on the required narrower band. As for the bottom subplot in Fig. 10, there are more resonances and narrower BW in the whole frequency range compared to the red-dashed curves in the top and middle subplots. This causes more difficulty in prediction for the well-trained model. However, there is a tendency for the FNO model to catch all ripples on the curve. A similar observation is that the prediction at the lower frequency range is better than that at the higher frequency range.

The image-based workflow is backward compatible with all four models in the tabular workflow: BC,

MC, regression for R_f, and BW. More than that, it breaks the limitation of the tabular dataset. The plane-cut images reserve much more information from the original antenna model. The dataset is no longer bothered by pre-defined labeling and imbalanced sampling issues. The FNO model could provide a near real-time prediction close to the simulation results for a given antenna described by the encoded image. CEMSPy developers and users could customize or truncate the frequency ranges based on specific applications and then fine-tune the antenna designs.

Furthermore, the I/O data formats allow generalization and scalability when more antenna configurations are involved. As the input matrix follows the shape (49152, 600, 600, 2), sample numbers at the 1st dimension will be increased if there are more configurations. More complicated configurations add more plane-cut views at the 4th dimension. Those views describe the antenna structure from different observation directions. The 4th dimension will always consider the maximum number of views compatible with different antennas. If some antennas don't need specific views, those images will be filled with NaN values to keep the uniform number of views at the 4th dimension. A total of 600×600 pixels at the 2nd and 3rd dimensions could accommodate the 0.1-mm dimension changes in the design. When considering the fabrication tolerance, this resolution is adequate in antenna design, and users can refine it. This 0.1-mm dimension is also the limitation of the CEMS cell size setting. In the current simulations, the minimum cell size is 0.1 mm along the x direction, and the other two cell sizes are 0.25 mm and 0.2 mm along the y and z directions, respectively. The image resolution and the CEMS cell size both ensure that the simulation results can be relied on as the true values in ML regression.

In the view of input encoded images, colors will hold all material information in the images with 600×600 resolution. Users can pick the color from the encoded card in Table 5 and then fill all pixels using the CEMSPy API for all plan-cut views. In the case there is no required material in the card, users can define the encoded values derived from the corresponding encoded ranges with solid boundaries. From another view of the output shape (49152, 996), the 1st dimension keeps the one-on-one mapping with the 1st dimension of inputs. The 2nd dimension reserves a list of predicted values for each sample. In this general workflow, it is an S_{11} list with 996 frequency points. Similarly, it can be the list like voltage standing wave ratio (VSWR), maximum gain (G), minimum axial ratio (AR), and so on. By modifying the final FC layer structure in the FNO model presented in Fig. 8, the pipeline could also predict the 2D matrix, like the whole spherical radiation pattern at defined frequency points.

However, there are also limitations to this image-based workflow. First, as for the input, since it only demonstrates the generalization and scalability purpose, only a classic patch antenna is utilized as the proof of concept. The authors' following work will generate a more diverse dataset in which there are more antenna configurations as input. Second, only S_{11} values are predicted as output in the current image-based workflow, and no other antenna performance is involved. It will be the extended work of this pipeline to consider more radiation parameters as output. For any developers or users applying the tabular or image-based workflow, except for customizing the antenna configuration and performance requirements, all parts will remain the same as the proposed workflow by applying the automatic pipeline with integrated CEMSPy APIs. The scalable pipeline will handle all work from simulation, data post-processing, and ML training to validation. Unlike the MLAO models, both tabular and image-based workflows are freed from the cost function customized by the trial-and-error approach, and neither need to calibrate the parameters with ML assistance during the iteration. CEMSPy packages all work inside the DIML black box in the training/validation process. With the well-trained model, users could get near-real-time predictions based on tabular or image inputs.

V. CONCLUSION

This paper proposes an automated architecture to predict the antenna performance S_{11} values using the DIML methods in different data-format levels. The tabular and image-based workflows take the same 49152 samples with 12 different material combinations but utilize different dataset formats. Both exhibit the properties of scalability and generalization from various points of view. In the tabular workflow, the binary and multi-class classifications achieved 0.970 and 0.933 F_1 scores on the test dataset with 9831 samples. The single-value regression models for R_f and BW accomplished 0.912 and 0.819 R_2 scores on 8663 test samples. In the image-based workflow, the 9800 validation samples reached a 0.873 R_2 score for prediction after hyperparameter optimization in the FNO DL model. The scalable workflows and the easy-to-append dataset format give the architecture great potential to accommodate other antenna types and more diverse performance needs. It can be regarded as a pre-trained model for other projects. This DIML is also a necessary part of the future PIML work, with much fewer samples required.

ACKNOWLEDGMENT

REFERENCES

[1] C. M. Bishop and M. N. Nasser, *Pattern Recognition and Machine Learning*. New York: Springer, 2006.

[2] K. P. Murphy, *Machine Learning: A Probabilistic Perspective*. Cambridge, MA: MIT Press, 2012.

[3] M. Martínez-Ramón, A. Gupta, J. L. Rojo-Álvarez, and G. C. Christos, *Machine Learning Applications in Electromagnetics and Antenna Array Processing*. London: Artech House, 2021.

[4] M. Li and S. Marco, *Applications of Deep Learning in Electromagnetics: Teaching Maxwell's Equations to Machines*. London: IET, 2023.

[5] J. Wang, Y. Hao, and Y. Cheng, "A comprehensive prediction model for VHF radio wave propagation by integrating entropy weight theory and machine learning methods," *IEEE Transactions on Antennas and Propagation*, vol. 71, no. 7, pp. 6249-6254, Apr. 2023.

[6] R. R. Alavi, R. Mirzavand, J. Doucette, and P. Mousavi, "An adaptive data acquisition and clustering technique to enhance the speed of spherical near-field antenna measurements," *IEEE Antennas and Wireless Propagation Letters*, vol. 18, no. 11, pp. 2325-2329, Aug. 2019.

[7] R. Adeogun, "Calibration of stochastic radio propagation models using machine learning," *IEEE Antennas and Wireless Propagation Letters*, vol. 18, no. 12, pp. 2538-2542, Sep. 2019.

[8] A. Bereyhi, A. Vagollari, S. Asaad, R. R. Müller, W. Gerstacker, and H. V. Poor, "Device scheduling in over-the-air federated learning via matching pursuit," *IEEE Transactions on Signal Processing*, vol. 71, pp. 2188-2203, June 2023.

[9] Q. Wu, W. Chen, C. Yu, H. Wang, and W. Hong, "Knowledge-guided active-base-element modeling in machine-learning-assisted antenna-array design," *IEEE Transactions on Antennas and Propagation*, vol. 71, no. 2, pp. 1578-1589, Feb. 2023.

[10] M. Salucci, L. Tenuti, G. Oliveri, and A. Massa, "Efficient prediction of the EM response of reflectarray antenna elements by an advanced statistical learning method," *IEEE Transactions on Antennas and Propagation*, vol. 66, no. 8, pp. 3995-4007, May 2018.

[11] D. R. Prado, P. Naseri, J. A. López-Fernández, S. V. Hum, and M. Arrebola, "Support vector regression-enabled optimization strategy of dual circularly-polarized shaped-beam reflectarray with improved cross-polarization performance," *IEEE Transactions on Antennas and Propagation*, vol. 71, no. 1, pp. 497-507, Oct. 2022.

[12] B. Liu, M. O. Akinsolu, C. Song, Q. Hua, P. Excell, Q. Xu, Y, Huang, and M. A. Imran, "An efficient method for complex antenna design based on a self adaptive surrogate model-assisted optimization technique," *IEEE Transactions on Antennas and Propagation*, vol. 69, no. 4, pp. 2302-2315, Jan. 2021.

[13] Y. Liu, B. Liu, M. Ur-Rehman, M. A. Imran, M. O. Akinsolu, P. Excell, and Q. Hua, "An efficient method for antenna design based on a self-adaptive Bayesian neural network-assisted global optimization technique," *IEEE Transactions on Antennas and Propagation*, vol. 70, no. 12, pp. 11375-11388, Oct. 2022.

[14] V. Loscrí, C. Rizza, A. Benslimane, A. M. Vegni, E. Innocenti, and R. Giuliano, "BEST-RIM: A mm wave beam steering approach based on computer vision-enhanced reconfigurable intelligent metasurfaces," *IEEE Transactions on Vehicular Technology*, vol. 72, no. 6, pp. 7613-7626, Feb. 2023.

[15] Z. Wei, Z. Zhou, P. Wang, J. Ren, Y. Yin, G. F. Pedersen, and M. Shen, "Fully automated design method based on reinforcement learning and surrogate modeling for antenna array decoupling," *IEEE Transactions on Antennas and Propagation*, vol. 71, no. 1, pp. 660-671, Jan. 2023.

[16] P. Naseri and S. V. Hum, "A generative machine learning-based approach for inverse design of multilayer metasurfaces," *IEEE Transactions on Antennas and Propagation*, vol. 69, no. 9, pp. 5725-5739, Sep. 2021.

[17] D. Sarkar, T. Khan, and A. A. Kishk, "Machine learning assisted hybrid electromagnetic modeling framework and its applications to UWB MIMO antennas," *IEEE Access*, vol. 11, pp. 19645-19656, Feb. 2023.

[18] M. Hoffmann and K. Pawel, "Reinforcement learning for energy-efficient 5G massive MIMO: Intelligent antenna switching," *IEEE Access*, vol. 9, pp. 30329-130339, Sep. 2021.

[19] F. Villa-Gonzalez, J. J. F. Sokoudjou, O. Pedrosa, D. Valderas, and I. Ochoa, "Analysis of machine learning algorithms for USRP-based smart chipless RFID readers," *2023 17th European Conference on Antennas and Propagation (EuCAP)*, Florence, Italy, pp. 1-5, May 2023.

[20] N. Rather, R. B. Simorangkir, J. Buckley, B. O'Flynn, and S. Tedesco, "Evaluation of machine learning models for a chipless RFID sensor tag," *2023 17th European Conference on Antennas and Propagation (EuCAP)*, Florence, Italy, pp. 1-5, May 2023.

[21] S. Costanzo, A. Flores, and G. Buonanno. "Fast and accurate CNN-based machine learning approach for microwave medical imaging in cancer

detection," *IEEE Access*, vol. 11, pp. 2169-3536, June 2023.

[22] Y. Kim and Y. Li, "Human activity classification with transmission and reflection coefficients of on-body antennas through deep convolutional neural networks," *IEEE Transactions on Antennas and Propagation*, vol. 65, no. 5, pp. 2764-2768, Mar. 2017.

[23] S. K. Singh and A. N. Yadav, "Machine learning approach in optimal localization of tumor using a novel SIW-based antenna for improvement of ablation zone in hepatocellular carcinoma," *IEEE Access*, vol. 11, pp. 26964-26978, Mar. 2023.

[24] E. N. Paulson, H. Park, J. Lee, and S. Kim, "Machine learning-based joint vital signs and occupancy detection with IR-UWB sensor," *IEEE Sensors Journal*, vol. 23, no. 7, pp. 7475-7482, Feb. 2023.

[25] F. Zardi, M. Salucci, L. Poli, and A. Massa, "SbD-driven microwave imaging for biomedical diagnosis," *2023 17th European Conference on Antennas and Propagation (EuCAP)*, Florence, Italy, pp. 1-4, May 2023.

[26] Q. Wu, Y. Cao, H. Wang, and W. Hong, "Machine-learning-assisted optimization and its application to antenna designs: Opportunities and challenges," *China Communications*, vol. 17, no. 4, pp. 152-164, Apr. 2020.

[27] H. M. El Misilmani, T. Naous, and S. K. Al Khatib, "A review on the design and optimization of antennas using machine learning algorithms and techniques," *International Journal of RF and Microwave Computer-Aided Engineering*, vol. 30, no. 10, pp. e22356, Oct. 2020.

[28] H. M. El Misilmani and T. Naous, "Machine learning in antenna design: An overview on machine learning concept and algorithms," *2019 International Conference on High Performance Computing & Simulation (HPCS)*, Dublin, Ireland, pp. 600-607, Sep. 2019.

[29] H. M. Yao, L. J. Jiang, and Y. W. Qin, "Machine Learning based Method of Moments (ML-MoM)," in *2017 IEEE International Symposium on Antennas and Propagation & USNC/URSI National Radio Science Meeting*, San Diego, CA, pp. 973-974, July 2017.

[30] T. Özdemir, D. N. Aloi, K. Bi, and R. J. Burkholder, "Numerical mesh truncation boundary conditions optimized via machine learning," in *2019 International Applied Computational Electromagnetics Society Symposium (ACES)*, Miami, FL, pp. 1-2, Apr. 2019.

[31] H. M. Yao and L. J. Jiang, "Machine-learning-based PML for the FDTD method," *IEEE Antennas and Wireless Propagation Letters*, vol. 18, no. 1, pp. 192-196, Jan. 2019.

[32] H. M. Yao and L. J. Jiang, "Machine learning based neural network solving methods for the FDTD method," in *2018 IEEE International Symposium on Antennas and Propagation & USNC/URSI National Radio Science Meeting*, Boston, MA, pp. 2321-2322, July 2018.

[33] S. Barmada, P. D. Barba, A. Formisano, M. E. Mognaschi, and M. Tucci, "Physics-informed neural networks for the resolution of analysis problems in electromagnetics," *ACES Journal*, vol. 38, no. 11, pp. 841-848, Nov. 2023.

[34] https://docs.nvidia.com/deeplearning/modulus/modulus-v2209/index.html.

[35] Z. Li, N. Kovachki, K. Azizzadenesheli, B. Liu, K. Bhattacharya, A. Stuart, and A. Anandkumar, "Fourier neural operator for parametric partial differential equations," [Online]. Available: arXiv:2010.08895, Oct. 2020.

[36] V. Demir and A. Z. Elsherbeni, "Computational Electromagnetics Simulator (CEMS)," Available: veysdemir@gmail.com, version 5, Oct. 2023.

[37] Simulia CST Microwave Studio, ver. 2023 S_2, Dassault Systems Simulia Corp, Framingham, MA, 2023.

[38] Ansys High Frequency Structure Simulation (HFSS), ver. 2023 R_1, Ansys Inc, Canonsburg, PA, 2023.

[39] A. Z. Elsherbeni and V. Demir, *The Finite-Difference Time Domain Method for Electromagnetics with MATLAB Simulations*, 2nd ed. Raleigh: SciTech Publishing, pp. 169-184, Nov. 2015.

[40] Y. Chen, A. Z. Elsherbeni, and V. Demir, "Machine learning for microstrip patch antenna design: Observations and recommendations," in *2022 United States National Committee of URSI National Radio Science Meeting (USNC-URSI NRSM)*, Boulder, CO, pp. 256-257, Jan. 2022.

[41] Y. Chen, A. Z. Elsherbeni, and V. Demir, "Machine learning design of printed patch antenna," in *2022 IEEE International Symposium on Antennas and Propagation and USNC-URSI Radio Science Meeting (AP-S/URSI)*, Denver, CO, pp. 201-202, July 2022.

[42] https://auto.gluon.ai/stable/index.html.
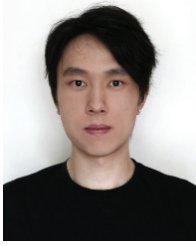
Yiming Chen received the M.S. degree in Electrical Engineering from the China University of Mining and Technology, Xuzhou, China, in 2019. Currently, he is a Ph.D. candidate from the ARC group at the Department of Electrical Engineering, Colorado School of Mines, Colorado, USA. His interests are in antenna design with machine learning, metasurface array optimization, on-body antenna, and RFID.

Veysel Demir is an Associate Professor at the Department of Electrical Engineering at Northern Illinois University, USA. He received his Bachelor of Science degree in Electrical Engineering from Middle East Technical University, Ankara, Turkey, in 1997. He studied at Syracuse University, New York, where he received both a Master of Science and Doctor of Philosophy degrees in Electrical Engineering in 2002 and 2004, respectively. During his graduate studies, he worked as a Research Assistant for Sonnet Software, Inc., Liverpool, New York. He worked as a visiting Research Scholar in the Department of Electrical Engineering at the University of Mississippi from 2004 to 2007. He joined Northern Illinois University in August 2007 and served as an Assistant Professor until August 2014. He has been serving as an Associate Professor since then.

Srirama Bhupatiraju received his master's degree in telecommunication engineering from the University of Texas, Dallas, USA, in 2012. He is a Senior Antenna Engineer with the Wireless and Radio Group at Nvidia, Santa Clara, USA. He has 10+ years of experience in the consumer electronics industry and his areas of interests are high performance computing, Desense, EMI, Antenna, and RF system design.

Atef Z. Elsherbeni received an honor B.Sc. degree in Electronics and Communications, an honor B.Sc. degree in Applied Physics, and a M.Eng. degree in Electrical Engineering, all from Cairo University, Cairo, Egypt, in 1976, 1979, and 1982, respectively, and a Ph.D. degree in Electrical Engineering from Manitoba University, Winnipeg, Manitoba, Canada, in 1987. He started his engineering career as a part time Software and System Design Engineer from March 1980 to December 1982 at the Automated Data System Center, Cairo, Egypt. From January to August 1987, he was a Post-Doctoral Fellow at Manitoba University. Dr. Elsherbeni joined the faculty at the University of Mississippi in August 1987 as an Assistant Professor of Electrical Engineering. He advanced to the rank of Associate Professor in July 1991, and to the rank of Professor in July 1997. He was the Associate Dean of the College of Engineering for Research and Graduate Programs from July 2009 to July 2013 at the University of Mississippi. He then joined the Electrical Engineering and Computer Science (EECS) Department at Colorado School of Mines in August 2013 as the Dobelman Distinguished Chair Professor. He was appointed the Interim Department Head for EECS from 2015 to 2016 and from 2016 to 2018 he was the Electrical Engineering Department Head. He spent a sabbatical term in 1996 at the Electrical Engineering Department, University of California at Los Angeles (UCLA) and was a visiting Professor at Magdeburg University during the summer of 2005 and at Tampere University of Technology in Finland during the summer of 2007. In 2009 he was selected as Finland Distinguished Professor by the Academy of Finland and TEKES. Dr. Elsherbeni is an IEEE Life Fellow and ACES Fellow. He is the Editor-in-Chief for ACES Journal, and a past Associate Editor to the Radio Science Journal. He was the Chair of the Engineering and Physics Division of the Mississippi Academy of Science, the Chair of the Educational Activity Committee for IEEE Region 3 Section, and the general Chair for the 2014 APS-URSI Symposium and the President of ACES Society from 2013 to 2015. Dr. Elsherbeni is selected as Distinguished Lecturer for IEEE Antennas and Propagation Society for 2020-2023. He is the recent recipient of the 2023 IEEE APS Harington-Mittra Award for his contribution to computational electromagnetics with hardware acceleration.

Joselito Gavilan holds a B.S. degree in Electrical Engineering and a master's in engineering degree with a focus on Electromagnetics and Wireless Communication, both earned from the University of Illinois at Chicago in '98 and '04 respectively. Joselito has over 20 years of product design experience, ranging from base station antenna products to mobile phones, tablets, laptops, gaming devices, and high-performance edge computers. His interest is product integration and simulation. He enjoys the challenges of tight integration and learning the constraints of cross-functional disciplines to make the right tradeoffs. Currently, he is at NVIDIA, leading efforts to reimagine computational simulations given the accessibility of high-performance supercomputers and AI technologies.
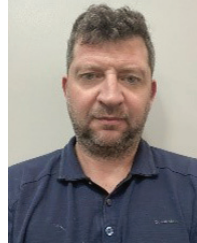
Kiril Stoynov received the M.S. degree in Electrical Engineering with concentration in Computational Electromagnetics from the University of Akron in 2008. Currently he is an EPM in the Systems Products Team at Nvidia working on Industrial and Embedded Products. Kiril has interests in antenna design, simulations, HPC, AI and simulations on a large scale.

Optimal Synthesis of Unequally Spaced Linear Arrays under Multiple Constraints

Zhong-Hui Zhao

College of Electronic and Information Engineering
Shandong University of Science and Technology, Qingdao, Shandong, 266590 China
zhaozh@sdust.edu.cn

Abstract – This paper proposes a differential evolution modified with adaptive ε-constraint handling and whale optimization algorithm (ε-WOA-DE) for the synthesis of unequally spaced linear arrays under array layout constraints and array pattern characteristics constraints. In particular, the success history based adaptive differential evolution with linear population reduction (LSHADE) serves as the basic search engine in this study. To ensure the searching ability of LSHADE under multiple constraints, an adaptive ε-constraint handling technique is implemented in LSHADE, in which the epsilon level is adjusted dynamically to make the solution scalable to the feasible region when it is in the infeasible region. In addition, the WOA mutation is implemented in the LSHADE to enhance the local search capability. Two array synthesis examples with multiple constraints are chosen to demonstrate the effectiveness of the proposed algorithm. The simulation results comparison and the convergence analysis of the ε-WOA-DE illustrate the superior capability of the proposed method.

Index Terms – adaptive ε-constraint handling, array synthesis, differential evolution, unequally spaced linear arrays, whale optimization algorithm.

I. INTRODUCTION

Synthesis of unequally spaced arrays has been widely explored in the last decades [1]. Compared with uniform spaced arrays, the element positions of the unequally spaced arrays can be exploited to achieve better pattern radiation characteristics. In particular, when array design is further combined with array amplitude and phase optimization, arrays with unequal spacing can achieve better array pattern performance [2].

Generally, the layouts of the unequally spaced arrays involve several constraints, such as element number, the total array length and the spacing between two adjacent elements [3–6]. Despite the array layout constraints, several array pattern characteristics, such as the maximum sidelobe level (SLL), the required mainlobe beamwidth (BW) and the maximum null depth (ND) in some specified directions, are required in the array synthesis. These multiple constraints and requirements in the antenna array design lead the synthesis of unequally spaced arrays to complicated nonlinear constrained optimization problems, which increase the difficulty of the antenna synthesis.

Various evolution algorithms, such as the genetic algorithm, differential evolution (DE), seagull optimization algorithm, comprehensive learning particle swarm optimization (CLPSO) and whale optimization algorithm (WOA), have been concerned about solving this complicated nonlinear constraint problem [7–11]. For the geometry constraints, [7] has successfully transformed the geometry constraints to the unconstrained model by employing the vector mapping method and has been widely used in array synthesis. However, there is difficulty in satisfying the array pattern characteristic constraints. To deal with the array pattern characteristic constraints, [8–12] incorporate the constraints into the fitness function, by which the fitness values of the infeasible vectors are large and will be discarded in the optimization process. To satisfy the array pattern characteristic constraints, [12] proposed the modified DE with constrained vector projection (MDE-CVP) algorithm, the CVP method is used to exclude the infeasible solutions which unsatisfy the desired null depth. Although the lower null depth was realized, the SLL could not reach the desired value.

When constrained array synthesis evolutionary algorithms give priority to the satisfaction of constraints [13], it is likely to cause the following two problems. On the one hand, it is likely to make the population fall into a local infeasible region, so that the algorithm cannot find a feasible solution, which may result in failing to satisfy some constraints. On the other hand, it is likely to make the population converge to a locally feasible region, but far away from the location of the constraint in which the complete pareto optimal solution set in the target space cannot be found. Thus, in the constraint array synthesis, instead of excluding the infeasible solutions directly,

exploring infeasible regions around the feasible region is very effective in searching for the global optimal solutions in the constraint optimization [14].

In this study, in order to find better layouts of the antennas under multiple constraints, a modified DE algorithm with the adaptive ε-constraint control method is proposed to deal with the constraints, in which the epsilon level dynamically is adjusted to enhance the exploration of the infeasible regions in the optimization process. To ensure the convergence speed of the optimization, the adaptive ε-constraint control method is incorporated with the success-history based differential evolution with linear population reduction (LSHADE), which has shown superiority in the single objective optimization [15]. In addition, WOA mutation is introduced in the mutation process to enhance exploitation [16, 17]. The optimization of the array geometry is initialized to generate optimal radiation pattern under geometry constraints and the SLL, the BW and the ND constraints. Compared with other synthesis techniques [9, 10, 12], the proposed method performs well in the constrained array synthesis.

II. PROBLEM FORMULATION

As shown in Fig. 1, consider a $2N$ element linear array symmetrically placed along the x-axis with the aperture of $2L$, the array factor can be written as follows:

$$AF(\theta, X) = \sum_{n=1}^{N} \cos\left(\frac{2\pi}{\lambda} x_n \cos\theta\right), \quad (1)$$

where θ is the steering angle, λ is the wavelength, $X = [x_1, x_2, ..., x_N]$ denote the element positions. Since the array aperture is $2L$, x_N is L. The SLL of the radiation pattern can be expressed as:

$$SLL(X) = \max_{\theta \in Sidelobe} \left| \frac{AF(\theta, X)}{AF(\theta_s, X)} \right|, \quad (2)$$

where $Sidelobe$ is the sidelobe region corresponding to X, θ_s is the mainbeam direction. The maximum ND is denoted as:

$$ND(X) = \max_{m=1,2,..,M} \left| \frac{AF(\theta_m, X)}{AF(\theta_s, X)} \right|, \quad (3)$$

where $ND(X)$ is the maximun nulldepth corresponded with X, and $\theta_m, (m = 1, 2, .., M)$ are the specific directions of the steering nulls.
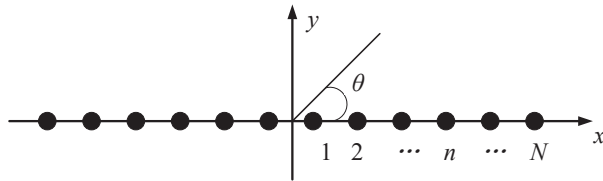

Fig. 1. Geometry of the 2N-element symmetric linear array.

In this study, we aim to design the layout of the linear array with the desired array aperture, the minimum element spacing constraints and limited SLL, BW and ND in some specific directions. Based on the vector mapping method in [7], the array layout constraints can be transformed in the element positions optimization:

$$\begin{cases} x_n = \sum_{j=1}^{n} \Delta x_j \\ \Delta x_n = \Delta d x_n + (L - (N - 0.5)d_c)) \times a_n / \sum_{j=1}^{N} a_j \end{cases}, \quad (4)$$

where $\Delta x_j = x_j - x_{j-1}$ is the element spacing, $A = [a_1, a_2, ..., a_N]$ is randomly generated among the range of $[0, 1]$, $\Delta dx = [0.5d_c, d_c, ..., d_c]$ is a N-dimensional vector, d_c is the required minimum element spacing and Δdx_n is the nth element of Δdx.

Inspired by the objective function implemented in [18], the new objective function, which not only aims to meet the BW, the SLL and the ND requirements, but also optimizes these array pattern characteristics is developed as follows:

$$\min_{A} \ |BW(A) - BW_d| + SLL(A) + ND(A)$$

$$s.t. \ SLL(A) \leq SLL_d$$
$$ND(A) \leq ND_d \quad , \quad (5)$$
$$|BW(A) - BW_d| \leq \tau BW_d$$

where $BW(A)$ is the beamwidth corresponded with A, BW_d is the desired beamwidth, SLL_d is the constraint SLL, ND_d is the desired maximum ND, and τ is the desired tolerance percentage of the beamwidth.

III. PROPOSAL OF THE ARRAY SYNTHESIZER

The array synthesis model in (5) is a nonconvex and highly nonlinear problem. With good global search capability, the success history based adaptive differential evolution with linear population reduction (LSHADE) is used in this study. Additionally, to handle the constraints and enhance the local search capability, the LSHADE is modified with the adaptive ε-constraint handling and WOA mutation, respectively.

A. Basic LSHADE

LSHADE is an improved DE algorithm, which adapts the parameters based on the success-history and employs the population size reduction (LPSR) mechanism [19]. The population of LSHADE is initialized as follows:

$$y_{i,j}^0 = lb_j + rand \cdot (ub_j - lb_j), \quad (6)$$

where $rand$ represents a random number which distributed uniformly in $[0, 1]$. $y_{i,j}^0$ is the jth component $(j = 1, 2, .., D)$ of the ith individual $(i = 1, 2, .., N)$ in the initial population, ub_j and lb_j are the upper and lower bounds of the jth variable. And then, these individuals are evolved by the mutation, crossover and selection operators with the successful history based parameter adaption and linear population reduction.

a) Mutation: in this operator, the mutant vector v_i^G is created according to current-to-pbest/1 mutation strategy:

$$v_i^G = y_i^G + F_i^G \left(y_{pbest}^G - y_i^G \right) + F_i^G \left(y_{r1}^G - y_{r2}^G \right), \quad (7)$$

where y_i^G represents the ith target vector of the Gth generation. y_{pbest}^G is randomly selected from the best $NP \times p, (p \in [0,1])$ vectors of current population. y_{r1} and y_{r2} is randomly chosen from the union of the current population and the external archive. F_i^G is the scaling factor and is updated according to its historical successful experience.

b) Crossover: in this operator, the trial vector $u_i^G = [u_{i,1}^G, u_{i,2}^G, ..., u_{i,D}^G]$ is generated according to the crossover rate, which can be expressed by:

$$u_{i,j}^G = \begin{cases} v_{i,j}^G & if \ \left(rand_{i,j} \leq Cr_i^G \ or \ j = j_{rand} \right) \\ y_{i,j}^G & otherwise \end{cases}, \quad (8)$$

where j_{rand} is an integer randomly selected from [1,D], Cr_i^G is the crossover rate and is updated according to its historical successful experience.

c) Selection: in this operator, not only the population is generated, but also the external archive is updated. After the selection of the vectors with better fitness function value, only NP_{G+1} best vectors will survive into the next generation, which is updated by linear population size reduction mechanism:

$$NP_{G+1} = round \left[\left(\frac{NP_{min} - NP_{ini}}{MFES} \right) \times FES + NP_{ini} \right], \quad (9)$$

where NP_{ini} is the initial population size, NP_{min} is the population size of the last generation, $MFES$ is the maximum number of fitness function evaluations, and FES is the current number of fitness function evaluations. The other $NP_G - NP_{G+1}$ vectors are removed to the external archive.

B. Adaptive ε-constraint handling

To ensure the searching ability under multiple constraints, this paper incorporates an adaptive ε-constraint handling technique in SHADE. In constraint problems optimization, the constraint violation is an important factor in measuring the constraints. In this array synthesis problem (5), the constraint violation is:

$$\begin{aligned} \varphi(A) = &max(0, SLL(A) - SLL_d) \\ &+ max(0, ND(A) - ND_d) \\ &+ max(0, |BW(A) - BW_d| - \tau BW_d) \end{aligned}, \quad (10)$$

For two solutions A_1 and A_2, their constraint violations are φ_1 and φ_2. Then, for any ε satisfies $\varepsilon \geq 0$, the ε-level comparison selects the better solutions as follows:

$$(A_1, \varphi_1) \preceq_\varepsilon (A_2, \varphi_1) \Leftrightarrow \begin{cases} A_1 \preceq A_2, & if \ \varphi_1, \varphi_1 \leq \varepsilon \\ A_1 \preceq A_2, & if \ \varphi_1 = \varphi_2 \\ \varphi_1 < \varphi_2, & otherwise \end{cases} . \quad (11)$$

Through the ε-level comparison, LSHADE algorithm can be used for constrained optimization directly [15]. Moreover, the ε-level comparison can extend the exploration of the infeasible regions around the feasible regions by setting appropriate ε value. Thus, to maintain the balance of searching between infeasible and feasible regions, an improved adaptive ε level control based on the exponential decline scheme is formulated in this study as:

$$\varepsilon(t) = \begin{cases} (1 - \frac{t}{T_c})^{cp} \varphi_{max} & if \ \varphi_{max} \leq Th \ or \ r_t \leq ap_1 \\ & and \ t \leq Tc \\ ap \times \varphi_{max} & if \ \varphi_{max} > Th \ or \ r_t > ap_1 \\ & and \ t \leq Tc \\ 0 & if \ t > Tc \end{cases}, \quad (12)$$

where φ_{max} is the maximum constraint violation in the current generation, cp controls the speed of declining constraints, r_t is the ratio of feasible vectors to total vectors in the tth generation, Th and ap_1 is to control the preference rule of setting ε value, ap is a small value.

Considering that in the exponential decline scheme, the ε may maintain a big value over a long period, which will degrade the search efficiency. When φ is larger than Th or there are enough feasible vectors, the ε value is set as a relatively small value to make the search focus on the feasible region and the infeasible region around the feasible region. In the final-stage, when the iteration number is larger than Tc, the ε value is set as 0 to enable the final exploitation in the feasible region.

C. WOA mutation

To enhance the exploitation around the best vectors, the spiral movement operator of WOA is incorporated into the mutation process[16]. The mutant vector v_i^G has a chance to make further updates using the spiral movement of WOA:

$$v_i^G = \begin{cases} wD_i e^l \cos(2\pi l) + y_{pbest}^G & if \ rand < 0.5 \\ v_i^G & otherwise \end{cases}, \quad (13)$$

where $w = \cos(\frac{0.5\pi G}{Gm})$ is the weight coefficient, $D_i = \left| y_{pbest}^G - v_i^G \right|$ and l is the uniform random number in the intervals $[-1, 1]$.

D. Synthesis procedure

The pseudo-code for the ε-WOA-DE is summarized in Algorithm 1.

Algorithm 1: ε-WOA-DE based array synthesis procedure

1: Set the number of elements N, the required array characters, the initial population size NP_{ini}, maximum generation number G_{max}.

2: Randomly generate NP_{ini} individuals

3: Calculate the fitness value by (5) and the constraint violation by (7)

4: Set $G = 1$

5: **while** $G < G_{max}$, **do**

6:   **for** $i = 1 : NP_G$, **do**

7:     Calculate F_i^G and CR_i^G

8:     Make mutant vector v_i^G by (10) and (12)

9:     Make trail vector u_i^G using (11)

10:     Calculate the fitness function by (5) and the constraint violation by (7)

11:     Select the next generation and update the external archive

12:    **end for**

13:   $G = G + 1$

14:**end while**

15: Output the best vector and the corresponding array element positions

IV. NUMERICAL RESULTS

To verify the effectiveness and efficiency of the ε-WOA-DE algorithm, two linear array synthesis examples are presented and compared with CLPSO [9], WOA [10] and MDE-CVP [12].

The initial population size NP_{ini}, the minimum population size NP_{min} and the maximum generation number G_{max} are set as 50, 10, 500, respectively. The other DE control parameters are the same as those in [19]. For the ε level handling, the decline speed cp is set as 2, ap is set as 0.2, the threshold parameters Th, Tc and ap_1 are set as 0.25, 150 and 0.2, respectively. For all examples, ten independent trails are performed and the best simulation results are evaluated.

The first example is a 28-element unequally spaced linear array synthesis. For comparison, we set $2L = 15.8 \lambda$, $d_c = 0.25 \lambda$, $\theta_s = 90°$, $\theta_m = [120° \ 122.5° \ 125°]$, $BW_d = 8.35°$, $\tau = 0.05$, $SLL_d = -23 \ dB$ and $ND_d = -90 \ dB$, respectively. The corresponding optimal array geometry is shown in Table 1. Figure 2 compares the radiation pattern obtained by the ε-WOA-DE algorithm
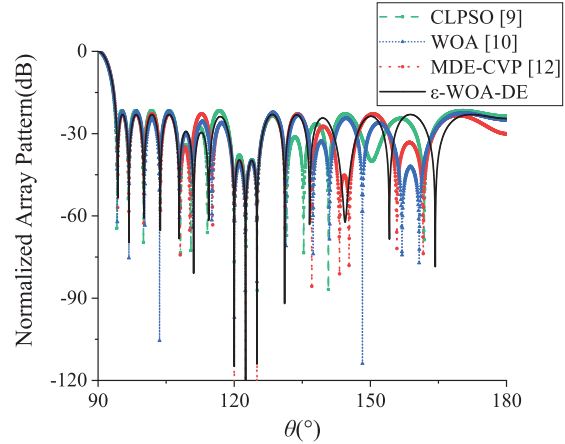

Fig. 2. Best radiation pattern of the 28-element array obtained by different algorithms.

and the other algorithm. The corresponding array pattern factors comparison of different algorithms are listed in Table 2. The ε-WOA-DE algorithm has achieved the lowest SLL and satisfied all the required array pattern characters in the two examples. The convergence plots of the objective function value, constraint violation, and the value of ε are shown in Fig. 3. The ε value is adjusted adaptively during the optimization process while the constraint violation declined gradually to 0. The algorithm converges in generations, respectively.

The second example is a 32-element linear array. The desired array factors are set as $2L = 16.8 \ \lambda$, $d_c = 0.25 \ \lambda$, $\theta_s = 90°$, $\theta_m = 99°$, $BW_d = 8.3°$, $SLL_d = -23.5 \ dB$ and $ND_d = -110 \ dB$, respectively. The optimal array geometry is shown in Table 1. The performance comparisons are presented in Fig. 4 and Table 3. The $\varepsilon-$WOA-DE algorithm has met all the required

Table 2: Comparison of the MDE-CVP algorithm with other algorithms for the 28-element array

Algorithm	SLL, dB	ND, dB	BW, deg
CLPSO [9]	-21.60	-60	8.35
WOA [10]	-21.86	-106.27	8.49
MDE-CVP [12]	-22.80	≤ -150	8.6
ε-WOA-DE	-23.03	-114.02	8.6

Table 1: Optimal geometries of the antenna arrays obtained by the the ε-WOA-DE algorithm

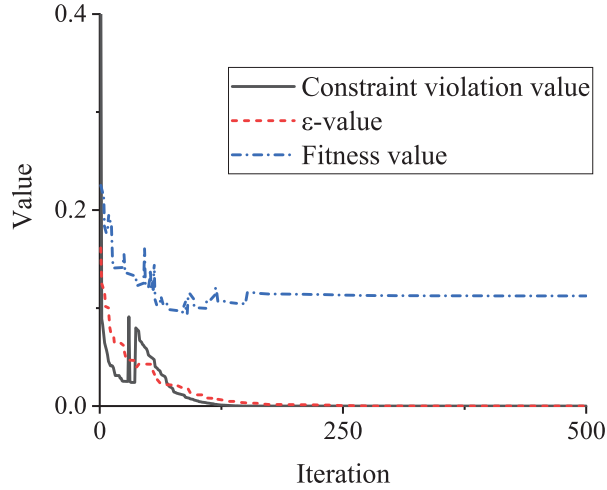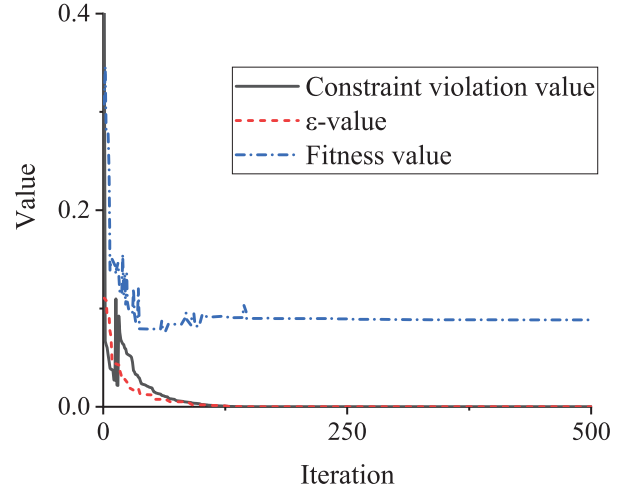| Example	$[x_1/\lambda, x_2/\lambda, ..., x_N/\lambda]$
Example 1	[0.3380 0.6104 1.3092 1.8184 2.1648 2.8049 3.1209 3.4471 4.1020 4.9288 5.8134 6.5189 7.1720 7.9]
Example 2	[0.2042 0.6589 1.0253 1.3998 1.8792 2.2190 2.7378 3.0639 3.5908 4.0176 4.5907 5.0038 5.7295 6.6059 7.5015 8.4]

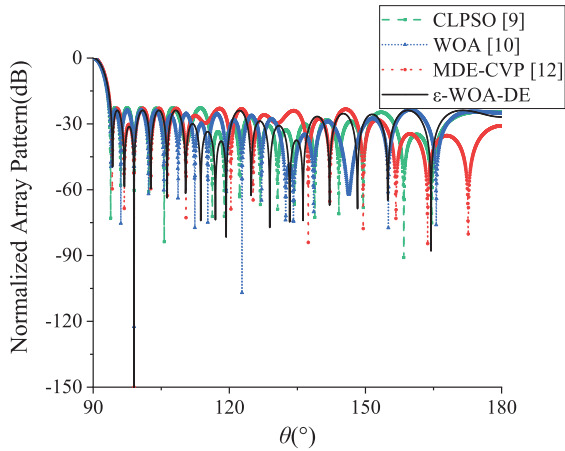Fig. 3. Convergence curve plots of the 28-element array.

Fig. 4. Best radiation pattern of the 32-element array obtained by different algorithms.

Table 3: Comparison of the MDE-CVP algorithm with other algorithms for the 32-element array

Algorithm	SLL, dB	ND, dB	BW, deg
CLPSO [9]	-22.73	-60.45	8.35
WOA [10]	-23.62	-122.41	7.86
MDE-CVP [12]	-22.98	≤ -150	8.4
ε-WOA-DE	-23.83	-151.17	8.5

array pattern characters with lower ND and lowest SLL. The convergence curves of the objective function, constraint violation, and the ε value can be seen in Fig. 5.

In order to investigate the convergence performance and computational costs of the proposed ε-WOA-DE, Table 4 compares the required number of fitness function evaluations for convergence (NEC) in all examples. In

Fig. 5. Convergence curve plots of the 32-element array.

Table 4: Convergence analysis of different methods

Algorithm	NECs	
	Example1	Example2
CLPSO [9]	47560	27360
WOA [10]	21460	7440
ε-WOA-DE	7711	6220

addition, the algorithm converges at around 24000 NECs for all the examples in MDE-CVP [12]. In comparison, the ε-WOA-DE algorithm not only has powerful search capability but also performs quick convergence rate.

V. CONCLUSION

In this study, in order to optimize the positions of the unequally spaced array under multiple constraints, we propose a modified DE algorithm. The algorithm is based on the LSHADE and modified by implementing the adaptive constraint handling technique and integrating the spiral movement of the DE mutation process. Simulation results show that the proposed ε-WOA-DE algorithm has an improved performance in the array pattern characteristics control and the efficient computation time. Although ε-WOA-DE is only used for linear array synthesis in this study, it is worth noting that the constraint handling implemented technique is suitable for the other geometry array synthesis such as the circular and planar array. In future, in order to more accurately simulate and optimize the performance of unequally spaced arrays, we will investigate the incorporation of mutual coupling into the synthesis of unequally spaced arrays.

REFERENCES

[1] P. Rocca, G. Oliveri, R. J. Mailloux, and A. Massa, "Unconventional phased array architectures and design methodologies−a review," *Proceedings of the IEEE,* vol. 104, no. 3, pp. 544-560, 2016.

[2] J. R. Mohammed, "Element selection for optimized multiwide nulls in almost uniformly excited arrays," *IEEE Antennas and Wireless Propagation Letters,* vol. 17, no. 4, pp. 629-632, 2018.

[3] K. Chen, Z. He, and C. Han, "A modified real GA for the sparse linear array synthesis with multiple constraints," *IEEE Transactions on Antennas and Propagation,* vol. 54, no. 7, pp. 2169-2173, 2006.

[4] Y. Pan and J. Zhang, "Synthesis of linear symmetric antenna arrays using improved bat algorithm," *Microwave and Optical Technology Letters,* vol. 62, no. 6, pp. 2383-2389, 2020.

[5] J. R. Mohammed and K. M. Younus, "Null steering implementation by controlling side elements positions," *International Journal of Microwave and Optical Technology,* vol. 16, no. 6, pp. 568-575, 2021.

[6] J. R. Mohammed, "Obtaining wide steered nulls in linear array patterns by optimizing the locations of two edge elements," *AEU International Journal of Electronics and Communications,* vol. 101, pp. 145-151, 2019.

[7] S. K. Goudos, K. Siakavara, T. Samaras, E. E. Vafiadis, and J. N. Sahalos, "Sparse linear array synthesis with multiple constraints using differential evolution with strategy adaptation," *IEEE Antennas and Wireless Propagation Letters,* vol. 10, pp. 670-673, 2011.

[8] E. Kurt, S. Basbug, and K. Guney, "Linear antenna array synthesis by modified seagull optimization algorithm," *The Applied Computational Electromagnetics Society Journal (ACES),* vol. 36, no. 12, pp. 1552-1562, 2022.

[9] S. K. Goudos, V. Moysiadou, T. Samaras, K. Siakavara, and J. N. Sahalos, "Application of a comprehensive learning particle swarm optimizer to unequally spaced linear array synthesis with sidelobe level suppression and null control," *IEEE Antennas and Wireless Propagation Letters,* vol. 9, pp. 125-129, 2010.

[10] C. Zhang, X. Fu, L. P. Ligthart, S. Peng, and M. Xie, "Synthesis of broadside linear aperiodic arrays with sidelobe suppression and null steering using whale optimization algorithm," *IEEE Antennas and Wireless Propagation Letters,* vol. 17, no. 2, pp. 347-350, 2018.

[11] G. X. Liu, Q. Qin, and Q. H. Zhang, "Linear array synthesis for wireless power transmission based on brain storm optimization algorithm," *International Journal of Antennas and Propagation,* vol. 2021, pp. 1-8, 2021.

[12] R. Q. Wang, Y. C. Jiao, H. Zhang, and Z. Zhou, "Synthesis of unequally spaced linear arrays using modified differential evolution algorithm," *IET Microwaves, Antennas & Propagation,* vol. 12, no. 12, pp. 1908-1912, 2018.

[13] T. Takahama and S. Sakai, "Constrained optimization by the ε constrained differential evolution with gradient-based mutation and feasible elites," in *2006 IEEE International Conference on Evolutionary Computation,* pp. 1-8, 2006.

[14] C. Zhang, A. K. Qin, W. Shen, L. Gao, K. C. Tan, and X. Li, "ε−Constrained differential evolution using an adaptive ε−level control method," *IEEE Transactions on Systems, Man, and Cybernetics: Systems,* pp. 1-17, 2020.

[15] R. Tanabe and A. S. Fukunaga, "Improving the search performance of SHADE using linear population size reduction," in *2014 IEEE Congress on Evolutionary Computation (CEC),* pp. 1658-1665, 2014.

[16] S. Mirjalili and A. Lewis, "The whale optimization algorithm," *Advances in Engineering Software,* vol. 95, pp. 51-67, 2016.

[17] D. Prabhakar, K. Srinivas, R. Spandana, D. Anusha, M. Srikanth, and Y. R. Krishna, "The synthesis of elliptical antenna array using hybrid SSWOA algorithm," *Applied Computational Electromagnetics Society Journal,* vol. 38, no. 5, p. 309, 2023.

[18] Q. Xu, S. Zeng, F. Zhao, R. Jiao, and C. Li, "On formulating and designing antenna arrays by evolutionary algorithms," *IEEE Transactions on Antennas and Propagation,* vol. 69, no. 2, pp. 1118-1129, 2021.

[19] S. M. Islam, S. Das, S. Ghosh, S. Roy, and P. N. Suganthan, "An adaptive differential evolution algorithm with novel mutation and crossover strategies for global numerical optimization," *IEEE Transactions on Systems, Man, and Cybernetics, Part B (Cybernetics),* vol. 42, no. 2, pp. 482-500, 2012.

Zhonghui Zhao received M.S. degree in electromagnetic field and microwave technology and Ph.D. degree in electrical engineering from Northwestern Polytechnical University, Xi'an, Shaanxi in 2016 and 2020, respectively. She is currently employed as a lecturer in College of Electronic and Information Engineering, Shandong University of Science and Technology. Her current research interests include antenna arrays, evolutionary algorithms and machine learning.

High-order Mode of Spoof Surface Plasmon Polaritons based on a Novel Compact Structure and its Application in Band-pass Filters

Siyu Yang[1], Shuang Liu[1], Huali Zhu[2], Fachun He[1], Dan Lei[1], Jun Yan[3], and Chan Gao[1]

[1]School of Mathematics and Science
Chengdu University of Technology, Chengdu 610000, China
894518884@qq.com, ranranshuangshuang@163.com, 1937604847@qq.com, leidan1008@163.com,
gaochan@cdut.edu.cn

[2]School of Electronic Science and Engineering
University of Electronic Science and Technology of China, Chengdu 610000, China
350342101@qq.com

[3]China Electronics Technology Group Corporation
10th Research Institute, Chengdu 610000, China
niko_robin@163.com

Abstract – In this paper, two band-pass filters based on the high-order mode of spoof surface plasmon polaritons (SSPPs) are introduced. A novel compact bow-folded strip is proposed as a cell, which exhibits perfect band-pass characteristics. By adjusting the width and groove of the bow-folded strips, high-order mode can be obtained to support the design of band-pass filters. Compared to the conventional single-side rectangular groove SSPPs cell, our proposed bow-folded strip structure cells reduce the electrical size by 59% and 70% at the same cut-off frequency. In addition, the transmission lines of the two proposed band-pass filters are microstrip lines and their over-conversion structures are simple trapezoidal over. A single-band and a dual-band band-pass filters using the proposed SSPPs cell are fabricated and measured, both having almost the same size. The measured results are in good agreement with simulated results, which verify the feasibility of our design.

Index Terms – band-pass filter, bow-folded strip, novel compact, SSPPs.

I. INTRODUCTION

Surface plasmon polaritons (SPPs) refer to electromagnetic waves that are excited along the surface of metallic media and propagate within the optical frequency range, which have field-bound and field-enhanced properties in the subwavelength range [1]. Due to their strong optical confinement in the subwavelength region and their ability to break the diffraction limit, SPPs have garnered growing attention due to their poten-tial applications in the design of integrated optical components and circuits with high density. In 2004, Pendry and his colleagues proposed the concept of spoof surface plasmon polaritons (SSPPs). SSPPs and SPPs have similar features [2]. The dispersion characteristics of the spoof surface plasmon polaritons can be controlled by directly changing the structure size of the SSPPs cell [3]. As a result, SSPPs research has received a lot of coverage in the microwave and terahertz bands.

However, previously proposed devices based on SSPPs are large-sized bulk structures, which poses a challenge for the integration of SSPPs with microwave and terahertz planar circuits. To solve this problem, Cui and his coworkers proposed the conformal surface plasmons (CSPs) waveguide based on an ultra-thin and flexible film printing grooved metal strip [4, 5], which accelerated the development of SSPPs technology. Since then, different shapes of SSPPs transmission lines have been reported, such as folded [6] and double-sided serrated [7]. Based on this, functional devices based on SSPPs transmission lines, such as filters [8–14], antennas [15–17], power dividers [18–20], frequency dividers [21], and so on, have been extensively investigated.

However, most of the above work is done based on the design of the fundamental mode of SSPPs, which requires complex transmission transitions in the design of transmission lines. For the high-order mode of SSPPs, there is no need to use the complex transmission, only simple microstrip lines are needed to excite effectively. When the groove depth in the SSPPs cell structure is greater than the period, the designed transmission line can operate in the high-order mode state [22].

Some band-pass filters based on the high-order mode of SSPPs have been reported [23–27]. However, these SSPPs structures cannot achieve better size advantages. The transitions of the SSPPs transmission lines are very complex in the instance of multi-frequency filters now being developed [28, 29]. Therefore, it is valuable to study the application of a compact multi-frequency filter based on the high-order mode of SSPPs and a simple SSPPs transmission line.

In this paper, we propose a novel bow-folded strip SSPPs structure based on high-order mode for single-band and dual-band band-pass filters. We study the conventional rectangular groove SSPPs cell and the bow-folded strip SSPPs structure. It is demonstrated that the bow-folded strip SSPPs structure outperforms the traditional SSPPs structure in terms of size and better field binding. The structural characteristics of the SSPPs cell with a bow-folded strip are then examined. The first-order high-order mode of the SSPPs structure is used to construct a single-band band-pass filter by designing the structural parameters. A dual-band band-pass filter is constructed by using the first high-order mode and the second high-order mode using a similar theoretical method. Hence, it indicates the structure's suitability for designing band-pass filters and the commendable performance of said filters. Moreover, the structure has the advantage of miniaturization.

II. STUDY OF HIGH-ORDER MODE OF SSPPs

In this section, we initially investigate the fundamental mode (Mode 0) and the first high-order mode (Mode 1) of the bow-folded strip SSPPs structure. Subsequently, by employing a straightforward trapezoidal transition, we can successfully excite the Mode 1 of the SSPPs, resulting in the generation of a passband that exhibits exceptional transmission capability.

The SSPPs unit structure based on the bow-folded strip structure is shown in Fig. 1 (b). Unlike the conventional single-side rectangular groove SSPPs unit structure (Fig. 1 (a)), it is formed by etching bow-folded strip on top of the rectangular groove SSPPs unit structure, based on Rogers RT5880 substrate with thickness of 0.508 mm, relative dielectric constant of 2.2 and tangent loss of 0.0009. In order to improve the SSPPs field confinement capability, the backside of the substrate is a continuous metal ground structure [30]. The dimensions of two-unit structures are listed in Table 1. The period is d, the deep grooves are h (slot depth of conventional rectangular groove) and h_1 (slot depth of bow-folded strip), the top edge is length l, and the line widths are W_1 and w, respectively.

As stated in the study conducted by [27], the single grating structure of SSPPs demonstrates the ability to
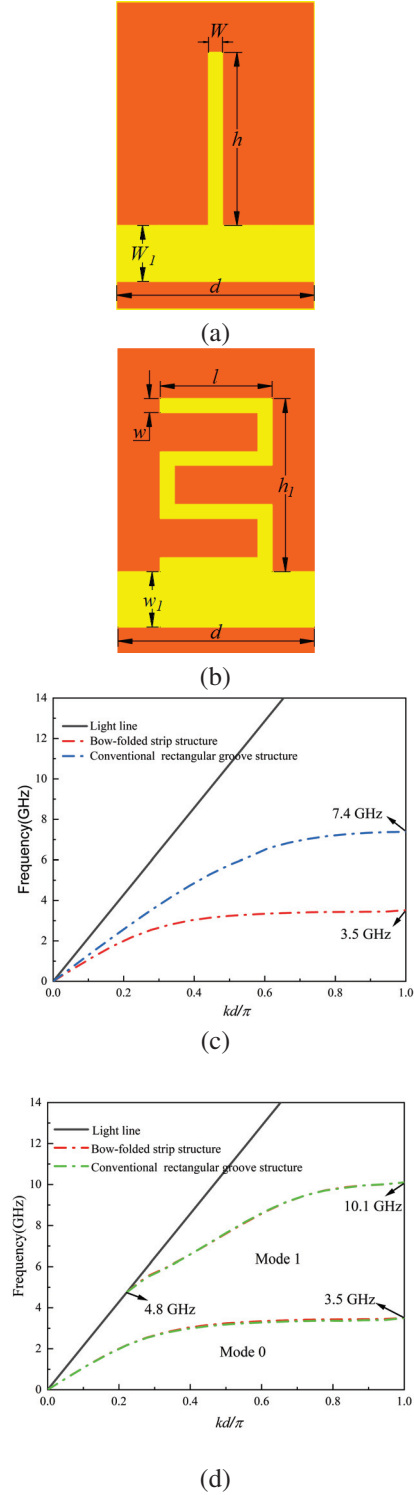

(a)

(b)

(c)

(d)

Fig. 1. (a) Conventional rectangular groove SSPPs cell structure, (b) bow-folded strip SSPPs cell structure, (c) dispersion characteristics of conventional rectangular groove and bow-folded strip SSPPs cells with $h_1=h=6.2$ mm, and (d) dispersion characteristics of conventional rectangular groove and bow-folded strip SSPPs cells with $h_1=6.2$ mm, $h=15$ mm.

sustain high-order modes of SSPPs if the depth of groove h exceeds the period d. The number of SSPPs modes (N) can be denoted by:

$$N = 1 + int(h/d). \tag{1}$$

Table 1: The dimensions of two-unit structures (unit=mm)

l	d	h	h_1	W_1	w_1	W	w
4	7	6.2	6.2	2	2	0.5	0.5

The SSPPs cell structure is simulated using the eigenmode solver of the commercial software CST Microwave Studio. The boundary conditions for the propagating x-direction are specified as periodic boundaries, and the non-periodic y- and z-boundaries are specified as either electric or magnetic boundaries. By setting the intrinsic phase shift between periodic boundary conditions to the parameter phase, one can use the parameter scan function to get the mode frequency. According to the definition, the conversion relation between the intrinsic phase shift value phase and the propagation constant k in the propagation direction is as follows [31]:

$$k = phase\pi/180d. \tag{2}$$

According to the dispersion curve in Fig. 1 (c), the dispersion curves of both modes of SSPPs start from the intersection with the dispersion curve of light in free space. As the intrinsic phase shift value increases, it gradually veers away from the light line until reaching the maximum frequency value, known as the cut-off frequency. When the dispersion curves closely approach the cut-off frequency, the field's binding capability to SSPPs reaches its maximum strength. When $h=h_1=6.2$ mm, the cut-off frequency of the conventional rectangular groove cell structure is 7.4 GHz and that of the bow-folded strip cell structure is 3.5 GHz. Therefore, the designed bow-folded strip cell structure in the same size has a lower cut-off frequency than the conventional rectangular groove cell structure, indicating that the transmission line of the bow-folded strip cell structure has a higher field-binding force in the frequency band range of 0 to 14 GHz.

Here we investigate the characteristics of the high-order mode, making $h=15$ mm and $h_1=6.2$ mm. At this point the transverse dimension of the designed bow-folded strip structure reduces to 59% of the conventional rectangular groove. The dispersion curves in Fig. 1 (d) show that both the conventional single-side rectangular groove structure and the bow-folded strip appear in high-order mode, and the cut-off frequencies of the fundamental and high-order mode are almost the same for both. The fundamental mode of their cut-off frequency is 3.5 GHz, featuring low-pass characteristics. The first

high-order mode cut-off frequency is 10.1 GHz, which exhibits an inherent band-pass. Thus, it is shown that the bow-folded strip structure occupies less area at the same cut-off frequency. The groove depth primarily determines the cut-off frequency of SSPPs, thus leading to this phenomenon. The curved groove of the bow-folded strip SSPPs unitary structure increases the relative effective groove depth of the SSPPs and further reduces the horizontal dimension. In addition, there is no overlap between the fundamental and high-order mode, indicating single-mode propagation for each mode, unlike the conventional rectangular waveguide.

Previous work has shown that the cut-off frequency of SSPPs' fundamental mode is mainly determined by the groove h_1. Further, it is also important to investigate the relationship between the high-order mode and the structural parameters of the bow-folded strip SSPPs cell. As shown in Fig. 2 (a), when the width l of the bow-folded strip SSPPs cell is increased from 2 mm to 4 mm, the intersection of the first high-order mode
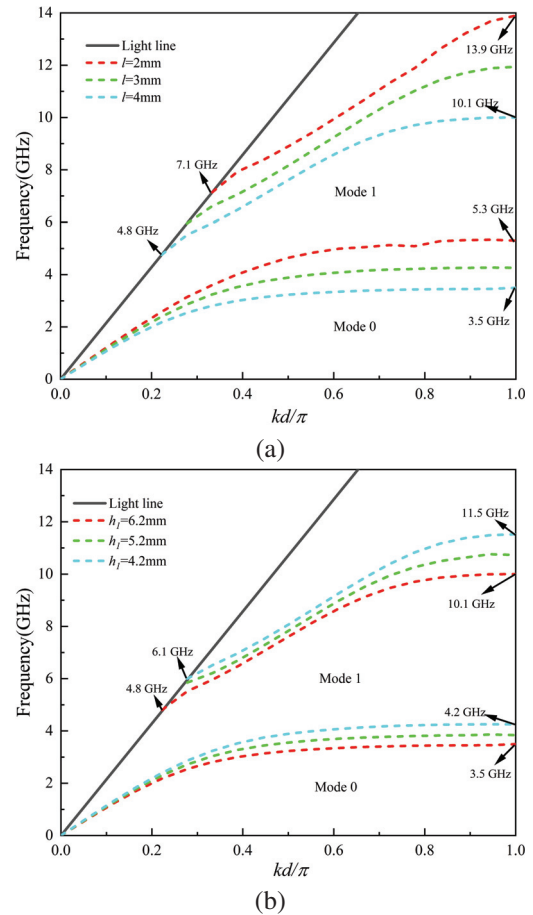

(a)

(b)

Fig. 2. (a) Dispersion characteristics of bow-folded strip SSPPs cells of different l and (b) dispersion characteristics of bow-folded strip SSPPs cells of different h_1.

with the light (i.e., the lower cut-off frequency) gradually decreases from 7.1 GHz to 4.8 GHz. The cut-off frequency (i.e., the upper cut-off frequency) gradually decreases from 13.9 GHz to 10.1 GHz. As shown in Fig. 2 (b), when the length h_1 of the bow-folded strip SSPPs cell is increased from 4.2 mm to 6.2 mm, the intersection of the first high-order mode with the light (i.e., the lower cut-off frequency) gradually decreases from 6.1 GHz to 4.8 GHz, and the cut-off frequency (i.e., the upper cut-off frequency) gradually decreases from 11.5 GHz to 10.1 GHz. As a result, the structural characteristics of the bow-folded strip can influence the passband frequency range created by the first-order higher mode, and the desired passband can be flexibly altered by choosing alternative structure sizes. As can be seen in Fig. 2, the groove depth h_1 and width l affect the cut-off frequency of the high-order mode, so the desired passband can be flexibly adjusted by setting different structural dimensions.

III. IMPLEMENTATION OF BAND-PASS FILTER WITH HIGH-ORDER MODE

A. Single-band band-pass filter

Based on the above high-order mode analysis and the proposed bow-folded strip SSPPs structure, a single-band band-pass filter is designed, as shown in Fig. 3 (a). It has an overall length of 53 mm. Table 2 shows the optimized dimensions of the single-band band-pass filter. Region I is a microstrip line with a characteristic impedance of 50 ohm which is adopted as the input/output waveguide. Region II serves as a straightforward trapezoidal interface, ensuring a smooth connection between the microstrip lines and the proposed SSPPs structure, thereby minimizing space occupation. Region III comprises four identical units of SSPPs cells.

Table 2: The optimized dimensions of single-band band-pass filter (unit=mm)

L_0	L_m	W_0	W_1	w	l	h_1
7	5.5	1.55	2	0.5	4	6.2

Figure 3 (b) presents the simulated S-parameters of single-band band-pass filter. Good band-pass characteristics and efficient propagation are obtained in the frequency range from 4.8 GHz to 10.1 GHz, with insertion loss less than 0.3 dB and in-band return loss better than 14 dB. The low and high frequency band edges of the passband are located at 4.8 and 10.1 GHz, respectively. This is essentially the same as the high-order mode cut-off frequency of the bow-folded strip SSPPs cell structure. While the fundamental mode produces a low-passband ranging from 0 to 3.5 GHz, the insertion loss in this range is significantly higher compared to the
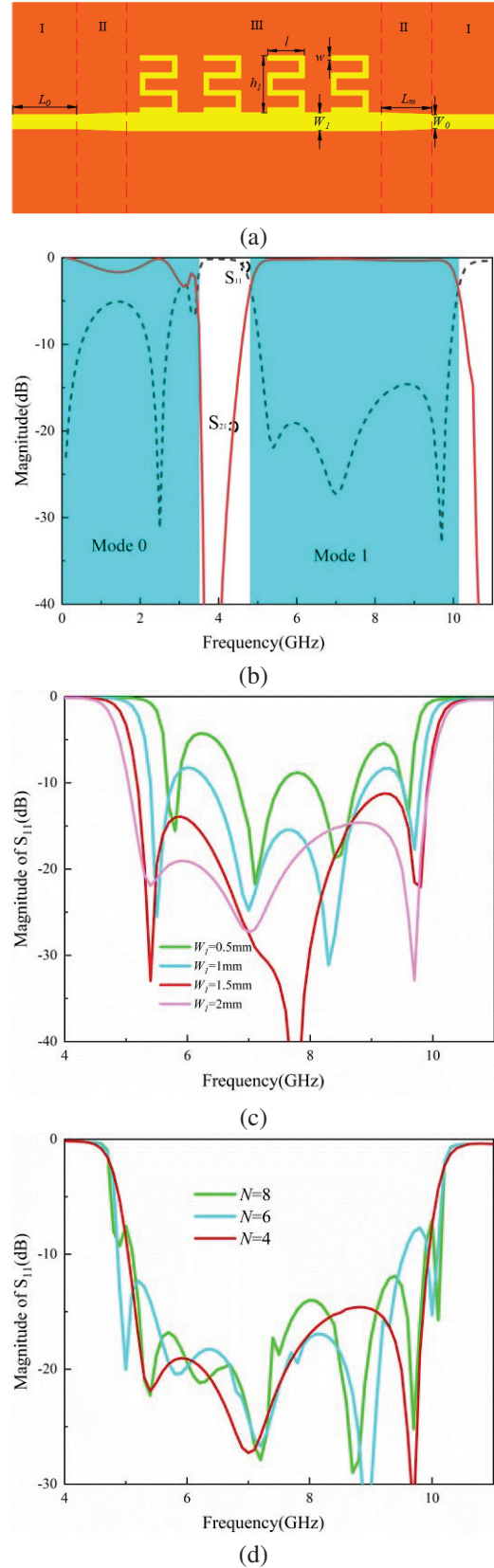

(a)

(b)

(c)

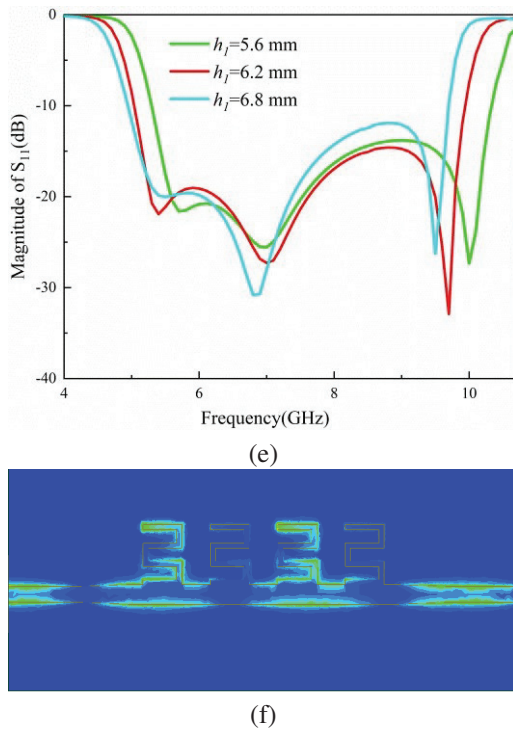

(d)

Fig. 3. (Continued.)

(e)

(f)

Fig. 3. (a) Schematic diagram of the structure of the single-band band-pass filter, (b) S-parameters of the single-band band-pass filter, (c) return loss of the single-band band-pass filter with different W_1, (d) return loss of the single-band band-pass filter with different N, (e) return loss of the single-band band-pass filter with different h_1, and (f) electric field distribution of the single-band band-pass filter at 7 GHz.

passband created by the first high-order mode. In this design, the transmission method without the addition of traditional staircase graduation SSPPs transition structures can effectively inhibit the low-pass effect of the fundamental mode and enhance the band-pass characteristics of the first high-order mode.

Among them, the return loss of the band-pass filter is affected by the width W_1, the groove depth h_1, the length l, and the number of cells. As shown in Figs. 3 (c-e), the return loss gradually decreases and shifts to the left when W_1 increases from 0.5 to 2 mm. The return loss increases when the number of cells is 8, and the best result is obtained when the number of cells is 4. The best result is obtained when the return loss is 6.2 mm when h_1 increases from 5.6 to 6.8 mm. Through the above analysis, it can be concluded that by optimizing the width, groove depth, length and cell number, the return loss can be improved, resulting in better performance of the band-pass filter.

To further examine the propagation properties of the high-order mode of SSPPs, we illustrate in Fig. 3 (e)

the electric field distribution of the single-band band-pass filter at 7 GHz. Evidently, the transmission of energy from the input port to the output port is done efficiently. Hence, the successful stimulation of the high-order mode enables the acquisition of a passband with high efficiency.

B. Dual-band band-pass filter

In order to delve deeper into the characteristics of the bow-folded strip SSPPs structure at high-order mode, we piloted another dual-band band-pass filter design. The dimensions of the bow-folded strip cell structure are smaller, with a transverse dimension reduced to 70% of the conventional rectangular groove cell structure with h=22 mm. The total length of dual-band band-pass filter is 64 mm. Figure 4 (a) shows the schematic diagram of the dual-band band-pass filter structure, and Table 3 shows the optimized dimensions.

The dispersion curve of the dual-band band-pass filter cell structure is illustrated in Fig. 4 (b), and it can be seen that the groove depth clearly affects the total number of modes in the SSPPs structure, and there are two high-order mode. There is a forbidden band between the fundamental mode and the first high-order mode. There is also a forbidden band between the second high-order mode and the first high-order mode. The cut-off frequency for the first high-order mode is 7.2 GHz, whereas the cut-off frequency for the second high-order mode is 11.5 GHz. It is worth noting that the fundamental mode has a lower cut-off frequency compared to the single-band band-pass filter unit structure. By observing Fig. 4 (c), it becomes evident that two passbands are generated by the first high-order mode and the second high-order mode, covering the frequency ranges of 3.57-7.2 GHz and 7.9-11.5 GHz, respectively. These frequency ranges align with the dispersion curves illustrated in Fig. 4 (b). The first high-order mode demonstrates an insertion loss of below 0.2 dB, accompanied by a return loss better than 19 dB. Similarly, the second-order high mode shows an insertion loss lower than 0.3 dB and a return loss better than 19.5 dB. Consequently, the system exhibits a favorable response in terms of dual-band filtering.

In order to obtain a comprehensive understanding of the transmission characteristics, Fig. 4 (d) illustrates the distribution of electric fields at frequencies of 5, 7.5, and 10 GHz. At 5 GHz and 10 GHz passband range, the microstrip line effectively converts the guided wave into the SSPPs mode, resulting in a passband that exhibits excellent transmission performance. It is important to highlight that the electric field intensity is higher at 5 GHz compared to 10 GHz, indicating potential energy losses during transmission. At the blocking band frequency of 7.5 GHz, the majority of the electric field is
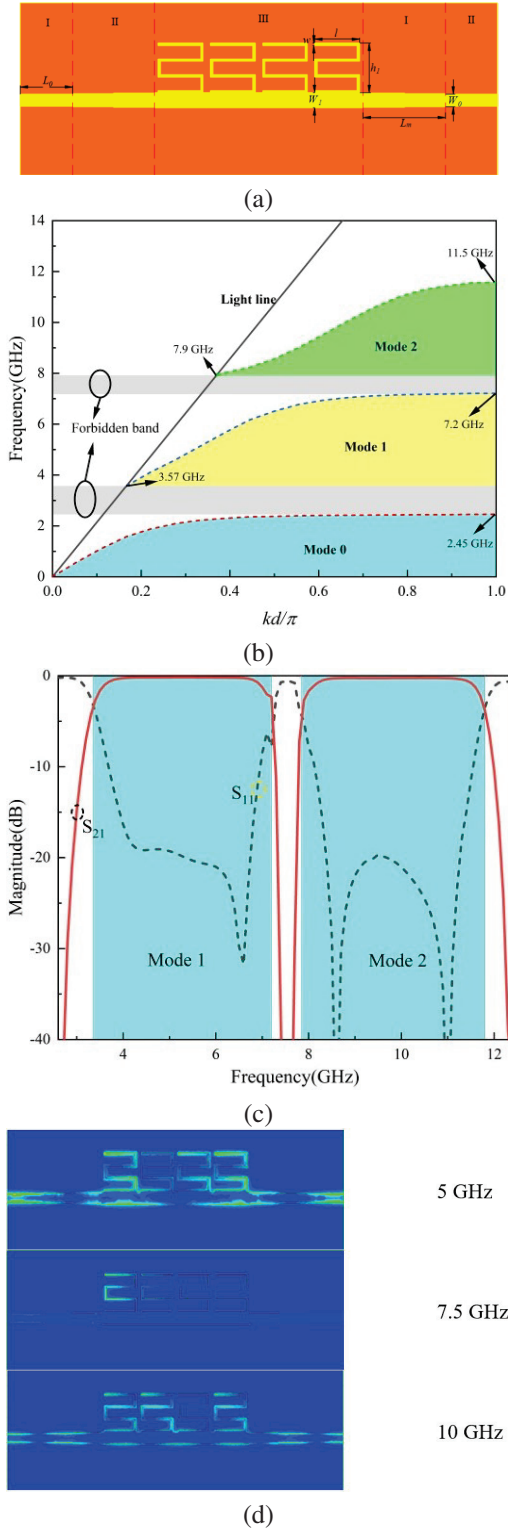
(a)

(b)

(c)

(d)

Fig. 4. (a) Schematic diagram of the structure of the dual-band band-pass filter, (b) dispersion characteristics of the dual-band band-pass filter SSPPs cell structure, (c) S-parameters of the dual-band band-pass filter, and (d) electric field distributions of the dual-band band-pass filter at 5 GHz, 7.5 GHz, and 10 GHz.

concentrated on the initial SSPPs cell, resulting in the blocking of signals within the blocking band range.

Table 3: The optimized dimensions of dual-band band-pass filter (unit=mm)

L_0	L_m	W_0	W_1	w	l	h_1
7	11	1.55	2	0.3	6	6.6

IV. TEST RESULTS

In an effort to confirm the possibility of employing the high-order mode SSPPs band-pass filter, we fabricated and measured two distinct types of filters. Figures 5 (a) and (b) show the single-band and dual-band band-pass filters, correspondingly. This was achieved by taking into account the correlation between the high-order mode dispersion attributes of the proposed SSPPs cell and the geometric alteration of the slot. To acquire
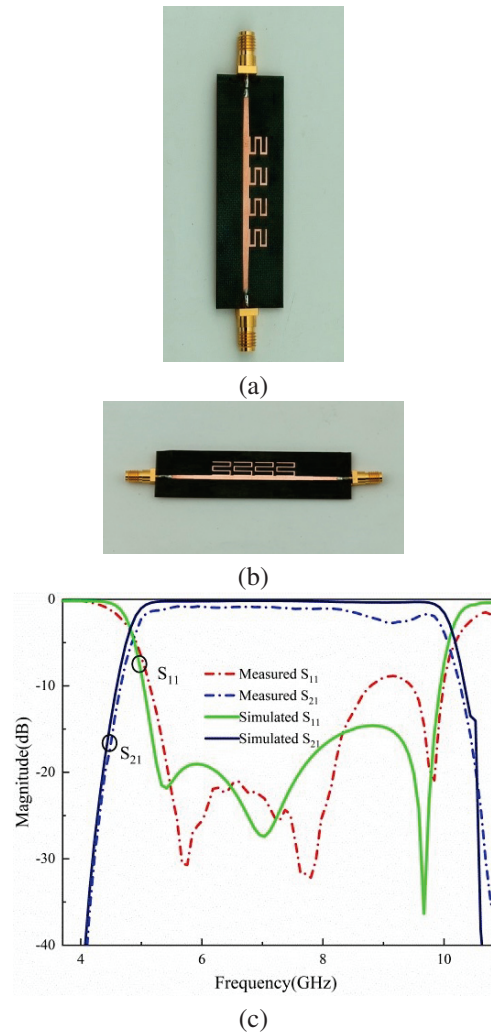

(a)

(b)

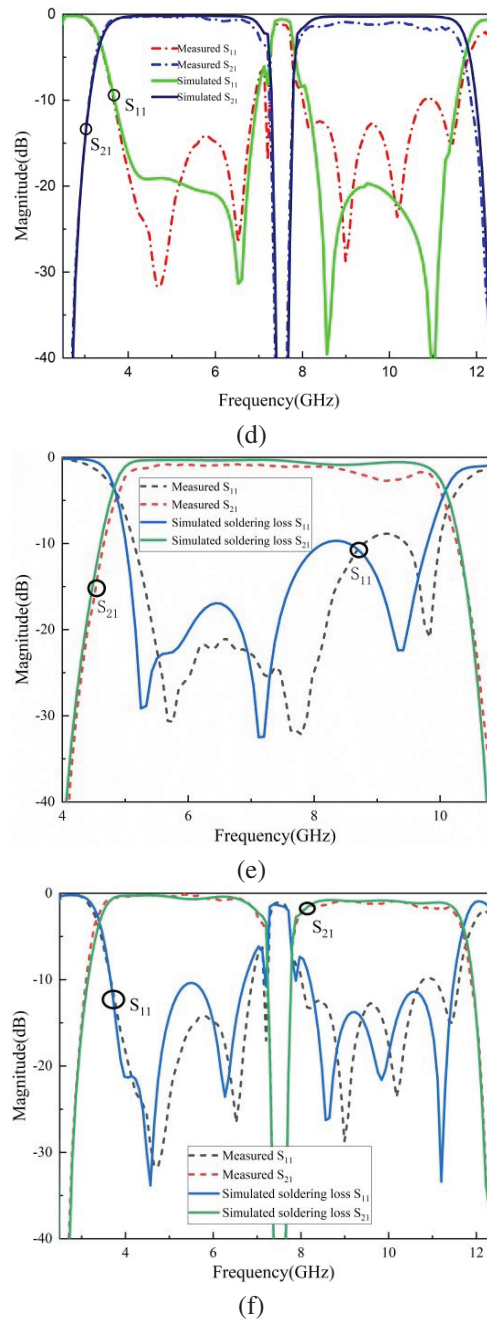(c)

Fig. 5. (Continued).

(d)

(e)

(f)

Fig. 5. (a) Fabricated samples of single-band band-pass filter, (b) fabricated samples of dual-band band-pass filter, (c) measured and simulated result of the single-band band-pass filter, (d) measured and simulated result of the dual-band band-pass filter, (e) comparison of simulated solder loss result for single-band band-pass filter with measured results, and (f) comparison of simulated solder loss result for dual-band band-pass filter with measured results.

the S-parameters of the filter, we joined the filter with two SMA connectors. The connectors were used to connect the 50-ohm microstrip lines, and they were securely

attached to both ends of two fabricated prototypes for the purpose of measurement. The results of the measurement are very similar to the simulation. As shown in Fig. 5 (c), the simulated return loss is better than 19 dB and the measured return loss is better than 10 dB in the passband from 4.8 GHz to 8 GHz, and the simulated return loss is better than 20 dB and the measured return loss is better than 10 dB in the passband from 8 GHz to 10.1 GHz. As shown in Fig. 5 (d), the simulated dual-band band-pass filter exhibits an insertion loss of less than 0.2 dB and a return loss better than 19 dB in the frequency range of 3.57 GHz to 7.2 GHz. Correspondingly, the measured dual-band band-pass filter showcases an insertion loss below 0.7 dB and a return loss greater than 14 dB in the identical frequency span. In the frequency range from 7.9 GHz to 11.5 GHz, the simulated dual-band band-pass filter attains an insertion loss below 0.3 dB and a return loss exceeding 19.5 dB. The measured dual-band band-pass filter exhibits an insertion loss less than 1dB and a return loss better than 10dB within the same frequency range.

It can be seen that the measured results match well with the simulation result curve, but the measured insertion loss and return loss are both higher than the simulation loss. This is mainly due to the SMA connector soldering and manufacturing tolerance. In order to reduce soldering loss, we can optimize the loss due to welding by simulating them before soldering, thus reducing the loss due to soldering during measurement. As shown in Figs. 5 (e) and (f), the S-parameters of the band-pass filter are simulated with the same environmental factors (with the same SMA connector and manufacturing tolerance) as in the measurement. It can be seen that the S-parameters of the single-band and dual-band band-pass filters with soldering loss agree with the curve fit of the measured S-parameters. Therefore, the soldering loss can be continuously optimized during the simulation process so that the simulation results can reach the best value to reduce the loss caused during soldering and make a better agreement between the measurement results and simulation results.

Table 4 presents a comparison of the performance and size of the band-pass filters proposed in this study with those previously reported based on the high-order mode of SSPPs. Both band-pass filters proposed in this research exhibit wider bandwidth fractions compared to the previously suggested filters. Compared to the single-band band-pass filters in [24, 27], the proposed single-band band-pass filter in this paper achieves a size reduction of nearly 50% while maintaining excellent performance. The proposed single-band band-pass filter has an insertion loss that is half of that in reference [23], and it also achieves a size reduction of nearly 67%. Compared to the single-band band-pass filters in [25],

Table 4: Comparison of the proposed band-pass filters based on the high-order mode of SSPPs with the previous work

Ref.	Number of Modes	f_0 (GHz)	IL (dB)	RL (dB)	Horizontal Dimension (λ_g)	FBW (%)
[23]	Mode 1	11.5	2.3 measured	10 measured	0.59	56.5
[24]	Mode 1	7.79	1.46 measured	10 measured	0.39	43.4
[25]	Mode 1	8	1.7 measured	12 measured	0.24	50
[26]	Mode 1 Mode 2	7.95, 14.65	0.2, 0.36 simulated	15, 15 simulated	0.2, 0.36	64.2 29.4
[27]	Mode 1	8.2	0.16 simulated	12.6 simulated	0.47	58
This work	Mode 1	7.5	0.3 simulated 1 measured	14 simulated 10 measure	0.2	78.5
	Mode 1 Mode 2	5.4, 9.7	0.2, 0.3 simulated 0.7, 1 measured	19, 19.5 simulated 14, 10 measured	0.15, 0.27	67.2 37.1

the proposed single-band band-pass filter demonstrates advantages in terms of insertion loss and size. With nearly identical dimensions, we have fabricated dual-frequency band-pass filters using first high-order mode and second high-order mode. According to Table 4, the size of the proposed dual-band band-pass filter is smaller than that of the dual-band band-pass filter of [26] and the performance of this filter is better.

Hence, both of the proposed band-pass filters possess the benefits of a compact structure and minimal insertion loss, and have potential application in integrated devices.

V. CONCLUSION

In this paper, we design two types of band-pass filters: single-band and dual-band filters. These filters utilize the high-order mode of spoof surface plasmon polaritons as their foundation. Compared to the conventional single-side rectangular groove SSPPs cell, our proposed cells reduce the electrical size by 59% and 70% at the same high-order cut-off frequency. By simulating the dispersion curves of the SSPPs cell structure, we examine the primary parameters that impact the cut-off frequency of both the fundamental and high-order mode of SSPPs. The simulation and measurement of the single-band and dual-band band-pass filters, which are based on the high-order mode of SSPPs with a bow-folded strip structure, are performed using microstrip line feed. The simulation results align well with the measured results, demonstrating the feasibility of applying the SSPPs high-order mode to band-pass filter design. We also verified the key factors that cause a slight difference between the measured and simulated results. The simplicity and small size of the proposed structure and design method suggest promising potential applications in plasma devices and systems.

REFERENCES

[1] W. L. Barnes, A. Dereux, and T. W. Ebbesen, "Surface plasmon subwave length optics," *Nature*, vol. 424, no. 6950, pp. 824-830, Aug. 2003.

[2] J. B. Pendry, L. Martín-Moreno, and F. J. Garcia-Vidal, "Mimicking surface plasmons with structured surfaces," *Science*, vol. 305, no. 5685, pp. 847-848, 2004.

[3] F. J. Garcia-Vidal, L. Martín-Moreno, and J. B. Pendry, "Surfaces with holes in them: New plasmonic metamaterials," *Journal of Optics A: Pure and Applied Optics*, vol. 7, no. 2, pp. S97-S101, 2005.

[4] X. P. Shen, T. J. Cui, D. Martin-Cano, and F. J. Garcia-Vidal, "Conformal surface plasmons propagating on ultrathin and flexible films," *Proc. Nat. Acad. Sci. USA*, vol. 110, no. 1, pp. 40-45, Jan. 2013.

[5] H. F. Ma, X. Shen, Q. Cheng, W. X. Jiang, and T. J. Cui, "Planar plasmonic metamaterial on a thin film with nearly zero thickness," *Applied Physics Letters*, vol. 102, no. 21, p. 211909, 2013.

[6] L. F. Ye, Y. F. Xiao, and N. Liu, "Plasmonic waveguide with folded stubs for highly confined terahertz propagation and concentration," *Optics Express*, vol. 25, no. 2, pp. 898-906, 2017.

[7] W. Feng, Y. Feng, W. Y. Ang, W. Che, and Q. Xue, "High-performance filtering antenna using spoof surface plasmon polaritons," *IEEE Trans. Plasma Sci.*, vol. 47, no. 6, pp. 2832-2837, June 2019.

[8] E. Mohamed, K. M. Ibrahim, and A. M. Attiya, "Analysis and design of a diplexer for satellite communication system," *Applied Computational Electromagnetics Society (ACES) Journal*, vol. 35, no. 10, pp. 1236-1241, 2020.

[9] R. S. Anwar, L. Mao, and H. Ning, "Role of surface geometric patterns and parameters in the dispersion relations of spoof surface plasmon polaritons

at microwave frequency," *Applied Computational Electromagnetics Society (ACES) Journal*, vol. 34, no. 1, pp. 172-179, 2021.

[10] Y. J. Guo, K. D. Xu, Y. H. Liu, and X. H. Tang, "Novel surface plasmon polariton waveguides with enhanced field confinement for microwave-frequency ultra-wideband bandpass filters," *IEEE Access*, vol. 6, pp. 10249-10256, Feb. 2018.

[11] K.-D. Xu, F. Zhang, Y. Guo, L. Ye, and Y. Liu, "Spoof surface plasmon polaritons based on balanced coplanar stripline waveguides," *IEEE Photon. Technol. Lett.*, vol. 32, no. 1, pp. 55-58, Jan. 2020.

[12] H. L. Zhu, Y. Zhang, and L. F. Ye, "Compact terahertz on-chip filter with broadband rejection based on spoof surface plasmon polaritons," *IEEE Electron Device Letters*, vol. 43, no. 6, pp. 970-973, June 2022.

[13] S. Sun, Y. Cheng, and H. Luo, "Notched-wideband bandpass filter based on spoof surface plasmon polaritons loaded with resonator structure," *Plasmonics*, pp. 165-174, 2023.

[14] L. Ye, Z. Chen, Y. Zhang, W. Li, Y. Zhang, and K. Wei, "High performance multiple passband substrate integrated plasmonic filters," *IEEE Transactions on Circuits and Systems II: Express Briefs*, vol. 70, no. 4, pp. 1445-1449, Apr. 2023.

[15] Y. J. Guo, K. D. Xu, X. Deng, X. Cheng, and Q. Chen, "Millimeter wave on-chip bandpass filter based on spoof surface plasmon polaritons," *IEEE Electron Device Lett.*, vol. 41, no. 8, pp. 1165-1168, Aug. 2020.

[16] W. Feng, Y. Feng, W. Y. Ang, W. Che, and Q. Xue, "High-performance filtering antenna using spoof surface plasmon polaritons," *IEEE Trans. Plasma Sci.*, vol. 47, no. 6, pp. 2832-2837, June 2019.

[17] X. F. Zhang, J. Fan, and J. X. Chen, "High gain and high-efficiency millimeter-wave antenna based on spoof surface plasmon polaritons," *IEEE Trans. Antennas Propag.*, vol. 67, no. 1, pp. 687-691, Jan. 2019.

[18] J. Wang, L. Zhao, Z. C. Hao, X. P. Shen, and T. J. Cui, "Splitting spoof surface plasmon polaritons to different directions with high efficiency in ultra-wideband frequencies," *Opt. Lett.*, vol. 44, no. 13, pp. 3374-3377, July 2019.

[19] X. Gao, J. H. Shi, X. P. Shen, H. F. Ma, W. X. Jiang, L. Li, and T. J. Cui, "Ultrathin dual-band surface plasmonic polariton waveguide and frequency splitter in microwave frequencies," *Appl. Phys. Lett.*, vol. 102, no. 15, Art. no. 151912, Apr. 2013.

[20] B. C. Pan, P. Yu, Z. Liao, F. Zhu, and G. Q. Luo, "A compact filtering power divider based on spoof surface plasmon polaritons and substrate integrated waveguide," *IEEE Microwave and Wireless Components Letters*, vol. 32, no. 2, pp. 101-104, Feb. 2022.

[21] C. Han, Z. H. Wang, Y. Y. Chu, X. D. Zhao, and X. R. Zhang, "Compact flexible multifrequency splitter based on plasmonic graded metallic grating arc waveguide," *Opt. Lett.*, vol. 43, no. 8, pp. 1898-1901, 2018.

[22] D. Yi, X. C. Wei, and R. Yang, "Modeling and analyzing high-order modes in periodic-stub-loaded stripline for wideband filter design," *IEEE Transactions on Electromagnetic Compatibility*, Vol. 62, no. 2, pp. 398-405, 2020.

[23] Y. Liu and K. D. Xu, "Bandpass filters using grounded stub-loaded microstrip periodic structure for suppression of modes," *Journal of Physics D: Applied Physics*, vol. 55, no. 42, p. 425104, 2022.

[24] Y. Liu, K. D. Xu, Y. J. Guo, and Q. Chen, "High-order mode application of spoof surface plasmon polaritons in bandpass filter design," *IEEE Photonics Technology Letters*, vol. 33, no. 7, pp. 362-365, 2021.

[25] Z. Lin, Y. Li, L. Li, Y. T. Zhao, J. Xu, and J. Chen, "Miniaturized bandpass filter based on high-order mode of spoof surface plasmon polaritons loaded with capacitor," *IEEE Transactions on Plasma Science*, vol. 51, no. 1, pp. 254-260, Jan. 2023.

[26] S. Zhu, P. Wen, and Y. Liu, "Multi-band propagation of spoof surface plasmon polaritons by its high-order modes," *Japanese Journal of Applied Physics*, vol. 61, no. 7, p. 070907, 2022.

[27] Y. Liu, K. D. Xu, Y. J. Guo, and Q. Chen, "High-order mode of spoof surface plasmon polaritons and its application in bandpass filters," *IEEE Transactions on Plasma Science*, vol. 49, no. 1, pp. 269-275, 2021.

[28] H. H. Zhao, P. Zhou, Z. Xu, S. Li, and X. Yin, "Tri-band band-pass filter based on multi-mode spoof surface plasmon polaritons," *IEEE Access*, vol. 8, pp. 14767-14776, 2020.

[29] W. Feng, S. Shi, S. Yin, H. Zhu, Y. Shi, and W. Che, "Novel wideband bandpass filters using double-sided quasi-SSPPs transmission line," *IEEE Transactions on Circuits and Systems II: Express Briefs*, vol. 69, no. 7, pp. 3174-3178, July 2022.

[30] X. Liu, Y. Feng, B. Zhu, J. Zhao, and T. Jiang, "High-order modes of spoof surface plasmonic wave transmission on thin metal film structure," *Opt. Exp.*, vol. 21, no. 25, pp. 31155-31165, 2013.

[31] H. C. Zhang, "Fundamental theory, device synthesis and system integration of spoof surface plasmon polaritons," dissertation, Nanjing: Southeast University, 2020.

Siyu Yang is studying for the master's degree at Chengdu University of Technology, Chengdu, China. Her current research interests include Spoof Surface Plasmon Polaritons and microwave circuits.

Shuang Liu received the PhD. degree in electromagnetic field and microwave technology from University of Electronic Science and Technology of China (UESTC), Chengdu, China, in 2016. She is currently a teacher in Chengdu University of Technology, Chengdu, China. Her current research interests include microwave, millimeter-wave and terahertz passive circuits, antenna, spoof surface plasmon polaritons, and physics.

Huali Zhu received the B.S. degree from the University of Electronic Science and Technology of China, Chengdu, China, in 2017. He is currently pursuing the Ph.D. degree with the University of Electronic Science and Technology of China, Chengdu, China, majoring in electronic science and technology. His current research interests include microwave/millimeter wave circuit theory and technology, mm-wave and terahertz integrated circuits and systems.

Fachun He is studying for the master's degree at Chengdu University of Technology, Chengdu, China. His current research interests include spoof surface plasmon polaritons and microwave circuits.

Dan Lei received the B.S. degree in applied physics from Chongqing University in 2000, M.Eng. in electromagnetic field and Microwave Technology from University of Electronic Science and Technology of China in 2007. She is currently teaching electrodynamics and microwave technology and antennas at Chengdu University of Technology. Her current research interests include numerical modeling methods of passive microwave circuits, microwave circuits and microwave test.
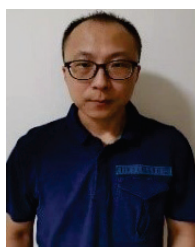
Jun Yan received the S. and Ph.D. degrees in electromagnetic and microwave engineering from the University of Electronic Science and Technology of China, Chengdu, China, in 2005 and 2016, respectively. He is currently an Engineer of microwave engineering at the China Electronics Technology Group Corporation 10th Research Institute, Chengdu. His research interests include wide-band, low-profile antenna array and feed-network design for microwave and millimeter-wave frequencies.

Chan Gao received the B.S. degree in applied physics from Henan University of Technology, Zhengzhou, China in 2012, and the Ph.D. degree in condensed matter physics from University of Science and Technology of China (USTC), Hefei, China, in 2018. From 2018-2021, she was a postdoctoral researcher in University of Science and Technology of China (USTC), Hefei, China. She is currently a lecturer in Chengdu University of Technology (CDUT), Chengdu, China. Her current research interests include the structure and photoelectrical properties of material under extreme condition and microwave circuits.

Investigation on Pulse Radiation Characteristics of Discretized Apertures in Time-domain

Binwen Wang, Hui Ning, Chengyun Cao, Qilong Liu, and Kaiyue Zhang

Northwest Institute of Nuclear Technology
Xi'an 710024, China
srxh_bingwen@aliyun.com, ninghuisun@aliyun.com, caochengyun12@163.com,
820091469@qq.com, kaiyo@163.com

Abstract – In view of the challenges and difficulties encountered in the analysis and application of time-driven ultra-wideband array antennas (TD-UWB arrays), this study investigates the pulse radiation characteristics of discretized apertures based on aperture radiation theory and space superposition principle. The impact of discretized aperture linear arrays and planar arrays to restore the radiation of original aperture is examined, along with an analysis of how discretization methods influence the radiated pulse waveforms. The potential application of discretized aperture radiation in research of TD-UWB array antennas is studied, and a method is proposed for predicting time-domain radiation characteristics of TD-UWB arrays. Numerical results demonstrate that the proposed method derived from the discretized aperture radiation can effectively predict the temporal pattern and radiation waveforms of TD-UWB arrays. The research expands and advances the practical applications of aperture radiation, thereby offering a novel perspective for analyzing the radiation characteristics of TD-UWB arrays.

Index Terms – discretized aperture, pulse radiation characteristics, tangential electric field, TD-UWB arrays, time-domain pattern.

I. INTRODUCTION

With the rich frequency components and short-pulse characteristics in time-domain [1], ultra-wideband pulses have demonstrated significant advantages and extensive potential applications in ground penetrating radar [2, 3], high-precision positioning [4, 5], biomedicine [6, 7], wireless communications [8, 9], nondestructive testing [10] and electromagnetic compatibility [11–14] as well as other domains. Sequentially, the ultra-wideband antenna has been a research focus within the field of antenna technology [15–17]. Time-driven ultra-wideband array antenna (TD-UWB array) enhances the radiation gain by increasing the aperture area, while also expanding the capabilities of the radiation sys-

tem through the introduction of multiple spatial degrees of freedom such as beam customization and waveform reconstruction [18]. This approach has emerged as a prominent method for generating and applying ultra-wideband time-domain pulses [19–23]. The radiation of ultra-wideband pulse falls within the realm of transient electromagnetics, which indicates that the study of ultra-wideband array antenna significantly deviates from conventional time-harmonic antennas. The introduction of time variable results in the radiation characteristics of UWB array antennas having dual dependencies on both time and space. In addition, the radiation performances are not only related to the element antenna structure and array scale but also depend on excitation pulse waveforms and delay constraint conditions [21]. Because of the influences of multiple factors, there is a dearth of robust research methodologies for the analysis of ultra-wideband array antennas. Specifically, array pattern synthesis and beamforming pose significant challenges due to the absence of universally applicable field distribution functions.

Analysis of array antennas is closely tied to the array factor, which serves as a concrete representation of the spatial arrangement of the array elements. Foo proposed the temporal array factor to describe the pattern characteristics of UWB array antenna in time-domain [22]. Yan et al. introduced the temporal array factor of planar array with the basis of the three-dimensional impulse point source response, and further proposed the theory of time-domain pattern convolution employing the temporal array factor of isotropic planar array and time-domain pattern of array element [23]. However, the measurements of time-domain pattern and radiation pulses is indispensable in practical applications. The extraction of array factors can solely investigate the impact of array layout and scale on the time-domain pattern. Nevertheless, a complete depiction of time-domain radiation characteristics necessitates integrating the array factors with the radiation characteristics of array elements. Fortunately, aperture radiation encompasses both aspects and

provides a direct assessment of the combined effect. That is the aperture radiation characteristics already demonstrate the influence of both tangential electric field and aperture dimensions, without requiring additional extraction of the array factor. Aperture radiation theory derived from the equivalent source theorem of electromagnetics is an effective means for analyzing the radiation characteristics of aperture antennas [24–26]. Nevertheless, the application of aperture radiation theory on the analysis and prediction of radiation characteristics for TD-UWB arrays remains a technical challenge.

To break the current dilemma and satisfy practical requirements, an investigation is conducted into discretized aperture radiation characteristics. Then the realistic applications of discretized aperture radiation are discussed. Subsequently, a method for rapidly predicting the pulse radiation characteristics of TD-UWB array antennas is proposed, thereby offering a novel approach to analyze TD-UWB arrays. This paper is organized as follows. The first section is the introduction of the research background. The second section reviews the derivation of aperture radiation theory and the solution method in time-domain and presents two discretization approaches for radiation apertures. The third section analyzes the radiation characteristics of the discretized aperture planar arrays. In the penultimate section, the potential applications of discretized aperture radiation are explored and a verified prediction method for pulse radiation characteristics of TD-UWB arrays is proposed. The final section is the conclusion of this paper.

II. APERTURE RADIATION THEORY
A. Derivation of aperture radiation in time-domain

A rectangular aperture is taken as an example to review and derive the aperture radiation field in time-domain. Figure 1 illustrates the radiation diagram of a rectangular aperture, which is positioned in the x-y plane with side lengths a and b. The tangential electric field on the aperture is uniformly distributed in the y direction. Point P represents the external field point of the radiation aperture. To differentiate the source point and field point, the coordinates of source points are denoted by a superscript.

Based on the surface equivalent source theorem, an ideal conductor is chosen as the medium within the aperture, allowing only for consideration of the equivalent magnetic current contribution on the aperture surface [27]. The equivalent magnetic current on the aperture surface can be obtained from the tangential electric field:

$$\overrightarrow{J}_m = -\overrightarrow{n} \times \overrightarrow{E}_t, \tag{1}$$

where $\overrightarrow{n}$ is the unit vector in the normal direction of the aperture and $\overrightarrow{E}_t$ refers to the tangential electric field.

Ignoring the edge effect of radiation aperture, the electric field at external field point can be obtained by
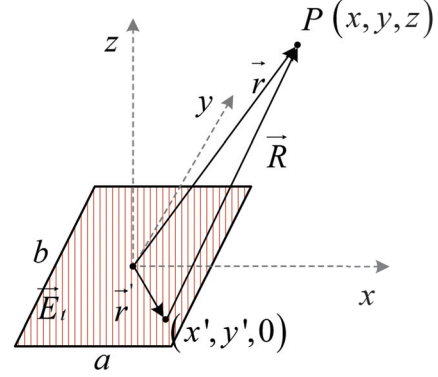

Fig. 1. Radiation diagram of the rectangular aperture.

Maxwell's equations with magnetic current source:

$$\overrightarrow{E}\left(\overrightarrow{r},t\right) = \frac{1}{4\pi} \int_S \nabla \times \left(\overrightarrow{n} \times \frac{\overrightarrow{E}_t\left(\overrightarrow{r},t-R/c\right)}{R} \right) ds', \tag{2}$$

where R refers to the distance between field point and source point.

Employing a series of vector analysis to simplify the integral term in equation (2), the electric field radiated from the equivalent magnetic source is derived as follows:

$$\overrightarrow{E}\left(\overrightarrow{r},t\right) = \frac{1}{4\pi} \int_S \left\{ \begin{array}{l} -\overrightarrow{n} \left[\begin{array}{l} \frac{\overrightarrow{R}}{cR^2} \frac{\partial \overrightarrow{E}_t\left(\overrightarrow{r},t-\frac{R}{c}\right)}{\partial t} + \\ \frac{\overrightarrow{E}_t\left(\overrightarrow{r},t-\frac{R}{c}\right)\cdot\overrightarrow{R}}{R^3} \end{array} \right] + \\ \overrightarrow{n} \cdot \left[\begin{array}{l} \frac{\overrightarrow{R}\overrightarrow{E}_t\left(\overrightarrow{r},t-\frac{R}{c}\right)}{R^3} + \\ \frac{\overrightarrow{R}}{cR^2} \frac{\partial \overrightarrow{E}_t\left(\overrightarrow{r},t-\frac{R}{c}\right)}{\partial t} \end{array} \right] \end{array} \right\} ds'. \tag{3}$$

It is assumed that the tangential electric field on the aperture is denoted as:

$$E_t\left(\overrightarrow{r},t-\frac{R}{c}\right) = f\left(\overrightarrow{r},t-\frac{R}{c}\right). \tag{4}$$

Then, the radiated electric field expressions in difference polarizations at external field point are presented:

$$E\left(\overrightarrow{r},t\right)\overrightarrow{e}_y = \frac{-1}{4\pi c} \int_s \left[\begin{array}{l} \frac{(z-z')}{R^2} \cdot \frac{\partial f\left(\overrightarrow{r},t-\frac{R}{c}\right)}{\partial t} \\ + \frac{c(z-z')}{R^3} f\left(\overrightarrow{r},t-\frac{R}{c}\right) \end{array} \right] ds', \tag{5}$$

$$E\left(\overrightarrow{r},t\right)\overrightarrow{e}_z = \frac{1}{4\pi c} \int_s \left[\begin{array}{l} \frac{(y-y')}{R^2} \cdot \frac{\partial f\left(\overrightarrow{r},t-\frac{R}{c}\right)}{\partial t} \\ + \frac{c(y-y')}{R^3} f\left(\overrightarrow{r},t-\frac{R}{c}\right) \end{array} \right] ds'. \tag{6}$$

The results illustrate that the tangential electric field in y direction generates two kinds of electric field components in orthogonal polarization directions. The electric field in y direction is the principal polarization component, which is the focus to be investigated. Additionally, it can be clearly observed from the electric field expressions that the distribution of the tangential electric field and the aperture dimensions are key points to determine the radiated pulse waveforms and amplitude. Specifically, there are many variations of the tangential electric fields, which is exactly the emphasis and significance to utilize the aperture radiation theory to conduct realistic problems.

The integration is transformed into summation through discretization approach to calculate the principle polarized electric field [28]. Firstly, the time variable is represented as follows:

$$t = n\Delta t + \frac{R}{c}. \tag{7}$$

Then, the discretization forms of equation (5) are conducted as:

$$E\left(\overrightarrow{r}, n\Delta t + \frac{R}{c}\right)\overrightarrow{e}_y = \sum_{i,j}\begin{bmatrix} A_{i,j}f((n+1)) \\ +B_{i,j}f(n) \\ +C_{i,j}f((n-1)) \end{bmatrix}\Delta x \Delta y, \tag{8}$$

where Δt refers to the time step, $\Delta x \Delta y$ is the cell area in summation, and other coefficients are defined as follows:

$$\begin{cases} A_{i,j} = \frac{1}{4\pi c}\frac{(z-z_i')}{2\Delta t R^2}, B_{i,j} = \frac{1}{4\pi c}\frac{c(z-z_i')}{R^3} \\ C_{i,j} = -\frac{1}{4\pi c}\frac{(z-z_i')}{2\Delta t R^2} \end{cases}. \tag{9}$$

Furthermore, rounding operation is conducted on equation (8), and a new coefficient α is introduced:

$$\alpha = n + \frac{R}{c\Delta t} - n^*\Big|_{n^*=round\left(n+\frac{R}{c\Delta t}\right)}. \tag{10}$$

The new coefficient describes the relationship between radiated electric field in different moments, which is the propagation characteristics of transient electromagnetic waves:

$$\begin{cases} E(\overrightarrow{r}, n^*) = (1-\alpha)E\left(\overrightarrow{r}, n+\frac{R}{c\Delta t}\right) \\ E(\overrightarrow{r}, n^*+1) = \alpha E\left(\overrightarrow{r}, n+\frac{R}{c\Delta t}\right) \end{cases}. \tag{11}$$

Finally, the discretized calculation expressions for principal polarized electric field are derived as:

$$\begin{cases} E(\overrightarrow{r}, n^*-1) = \sum_{i,j}[(1-\alpha)A_{i,j}f_2(n)]\Delta x \Delta y \\ E(\overrightarrow{r}, n^*) = \sum_{i,j}\begin{bmatrix}(1-\alpha)B_{i,j}f_2(n) \\ +\alpha A_{i,j}f_2(n)\end{bmatrix}\Delta x \Delta y \\ E(\overrightarrow{r}, n^*+1) = \sum_{i,j}\begin{bmatrix}(1-\alpha)C_{i,j}f_2(n) \\ +\alpha B_{i,j}f_2(n)\end{bmatrix}\Delta x \Delta y \\ E(\overrightarrow{r}, n^*+2) = \sum_{i,j}[\alpha C_{i,j}f_2(n)]\Delta x \Delta y \end{cases}. \tag{12}$$

It is worth mentioning that the time step in the above calculations must be much less than the rise time or fall time of the excitation pulse. The derived expressions are the specific calculation process of the electric field, not

the aperture discretization involved in this paper. In the next section, the aperture discretization methods will be discussed in detail.

B. Aperture discretization approach

The aperture radiation process and expressions of its radiated electric field show that there are two kinds of discretization approaches for radiation aperture.

The first approach is focused on the discretization to the tangential electric field distribution function. That means, the tangential electric field with different amplitudes and time sequences on different aperture positions are expressed by special functions. With the basis of above analysis, the tangential electric field in equation (4) can be represented as follows:

$$f\left(\overrightarrow{r}, t\right) = f_1\left(\overrightarrow{r}\right)f_2\left(t - t_d\left(\overrightarrow{r}\right)\right), \tag{13}$$

where f_1 refers to the amplitude function of the tangential electric field varying with positions, and t_d describes the time delay between different source points.

Let us take a simple example to demonstrate the calculation of radiated electric field. It is assumed that the amplitudes of the tangential electric field on the aperture vary along the x direction, and the time delay for each source point is the ratio between source point coordinate x' and light velocity. Then, equation (5) can be further crystallized:

$$E(\overrightarrow{r}, t) \tag{14}$$

$$= \frac{-1}{4\pi c}\int_s\begin{bmatrix} \frac{(z-z')}{R^2}\cdot\frac{f_1\left(\overrightarrow{r}\right)\partial f\left(t-\frac{x'}{c}-\frac{R}{c}\right)}{\partial t}+ \\ \frac{c(z-z')}{R^3}f_1\left(\overrightarrow{r}\right)f\left(t-\frac{x'}{c}-\frac{R}{c}\right) \end{bmatrix}ds'.$$

To simplify the practical calculation, the time delay term can be denoted as:

$$x_i' = m_i c\Delta t. \tag{15}$$

Next, the radiated electric field of the aperture excited by discretized tangential electric field can be calculated as:

$$\begin{cases} E(\overrightarrow{r}, n^*-1) = \sum_{i,j}[(1-\alpha)A_{i,j}f_1(i,j)f_2(n-m_i)]\Delta x \Delta y \\ E(\overrightarrow{r}, n^*) = \sum_{i,j}\begin{bmatrix}\alpha A_{i,j}f_1(i,j)f_2(n-m_i)+ \\ (1-\alpha)B_{i,j}f_1(i,j)f_2(n-m_i)\end{bmatrix}\Delta x \Delta y \\ E(\overrightarrow{r}, n^*+1) = \sum_{i,j}\begin{bmatrix}\alpha B_{i,j}f_1(i,j)f_2(n-m_i)+ \\ (1-\alpha)C_{i,j}f_1(i,j)f_2(n-m_i)\end{bmatrix}\Delta x \Delta y \\ E(\overrightarrow{r}, n^*+2) = \sum_{i,j}[\alpha C_{i,j}f_1(i,j)f_2(n-m_i)]\Delta x \Delta y \end{cases}. \tag{16}$$

Equation (16) shows that, when taking the first approach to solve the discretized aperture radiation characteristics, the amplitude matrix of the tangential electric field should be given in advance. Time delay should be transformed into m_i. If the time delay varies along both x and y directions, the matrix of time delay is necessary written as m_{ij}. These operations ahead of radiation calculation brings additional complexities, resulting in obvious inconveniences.

The second discretization approach can be derived from TD-UWB array antennas. The key point is dividing the original aperture into several small apertures with the same area. Employing the calculation method in section II.A, the radiated electric field of arbitrary small aperture with uniform tangential electric field can be calculated easily. Then, simple translations are conducted to obtain the electric field waveforms radiated by small apertures at the external field point. The translations are determined by distances between field point and the centers of these small apertures. It should be noted that, the amplitudes and time delays of the tangential electric fields for each small aperture can also be considered in the translation operations. The final step is space superposition, and the radiated electric field is calculated as follows:

$$\overrightarrow{E}\left(\overrightarrow{r},t\right)\overrightarrow{e}_y = \sum_{i}^{N} f_i \overrightarrow{E}_i\left(\overrightarrow{r}_i, t-t_{di}\right)\overrightarrow{e}_y, \quad (17)$$

where f_i refers to the tangential electric field amplitude of the i_{th} small aperture, $\overrightarrow{E}_i$ refers to the radiated electric field at the external field point of the i_{th} small aperture, and t_{di} is the time delay of the corresponding small aperture.

Compared with the first discretization approach, the second approach obviously simplifies the calculations by putting the operations to amplitude and time delay of small aperture in the middle step, and the physical meaning of the time delay distribution is clearer.

III. DISCRETIZED APERTURE RADIATION CHARACTERISTICS

The calculation expressions of radiated electric field and the physical process of aperture radiation illustrate that the number of integral cells decreases after discretization operations, leading to an increase of the calculation efficiency. However, how to discretize the aperture reasonably and the corresponding discretized aperture radiation performances are significant problems to investigate. Therefore, an example is employed to further verify and illustrate the radiation characteristics of the discretized aperture array.

It is assumed that there is a rectangular aperture as shown in Fig. 1 with side lengths of 1.2 m and 0.6 m. The second discretization approach is operated on this aperture to obtain two discretized aperture linear arrays and three discretized aperture planar arrays. Typical discretized arrays are drawn in Fig. 2. Other discretized array parameters are listed in Table 1.

Two Gaussian pulses with pulse widths of 0.6 ns and 1 ns are employed as the tangential electric field as shown in Fig. 3. All tangential electrical fields are uniformly distributed in each discretized aperture, so as to study the differences and connections between the radiation characteristics of the single and these discretized aperture arrays.
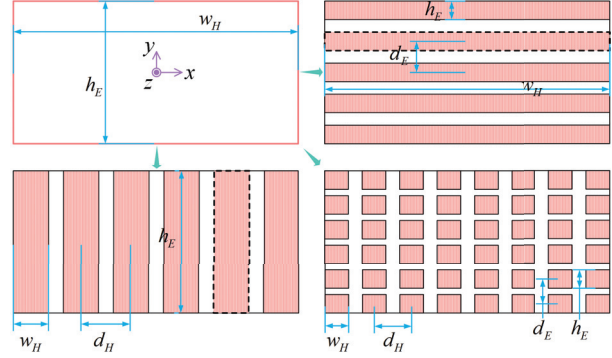
Fig. 2. Typical discretization of the rectangular aperture.
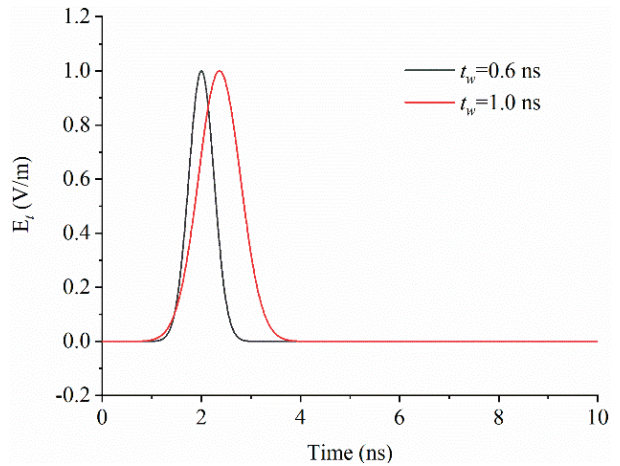
Fig. 3. Two Gaussian pulses with different pulse widths.

Table 1: Array parameters of discretized aperture arrays

No.	1	2	3	4	5	6
Type	Single	Linear		Planar		
Row	1	5	1	3	6	12
Column	1	1	6	4	8	12
h_E/m	0.60	0.08	0.60	0.18	0.075	0.028
w_H/m	1.20	1.20	0.15	0.27	0.115	0.056
d_E/m	—	0.13	—	0.21	0.105	0.052
d_H/m	—	—	0.21	0.31	0.155	0.104

According to the calculation method outlined in section II, the radiation field waveforms of each aperture excited by different tangential electric field pulses are obtained and compared. Specifically, Figs. 4 and 5 illustrate a comparison of radiation field waveforms at three field points radiated by apertures 1 and 4 under different excitation pulses. The coordinates of these three field points are (0,0,10), (8,0,10), and (8,8,10), respectively.

Figures 4 and 5 demonstrate intuitively that the field waveform characteristics of discretized aperture planar
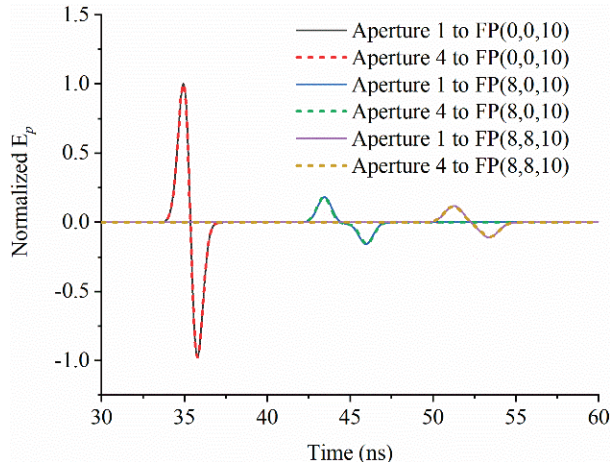
Fig. 4. Electric field waveforms of aperture 1 and 4 excited by Gaussian pulse with pulse width of 1 ns.
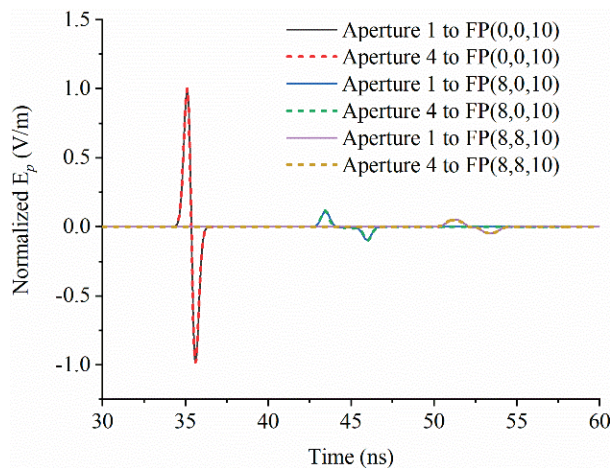

Fig. 5. Electric field waveforms of aperture 1 and 4 excited by Gaussian pulse with pulse width of 0.6 ns.

array 4 at three field points are essentially consistent with those of aperture 1 when excited by the same tangential electric field distributions.

To provide a more general comparison, the radiation field waveforms of aperture 1 are taken as references at each field point, and the pulse mean square error (pulse RMS) is utilized to quantify the impact of aperture discretization on the radiation field waveform. The calculation for pulse RMS is as follows [29]:

$$\sigma = \sqrt{\frac{\int_T \left[\frac{E_i(t)}{|(E_i(t)_{\max})|} - \frac{E_0(t)}{|E_0(t)_{\max}|} \right]^2 \mathrm{d}t}{\int_T \left(E_0(t) / |E_0(t)_{\max}| \right)^2 \mathrm{d}t}}, \qquad (18)$$

where E_i and E_0 refer to the electric field waveforms of the i_{th} aperture and the aperture 1, E_{imax} and E_{0max} are the corresponding electric field amplitudes, and T represents the duration time. According to equation (18), the pulse

RMS of the radiation field waveforms for each aperture relative to aperture 1 can be computed under varying tangential electric fields, as illustrated in Fig. 6.
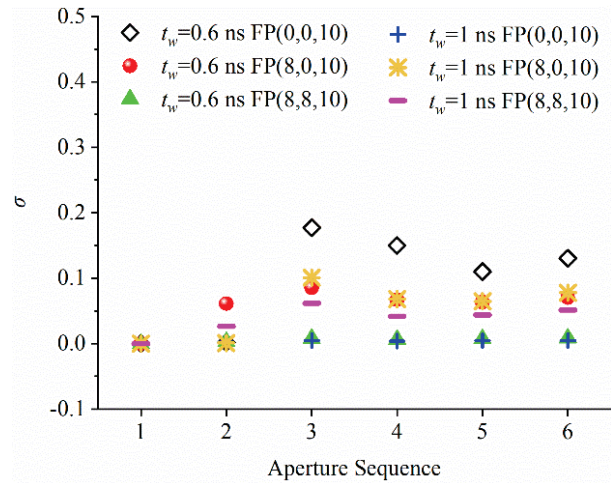
Fig. 6. The pulse RMS of the electric field waveforms for each aperture excited by Gaussian pulses.

As observed from Fig. 6, the discretization to the rectangular aperture introduces a slight distortion to the waveforms of the radiation field. The extent of this distortion is dependent on both the tangential electric field and the chosen approach of discretization. This phenomenon can be analyzed by the principles and processes involved in aperture radiation. Specifically, when an aperture is decomposed into a discretized aperture array, empty gaps devoid of tangential electric field distribution emerge between individual element apertures. These gaps, illustrated in Fig. 2, do not contribute to the overall radiation field and consequently result in discontinuities during superposition with adjacent aperture cells. Consequently, a subtle waveform distortion becomes apparent. Furthermore, this distortion is influenced by both the tangential electric fields and the size of these blank gaps. In other words, for tangential electric fields of different pulse widths, it may be possible to select an appropriate gap size or discretization method that closely approximates the radiation performances of the original aperture.

The above analysis suggests that reasonable selection of discretized aperture can be further investigated by incorporating the following variables:

$$D_c = \frac{\sqrt{d_E^2 + d_H^2}}{\tau c}, \qquad (19)$$

where τ is the time constant of the Gaussian pulse and c denotes the speed of light.

Taking aperture 4 and 6 as examples, the variation curves of pulse RMS of radiation field waveform versus

D_c at the field point of (8,8,10) under different tangential electric field pulses are solved and compared in Figs. 7 and 8.
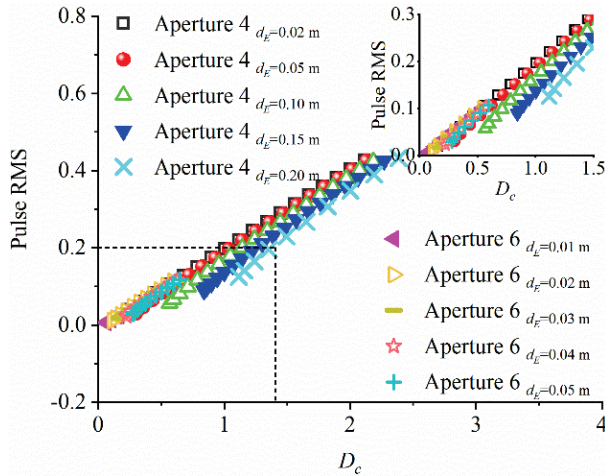
Fig. 7. Radiated pulse RMS at (8,8,10) of aperture 4 and 6 excited by Gaussian pulse with pulse width of 1 ns.
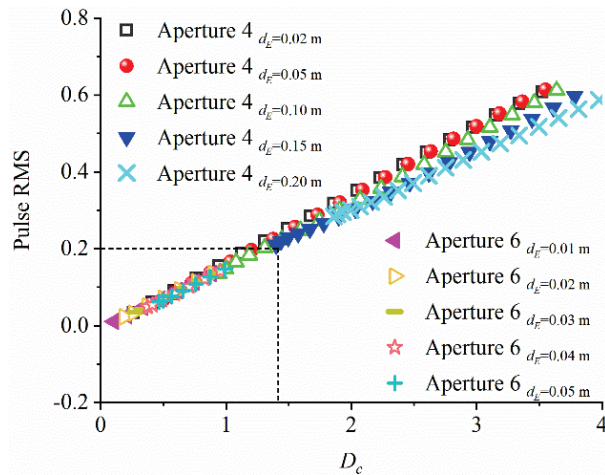
Fig. 8. Radiated pulse RMS at (8,8,10) of aperture 4 and 6 excited by Gaussian pulse with pulse width of 1 ns.

The raising of D_c leads to a linear increase of the pulse RMS as observed from Figs. 7 and 8, which means the distortion is more serious. When D_c is below 1.4, all pulse RMS are less than 0.2. These results demonstrate that when employing a discretized aperture planar array to restore the original aperture for reducing computation consumption, certain conditions must be met to ensure close resemblance to the radiation field waveforms of original aperture.

Despite the calculations and comparisons of radiation field waveforms, an investigation into the temporal pattern of each aperture is also conducted. Figure 9 depicts the E-plane and H-plane time-domain patterns of each aperture excited by the Gaussian pulse with pulse width of 1 ns.
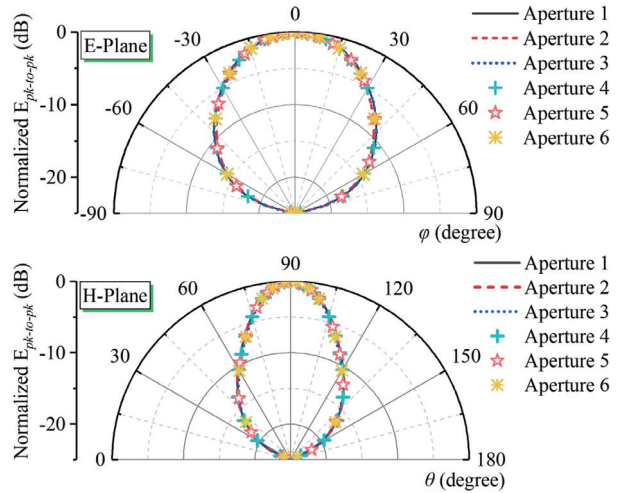
Fig. 9. Time-domain patterns of each aperture excited by the tangential electric field with pulse width of 1 ns.

The time-domain patterns in E-plane and H-plane of each aperture exhibit a relatively consistent behavior when excited by the same tangential electric field waveforms. This indicates that the discretized aperture planar arrays still retain original pattern characteristics, which essentially correspond to the array factor. Discretization accurately restores the array factor of the original aperture. In general, more emphasis is placed on the 3-dB beam width. The differences of each aperture's 3-dB beam width with respect to aperture 1 are depicted in Fig. 10.

In the case of the planar array, apertures 4, 5, and 6 exhibit distinct differences in time-domain patterns compared to aperture 1, as clearly depicted in Fig. 10. However, for the linear array, both the H-plane pattern of aperture 2 and the E-plane pattern of aperture 3 remain consistent with that of aperture 1. This indicates that the discretizing way of linear array effectively preserves the array factor in respective planes. Consequently, two additional small apertures (aperture 7 and aperture 8) are constructed for further analysis. They are the dashed boxes in Fig. 2. The dimensions of aperture 7 are w_H=1.2 m and h_E=0.1 m, while those of aperture 8 are w_H=0.1 m and h_E=0.6 m.

Figure 11 presents the calculated time-domain patterns for these two apertures excited by a tangential electric field with pulse width of 1 ns. The time-domain pattern in H-plane of aperture 7 is observed to be nearly identical to that of aperture 1, while the pattern in E-plane of aperture 8 closely resembles that of aperture 1.
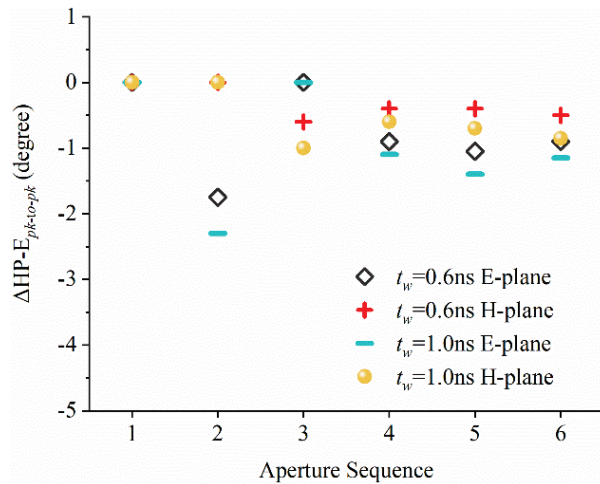
Fig. 10. The differences of the 3-dB beam width with respect to aperture 1.

Fig. 12. The radiated electric field waveforms at typical field point.

Fig. 11. Time domain patterns of aperture 7 and 8.

This suggests that the time-domain pattern in the corresponding plane can be equivalently calculated using two smaller apertures.

When a Gaussian pulse with pulse width of 1 ns and an amplitude of 1 kV/m is employed as the tangential electric field waveform, the comparisons between the electric field waveforms radiated by these apertures at typical field points are made in Fig. 12. The change in the number of integral aperture elements leads to a modification in the amplitude of the radiation electric field. Therefore, the ratio between the area of new constructed aperture and aperture 1 is employed as an amplitude coefficient, enabling us to obtain the complete waveform of the radiation field.

Figure 12 clearly shows that the accurate calculation of the radiation field waveform at the field points on the E-plane and H-plane can be achieved by utilizing two narrow apertures. This is attributed to the symmetric time delay effect caused by the distance R between the field and source points when solving for the radiation field waveform at either E-plane or H-plane. In other words, the radiation field waveform at a given field point in E-plane or H-plane solely depends on the source point located in that respective plane.

IV. ANALYSIS AND DISCUSSION OF POTENTIAL APPLICATIONS

This section focuses on exploring potential applications of discretized aperture for analyzing TD-UWB array antennas. Figure 13 (a) depicts an antipodal Vivaldi antenna with the dimensions indicated, which is a typical UWB antenna. The dielectric substrate utilized is FR4, with the relative dielectric constant of 4.3 and loss tangent of 0.025. Employing the antipodal antenna as the array element, an 8×8 time-driven array is constructed as illustrated in Fig. 13 (b). The spacing between array elements on the E-plane is d_E=0.27 m, while on the H-plane the spacing is d_H=0.15 m. The reduced scale of this array antenna aims to alleviate computational burden during numerical simulations.

Based on the aperture radiation theory, there are two crucial factors for predicting the time-domain radiation characteristics of the TD-UWB arrays. The first is the equivalent aperture, while the second is the tangential electric field on the aperture. According to the analysis in section III, two narrow apertures can be employed separately to solve and estimate the time-domain radiation characteristics of this array antenna under synchronous excitation mode. The dimensions of these two narrow
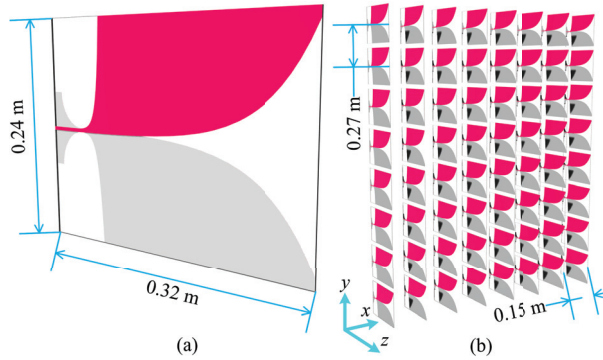
Fig. 13. The antipodal Vivaldi antenna and the 8×8 array antenna.

apertures are 1.2 m × 0.1 m (aperture E) and 0.1 m × 2.16 m (aperture H), respectively.

According to the radiation process of the array antenna, the tangential electric field of its equivalent aperture is an intermediate quantity that relies on both the excitation pulse of the array antenna and element antenna structure. Also, it serves as the source for the aperture radiation field. For simplicity, numerical simulation based on finite integral techniques is employed to obtain the tangential electric field waveform. First, to construct a 5×5 subarray, the layout of which is the same as the 8×8 array antenna in Fig. 13 (b). Then, the electric field in the reactive near-field region of the middle element of the subarray is extracted and serves as the tangential electric field on the aperture surface. This operation has taken the mutual coupling of the array elements into account. It is assumed that the excitation pulse is still the Gaussian pulse with pulse width of 1 ns and amplitude of 7.07 V/m. The extracted tangential electric field waveform by numerical simulation is displayed in Fig. 14.
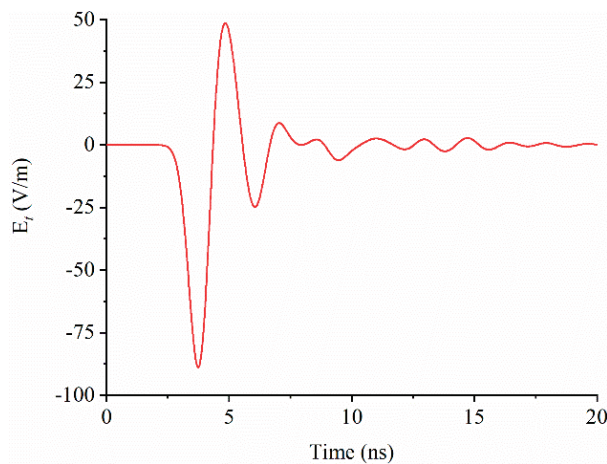
Fig. 14. The extracted tangential electric field waveform.

The distribution of tangential electric field on the radiation aperture surface of the array antenna is non-uniform. This means that there exists a certain amplitude and time delay distribution of tangential electric fields on the equivalent aperture. However, for simplicity purposes, the uniform distribution of tangential electric field on each narrow aperture is assumed as the precondition. Then, the time-domain patterns in E-plane and H-plane of the 8×8 array antenna are predicted, employing aperture E and H, as illustrated in Fig. 15.
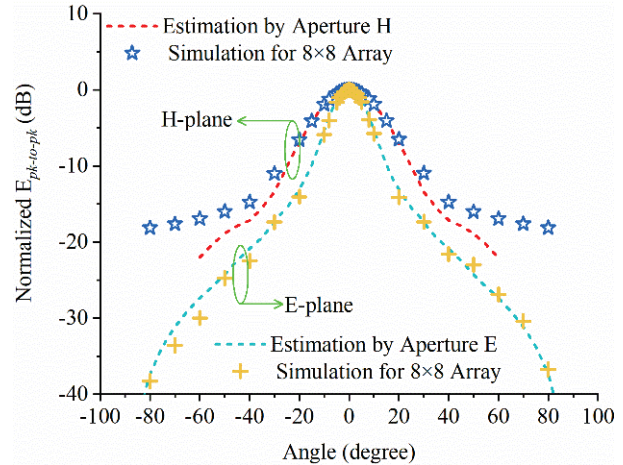
Fig. 15. The predicted time-domain patterns in the H-plane and E-plane of the 8×8 array antenna.

As can be clearly seen from Fig. 15, the time-domain pattern in E-plane predicted by aperture E (2.16 m × 0.1 m) exhibits excellent agreement with the simulated results of the 8×8 array antenna, while for the H-plane pattern, the agreement is only observed within the range of ±30°. However, notable disparities emerge beyond this range due to the fact that the prediction solely considers radiation contributions from the front of the array, whereas there are additional contributions emitted by the side array elements outside ±30° in numerical simulations. Remarkably, considering that the 3-dB beam width in H-plane is merely ±12°, these findings adequately meet estimation requirements.

Additionally, the radiation field waveforms at typical field points can be accurately predicted using the two narrow apertures, as depicted in Figs. 16 and 17. The radiated electric field waveforms predicted by the two narrow apertures exhibit remarkable concordance with the numerical results in terms of both amplitude and waveform characteristics. This further exemplifies the efficacy of utilizing narrow apertures to predict the radiation characteristics of array antenna.

Similar to phased arrays, TD-UWB array antennas are capable of beam scanning. In this case, the narrow aperture can be discretized to predict the time-domain

pattern during beam scanning mode. For instance, when the 8×8 array antenna operates in beam scanning mode in E-plane, the aperture E is discretized into an 8×1 linear array consisting of small apertures measuring 0.24 m $\times 0.1$ m.
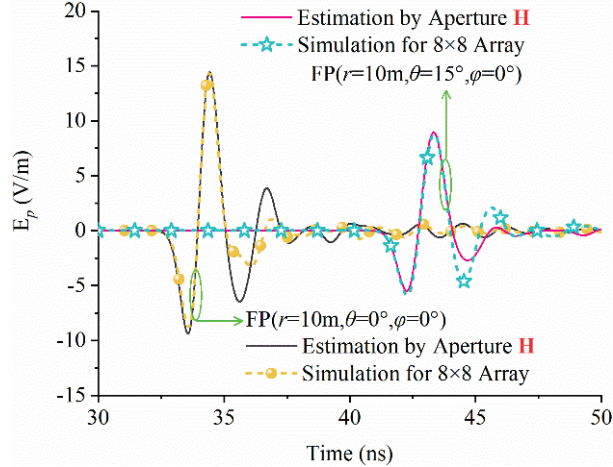

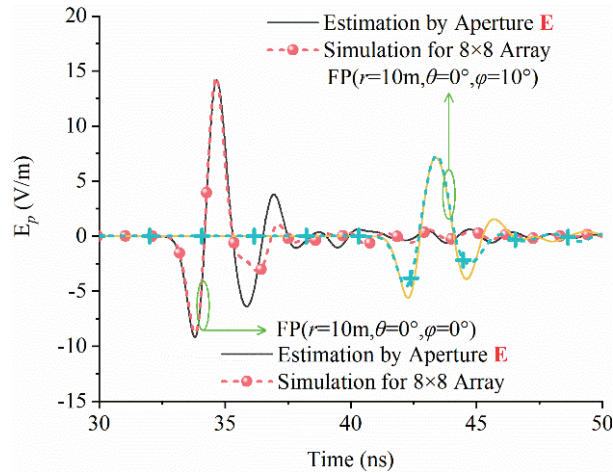Fig. 16. The electric field waveforms at two field points predicted by aperture H.

Fig. 17. The electric field waveforms at two field points predicted by aperture E.

The waveform shown in Fig. 14 is still utilized as the excitation tangential electric field, but the excitation time sequence (i.e., t_{di} in equation (17)) is reset according to beam scanning mode [30]. The time-domain patterns operating in E-plane beam scanning mode are predicted and compared with simulated results, as depicted in Fig. 18. Notably, the field strengths working in beam scanning mode are normalized relative to that of principal axis radiation field strength during synchronous excitation.

Figure 18 demonstrates that the time-domain patterns in E-plane with different scanning angles are all in good agreement with the simulated results. Moreover, it is observed that the field strength on the principal axis decreases as the scanning angle increases. The quantitated results for both 3-dB beam widths and scanning angles are presented in Table 2.
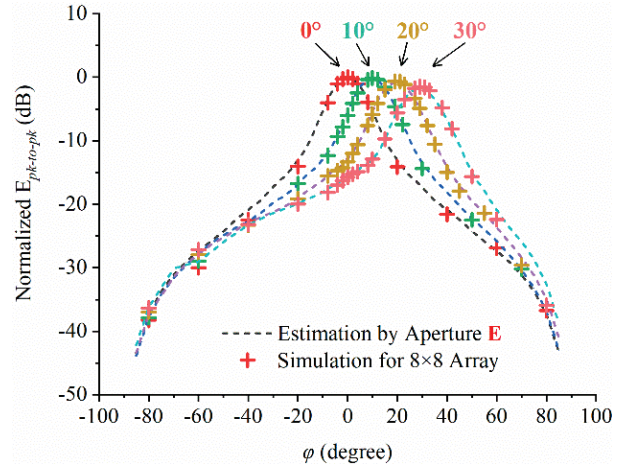
Fig. 18. Comparisons of time-domain patterns in E-plane beam scanning mode.

Table 2: The quantitated results of time-domain pattern in E-plane beam scanning mode

Time delay/ns	0	0.16	0.31	0.45
Desired angle/°	0	10.24	20.15	30.00
Simulated angle/°	0	10.00	20.00	29.00
Simulated BW/°	13.54	13.95	14.69	15.90
Predicted angle/°	0	10.00	19.00	28.00
Predicted BW/°	14.63	14.86	15.57	16.26

The results presented in Table 2 demonstrate a close agreement between the predicted scanning angles and both the simulated and desired values. Although the predicted 3-dB beam width (BW) slightly exceeds the numerical results, the consistent trend suggests that this method is suitable for analyzing radiation characteristics of TD-UWB arrays operating on beam scanning mode. Additionally, Fig. 19 compares the predicted and simulated radiation field waveforms at two different field points when the beam scanning angle is set to $20°$.

Figure 19 demonstrates that the method can also correctly predict the amplitude and oscillating characteristics of electric field waveforms for the TD-UWB array within beam scanning mode.

In this section, the tangential electric field waveform on the equivalent aperture is extracted by numerical simulation to simplify the whole prediction process,
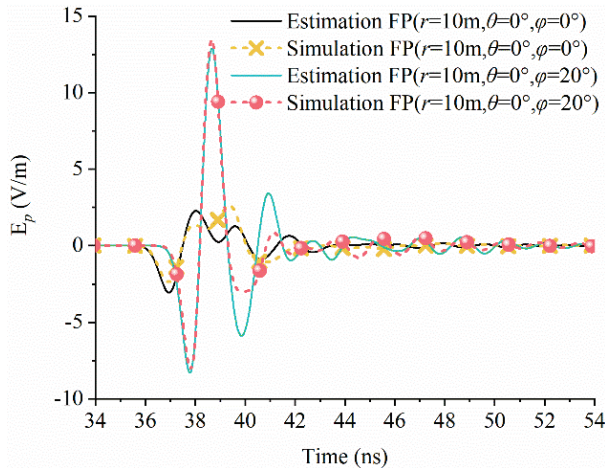
Fig. 19. The predicted radiated electric field waveforms at typical field points (FP) with the E-plane beam scanning angle of $20°$.

and aimed to demonstrate the potential applications of discretized aperture radiation. There are various methods to obtain equivalent tangential electric field waveforms, such as using normalized waveforms or combining impulse responses with measured radiation fields for inversion. All of these approaches allow for predicting time-domain patterns and radiated electric fields of TD-UWB array antennas through aperture radiation, enabling further study and design of TD-UWB arrays and facilitating pattern synthesis.

V. CONCLUSION

Aperture radiation theory is derived from the equivalent source theorem of electromagnetics, which provides an effective approach for analyzing the radiation characteristics of array antennas. This paper presents a comprehensive review of the derivation process and solution method for aperture radiation theory. Various discretized aperture planar arrays were constructed to investigate the radiation characteristics, such as waveform analysis, pulse mean square error evaluation, and time-domain pattern examination. The results demonstrate that a reasonable discretization accurately reflects and restores the radiation characteristics of the original aperture while significantly improving computational efficiency through reduced integral surface elements. Moreover, employing narrow apertures with dimensions identical to the original aperture in E-plane or H-plane enables rapid calculation of radiation field waveforms and time-domain patterns within these planes. Building upon the analysis of discretized aperture radiation, the potential applications in TD-UWB array antennas are discussed, and a fast method for predicting the time-domain radiation characteristics of TD-UWB arrays is

proposed and validated through numerical simulation. The findings and research expand upon practical applications of aperture radiation theory while providing novel ideas and methods for analysis and design of TD-UWB arrays. Furthermore, the proposed method can serve as a foundation for array antenna synthesis while offering guidance towards engineering implementation.

REFERENCES

[1] R. J. Fontana, "Recent system applications of short-pulse ultra-wideband (UWB) technology," *IEEE Trans. Microwave Theory Tech.*, vol. 52, no. 9, pp. 2087-2104, Sep. 2004.

[2] T. Saeidi, A. R. H. Alhawari, A. H. M. Almawgani, T. Alsuwian, M. A. Lmran, and Q. Abbasi, "High gain compact UWB antenna for ground penetrating radar detection and soil inspection," *Sensors*, vol. 22, no. 14, p. 5813, July 2022.

[3] J. Guo, J. Tong, Q. Zhao, J. Jiao, J. Huo, and C. Ma, "An ultrawide band antipodal Vivaldi antenna for airborne GPR application," *IEEE Geosci. Remote Sens. Lett.*, vol. 16, no. 10, pp. 1560-1564, Oct. 2019.

[4] M. Elsanhoury, P. Mäkelä, J. Koljonen, P. Välisuo, A. Shamsuzzoha, T. Mantere, M. Elmusrati, and H. Kuusniemi, "Precision positioning for smart logistics using ultra-wideband technology-based indoor navigation: A review," *IEEE Access*, vol. 10, pp. 44413-44445, Apr. 2022.

[5] W. Wang, D. Marelli, and M. Fu, "Multiple-vehicle localization using maximum likelihood Kalman filtering and ultra-wideband signals," *IEEE Sens. J.*, vol. 21, no. 4, pp. 4949-4956, Oct. 2020.

[6] I. M. Danjuma, M. O. Akinsolu, C. H. See, R. A. Alhameed, and B. Liu, "Design and optimization of a slotted monopole antenna for ultra-wide band body centric imaging applications," *IEEE J. Electromagn. RF Microwaves Med. Biol.*, vol. 4, no. 2, pp. 140-147, June 2020.

[7] A. Martínez, C. Blanco, H. García, R. Gutiérrez, G. Torregrosa, E. Ávila, and J. M. Sabater, "UWB-printed rectangular-based monopole antenna for biological tissue analysis," *Electronics*, vol. 10, no. 3, p. 304, Jan. 2021.

[8] B. Hu and N. C. Beaulieu, "Pulse shapes for ultra-wideband communication systems," *IEEE Trans. Wireless Commun.*, vol. 4, no. 4, pp. 1789-1797, July 2005.

[9] A. A. Omar, S. Naser, M. I. Hussein, N. I. Dib, and M. W. Rashad, "Superformula-based compact UWB CPW-fed-patch antenna with and without dual frequency notches," *Appl. Comput. Electromagn. Soc. J.*, vol. 32, no. 11, pp. 979-986, Nov. 2017.

[10] W. B. Abbas, F. Che, Q. Z. Ahmed, F. A. Khan, and T. Alade, "Device free detection in impulse radio ultrawide bandwidth systems," *Sensors*, vol. 21, no. 9, p. 3255, May 2021.

[11] D. V. Giri and F. M. Tesche, "Classification of intentional electromagnetic environments (IEME)," *IEEE Trans. Electromagn. Compat.*, vol. 46, no. 3, pp. 322-328, Aug. 2004.

[12] F. Brauer, S. Fahlbusch, J. L. Haseborg, and S. Potthast, "Investigation of hardening measures for IT equipment against radiated and conducted IEMI," *IEEE Trans. Electromagn. Compat.*, vol. 54, no. 5, pp. 1055-1065, Oct. 2012.

[13] S. K. Singh, R. Chandra, S. Mitra, R. Kumar, S. Kalyansundaram, A. Roy, J Mukherjee, and A. Sharma, "High power balanced TEM horn antenna for ultra wide band radiator," *Microwave Opt. Techn. Let.*, vol. 65, no. 6, pp. 1686-1694, Dec. 2023.

[14] T. A. Mehlhorn, "National security research in plasma physics and pulsed power: Past, present, and future," *IEEE Trans. Plasma Sci.*, vol. 42, no. 5, pp. 1088-1117, May 2014.

[15] R. Cicchetti, E. Mioozzi, and O. Testa, "Wideband and UWB antennas for wireless applications: A comprehensive review," *Int. J. Antennas Propag.*, vol. 2017, pp. 1-45, Feb. 2017.

[16] O. P. Kumar, P. Kumar, T. Ali, P. Kumar, and S. Vincent, "Ultrawideband antennas: Growth and evolution," *Micromachines*, vol. 13, no. 1, p. 60, Dec. 2021.

[17] D. Potti, Y. Tusharika, M. G. N. Alsath, S. Kirubaveni, M. Kanagasabai, R. Sankararajan, S. Narendhiran, and P. B. Bhargav, "A novel optically transparent UWB antenna for automotive MIMO communications," *IEEE Trans. Antennas Propagat.*, vol. 69, no. 7, pp. 3821-3828, July 2021.

[18] W. Zhao, T. Jiang, Y. Yan, and B. Wang, "Study on broadening FWHM of combined microwave short-pulse in time domain," in *Int. Conf. Microw. Millim. Wave Technol., ICMMT - Proc.*, Nanjing, pp. 1-3, May 2021.

[19] T. Latha, G. Ram, G. A. Kuamr, and M. Chakravarthy, "Review on ultra-wideband phased array antennas," *IEEE Access*, vol. 9, pp. 129742-129755, Sep. 2021.

[20] A. M. Efremov, V. I. Koshelev, B. M. Kovalchuk, V. V. Plisko, and K. N. Sukhushin, "Generation and radiation of ultra-wideband electromagnetic pulses with high stability and effective potential," *Laser Part Beams*, vol. 32, no. 3, pp. 413-418, June 2014.

[21] V. M. Fedorov, M. V. Efanov, V. Y. Ostashev, V. P. Tarakanov, and A. V. UI'yanov, "Antenna array with TEM-horn for radiation of high-power ultra short electromagnetic pulses," *Electronics*, vol. 10, no. 9, p. 1011, Apr. 2021.

[22] S. Foo and S. Kashyap, "Time-domain array factor for UWB antenna array," *Electronics Letters*, vol. 39, no. 18, pp. 1304-1305, Jan. 2003.

[23] X. Jiang, Y. Yan, L. Meng, B. Wang, L. Bi, and Y. Yin, "Theoretical study on directivity of ultra-wideband time-domain antenna array based on 3D impulse point sources," in *National Conference on Antennas*, Harbin, pp. 816-818, Aug. 2023.

[24] C. E. Baum, "Radiation of impulse-like transient fields," *Sensor and Simulation Notes*, no. 321, Nov. 1989.

[25] S. P. Skulkin, V. I. Turchin, N. I. Kascheev, and D. M. Ponomarev, "Transient field calculation of aperture antennas for various field distributions over the aperture," *IEEE Antennas Wirel. Propag. Lett.*, vol. 16, pp. 2295-2298, 2017.

[26] S. P. Skulkin, N. A. Lysenko, G. K. Uskov, and N. I. Kascheev, "Transient far fields of aperture antennas," *IEEE Antennas Wirel. Propag. Lett.*, vol. 18, no. 5, pp. 1036-1040, May 2019.

[27] C. A. Balanis, *Antenna Theory: Analysis and Design*. Hoboken: John Wiley & Sons, 2005.

[28] X. Liu, X. Wang, W. Wang, and Y. Jiang, "Radiant characteristics of subnanosecond and monopolar pulse-excited aperture," *High Power Laser and Particle Beams*, vol. 15, no. 11, pp. 1106-1109, Nov. 2003.

[29] В. И. Кошелев, В. П. Беличенко, and Ю. И. Буянов, "Ultra-wideband electromagnetic radiation technology," National Defense Industry Press, CN, 2018.

[30] B. Wang, Q. Liu, H. Cai, T. Jiang, and Y. Yan, "Estimation of time-domain radiation characteristics for dipole antenna array," in *IEEE Int. Conf. Inf. Commun. Networks*, Xi'an, pp. 144-148, Aug. 2023.

Binwen Wang was born in Gansu, China, in 1993. He received his B.S. degree in Nuclear Science from Xi'an Jiaotong University, Xi'an, China, in 2015, and his M.S. degree in Electromagnetic Field and Microwave Technology from the Northwest Institute of Nuclear Technology, Xi'an, China, in 2017. He is currently an Engineer at the Northwest Institute of Nuclear Technology. His research interests include time-domain electromagnetics and ultra-wideband antenna.

Hui Ning was born in Zhejiang, China, in 1969. He received his M.S. and Ph.D. degrees in Nuclear Science and Technology from Tsinghua University, Beijing, China, in 1997 and 2001, respectively. He is currently

a Professor at the Northwest Institute of Nuclear Technology, Xi'an, China, specializing in time-domain electromagnetics and the pulse power technique and its applications.

Chengyun Cao was born in Qinghai, China, in 1994. He received his B.S. and M.S. degree in Electromagnetic Field and Microwave Technology from the National Defense University of Science and Technology, Changsha, China, in 2016 and 2021. He is currently an Engineer at the Northwest Institute of Nuclear Technology, specializing in ultra-wideband antenna.

Qilong Liu was born in Hubei, China, in 1997. He received his B.S. degree in Power System and Automa-

tion from the Army Engineering University of PLA, Shijiazhuang, China, in 2019. He is currently an Assistant Engineer at the Northwest Institute of Nuclear Technology, specializing in ultra-wideband antenna.

Kaiyue Zhang was born in Anhui, China, in 1992. He received his B.S. and M.S. degrees in Electromagnetic Field and Microwave Technology from the National Defense University of Science and Technology, Changsha, China, in 2016 and 2018. He is currently an Engineer at the Northwest Institute of Nuclear Technology, specializing in ultra-wideband antenna and array.

Performance Analysis of Eight-element MIMO Mobile Phone Antenna for Sub-6 GHz 5G Applications

Dhananjeyan Rajendran[1], Ramesh Subramaniam[1], and Rajesh Kumar Dhandapani[2]

[1]Department of Electronics and Communication Engineering
SRM Valliammai Engineering College, Chennai, Tamil Nadu, India
dhananj13@gmail.com, rameshsvk@gmail.com

[2]Department of Electronics and Communication Engineering
Vel Tech Rangarajan Dr. Sagunthala R&D Institute of Science and Technology, Chennai, Tamil Nadu, India
sdrk@gmail.com

Abstract – This paper presents an 8-port MIMO antenna array for use with 5G handsets. The proposed MIMO antenna array comprises eight U-shaped, coupled-fed slot antenna components placed symmetrically on a 0.8 mm thick FR4 substrate. Each antenna has 200 MHz bandwidth and covers 3.4-3.6 GHz. The operational frequency range includes LTE band 48 for 5G cellular applications. Using spatial and polarisation diversity, antenna components are isolated by over 15 dB. The prototype antenna is fabricated and measured, and the experimental results agree with the simulated results. The estimated Envelope Correlation Coefficient (ECC), less than 0.035 based on radiation characteristics, shows that the suggested MIMO antenna array performs well in diversity. These characteristics indicate that the proposed MIMO antenna is a viable solution for 5G smartphone applications.

Index Terms – 5G, 8-port, ECC, MIMO, sub-6 GHz.

I. INTRODUCTION

5G wireless communication will make it feasible to move large amounts of data at a high pace and engage in intelligent wireless communication. However, communication through 5G has unique challenges, such as high data rates and stringent requirements for channel capacity. The MIMO technology that supports wideband operation may be the best choice for accomplishing these goals [1, 2]. Compared to 3G and 4G smartphones, 5G devices must have MIMO that is 8×8, and must also have broadband capabilities [3, 4]. Adding more antenna components may enhance transmission rates and channel capacity. As a result, the MIMO system's overall performance would deteriorate [5–8]. Because of their restricted design, mobile phones make it hard for users to experience a greater sensation of separation from others. These technologies (MIMO), which are now accessible for commercial use, have been shown to increase system performance in terms of high data rate and channel capacity [8–14], and they are now in widespread use. Several publications have presented narrowband MIMO antenna designs for 5G smartphones. The impedance bandwidth was increased to encompass more sub-6 GHz operating bands [15–19]. The increasing distance between antenna components requires various decoupling solutions. Several different decoupling strategies have been used in the fight against isolation. MIMO isolation was enhanced by the use of spatial and polarization diversity techniques and an increase in the distance between the various antenna components [20, 21]. Improved isolation has also been achieved using hybrid resonators, EBG structures, neutralising lines, FSC, and inverted-I ground slot technologies [22, 23]. According to research, additional decoupling techniques have the potential to improve isolation, yet they also increase the complexity of production and take up valuable real estate on the system board. The significance of this work may be summed up as follows. This article proposes an eight-input MIMO antenna for 3.4-3.6 GHz.

We have raised the isolation between antenna components by more than 15 dB, improving radiation efficiency by 68-76% in our target band of operation. This was accomplished without the assistance of decoupling structures. The MIMO antenna with an ECC of 0.035 and a channel capacity of 38.789 bps/Hz is the one that is suggested. All design particulars of the proposed antenna have been validated using HFSS electromagnetic simulator.

The originality of the work may be summed up as follows:

(1) Better than 15 dB of mutual coupling may be achieved between the antenna elements without specialised processes or methods.

(2) A reduction in the mutual coupling leads to higher MIMO performance in terms of overall

radiation efficiency (68-76%) and Envelope Correlation Coefficient (ECC). This is because a decrease in the mutual coupling leads to fewer interactions between the antennas (ECC<0.035).

(3) The total diameter of the individual antenna is very small which leads to the system PCB board being able to accommodate up to eight antennas.

(4) Despite its small size, the suggested antenna can cover a reasonable range of the electromagnetic spectrum, from 3.4 to 3.6 GHz.

II. ANTENNA DESIGN AND ANALYSIS

The geometry and general construction of the proposed 8-port MIMO antenna array are depicted in detail in Figs. 1 (a) and (b), respectively. As shown in Fig. 1 (a), each antenna component is printed on an FR4 substrate with the following dimensions: 150 millimetres long, 80 millimetres wide, and 0.8 millimetres thick. These measurements make the substrate suitable for smartphones with screens measuring up to 5.7 inches in diagonal length.

Antenna elements 6 to 8 occupy the substrate's left-side edges, and antenna elements 2 to 4 occupy the right-side edges of the substrate. Figure 1 provides a comprehensive illustration of the particulars of antenna 1's

(a)   (b)

(c)   (d)

Fig. 1. *Continued*

(e)

(f)   (g)
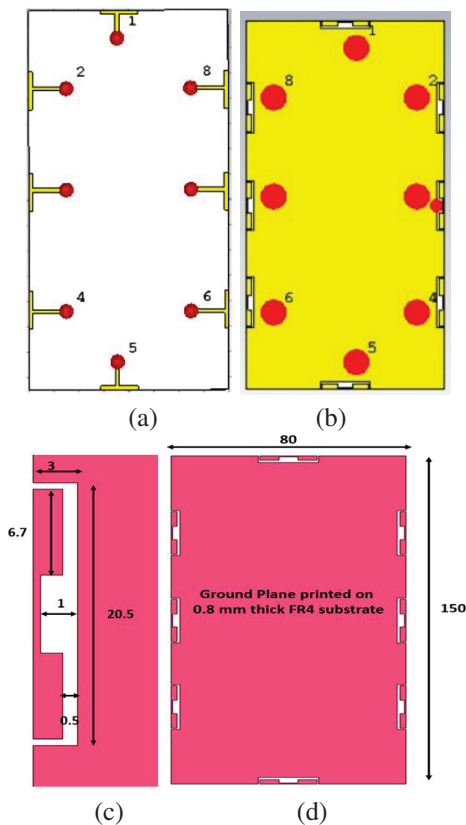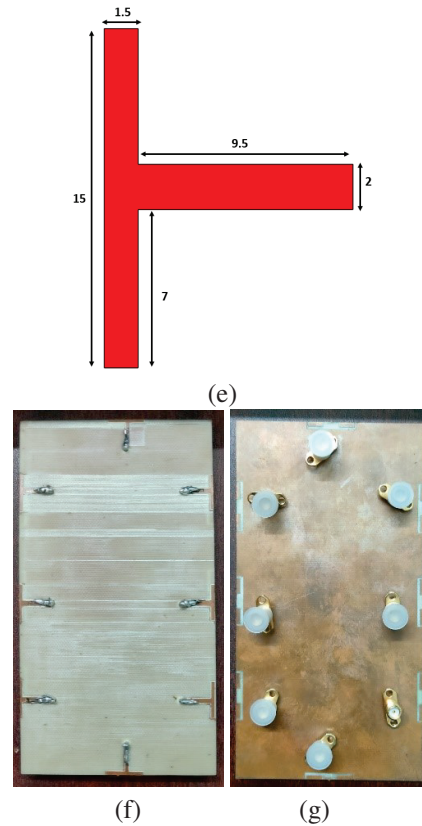
Fig. 1. (a,b) Front and back view of the simulated antenna, dimensions of (c) slot in the ground plane, (d) ground plane, (e) feeding stub, and (f,g) front and back view of the prototype of the proposed antenna.

construction and its dimensions. The slot radiator, also known as antenna 1, is made up of three different rectangular slots connected to one another to produce a U-shaped open-ended slot. The initial step of the technique involves cutting the ground plane along its top short edge to create a rectangular slot with dimensions 9.5×6.5 mm. Figure 1 (b) illustrates the process of carving two rectangular slots, each of which has the following dimensions: 15×7 mm and 5.5×0.2 mm, respectively. A minute slit open on all four sides and shaped like a square is cut into the surface of the ground plane that is closest to the top of the structure. All of the carved slots mentioned earlier are combined, and then the combined slot is tuned to resonate at 3.4-3.6 GHz, creating an open-ended T-shaped slot.

III. RESULTS AND DISCUSSION

Figures 2 (a-e) depict the manufacturing process as well as the testing of the 8-port MIMO antenna array prototype that has been proposed. To carry out the measurements, 50-ohm SMA female connectors are attached to the feeding strips associated with the antenna components. An antenna's S-parameters, isolation, and

radiation pattern can be evaluated by first exciting the antenna to be tested and then connecting all of the antenna's elements to matched loads of 50 ohms. The reflection and transmission coefficients, both simulated and measured, for the 8-port antenna array under consideration are illustrated in Figs. 2 (a) and (d) and Figs. 2 (b) and (e), respectively.

(a)

(b)

(c)

Fig. 2. *Continued*
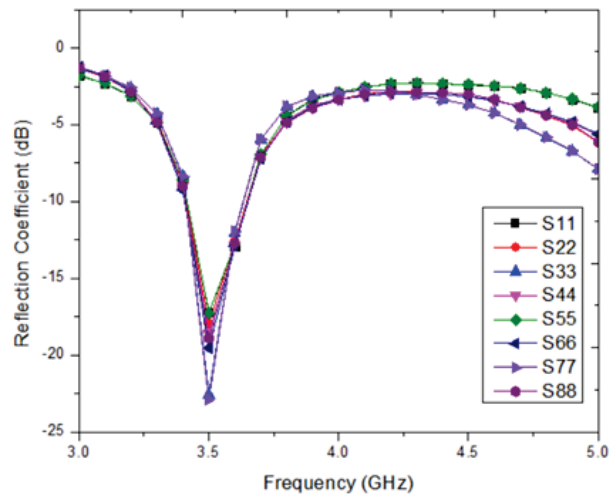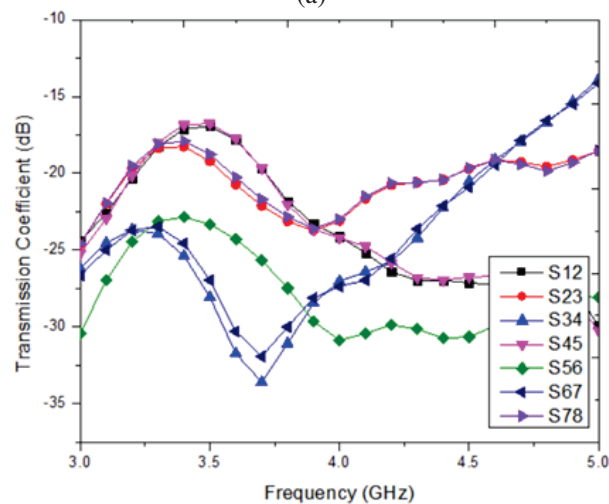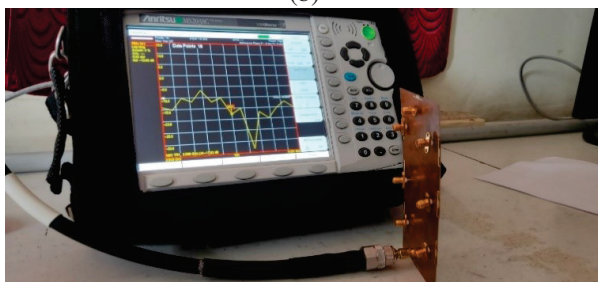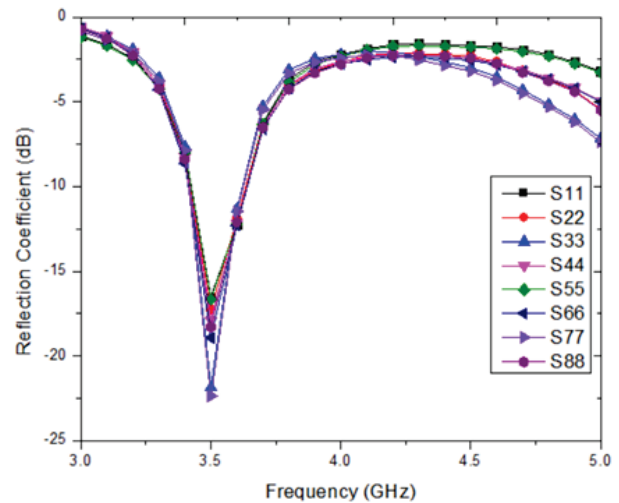
(d)
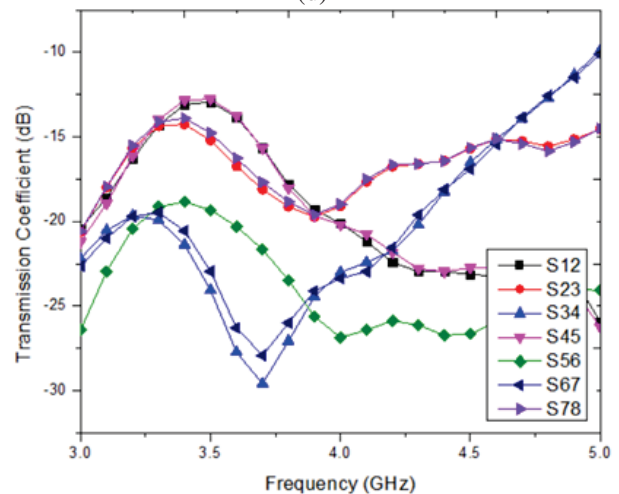
(e)

Fig. 2. (a,b) Simulated scattering parameters, (c) measurement setup, and (d,e) measured scattering parameters.

As a result of the fact that all antenna components are designed to be vertically symmetrical with respect to the centre line of the PCB, the S-parameters of antenna 2 to antenna 4 will typically be the same as those of antenna 6 to antenna 8. As can be seen in Figs. 2 (a) and (d), the simulated and measured reflection coefficients of antenna 1-8 in the 3.4-3.6 GHz operating bands, which correspond to the frequencies used for 5G applications, are less than -10 dB (2:1 Voltage Standing Wave Ratio). As shown in Figs. 2 (b) and (e), the transmission coefficients of neighbouring pairs are more than -15 dB if there is adequate distance between each antenna. In the work that is being suggested, no decoupling technique has been used to increase the isolation between the components.

This is because the open end has the lowest current, and the closed end has the highest current. Figures 3 (a) and (b) show surface currents at 3.5 GHz for antenna 1 and 2, respectively. This indicates that the T-shaped slot's fundamental mode is quarter wavelength mode. Open-ended slots of varying lengths generate the resonances at 3.5 GHz.

(a)   (b)
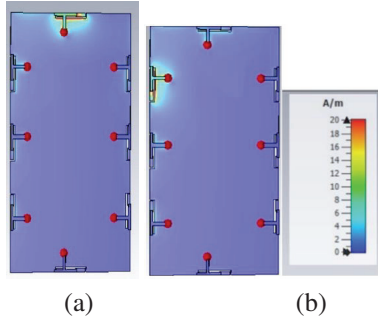
Fig. 3. Surface current distribution at 3.5 GHz: (a) antenna 1 and (b) antenna 2.

To provide a design insight of the proposed antenna, a parametric study has been carried out (with a limited number of points during simulation) as shown in Figs. 4 (a) and (b), respectively. As shown in Fig. 4 (a), when altering the slot length L1 from 17.5 mm to 20.5 mm, centre frequency has been shifted with a poor reflection coefficient. It is observed that the higher the value of slot length, the better the impedance matching of the antenna. A similar response has been observed when changing feed length L1 from 12 to 15 mm as illustrated in Fig. 4 (b). For brevity, other performance metrics concerning other antenna design parameters have not been shown here.

Figures 5 (a) and (b) depict the measured radiation patterns of antennas 1 and 2, respectively. Each antenna has an omnidirectional radiation pattern (no deep null is visible throughout the pattern). The radiation patterns exhibit mutual reinforcement and symmetry, indicating that the proposed antenna possess diverse patterns.

Figure 6 illustrates the radiation efficiency of antennas 1-8, which varies from 68 to 76% over the necessary working band of the device. The large gain in overall efficiency is primarily attributable to the greater isolation between antenna components.

$$ECC = \left| \frac{\oiint A_{ij}(\theta, \varphi) \sin\theta \, d\theta \, d\varphi}{\oiint A_{ii}(\theta, \varphi) \sin\theta \, d\theta \, d\varphi \cdot \oiint A_{jj}(\theta, \varphi) \sin\theta \, d\theta \, d\varphi} \right|^2,$$

$$(1)$$

where:

$$A_{ij} = E_{\theta,i}(\theta, \varphi) \cdot E^*_{\theta,j}(\theta, \varphi) + E_{\varphi,i}(\theta, \varphi) \cdot E^*_{\varphi,j}(\theta, \varphi).$$

$$(2)$$

The observed ECCs of all array pairs are less than 0.5, as demonstrated in Fig. 7 (a), well within accept-
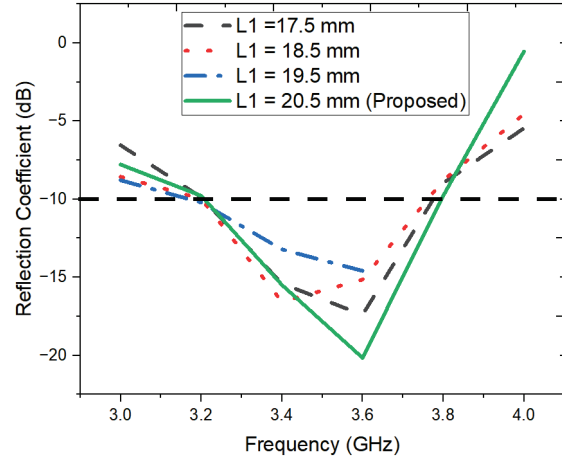
(a)
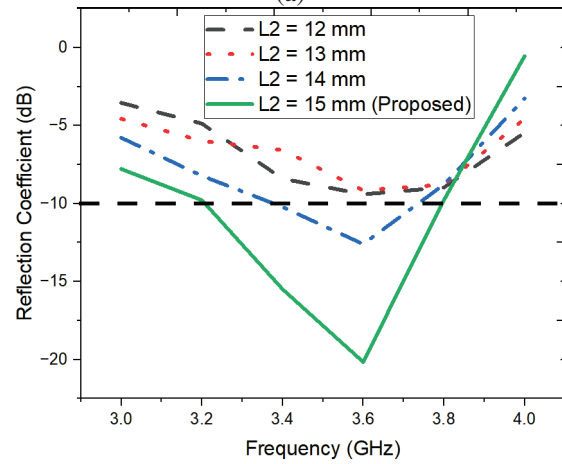
(b)

Fig. 4. Parametric analysis when altering: (a) L1 and (b) L2.

(a)   (b)
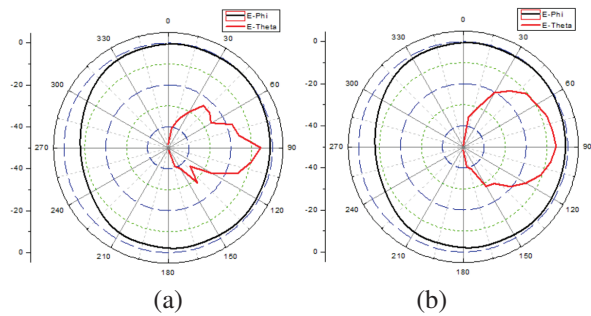
Fig. 5. Two-dimensional measured radiation pattern of the (a) antenna 1 and (b) antenna 2.

able ranges. An 8-port antenna array that can achieve a high diversity gain with a low ECC value is a significant achievement.

To confirm the efficiency of the antenna's bandwidth, the Total Active Reflection Coefficient (TARC)
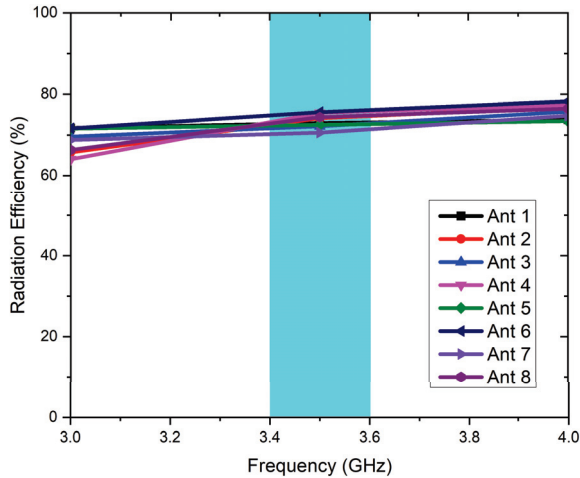
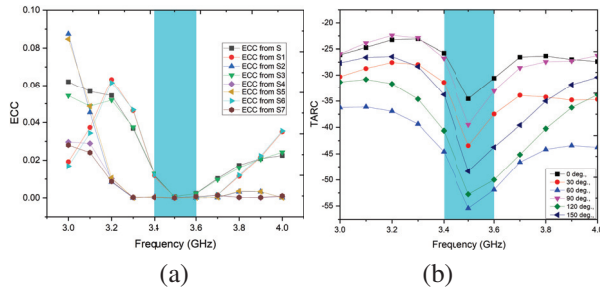Fig. 6. Radiation efficiency of antenna (Ant) 1-8.

Fig. 7. (a) ECC and (b) TARC of the proposed antenna.

has been graphed by adjusting the phase angle of port 1 [20], as depicted in Fig. 7 (b). All antenna elements can cover the desired frequency spectrum:

$$C = E\left(\log_2\left(\det\left(I_M + \frac{SNR_{20}dB}{M}H\left(H^T\right)\right)\right)\right). \quad (3)$$

Using equation (3), the channel capacity of the proposed antenna has been calculated.

A. Effects of handgrip

The hand phantom's impact on the antenna's performance will be discussed in this part. The Single-Handed Mechanism (SHM) and the Two-Handed Mechanism (THM) are two common types of implementations shown in Figs. 9 and 10, respectively. However, the effects of the user's head hits are not discussed, and multi-port MIMO operating at frequencies sub-6 GHz may be used for the data mode. Antennas 2, 3, and 4 are all attached to the fingers in SHM by a direct connection. This arrangement considerably influences the reflection coefficients of antennas 2, 3, and 4, as shown in Fig. 9 (a). In this scenario, antenna 8 also shows unfavourable impedance matching. Other antennas show very slight variations in their resonant modes due to the significant distance separating them from the fingers.
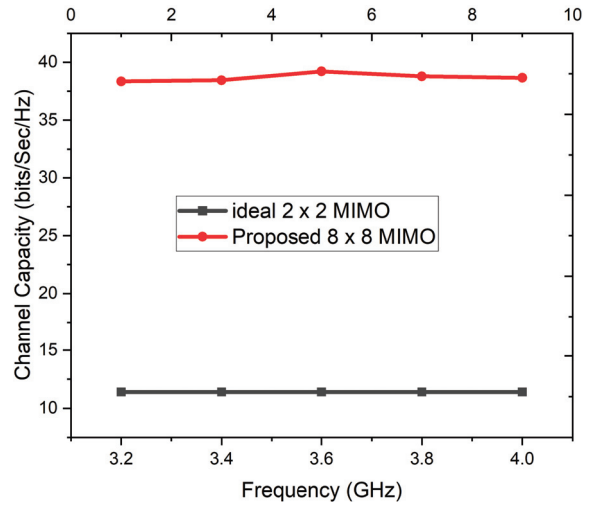
Fig. 8. Channel capacity of the proposed antenna.

Nevertheless, as shown in Fig. 9 (b), a strong barrier to outside interference (>10 dB) is achievable across the whole usable frequency range.

Due to the absorption of radiation by the hand tissue, the efficiency of antennas 2, 3, and 4 has decreased to below 40%. Because antennas 2, 3, and 4 are positioned close to the fingers, the palm's ability to absorb power has also reduced their efficiency to somewhere about 30%. Other antennas have achieved overall efficiencies of higher than 45%. This is because they are placed further away from the hand. As may be observed in
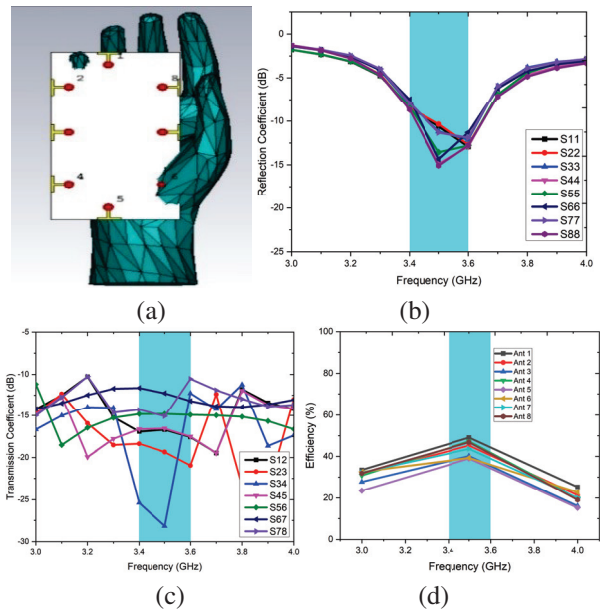
Fig. 9. (a) Antenna with single hand phantom and (b-d) performance of the antenna with single hand phantom.

(a) (b)

(c) (d)
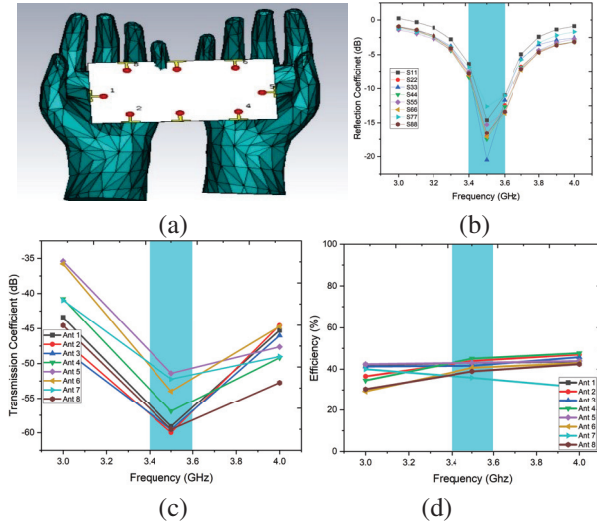
Fig. 10. (a) Antenna with two hand phantom and (b-d) performance of the antenna with two hand phantom.

Fig. 9 (a), the reflection coefficients of antennas 6, 7, and 8 suffer a small degradation when thumbs are used to cover them. Because the other antenna elements are situated near the hand phantom, their resonance properties are the same. As can be observed in Fig. 9 (c), the isolation is more than 10 dB over the whole operational spectrum. As shown in Fig. 9 (d), the overall efficiency of all antenna elements is less than 50% due to the presence of a hand phantom.

However, the overall efficiency of other antennas (located above the little fingers) is greater than 48%. As a consequence of this, it indicates that the 8-port antenna that was recommended has significant performance in contexts that operate in real-time. The effect of the head phantom model has also been investigated to validate the antenna's performance, and corresponding SAR values have been listed in Table 1. It proves the antenna exhibits maximum SAR below 1 W/kg for both 1 g and 10 g of tissue.
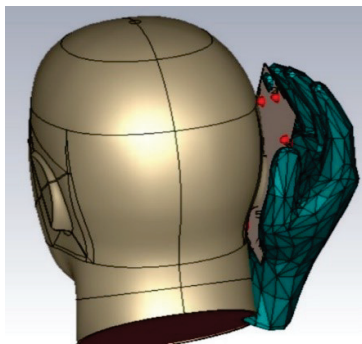
Fig. 11. Antenna with head phantom.

Table 1: SAR values of antenna 1 and antenna 2

SAR (W/kg)	Antenna 1	Antenna 2
1 g tissue	0.985	0.97458
10 g tissue	0.654	0.6845

Table 2: Performance comparison of the proposed antenna

Ref No	S (mm)	BW (MHz)	I (dB)	E (%)	ECC	N	CC (bps /Hz)
3	17.4×6	200	19.6	65-70	<0.0125	8	34
5	7.5×6	300	15	40	<0.15	8	35
8	21×3	200	17.5	62	<0.05	8	40.8
9	30×30	600	13	75	<0.01	8	NA
15	9.6×10	200	11.2	51-59	<0.1	8	36.9
17	6.6×6	300	15.1	60-80	<0.21	8	NA
This work	13×5.2	200	15	68-76	<0.035	8	38.78

Key: S=size of the antenna, BW=bandwidth, I=isolation, E=efficiency, N=no. of elements, CC=channel capacity.

Table 1 compares the performance of the recommended MIMO antenna array and the performance of other present MIMO antenna arrays for 5G mobile devices. In addition to its many benefits, the recommended method offers significant radiation and MIMO performance, superb isolation (more than 15 dB), and a low ECC of 0.035.

The proposed antenna, measuring 13×5.2 mm, delivers a bandwidth of 200 MHz and 15 dB isolation. With an efficiency ranging from 68 to 76%, it surpasses most counterparts. Its error correction coding of <0.035 ensures robust performance. Offering 8 ports and a channel capacity of 38.78 bps/Hz, it excels in efficiency and error correction. These attributes position it as a competitive choice, balancing size, performance, and capability effectively for the intended application.

IV. CONCLUSION

An 8-port MIMO antenna system for a 5G mobile phone operating at 3.5 GHz has been tested and successful. Neighbouring antenna components have high isolation (>15 dB). Consequently, the radiation efficiency might be increased to 68-76% throughout the operational spectrum, bringing the ECC down to less than 0.01. When the signal-to-noise ratio is 20 dB, the expected peak channel capacity in an eight-element MIMO configuration is 38.789 bps/Hz, over 11 times more than the capacity of a Single Input Single Output system. As a result, the 8-port antenna described in this paper may be a great option for the hardware and software of future generations of mobile phones.

ACKNOWLEDGMENT

REFERENCES

[1] J. G. Andrews, S. Buzzi, W. Choi, S. V. Hanly, A. Lozano, A. C. K. Soong, and J. C. Zhang, "What will 5G be?," *IEEE Journal on Selected Areas in Communications*, vol. 32, no. 6, pp. 1065-1082, 2014.

[2] M. A. Jensen and J. W. Wallace, "A review of antennas and propagation for MIMO wireless communications," *IEEE Transactions on Antennas and Propagation*, vol. 52, no. 11, pp. 2810-2824, 2004.

[3] A. Zhao and Z. Ren, "Size reduction of self-isolated MIMO antenna system for 5G mobile phone applications," *IEEE Antennas and Wireless Propagation Letters*, vol. 18, no. 1, pp. 152-156, 2019.

[4] Jiagang He, Shichao Zhu, Jie Yu, Hao Li, and Gaosheng Li, "Wideband decoupled 8-element MIMO mobile phone antenna for sub-6 GHz 5G NR bands," *ACES Journal*, vol. 37, no. 12, pp. 1208-1215, 2022.

[5] W. Jiang, B. Liu, Y. Cui, and W. Hu, "High-isolation eight-element MIMO array for 5G smartphone applications," *IEEE Access*, vol. 7, pp. 34104-34112, 2019.

[6] M.-Y. Li, Y.-L. Ban, Z.-Q. Xu, J. Guo, and Z.-F. Yu, "Tri-polarized 12-antenna MIMO array for future 5G smartphone applications," *IEEE Access*, vol. 6, pp. 6160-6170, 2018.

[7] X. Zhao, S. P. Yeo, and L. C. Ong, "Decoupling of inverted-F antennas with high-order modes of ground plane for 5G mobile MIMO platform," *IEEE Transactions on Antennas and Propagation*, vol. 66, no. 9, pp. 4485-4495, 2018.

[8] Y. Li, C.-Y.-D. Sim, Y. Luo, and G. Yang, "High-isolation 3.5 GHz eight-antenna MIMO array using balanced open-slot antenna element for 5G smartphones," *IEEE Transactions on Antennas and Propagation*, vol. 67, no. 6, pp. 3820-3830, 2019.

[9] S. Syedakbar, S. Ramesh, and V. Ramya "Orthogonally integrated hybrid antenna for intelligent transportation systems," *Applied Computational Electromagnetics Society (ACES) Journal*, vol. 36, no. 05, pp. 519-524, May 2021.

[10] N. O. Parchin, Y. I. A. Al-Yasir, A. H. Ali, I. Elfergani, J. M. Noras, J. Rodriguez, and R. A. Abd-Alhameed," Eight-element dual-polarized MIMO slot antenna system for 5G smartphone applica-

tions," *IEEE Access*, vol. 7, pp. 15612-15622, 2019.

[11] Z. Ren, A. Zhao, and S. Wu, "MIMO antenna with compact decoupled antenna pairs for 5G mobile terminals," *IEEE Antennas and Wireless Propagation Letters*, vol. 18, no. 7, pp. 1367-1371, 2019.

[12] L. Sun, H. Feng, Y. Li, and Z. Zhang, "Compact 5G MIMO mobile phone antennas with tightly arranged orthogonal-mode pairs," *IEEE Transactions on Antennas and Propagation*, vol. 66, no. 11, pp. 6364-6369, Nov. 2018.

[13] Y. Liu, A. Ren, H. Liu, H. Wang, and C.-Y.-D. Sim, "Eight-port MIMO array using characteristic mode theory for 5G smartphone applications," *IEEE Access*, vol. 7, pp. 45679-45692, 2019.

[14] N. Kumaran, S. Ramesh, and S. Chitra, "Bandwidth and frequency agile MIMO antenna for cognitive vehicular communications," *International Journal of Communication Systems*, vol. 36, no. 14, pp. 1-18, Sep. 2023.

[15] Y. Li, C.-Y.-D. Sim, Y. Luo, and G. Yang, "Multiband 10-antenna array for sub-6 GHz MIMO applications in 5-G smartphones," *IEEE Access*, vol. 6, pp. 28041-28053, 2018.

[16] J. Li, X. Zhang, Z. Wang, X. Chen, J. Chen, Y. Li, and A. Zhang," Dualband eight-antenna array design for MIMO applications in 5G mobile terminals," *IEEE Access*, vol. 7, pp. 71636-71644, 2019.

[17] Y.-L. Ban, C. Li, C.-Y.-D. Sim, G. Wu, and K.-L. Wong, "4G/5G multiple antennas for future multimode smartphone applications," *IEEE Access*, vol. 4, pp. 2981-2988, 2016.

[18] A. Zhao and Z. Ren, "Wideband MIMO antenna systems based on coupled-loop antenna for 5G N77/N78/N79 applications in mobile terminals," *IEEE Access*, vol. 7, pp. 93761-93771, 2019.

[19] Q. Chen, H. Lin, J. Wang, L. Ge, Y. Li, T. Pei, and C.-Y.-D. Sim," Single ring slot-based antennas for metal-rimmed 4G/5G smartphones," *IEEE Transactions on Antennas and Propagation*, vol. 67, no. 3, pp. 1476-1487, 2019.

[20] X. Zhang, Y. Li, W. Wang, and W. Shen, "Ultra-wideband 8-Port MIMO antenna array for 5G metal-frame smartphones," *IEEE Access*, vol. 7, pp. 72273-72282, 2019.

[21] K. Kayalvizhi and S. Ramesh, "A novel MIMO antenna with switchable UWB/5G modes for vehicular terminals," *Microwave and Optical Technology Letters*, vol. 65, no. 9, pp. 2640-2645, Sep. 2023.

[22] Yonghao Wang, Xin Wang, Junlin Wang, and Rui Shao," Dual-band highly isolated eight-element MIMO antenna for 5G mobile phone," *ACES Journal*, vol. 37, no. 5, pp. 588-596, 2022.

[23] J. Deng, J. Li, L. Zhao, and L. Guo, "A dual-band inverted-F MIMO antenna with enhanced isolation for WLAN applications," *IEEE Antennas and Wireless Propagation Letters*, vol. 16, pp. 2270-2273, 2017.

Dhananjeyan Rajendran is an Assistant Professor with 14 years' teaching experience at SRM Valliammai Engineering College, Chennai. His research interests include MIMO antenna design. He is a lifetime member of IETE, ISTE.

Ramesh Subramaniam is a professor with 21 years' teaching experience at SRM Valliammai Engineering College in Chennai. He is a senior member of the IEEE Antennas & Propagation Society (S'10-M'17-SM'18). His research interests include antenna design.

Rajesh Kumar Dhandapani is an Assistant Professor with 11 years' teaching experience at Vel Tech Rangarajan Dr. Sagunthala R&D Institute of Science and Technology, Chennai. His research interests include mobile phone antenna design and RF system design.

Metamaterial-filled Quarter Circular Microstrip Antenna in the Subwavelength Scale for 3.5 GHz Band Communications

Hao Lu, Xiaofei Xu*, and Hu Wei

School of Communication and Information Engineering
Shanghai University, Shanghai, 200444, China
*xfxu@shu.edu.cn

Abstract – A metamaterial-filled quarter circular microstrip antenna (meta-QCMSA) is proposed for 5G communications in the 3.5 GHz band. Compared with traditional CMSAs, the new meta-QCMSA is superior in its small patch in the subwavelength scale realized by collaboratively using metamaterial and field symmetry techniques. This combination method is observed to be more powerful than a single method solely used. One practical meta-QCMSA is designed and experimentally demonstrated near 3.5 GHz. Its patch length is $0.1\lambda_0$, much smaller than the traditional CMSA. In addition, the compact meta-QCMSA is observed to have a considerable bandwidth of 3.8% and antenna gain of 3.9 dBi in experiments.

Index Terms – Metamaterials, quarter circular microstrip antenna, subwavelength.

I. INTRODUCTION

With the continuous development of 5G/B5G wireless communications [1], compact microwave microstrip antennas (MSAs) [2–3] are of much interest in both academic and industry areas. To make the MSAs smaller, the filling materials for the substrate can have a high relative permittivity (ε_r) and/or permeability (μ_r) by using ceramics and magnets [4–6]. However, these high-index materials are usually difficult to fabricate with low-cost printed circuit board (PCB) technology.

To address the problem, alternative microwave artificial metamaterials [7–17] were proposed in recent decades. These microwave metamaterials do not need high-index ceramics or magnets as substrates. In contrast, they can be realized by using common low-index dielectrics, which are well-compatible with the PCB process. By further loading new functional structures into the low-index dielectrics, the metamaterials may have effective high relative permittivity (ε_{reff}) and/or permeability (μ_{reff}), which are equivalent to the natural high-index materials.

In addition to material technology, there is another useful technique to condense a MSA that takes advantage of electromagnetic (EM) field symmetry for a regular (such as square or circular) patch [2–3]. For instance, regarding the circular MSA (CMSA) operating at its fundamental TM_{11} mode [2], the EM fields in the CMSA cavity are symmetric in different quarters [2]. Hence, according to the uniqueness theorem [18], it is possible to realize a half CMSA (HCMSA) or even a quarter CMSA (QCMSA) (see Fig. 6.7 in [3]) by cutting the original full circle in the CMSA into a half or quarter [2–3] if the boundary conditions are well kept as a magnetic wall or electric wall. Note that the resonant frequencies (f_0s) for these three antennas (CMSA, HCMSA and QCMSA) are almost the same [2–3] if the margin effects are not accounted for. The patch area for the new HCMSA (or QCMSA) is nevertheless only half (or quarter) of the original CMSA.

Metamaterial and EM field symmetry are two independent techniques to shrink traditional MSAs. Inspired by these two techniques, a new compact metamaterial-filled QCMSA (meta-QCMSA) is proposed in this work by synthetically using both technologies. Regarding metamaterial technology, some sector mushroom structures [15] are chosen to fill into the substrate which can be physically constituted from a two-layer substrate. Furthermore, as to form a QCMSA [2–3], the magnetic wall boundary condition is fulfilled by simply using an open edge. The electric wall boundary condition is realized by employing numerous shorting (conducting) pins [2–3].

This combination method is more powerful than a single method solely used. One practical meta-QCMSA was designed for 5G mobile communications in the 3.5 GHz band. It is experimentally demonstrated to resonate at 3.51 GHz (free space wavelength λ_0=85.5 mm, guided wavelength λ_g=57.6 mm). Considering that the dielectric constant for the substrate is 2.2, and the physical length for the quarter circular patch is 8.8 mm, the electrical length is therefore only about $0.1\lambda_0$ or $0.15\lambda_g$ in the subwavelength scale. It is much smaller than the traditional CMSA [2–3] or meta-CMSA [15].

Although with a small patch, the new meta-QCMSA has a considerable bandwidth (BW) of 3.8% and
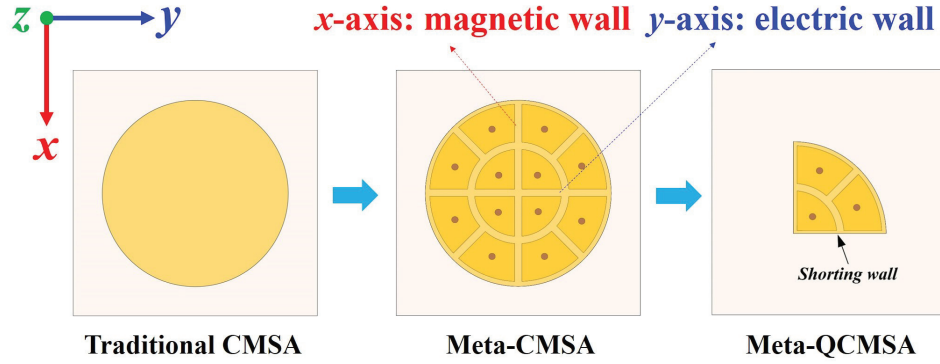
Fig. 1. The designing roadmap of the meta-QCMSA (feedings are not considered).

reasonably high gain of 3.9 dBi in the experimental demonstration. These performances make the new antenna suitable to be applied in 5G/B5G mobile applications.

II. CONCEPT

The subwavelength meta-QCMSA is designed using both the metamaterial substrate and field symmetry techniques. We start from the traditional CMSA [2–3]. A two-step designing roadmap is shown in Fig. 1. First, the traditional CMSA is designed to become a metamaterial CMSA (meta-CMSA) by choosing some particular sector mushroom metamaterial structures [15] to fill into the host low-index dielectric. These mushroom structures were found to be able to increase the ε_{reff} of the antenna. Details for this meta-CMSA can be found in our previous work [15].

Second, on the basis of the meta-CMSA [15], the full circular patch is further reduced to a quarter circle, forming a new meta-QCMSA as proposed in this work. Inspired by the design in [3] (see Fig. 6.7 in [3]), if a CMSA operates at its fundamental TM_{11} mode and the feeding position is along the x-axis, the x-axis can be regarded as the magnetic wall and the y-axis regarded as the electric wall. In a practical antenna, this magnetic wall boundary condition can be fulfilled by directly using an open edge, providing that the antenna is very thin. The electric wall is realized by using numerous shorting (conducting) pins [2–3]. We remark that at the second step, the f_0 for the meta-QCMSA is nearly the same as the meta-CMSA if the margin effects are not accounted for, but its patch area is much reduced. In the following section, we will show the detailed design and results of the conceptual meta-QCMSA.

III. DESIGN AND RESULTS

The configuration of a practical meta-QCMSA is given in Fig. 2. Its overview is shown in Fig. 2 (a), top view in Fig. 2 (b) and side view in Fig. 2 (c). The antenna architecture is similar to [15] but different in the

(a)

(b)

(c)
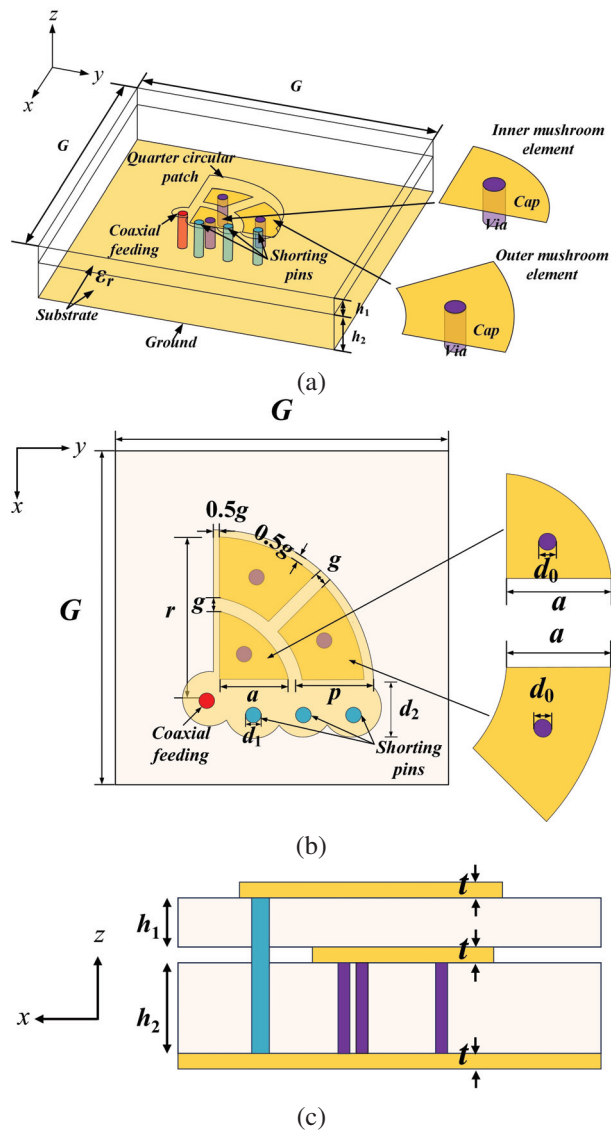
Fig. 2. Configuration of the meta-QCMSA in (a) overview, (b) top view, and (c) side view (feeding is not shown).
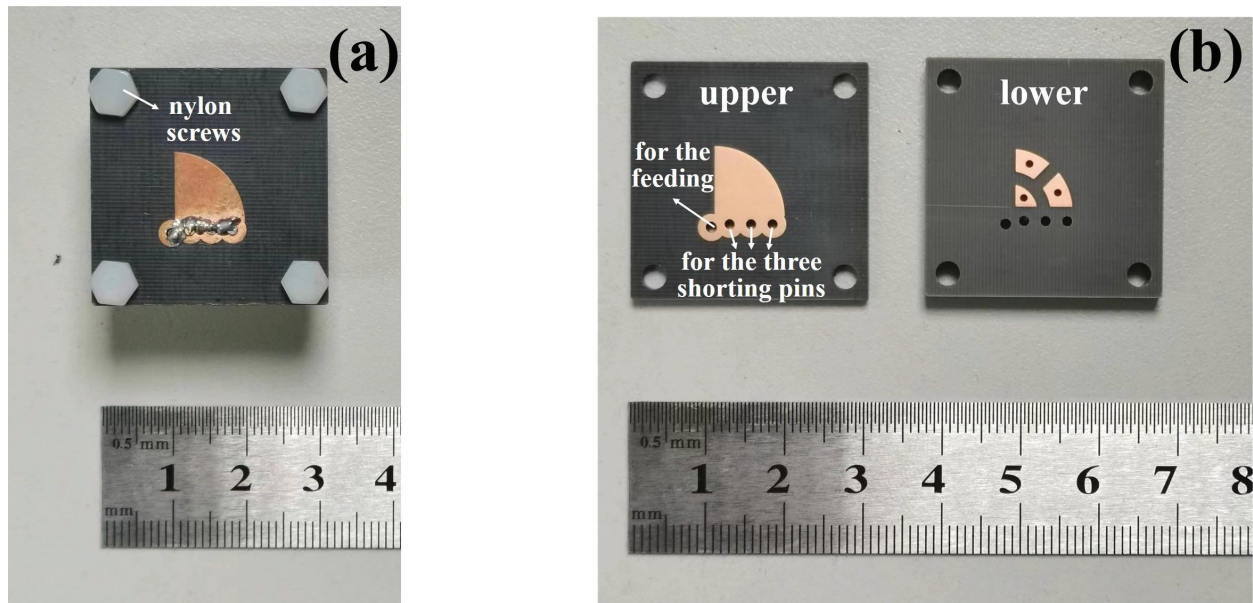
Fig. 3. (a) Antenna sample and (b) upper and lower dielectric layers.

patch shape. Note that the patch is a quarter circular disc herein, and a full disc in [15].

From Fig. 2 (b), we see that the patch radius for the quarter circle (note that it is also the patch length) is r. The ground plane is a square with length G. Beneath the quarter circular patch, there are three sector metallic mushroom elements included in the host substrate. Each mushroom element has a sector-shaped metal cap (with radial length of a) that is linked to the ground plane by a metallic via. The gap between the mushrooms is g. As shown in Fig. 2 (b), the period for the mushrooms along the ρ-axis is $p=a+g=r/2$.

The host substrate has relative permittivity ε_r and loss tangent $\tan\delta$, which is separated by the mushroom caps into two sub-layers with thickness of h_1 and h_2, respectively. The via is supposed with a diameter of d_0 and height of h_2. All three (patch, cap, ground) metal layers have a thickness of $t=0.035$ mm. Figure 2 (c) clearly shows its vertical profile including the two substrate layers and three metal layers (feeding is not shown).

As illustrated in Fig. 1, the y-axis radius on the edge of the meta-QCMSA is an electric wall. In practical implementations, this electric wall is realized by aligning three shorting pins along the edge. These shorting pins have a diameter of d_1. In addition, to make it easier to solder, each shorting pin is set to be located in a larger soldering pad with a diameter of d_2 ($d_2>d_1$). The antenna is fed by a 50 Ω coaxial SMA probe at the left lower corner of the quarter circular patch.

We now consider a meta-QCMSA with the following default parameters: $r=8.8$ mm, $G=30$ mm, $\varepsilon_r=2.2$, $\tan\delta=0.001$, $h_1=2$ mm, $h_2=4$ mm, $d_0=1$ mm, $d_1=1.2$ mm,

$d_2=3.4$ mm, $p=4.4$ mm, $a=2.8$ mm and $g=1.6$ mm. The metals are all copper with a conductivity of 5.8×10^7 S/m.

The meta-QCMSA is experimentally demonstrated with the above parameters. The antenna sample is shown in Fig. 3 (a), which is assembled from two dielectric layers as shown in Fig. 3 (b). Generally, it needs four steps to realize such a practical antenna. First, the two dielectric layers are fabricated using the PCB process that work as the upper and lower layer, respectively, for the antenna. The dielectric layers are both with nominal $\varepsilon_r=2.2$ and $\tan\delta=0.001$, provided by Taizhou Wangling Corp. Second, the two dielectric layers in Fig. 3 (b) are manually assembled using nylon screws located at the four corners of the boards. The third step is to add three solid shorting pins along the patch edge, which are subsequently soldered to connect the quarter patch and ground plane. The fourth (final) step is to solder the coaxial SMA probe that feeds the antenna.

The simulated and measured S_{11} results for the meta-QCMSA are given in Fig. 4 (a). It is observed that the simulated f_0 for the meta-QCMSA is 3.5 GHz from the numerical solver HFSS. The measured f_0 is however slightly upshifted to 3.51 GHz. By normalizing r (8.8 mm) to the λ_0 (85.5 mm) or λ_g (57.6 mm) at 3.51 GHz, we conclude that the patch radius is nearly $0.1\lambda_0$ or $0.15\lambda_g$ for this meta-QCMSA. The simulated BW is 168 MHz (4.8%) while the measured one is 135 MHz (3.8%) from 3.445 to 3.58 GHz. The reduction in BW is attributed to the imperfection of the antenna sample, which results in an increased S_{11} level in the experiment.
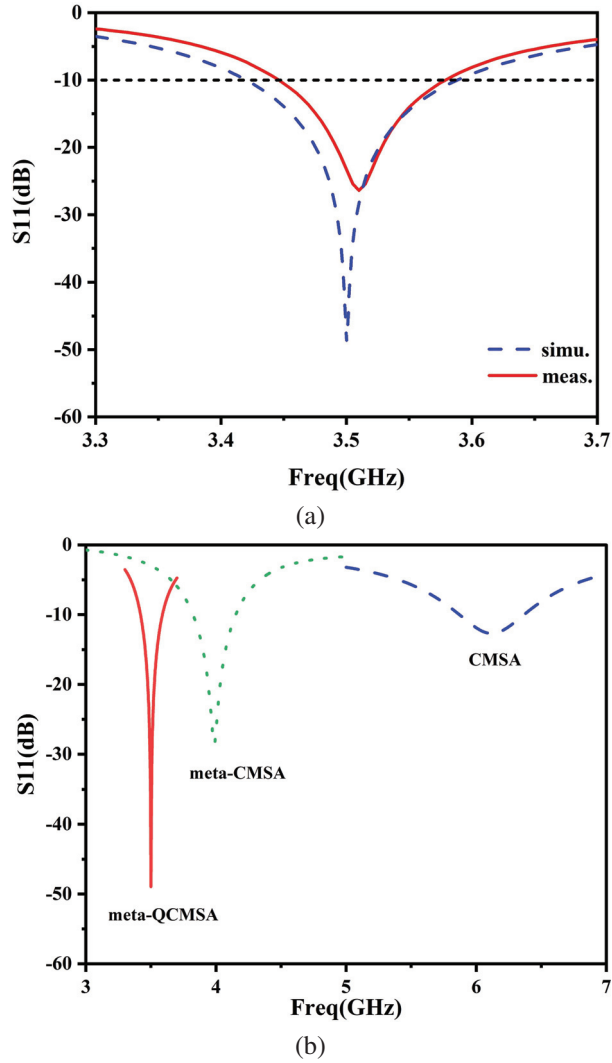
(a)

(b)

Fig. 4. (a) S_{11} for meta-QCMSA, and (b) a comparison of CMSA, meta-CMSA and meta-QCMSA.

To better feature the new meta-QCMSA, we also consider the original CMSA [2–3] and meta-CMSA [15]. Note that the patches for the CMSA and meta-CMSA are both full circles with diameter $d=2r=17.6$ mm. The other parameters are all the same as the meta-QCMSA. The CMSA and meta-CMSA are numerically calculated. Their S_{11} curves, in association with the meta-QCMSA, are shown in Fig. 4 (b). We see that the original simplest CMSA resonates at 6.12 GHz ($\lambda_0=49.0$ mm, $\lambda_g=33.1$ mm). The patch length is its diameter and is 17.6 mm ($0.36\lambda_0$ or $0.53\lambda_g$). The meta-CMSA however resonates at a lower 3.986 GHz ($\lambda_0=75.3$ mm, $\lambda_g=50.7$ mm). Its patch length is still the diameter (17.6 mm) normalized as $0.23\lambda_0$ or $0.35\lambda_g$.

We remark that for the new meta-QCMSA, its patch length is the radius of nearly $0.1\lambda_0$. It is much smaller

than the CMSA ($0.36\lambda_0$) and meta-CMSA ($0.23\lambda_0$). In addition, we note that the f_0 values for the meta-CMSA and meta-QCMSA in Fig. 5 (b) are close but not exactly equal. This is due to the different margin effects for these two antennas, as one patch is a full circle while the other is a quarter.

As reported in [15], the resonances for the meta-CMSA are greatly affected by the thicknesses h_1 and h_2 (see Fig. 3 in [15]). Herein we observe their effects on the meta-QCMSA. It is numerically studied for different h_1 and h_2 values. Their S_{11} curves are shown in Figs. 5 (a) and (b), respectively. The default thicknesses are $h_1=2$ mm and $h_2=4$ mm. As revealed from Fig. 5 (a), f_0 becomes higher when h_1 increases; from Fig. 5 (b), f_0 will be lower when h_2 increases. These trends are consistent with [15].

(a)

(b)
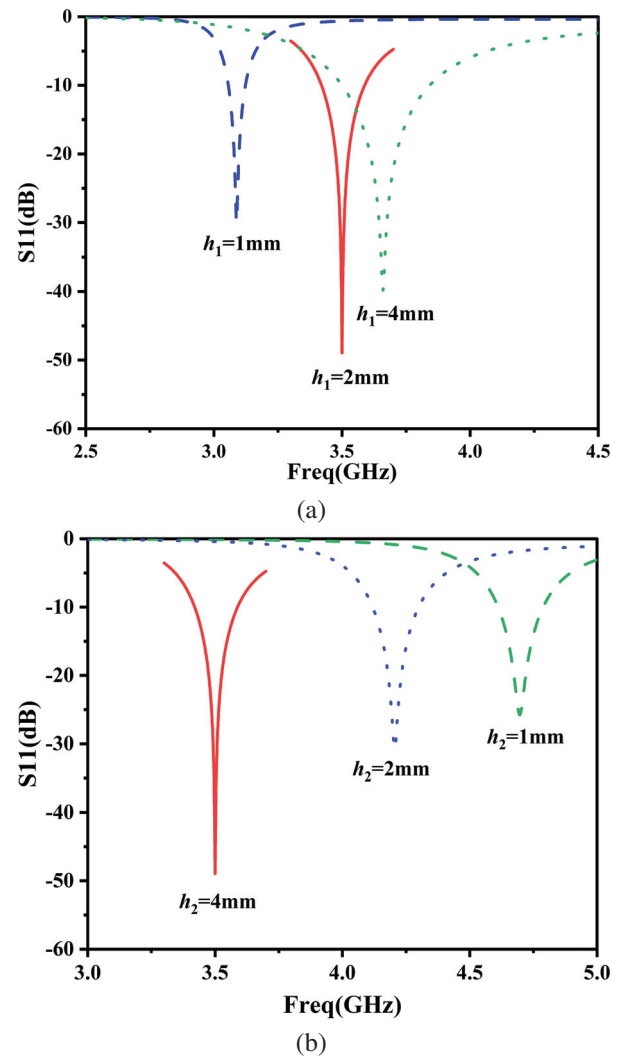
Fig. 5. S_{11} for meta-QCMSA with different (a) h_1 and (b) h_2 values.

The far-field characteristics for the new meta-QCMSA are also evaluated in both simulations and experiments in the microwave chamber. The realized antenna gains are shown in Fig. 6. The peak antenna gain predicted from the numerical solver HFSS is 4.15 dBi. The measured gain values are however slightly lower than simulation in that its peak value is 3.9 dBi. Nonetheless, within the -10 dB impedance BW, the measured antenna gains are all above 2.78 dBi.
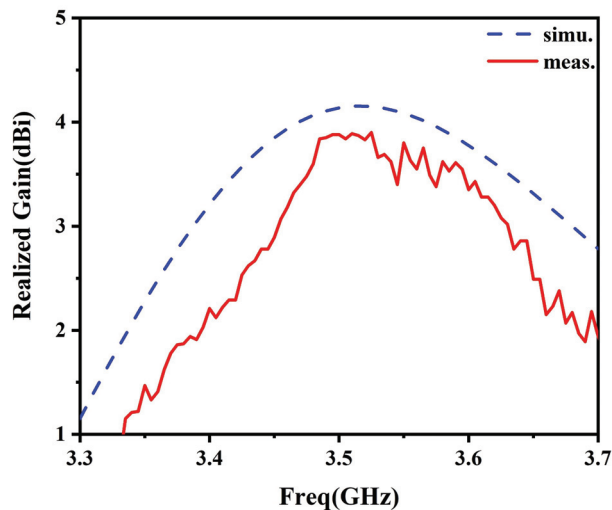
Fig. 6. The realized antenna gains of meta-QCMSA.

Efficiency was not measured. The simulated peak realized efficiency is greater than 90% in HFSS. The radiation efficiency (without considering the mismatching loss) is even higher at over 95% predicted from HFSS.

The radiation patterns of the meta-QCMSA are shown in Fig. 7, obtained at 3.51 GHz. Generally, the simulated and measured co-polarizations are always in good agreement. However, the measured cross-polarizations seem larger than simulation. In addition, it is found that the cross-polarization levels on the H plane (*yoz*) are larger than those on the E plane (*xoz*). In particular, at the bore sight (0°) direction, the measured cross-polarizations on both planes are suppressed lower than -10 dB.

This meta-QCMSA is compared with several other miniaturized MSAs in Table 1. We find that this antenna is featured with a very small patch size ($0.1\lambda_0 \times 0.1\lambda_0$) while maintaining considerable BW (3.8%) and reasonably high antenna gain (3.9 dBi). As for the antenna in [6], it is smaller ($0.04\lambda_0 \times 0.05\lambda_0$) than our work by loading a ferrite. However, its antenna gain is very low (-9.06 dBi). In addition, regarding the antennas in the other literatures [8, 10, 12–17], their patch sizes are all larger than this work. The antenna gains are observed to vary
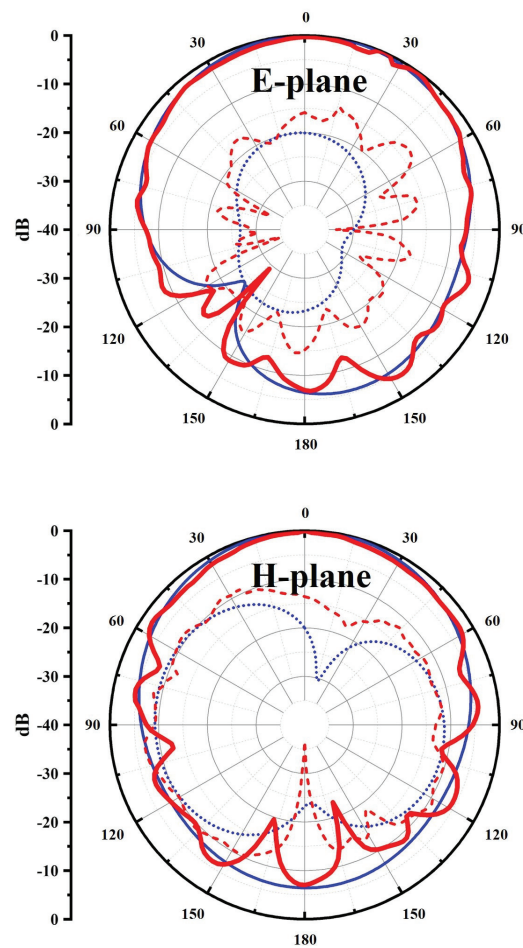
Fig. 7. Radiation patterns at 3.51 GHz.

Table 1: Comparison of several miniaturized metamaterial MSAs

Ref	Patch Size	Thickness	BW	Gain (dBi)
[6]	$0.04\lambda_0 \times 0.05\lambda_0$	$0.034\lambda_0$	4%	-9.06
[8]	$0.145\lambda_0 \times 0.203\lambda_0$	$0.008\lambda_0$	0.5%	3.2
[10]	$0.233\lambda_0 \times 0.233\lambda_0$	$0.018\lambda_0$	3.29%	5
[12]	$0.127\lambda_0 \times 0.123\lambda_0$	$0.03\lambda_0$	0.93%	2
[13]	$0.20\lambda_0 \times 0.20\lambda_0$	$0.01\lambda_0$	3.9%	3.71
[14]	$0.23\lambda_0 \times 0.23\lambda_0$	$0.044\lambda_0$	16.1%	5
[15]	$0.232\lambda_0 \times 0.232\lambda_0$	$0.035\lambda_0$	3%	5.9
[16]	$0.19\lambda_0 \times 0.19\lambda_0$	$0.11\lambda_0$	-	4.76
[17]	$0.17\lambda_0 \times 0.25\lambda_0$	0.026λ	7.22%	1.94
This work	$0.1\lambda_0 \times 0.1\lambda_0$	$0.07\lambda_0$	3.8%	3.9

from 2 to 5.9 dBi, which are in the same order of this meta-QCMSA.

IV. CONCLUSION

A subwavelength meta-QCMSA is designed by jointly using metamaterial and field symmetry techniques. One practical meta-QCMSA is demonstrated in both full-wave simulations and experiments, operating at the 3.5 GHz band. The patch length for the meta-QCMSA is about $0.1\lambda_0$ or $0.15\lambda_g$. The BW, antenna gain and radiation patterns for the new antenna are also studied in the experiments, which can promisingly meet the demands of portable devices for 3.5 GHz communications.

ACKNOWLEDGMENT

REFERENCES

[1] 3GPP TS 38.104, V17.5.0 [Online]. Available: https://www.3gpp.org.

[2] R. Garg, P. Bhartia, I. Bahl, and A. Ittipiboon, *Microstrip Antenna Design Handbook*. Boston: Artech House, 2001.

[3] G. Kumar and K. P. Ray, *Broadband Microstrip Antennas*. Boston: Artech House, 2003.

[4] J. S. Kula, D. Psychoudakis, W.-J. Liao, C.-C. Chen, J. L. Volakis, and J. W. Halloran, "Patch-antenna miniaturization using recently available ceramic substrates," *IEEE Antennas and Propagation Magazine*, vol. 48, pp. 13-20, 2006.

[5] W. Lee, Y. Hong, H. Won, M. Choi, K. Isbell, J. Lee, T. Kim, and S. Park, "Lossy ferrite core-dielectric shell structure for miniature GHz axial-mode helical antenna," *IEEE Antennas and Wireless Propagation Letters*, vol. 18, pp. 951-955, 2019.

[6] S. Jemmeli, T. Monediere, E. Arnaud, and L. Huitema, "Ultra-miniature and circularly polarized ferrite patch antenna," *IEEE Transactions on Antennas and Propagation*, vol. 71, pp. 6435-6443, 2023.

[7] S. Jahani, J. Rashed-Mohassel, and M. Shahabadi, "Miniaturization of circular patch antennas using MNG metamaterials," *IEEE Antennas and Wireless Propagation Letters*, vol. 9, pp. 1194-1196, 2010.

[8] F. Farzami, K. Forooraghi, and M. Norooziarab, "Miniaturization of a microstrip antenna using a compact and thin magneto-dielectric substrate," *IEEE Antennas and Wireless Propagation Letters*, vol. 10, pp. 1540-1542, 2011.

[9] B. Zarghooni, A. Dadgarpour, and T. A. Denidni, "Greek-key pattern as a miniaturized multiband metamaterial unit-cell," *IEEE Antennas and Wireless Propagation Letters*, vol. 14, pp. 1254-1257, 2015.

[10] T. Cai, G. Wang, X. Zhang, Y. Wang, B. Zong, and H. Xu, "Compact microstrip antenna with enhanced bandwidth by loading magneto-electro-dielectric planar waveguided metamaterials," *IEEE Transactions on Antennas and Propagation*, vol. 63, pp. 2306-2311, 2015.

[11] M. Li, K. Luk, L. Ge, and K. Zhang, "Miniaturization of magnetoelectric dipole antenna by using metamaterial loading," *IEEE Transactions on Antennas and Propagation*, vol. 64, pp. 4914-4918, 2016.

[12] Q. Huang, X. Xu, and R. Zhang, "Study of the combination method and its application to shrink a patch antenna operating in the UHF band," *Applied Computational Electromagnetics Society Journal*, vol. 37, pp. 209-214, 2022.

[13] S. Painam and C. Bhuma, "Miniaturizing a microstrip antenna using metamaterials and meta-surfaces," *IEEE Antennas and Propagation Magazine*, vol. 61, pp. 91-135, 2019.

[14] S. Liu, Z. Wang, and Y. Dong, "Compact wideband SRR-inspired antennas for 5G microcell applications," *IEEE Transactions on Antennas and Propagation*, vol. 69, pp. 5998-6003, 2021.

[15] H. Lu, G. Dai, X. Xu, and X. Deng, "Miniaturized circular microstrip antenna designed with quasi-periodic sector metamaterials," *Microwave and Optical Technology Letters*, vol. 64, pp. 1614-1620, 2022.

[16] H. Lu and X. Xu, "Comparative study of miniaturized microstrip antennas designed with different super-substrate materials operating at 900 MHz," *Applied Physics A*, vol. 128, p. 297, 2022.

[17] M. Ameen and R. K. Chaudhary, "ENG-TL inspired dual-polarized antenna using curved meander, two-arm Archimedean spirals and CSRR mushroom," *Microwave and Optical Technology Letters*, vol. 65, pp. 1778-1786, 2023.

[18] C. A. Balanis, *Advanced Engineering Electromagnetics*. Hoboken: Wiley, 2012.

Hao Lu was born in Hubei, China, in 1998. He received the M.S. degree from Shanghai University, Shanghai, China, in 2023. His research interest includes antenna miniaturization technology.

Xiaofei Xu received the B.S. degree in 2007 and the Ph.D. degree in 2011, both from Nanjing University, Nanjing, China. He is currently with the School of Communication and Information Engineering in Shanghai University, Shanghai, China.

Dr. Xu's research areas include electromagnetics, antennas and microwave technology. He has authored over 50 papers published in peer-reviewed journals and conference proceedings. He also serves a number of journals and society workshops as the reviewer or organizer.

Hu Wei was born in Anhui, China, in 1998. He is currently pursuing the M.S. degree from Shanghai University, Shanghai, China. His research interest includes antenna technology.

A Compact Wideband Branch Line Coupler for Lower 5G Applications

Balasem S. Samet and Ahmed A. Abbas

Department of Electrical Engineering
Faculty of Engineering, University of Anbar, Anbar, Iraq
balasem.sumait@uoanbar.edu.iq, Ahmed.abbas@uoanbar.edu.iq

Abstract – This paper presents a new design approach of a compact wideband branch line coupler based on waveguide technique at 3.5 GHz. At the lower band of 5G technology, microwave devices such as hybrid couplers tend to be narrower in bandwidth and big in size, in addition to the phase difference error produced by using common planar technology. Therefore, waveguide technology aims to solve those challenges. This work aims to design a compact wideband coupler by implementing a direct coupling aperture between two waveguides with a cutting in the narrow wall of the structure. This technique helps in obtaining a wide bandwidth and reduces the size of the whole structure. The coupler is simulated using computer software technology and fabricated using CNC machining. The measured S-parameters of the coupler are observed to have low loss properties with return loss and isolation less than -10 dB. The coupling factor at the outputs are -3.21 dB with low loss of -0.2 dB. The measured phase error is about $2°$ at 3.5 GHz. A size reduction of 70% is observed compared to conventional waveguides and planar couplers. Overall, this coupler shows great performance that could be used for 5G beamforming applications.

Index Terms – 5G, branch line coupler, compact size, direct coupling, waveguide.

I. INTRODUCTION

Hybrid couplers, better known as branch line couplers (BLCs), are widely implemented in microwave and millimeterwave devices specifically for beamforming network and antenna array systems [1–3]. Hybrid couplers play significant component roles in designing accurate antenna beamforming systems. This is due to its importance in controlling the output power and the phase difference for such complex systems [2]. Generally, a hybrid coupler is a two-port network with two inputs and two outputs. It acts as a power divider which equally splits the input power at the outputs with a phase difference of $90°$ or $180°$ [3]. As one of the inputs is excited, the outputs receive an equal magnitude of -3 dB with different phase of $90°$ between the output ports. However, hybrid couplers are popularly known for their narrow bandwidth properties [4]. In addition, at lower frequency the size occupied by the planar couplers is quite big and unfixable. Hence, various methods and techniques are presented to enhance the coupler bandwidth and the size by introducing waveguide and substrate integrated waveguide technologies [5–7].

Waveguide couplers are usually presented in the high frequency bands [8]. This is due to the small size and high coupling that could be obtained in such frequencies. Yet, few attempts have been done to implement the waveguide structure in the coupler design at lower bands (lower than 10 GHz). For example, a directional waveguide coupler is designed from 7.7 GHz to 12 GHz using coupling of two rectangular waveguides by [9]. A good return loss and isolation are obtained of less than -20 dB. However, the size of the coupler is not suitable for further beamforming implementation. Another waveguide coupler at X-band is introduced by [10]. The coupler is designed using a single waveguide structure with slots cut in the broad wall of the waveguide structure. The obtained results showed a good performance at 10 GHz, with a size reduction of 44% and FBW of 50%. As a result, this work aims to present a first attempt to design a waveguide coupler using two waveguides with modified narrow walls and a coupling aperture between them at a lower band of 5G (sub-6 GHz).

The contribution of this paper is summarized in two major points. First, modification of the narrow wall of the waveguide to reduce the size at 3.5 GHz by more than 70%. Second, provide a high-performance coupler compared to the existing ones with different planar technology at the same frequency. Section II presents the design method. Section III discusses the results. Section IV summaries the paper.

II. DESIGN OF COUPLER

Figure 1 shows the common hybrid coupler structure with four ports implementation. The input port (port 1) is the return loss port denoted as $|S_{11}|$. The isolation port (port 4) is the port that blocks the signal and denoted as $|S_{41}|$. The through port (port 2) and the coupling port (port 3) are the output ports and named as $|S_{21}|$ and $|S_{31}|$, respectively [11, 12]. The hybrid cou-

pler is designed with four branches with quarter wavelength transmission lines in which the input impedance is equal to 50 Ω. To convert this hybrid coupler into a waveguide structure form, two rectangular waveguides replace two branches. The coupling branch is replaced with a coupling waveguide aperture placed in the middle of the two rectangular waveguides as illustrated in Fig. 2.
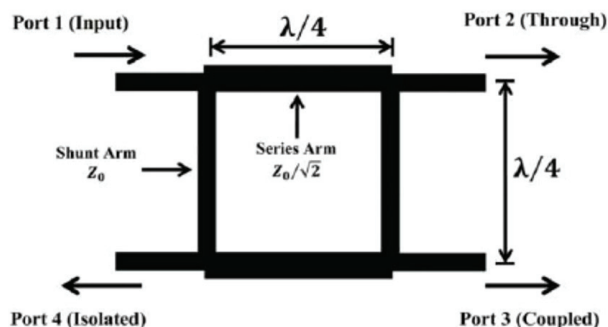

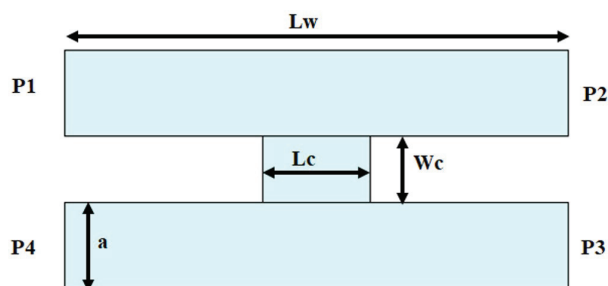Fig. 1. The common hybrid coupler structure.

Fig. 2. The waveguide structure replacement of the hybrid coupler in Fig. 1. (Lw = length of section, Wc = width of coupled section, Lc = coupling area, P1 = input port, P2 = output port, P3 = coupling port, P4 = isolation port).

The first step is to calculate the guided wavelength and the cut-off frequency of the waveguide structure. This could be found by [13]:

$$f_c = \frac{c}{2\pi\sqrt{\varepsilon\mu}} \sqrt{\left(\frac{m\pi}{a}\right)^2 + \left(\frac{n\pi}{b}\right)^2 + \left(\frac{l\pi}{d}\right)^2}, \quad (1)$$

$$\lambda_g = \frac{\lambda_0}{\sqrt{1 - \frac{\lambda_0}{2a}}}, \quad (2)$$

where the waveguide is air-filled with permittivity (ε_0) and permeability (μ_0), the mode of TE_{10} of m and n, and $a \times b$ as waveguide inner dimensions, and λ_0 is the desired wavelength. At 3.5 GHz, the initial dimensions of the waveguide coupler are: $L_w = 80$ mm, $L_c = 20$ mm, $W_c = 20$ mm, $a = 22.55$ mm, $b = 21.5$ mm).
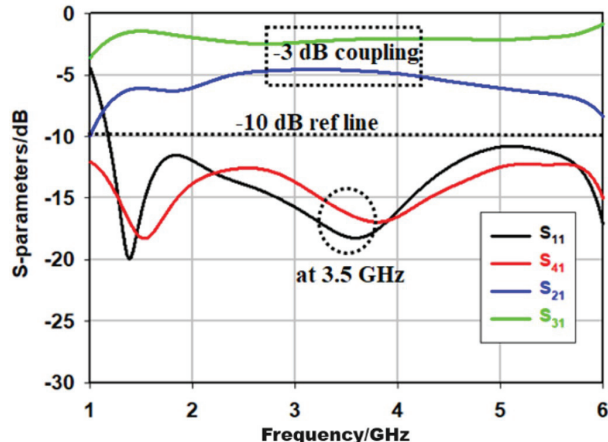
Fig. 3. S-parameters of the conventional waveguide coupler.

The conventional coupler is simulated in order to analyze its S-parameters as shown in Fig. 3. The performance of the return loss and the isolation at 3.5 GHz show good values below -10 dB with $|S_{11}| = -17$ dB and $|S_{41}| = -16$ dB, whereas the outputs power varies from -3.5 dB at port 2 to -4.8 dB at port 3. As a result, the coupler is operated at its minimal requirements.

The second step is to modify the coupler in order to reduce the size and match the output powers to have equally split a -3 dB coupling. Figure 4 (a) shows the coupler modification by adding two aperture slot couplings to the middle aperture. This technique enhances the S-parameters of the coupler. Figure 4 (b) demonstrates the adding of slot cutting arms in the narrow wall of the two waveguides. This method is used to reduce the size of the two rectangular waveguides and improve the output powers at port 2 and port 3.

To analyze the performance of the modified coupler, a parametric study on the length (L_{sc}) and the width (W_{sc}) of the two slots coupling aperture with arms coupling length (L_{nc}) is done with the aid of CST 3D model software as shown in Fig. 5.

From Fig. 5 (a), the length of the coupling slot apertures affects the return loss in that it increases and shifts the value of the return loss and the frequency, respectively. As L_{sc} decreases, the return loss increases to be -41 dB and shifts to 3.5 GHz. Hence, at $L_{sc} = 6$ mm, the bandwidth is more than 2 GHz and the isolation is below -20 dB. The width of the coupling slot apertures can be varied in order to achieve a perfect -3 dB through power at port 2 as seen in Fig. 5 (b). As W_{sc} increases the through power tends to be -3 dB and return loss remains unchanged. Hence, the optimal value for the width of the coupling aperture is 8 mm. Finally, the coupling power at port 3 increases as the arms coupling length increases
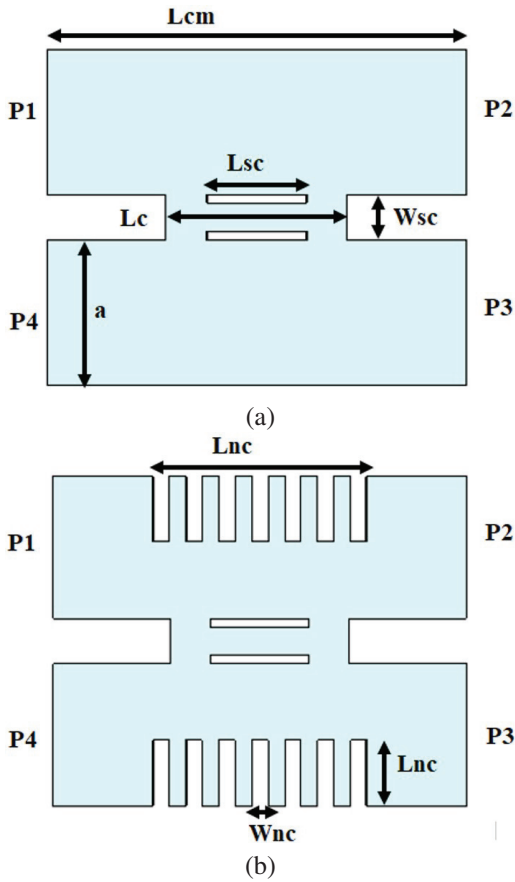
Fig. 4. The proposed waveguide coupler. (a) Two slots coupling apertures (Lcm = waveguide length, Lc = coupling length, Wsc = width of coupling, Lc = coupling area length) and (b) waveguide narrow wall modified with arms coupling apertures (Lnc = arm length, P1 = port 1, P2 = port 2, P3 = port 3, P4 = port 4).

as shown in Fig. 5 (c). Hence, the optimal value for the arms coupling length in the waveguide narrow wall is 12 mm.

As all the dimensions of the proposed coupler are obtained from the parametric study and the S-parameters performance, the final dimension for the proposed coupler are as follows: $L_{cm} = 25$ mm, $W_{sc} = 8$ mm, $L_{sc} = 6$ mm, $a = 8.36$ mm, $L_c = 10.8$ mm, $L_{nc} = 12$ mm, $L_{nc1} = 4$ mm, and $W_{nc} = 1$ mm.

Figure 6 shows the final structure for the proposed coupler for the fabrication process. The structure has been added with four additional arms bent to make the measurements possible. The four ports couplers are attached with waveguide adaptors in order to measure the amplitudes and the phases.

The optimized coupler performance is plotted in Fig. 7 in terms of S-parameters and phases. A fractal
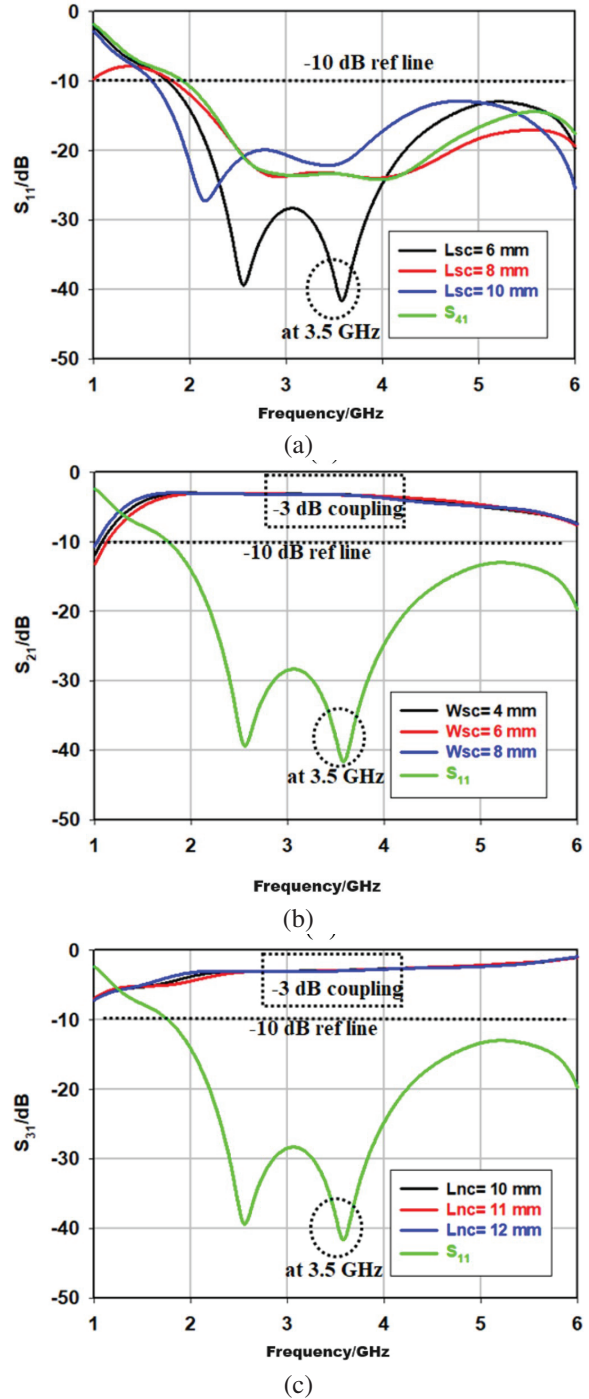
Fig. 5. S-parameters parametric study of the proposed coupler. (a) Return loss with respect to the length of coupling aperture, (b) through power with respect to the width of coupling aperture, and (c) coupling with respect to the length of arms.

bandwidth of 97% is obtained with equal power split of −3 dB over the bandwidth. A 90° phase difference at 3.5 GHz is also achieved at the output ports.
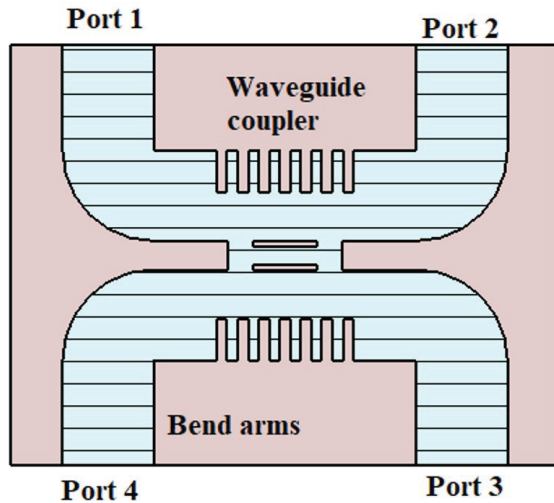
Fig. 6. The final structure of the proposed coupler.
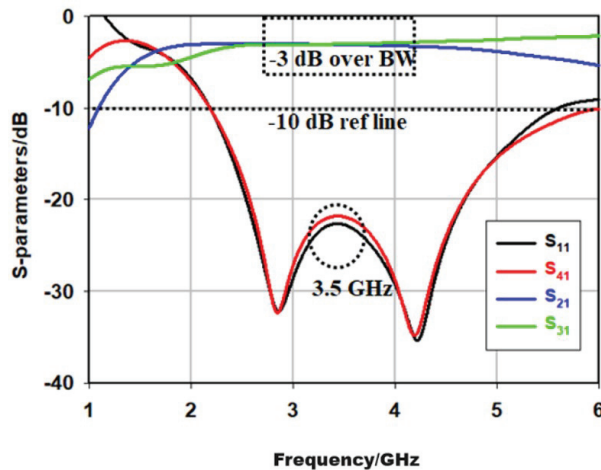
(a)
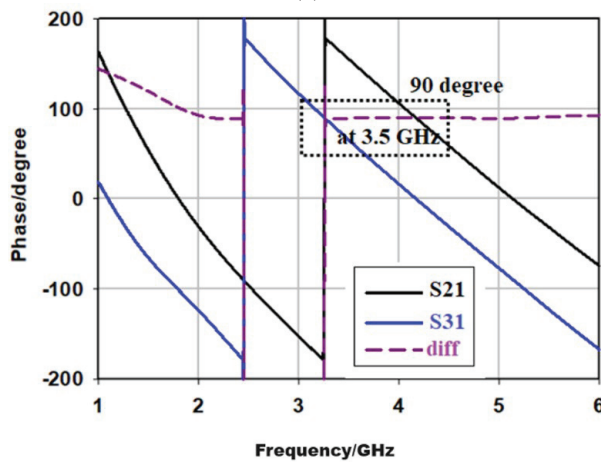
(b)

Fig. 7. (a) S-parameter responses of the proposed coupler and (b) phases of the outputs.

III. RESULTS AND DISCUSSION

The coupler is fabricated using a metal plate of aluminum by CNC machining with depth of cut of 0.6 mm, feed rate of 0.2 mm, and cutting speed of 3500 rpm. Figure 8 shows the fabricated prototype with total dimensions of 30 mm × 20 mm. The prototype highlighted a small size compared to the conventional coupler (waveguide) of 80 mm × 40 mm with a size reduction of 89%.
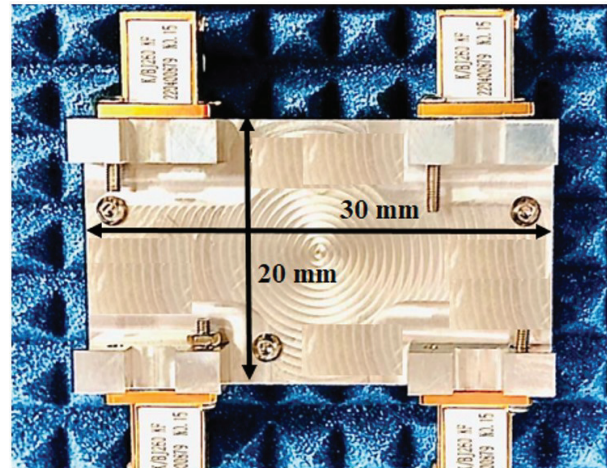
Fig. 8. The coupler prototype.

The S-parameter measurements are done as follows. First, terminator loads are connected at port 2, port 3, and port 4, respectively. Then, port 1 is connected with a measurement cable of a standard vector network analyzer (VNA) port 1 to measure the return loss (S_{11}). Second, remove the terminator load at port 2 and connect it to the measurement output cable of VNA port 2. This step is to measure the output power at port 2. The same procedure is repeated for port 3 and port 4 whilst port 1 is still connected to the input port of the VNA. This allows us to measure the coupling and isolation at port 3 and port 4. The measurement process includes the results in the form of magnitude and phase at all ports. Slight loss can occur due to cable loss and mismatched port connections.

Figure 9 illustrates the measured responses of the fabricated coupler in terms of the input and isolation ports. The input port has a measured bandwidth of 3.22 GHz ranging from 2.1 GHz to 5.32 GHz with a peak return loss of −23.78 dB at 3.5 GHz at shown in Fig. 9 (a). The isolation value over the bandwidth is less than −10 dB as seen in Fig. 9 (b). Hence, low loss properties are achieved compared with the simulated results.

Figures 10 (a) and (b) show the through and coupling measured performances at output port 2 and port 3, respectively. The measured port 2 power is −3.12 dB
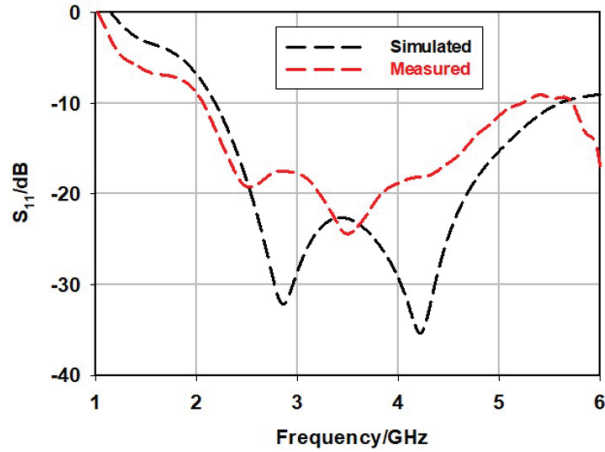
(a)
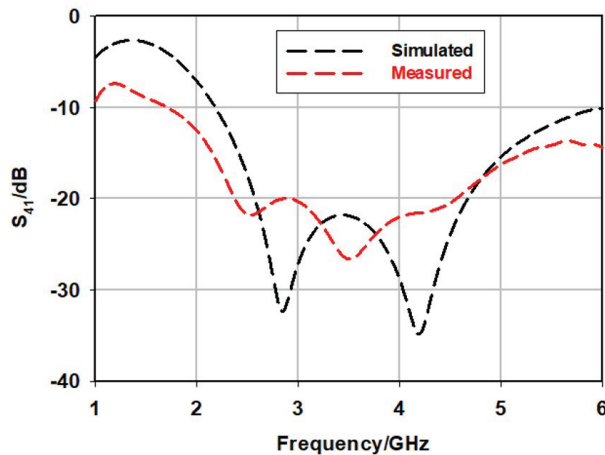
(b)

Fig. 9. Comparison of (a) return loss and (b) isolation of the coupler.

(a)

(b)

Fig. 10. Comparison of (a) through power and (b) coupling of the coupler.

compared to the simulated power of −3.05 dB. Similar results are obtained at output port 3 with a measured power of −3.16 dB compared to the simulated one of −3.22 dB. This indicates a low loss is achieved with −0.1 dB error.

Figure 11 plots the measured phases of port 2 and port 3 with the phase differences at these output ports. It is clearly seen that the measured phases along with the phase difference agreed well with the simulated phases. The phase error is very low with a value of 2°. Table 1 compares the measured and the simulated responses of the proposed coupler. Comparison between the performances of the fabricated prototype with respect to other existing work in shown in Table 2. The comparison shows that the proposed coupler has better bandwidth, low loss, low phase difference error, and size reduction among other designs. Overall, it is proven that using

Fig. 11. Comparison of the phases of the coupler at port 2 and port 3.

this waveguide coupler with the coupling slot structure and arms coupling slot in the narrow wall could work well in reducing the size and maintaining the same performance.

Table 1: Measured and simulated responses of the proposed coupler at 3.5 GHz

Parameters	Simulated	Measured
$|S_{11}|$	−23.52 dB	−23.78 dB
$|S_{21}|$	−3.05 dB	−3.12 dB
$|S_{31}|$	−3.22 dB	−3.16 dB
$|S_{41}|$	−22.5 dB	−25.4 dB
Bandwidth	3.4 GHz	3.22 GHz
Phase Diff.	90°	88°

Table 2: Comparison of other related works with the proposed coupler

Ref	Method	Freq. (GHz)	BW (GHz)	Size %	Phase error (°)
[3]	Microstrip	3.5	2.3	25	5.6
[4]	Microstrip	3.5	1.9	34	7.2
[10]	Waveguide	10	2	15	6
[11]	Waveguide	20	5	10	11
[12]	Waveguide	12	4.3	18	8
[13]	SIW	8.8	4	20	4.6
This work	Waveguide	3.5	3.22	89	2

IV. CONCLUSION

This paper proposes a new method of designing a waveguide hybrid coupler at lower bands of 5G technology. The designed waveguide hybrid coupler is implemented with two coupling aperture slots and arms waveguide coupled structure in the narrow wall. The performance of the coupler showed a size reduction of 89% and a bandwidth of 3.22 GHz. The coupler has low loss properties in terms of S-parameter and phase difference with −0.1 dB loss and 2° phase error. Hence, this coupler is a good candidate for future 5G applications.

REFERENCES

[1] M. Almeshehe, N. Murad, M. Rahim, O. Ayop, N. Samsuri, M. Aziz, and M. Osman, "Surface roughness impact on the performance of the 3D metal printed waveguide coupler at millimeter-wave band," *Engineering Science and Technology, an International Journal*, vol. 35, pp. 129-139, 2022.

[2] R. Dehdasht-Heydari, K. Forooraghi, and M. Naser-Moghadasi, "Efficient and accurate analysis of a substrate integrated waveguide (SIW) rat-race coupler excited by four U-shape slot-coupled transitions," *Applied Computational Electromagnetics Society (ACES) Journal,* vol. 30, no. 1, pp. 42-49, 2015.

[3] N. Shukor, N. Seman, and T. Abd Rahman, "Wideband multi-port network integrated by 3-dB branch-line couplers," *Applied Computational Electromagnetics Society (ACES) Journal,* vol. 33, no. 7, pp. 764-771, 2018.

[4] A. Bekasiewicz, "Miniaturized dual-band branch-line coupler with enhanced bandwidth," *Microwave and Optical Technology Letters*, vol. 61, no. 6, pp. 1441-1444, 2019.

[5] A. K. Vallappil, M. K. A. Rahim, B. A. Khawaja, and M. Aminu-Baba, "Metamaterial based compact branch-line coupler with enhanced bandwidth for use in 5G applications," *Applied Computational Electromagnetics Society (ACES) Journal*, vol. 35, no. 6, pp. 700-708, 2020.

[6] Z. Mansouri, M. Kishihara, F. B. Zarrabi, and F. Geran, "Modified broadband half mode substrate integrated waveguide cruciform coupler," *Applied Computational Electromagnetics Society (ACES) Journal,* vol. 29, no. 11, pp. 881-886, Aug. 2021.

[7] T. Yasui, J.-I. Sugisaka, and K. Hirayama, "Structural optimization of an optical 90 degree hybrid based on a weakly guided 4x4 multimode interference coupler using a parallelized real-coded micro-genetic algorithm," *Applied Computational Electromagnetics Society (ACES) Journal*, vol. 36, no. 05, pp. 526-532, July 2021.

[8] A. A. Abbas and B. S. Samet, "A compact high gain wideband metamaterial antenna for sub-6 GHz applications," *Applied Computational Electromagnetics Society (ACES) Journal*, vol. 37, no. 08, pp. 886-892, Jan. 2023.

[9] Z. Mousavirazi, M. M. M. Ali, H. N. Gheisanab, and T. A. Denidni, "Analysis and design of ultra-wideband PRGW hybrid coupler using PEC/PMC waveguide model," *Scientific Reports*, vol. 12, no. 1, pp. 2-15, 2022.

[10] G. Simoncini, R. Rossi, F. Alimenti, and R. Vincenti Gatti, "Single-ridge waveguide compact and wideband hybrid couplers for X/Ku-band applications," *Electronics*, vol. 11, no. 10, pp. 1538-1550, 2022.

[11] D. Sun and J. Xu, "Rectangular waveguide coupler with adjustable coupling coefficient using gap waveguide technology," *Electronics Letters*, vol. 53, no. 3, pp. 167-169, Feb. 2017.

[12] J. Ma, "A highly directional eight-hole coupling circular waveguide coupler," *International Journal of RF and Microwave Computer-Aided Engineering*, vol. 32, no. 8, 2022.

[13] Z. Zhang, Y. Fan, and Y. Zhang, "Multilayer half-mode substrate integrated waveguide wideband coupler with high selectivity," *Applied Computational Electromagnetics Society (ACES) Journal*, vol. 34, no. 9, pp. 1418-1425, 2019.
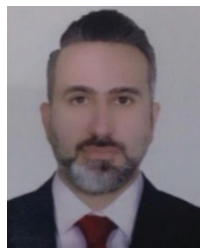
Balasem Salem Samet is lecturer in Electrical Engineering Department, College of Engineering, and University of Anbar. He received the B.Sc. degree in Electrical Engineering/University of Technology in 2000, he received M.Sc. in communication Engineering /University of Technology in 2005 and he received Ph.D. in communication Engineering in 2013. Dr. Balasem is researcher in wireless communication and smart antenna.

Ahmed A. Abbas is a head of Electrical Engineering Department, College of Engineering, University of Anbar from 2018 till now. He received the B.Sc. degree in Electrical Engineering/University of Technology in 1994, he received M.Sc. in communication Engineering /University of Technology in 2005 and he received Ph.D. in communication Engineering/Ankara Yıldırım Beyazıt University in 2017. Dr. Ahmed is researcher in communication field especially in optical wave propagation through random media.

Research on Variable Direction Wireless Power Transfer System based on Auxiliary Coils: Theory, Simulation and Experimental Verification

Feihang Xiao[1] and Hao Qiang[1,2]

[1]School of Mechanical Engineering and Rail Transit
Changzhou University, Changzhou 213164, China
xiaofeihang2000@163.com, qhao@cczu.edu.cn

[2]Jiangsu Province Engineering Research Center of High-Level Energy and Power Equipment
Changzhou University, Changzhou 213164, China

Abstract – In complex environments such as mines and pipelines, wireless power transfer (WPT) technology stands as a safe and convenient method for supplying power. However, in practical applications, the unavoidable angular misalignment between the sending and receiving coils results in decreased power. To address this issue, this paper proposes a variable direction WPT design method based on auxiliary coils. The mutual inductance of the system is analyzed with coils placed at different positions and incorporating multiple auxiliary coils. This paper conducts simulation and experimental analysis based on a 45° angle between the horizontal shaft and the slant shaft, showing a 14.92% increase in received power. The effectiveness of the proposed design method validates the feasibility of the technology and offers substantial support for practical applications.

Index Terms – Codirectional coil, variable direction coil, variable direction transfer, wireless power transfer.

I. INTRODUCTION

Wireless power transfer (WPT) technology has lately gained increasing attention as an alternative way to transfer power with respect to a cabled connection [1]. Due to its advantages of high reliability [2], safety [3], flexible usage [4], low maintenance cost [5] and better adaptability in some extreme or special conditions [6, 7], it is widely used in various fields, including internet of things [8], electric vehicles [9], medical devices [10], etc.

In 2007, MIT successfully illuminated a 60 W bulb one meter away using magnetic field resonance [11]. Magnetic coupled resonant wireless power transfer (MCR-WPT) has emerged as the most promising medium-distance wireless transfer mode.

Coupling coils are a key part of a WPT system [12]. Currently, the majority of WPT systems impose strict requirements on the coil's positioning during operation.

Misalignment between the sending and receiving coils significantly reduces received power [13].

In certain application scenarios, coil placement is restricted, preventing direct alignment. As shown in Fig. 1, in the mining industry, the sending coil on the mining car moves with the slant shaft, while the receiving coil is positioned on the wellbore. When the mining car supplies power to electrical equipment on the slant shaft, direct alignment is possible. However, when powering equipment on the horizontal shaft, an angle between the sending and receiving coils reduces received power [14].
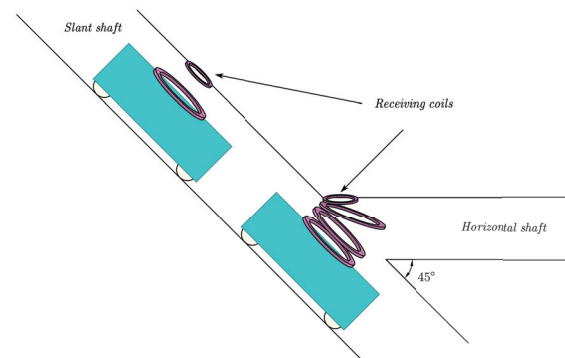

Fig. 1. Schematic of the location of WPT coils in coal mines.

To enhance coil transfer efficiency in diverse scenarios, [15] introduced ferrite between the sending and receiving ends to increase the transfer power when misaligned. However, maintaining consistent shapes for the sending and receiving coils is necessary. By winding Litz lines at different positions on the ferrite, [16] altered the magnetic field distribution, providing improved resistance to misalignment.

To supply power to receiving coils at various angles, [17] utilizes multiple relay coils for equipment power,

but requiring separate capacitors to be configured for each coil. Although multi degree of freedom WPT technology energizes devices at different positions and angles, its structure is generally complex and demands sophisticated control methods [18].

Due to the angular misalignment between the sending coil and the receiving coil, the distribution of the electromagnetic field and the process of power transfer become complex. Therefore, based on electromagnetic field analysis and finite element simulation, a design method for a variable direction WPT system was proposed. Through mutual inductance calculation and simulation, the case of a horizontal shaft and a slant shaft with an angle of 45° was analyzed. The proposed method is applicable for cases where the angle is less than 90°. The main contributions of this paper are as follows:

(1) This paper analyzes the mutual inductance between multiple coils and the occurrence of angular errors between coils.
(2) A design method for variable direction WPT based on auxiliary coils was proposed.
(3) The experimental prototype is designed to measure the power transfer of different numbers of auxiliary coils and auxiliary coils at different positions. With the proposed design method, the received power can be increased by 14.92%.

II. THEORETICAL ANALYSIS

A. Basic WPT analysis

The equivalent circuit method was utilized to model the WPT system in our research. The equivalent circuit method simplifies complex electromagnetic systems into circuit models for analysis, providing an intuitive description of the power conversion and transfer processes among system components.

The MCR-WPT system mainly consists of a high-frequency (HF) power supply, sending module (sending coil), receiving module (receiving coil) and load [12, 19]. The equivalent circuit is depicted in Fig. 2.

R_{AC} represents the equivalent impedance of the HF power supply AC. L_S, C_S and R_{LS} denote the equiv-
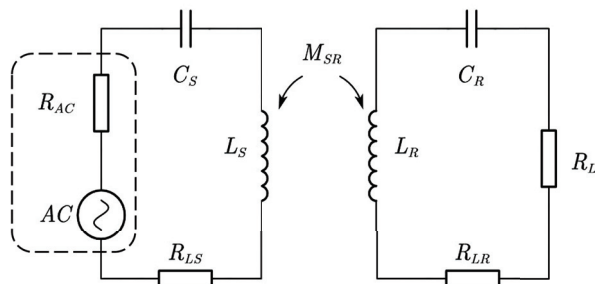
Fig. 2. Equivalent circuit of MCR-WPT system.

alent inductance, resonant capacitance and equivalent resistance of the sending module. Similarly, L_R, C_R and R_{LR} represent the equivalent inductance, resonant capacitance and equivalent resistance of the receiving module. R_L signifies the load resistance, while M_{SR} stands for the mutual inductance between the two coils. In accordance with Fig. 2, deducing the Kirchhoff's Voltage Law (KVL) equations of the two circuits with the operating angular frequency ω is straightforward:

$$\begin{bmatrix} Z_S & j\omega M_{SR} \\ j\omega M_{SR} & Z_R \end{bmatrix} \begin{bmatrix} \dot{I}_S \\ \dot{I}_R \end{bmatrix} = \begin{bmatrix} \dot{U}_{AC} \\ 0 \end{bmatrix}. \tag{1}$$

$\dot{I}_S$ and $\dot{I}_R$ are the currents of the sending circuit and the receiving circuit, $\dot{U}_{AC}$ is the input voltage and P_L is the power of load. The transfer efficiency η is defined as the ratio of load power to input power. Z_S and Z_R represent the equivalent impedance of the sending coil circuit and the receiving coil circuit, respectively. When resonance occurs between the sending and receiving coils, the load power P_L and efficiency η are highest:

$$\eta = \frac{P_L}{\dot{U}_{AC}\dot{I}_S} \times 100\% = \frac{\dot{I}_R{}^2 R_L}{\dot{U}_{AC}\dot{I}_S} \times 100\%. \tag{2}$$

In the MCR-WPT system, the coupling coefficient k represents the coupling strength between two coils, defined as follows:

$$k = \frac{M_{SR}}{\sqrt{L_S L_R}}. \tag{3}$$

According to the definition of coupling coefficient, the mutual inductance directly determines the coil coupling strength when the coil parameters are fixed. Therefore, mutual inductance is key to analyzing the transfer capacity of WPT systems.

B. Variable direction WPT analysis

In WPT systems, power is transmitted from the transmitter module to the receiving module through electromagnetic field coupling, where mutual inductance serves as a crucial parameter to describe this coupling strength [20]. When dealing with complex electromagnetic systems, the simple equivalent circuit method may not provide sufficiently accurate analysis results. To calculate the mutual inductance between coils, the Neumann formula from computational electromagnetics was employed for analysis. This method enables precise calculation of mutual inductance between coils at different positions and angles, serving as a reference for system design and optimization.

The coils used in this paper are all coaxial multi-turn circular coils. For ease of observation, they are depicted as single-turn coils in the figures.

Establishing a coordinate system with the center of the sending coil as the origin, the center of the receiving coil remains in the yz plane and shifts towards the

positive y-axis until the outer radius of the receiving coil is tangent to the inner radius of the sending coil. Subsequently, using the tangent point as the center of rotation, a 45° rotation is performed about an axis parallel to the x-axis, directed away from the sending coil. The positional relationship between the sending and receiving coils post-rotation is illustrated in Fig. 3.
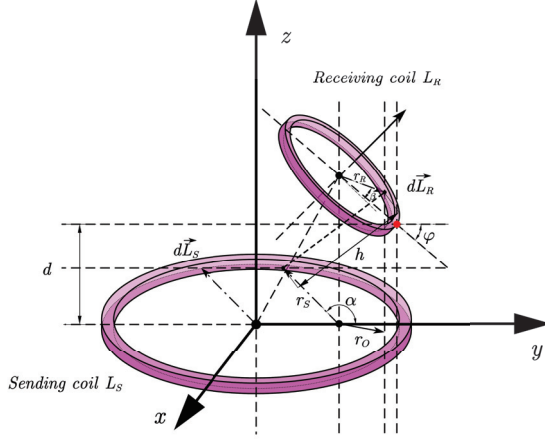

Fig. 3. Schematic of coil position.

The spatial position of the sending coil and the receiving coil undergo changes after rotation, introducing complexity to the calculation of mutual inductance. To simplify the calculation, assuming uniform flow of coil current through the conductor element and neglecting skin effect, mutual inductance can be expressed as [21]:

$$M_{SR} = \frac{\mu_0 N_S N_R}{4\pi} \oint_{L_S} \oint_{L_R} \frac{d\vec{L}_S \cdot d\vec{L}_R}{h}. \quad (4)$$

μ_0 represents the vacuum magnetic permeability. N_S and N_R are the turns of the sending coil and receiving coil, respectively. Based on the proposed equivalent model:

$$d\vec{L}_S \cdot d\vec{L}_R = r_s r_o \cos\alpha \cos\beta, \quad (5)$$

where r_o signifies the length of the projection of the differential element $d\vec{L}_R$ of the receiving coil in the xy plane. Its value depends on the rotation angle φ of the receiving coil and the angular relationship β of the differential element with respect to the point of rotation. Its expression is:

$$r_o = r_R \oint_{L_R} \sqrt{1 + \cos^2\beta \sin^2\varphi}. \quad (6)$$

The airline distance between $d\vec{L}_S$ and $d\vec{L}_R$ is h,

derived by:

$$h = \sqrt{(r_R - r_o)^2 + [d_{SR} + r_R(1 - \cos\beta)\sin\varphi]^2}. \quad (7)$$

Compared with the topology before rotation, the coupling between coils is reduced. Auxiliary coils with the same radius as the sending coil can be added between the sending coil and receiving coil to enhance transfer efficiency.

This paper introduces two auxiliary coils, namely the codirectional auxiliary coil L_i and the variable direction auxiliary coil L_j, positioned between the sending and receiving coils. As illustrated in Fig. 4, the codirectional auxiliary coil is placed near the sending coil, aligned coaxially with it. The variable direction auxiliary coil is placed close to the receiving coil, with its axis in the positive half of the yz plane. The angle between the coil plane and xy plane is denoted as θ_n ($\theta_n < \varphi$). The codirectional auxiliary coil enhances the magnetic field intensity, while the variable direction auxiliary coil is designed to alter the direction of magnetic field propagation, facilitating variable direction transfer.
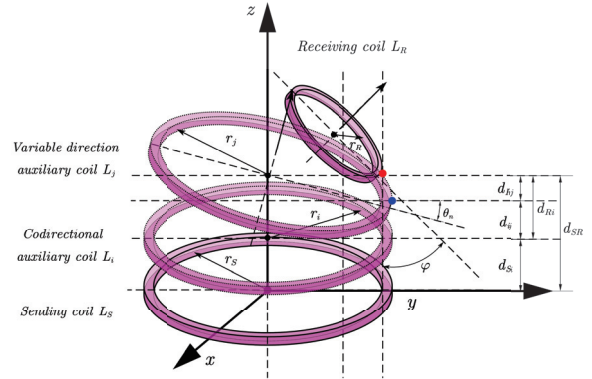
Fig. 4. Schematic of coil position (with auxiliary coils).

d represents the distance between coils, and the two letters after d represent the corresponding coils. For coils with an angle between the xy plane (L_j and L_R), when representing their position with other coils, the point with the highest y-value on the yz plane is used as the reference, as shown by the red and blue dots in Fig. 4.

Both the codirectional auxiliary coil and the variable direction auxiliary coil are multi-turn coils, with subscripts added after the coil name to indicate a particular turn of coil, denoted as $L_{i1}, L_{i2}, \ldots, L_{in}$ and $L_{j1}, L_{j2}, \ldots, L_{jn}$. According to equation (4), the mutual inductance between each coil can be calculated:

$$M_{Sin} = \frac{\mu_0 N_S N_{in}}{4\pi} \oint_{L_S} \oint_{L_{in}} \frac{r_s^2 \cos\alpha_S d\alpha d\beta_{in}}{\sqrt{2r_s^2(1 - \cos\alpha_S) + d_{Sin}^2}}, \quad (8)$$

$$M_{Sjn} = \frac{\mu_0 N_S N_{jn}}{4\pi} \oint_{L_S} \oint_{L_{jn}} \frac{r_S^2 \cos\alpha_S d\alpha_S d\beta_{jn} \oint_{L_{jn}} \sqrt{1-\cos^2\beta_{jn}\sin^2\theta_n}}{\sqrt{\left(r_{jn} - \oint_{L_{j1}} r_{jn}\sqrt{1-\cos^2\beta_{jn}\sin^2\theta_n}\right)^2 + [d_{sjn} + r_{jn}(1-\cos\beta_{jn})\sin\theta_n]^2}}, \tag{9}$$

$$M_{Rjn} = \frac{\mu_0 N_{jn} N_R}{4\pi} \oint_{L_{jn}} \oint_{L_R} \frac{r_S \cos\alpha_R d\alpha_R d\beta_{jn} \oint_{L_R} r_{jn}\sqrt{1-\cos^2\beta_{jn}\sin^2(\varphi-\theta_n)}}{\sqrt{\left(r_R - \oint_{L_R} r_R\sqrt{1-\cos^2\beta_{jn}\sin^2(\varphi-\theta_n)}\right)^2 + [d_{Rjn} + r_R(1-\cos\beta_{jn})\sin(\varphi-\theta_n)]^2}}, \tag{10}$$

$$M_{Rin} = \frac{\mu_0 N_{in} N_R}{4\pi} \oint_{L_{in}} \oint_{L_R} \frac{r_{in} \cos\alpha_R d\alpha_R d\beta_{in} \oint_{L_R} r_R\sqrt{1-\cos^2\beta_{in}\sin^2\varphi}}{\sqrt{\left(r_R - \oint_{L_R} r_R\sqrt{1-\cos^2\beta_{in}\sin^2\varphi}\right)^2 + [d_{Rin} + r_R(1-\cos\beta_{in})\sin\varphi]^2}}. \tag{11}$$

The wire of the coil has a conductivity of 6×10^7 S/m, and the cross-sectional diameter of the coil wire is 1 mm. The coil L_S has a turn number of 30, while coils L_i, L_j and L_R have turn numbers of 10. The radius of coils L_S, L_i and L_j are 10 cm, and the radius of coil L_R is 5 cm.

The mutual inductance M_{SR} varies with the frequency f ($f=\omega/2\pi$) and can be obtained using the above parameters, as shown in Fig. 5. When $f=70$ kHz, the mutual inductance is maximum. As φ increases, M_{SR} decreases.

Fig. 6. Curves of M_{SR} varied with f at different d_{Si}.
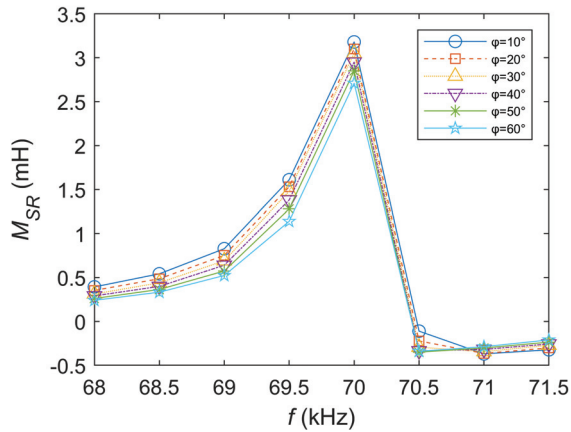
Fig. 5. Curves of M_{SR} varied with f at different φ.

For WPT systems, the maximum power can be realized only at specific angles and distances [22]. Figure 6 illustrates the variation of M_{SR} with respect to f at different d_{Si} when $d_{SR}=8$ cm. Similarly, when $f=70$ kHz, the mutual inductance reaches its maximum. It is noteworthy that the maximum value of mutual inductance is obtained at $d_{Si}=5$ cm.

All auxiliary coils are connected in series with corresponding resonant capacitors C_{in} or C_{jn}, and work reso-

nantly with the system operating frequency. Based on the equivalent circuit model, it is easy to deduce the voltage KVL equations of the system with the operating angular frequency ω:
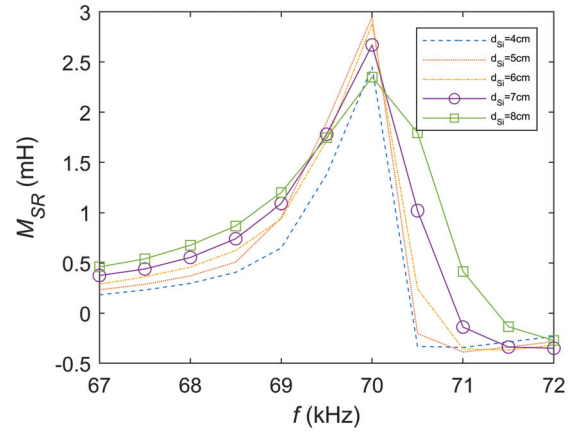
$$\begin{bmatrix} \dot{I}_S \\ \dot{I}_{i1} \\ \vdots \\ \dot{I}_{j1} \\ \vdots \\ \dot{I}_R \end{bmatrix} \begin{bmatrix} Z_S & j\omega M_{Si1} & \dots & j\omega M_{Sj1} & \dots & j\omega M_{SR} \\ j\omega M_{Si1} & Z_{i1} & \dots & j\omega M_{i1j1} & \dots & j\omega M_{Ri1} \\ \dots & j\omega M_{i1i2} & \dots & \dots & \dots & \dots \\ j\omega M_{Sj1} & \dots & \dots & Z_{j1} & \dots & j\omega M_{Rj1} \\ \dots & j\omega M_{i1j1} & \dots & j\omega M_{i1j2} & \dots & \dots \\ \dots & \dots & \dots & \dots & \dots & \dots \\ j\omega M_{SR} & j\omega M_{Ri1} & \dots & j\omega M_{Rj1} & \dots & Z_R \end{bmatrix}$$

$$= \begin{bmatrix} \dot{U}_{AC} \\ 0 \\ \dots \\ \dots \\ \dots \\ 0 \end{bmatrix}. \tag{12}$$

$\dot{I}_S$, $\dot{I}_{in}$, $\dot{I}_{jn}$ and $\dot{I}_R$ represent the currents in the sending circuit, codirectional coil circuit, variable direction coil circuit and receiving circuit, respectively. The total impedance for each circuit is shown in Table 1.

Table 1: Equivalent total impedance of the circuit

Circuit	Total Circuit Impedance
Sending circuit	$Z_S = R_{AC} + \frac{1}{j\omega C_S} + j\omega L_S$
Codirectional coil circuit	$Z_{in} = \frac{1}{j\omega C_{in}} + j\omega L_{in}$
Variable direction coil circuit	$Z_{jn} = \frac{1}{j\omega C_{jn}} + j\omega L_{jn}$
Receiving circuit	$Z_R = R_L + \frac{1}{j\omega C_R} + j\omega L_R$

Furthermore, the current $\dot{I}_R$ in the receiving circuit at various angles of φ and distances d_{Si} can be calculated, which is illustrated in Figs. 7 and 8. Similar to the analysis of mutual inductance, the current reaches its maximum when $f=70$ kHz, and its magnitude decreases with increasing φ.
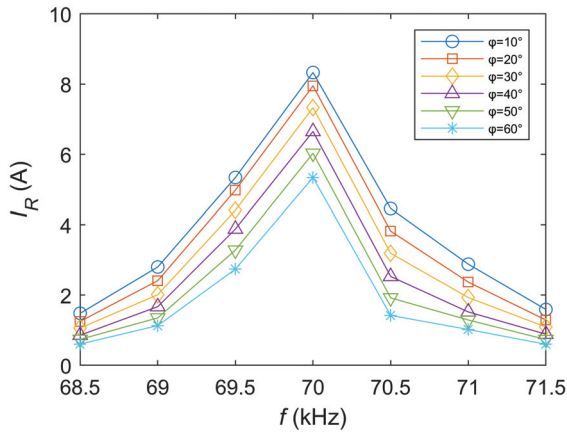
Fig. 7. Curves of $\dot{I}_R$ varied with f at different φ.

As shown in Fig. 8, the current reaches its maximum when $d_{Si}=5$ cm at a frequency of 70 kHz. The magnitude of the current is directly proportional to the power.

Through mutual inductance calculations, the impact of auxiliary coils on transfer characteristics at different positions and angles was analyzed. The combination of the equivalent circuit method and the Neumann formula provides us with an effective analytical tool, offering essential insights for system design and optimization. Therefore, the addition of auxiliary coils can enhance the magnetic field near the receiving coil from within the geometric structure of the system, thereby improving transfer power.
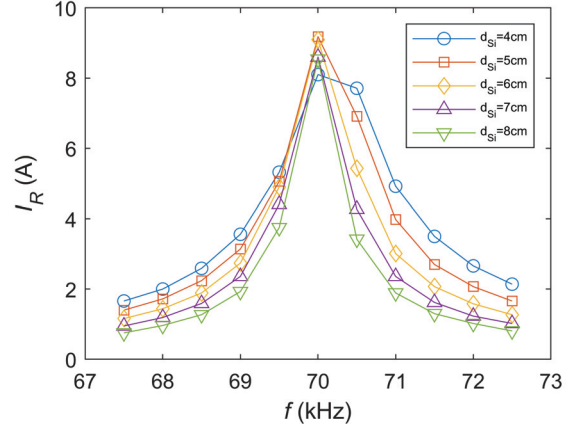
Fig. 8. Curves of $\dot{I}_R$ varied with f at different d_{Si}.

Due to the proposed system having multiple coils and the existence of angular misalignment, there is a lack of explicit formulas to calculate the power. According to equations (1) and (2), mutual inductance and current are key parameters that affect the power transfer. Therefore, feasibility needs to be validated through simulations and experiments.

III. SIMULATION ANALYSIS

A. Design method

After determining the basic structure of the system, it is necessary to further determine the specific positions of the two auxiliary coils. To achieve the maximum received power, the goal can be accomplished through the following steps. The specific process is illustrated in Fig. 9.

The first step involves determining the positions of the sending coil and the receiving coil. The angle between the sending coil and the receiving coil is application-specific, set at $45°$ in this paper.

In the second step, vary the position of the codirectional auxiliary coil, measure the power received by the receiving coil, and record the maximum power point along with its corresponding position. Moving on to third step, fix the codirectional auxiliary coil at the identified maximum power point.

In the fourth step, determine the rotation center (blue dot) and axis of the variable direction auxiliary coil. The center position of d_{Ri} on the yz plane is the midpoint, i.e., $d_{Rj}=d_{ij}$. The rotation axis passes through the rotation center and is parallel to the x-axis.

For the fifth step, rotate the variable direction auxiliary coil around the rotation axis towards the direction of the receiving coil, recording the maximum power point and its corresponding position.

Finally, the sixth step involves fixing the variable direction auxiliary coil at the maximum power point.
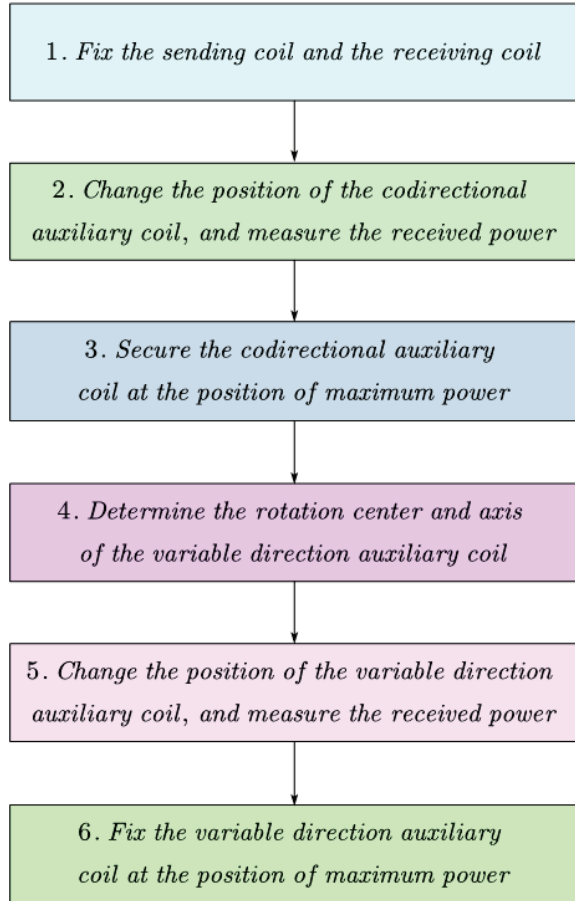
1. *Fix the sending coil and the receiving coil*

2. *Change the position of the codirectional auxiliary coil, and measure the received power*

3. *Secure the codirectional auxiliary coil at the position of maximum power*

4. *Determine the rotation center and axis of the variable direction auxiliary coil*

5. *Change the position of the variable direction auxiliary coil, and measure the received power*

6. *Fix the variable direction auxiliary coil at the position of maximum power*

Fig. 9. Variable direction transfer design process.

B. Electromagnetic field simulation

Here we match capacitors according to the coil inductance to construct a resonant circuit. The coil parameters are shown in Table 2.

Table 2: Coil parameters

Coils	Inductance	Series Capacitor	Resistance
Sending coil L_S	170 μH	30 nF	0.422 Ω
Codirectional auxiliary coil L_i	18 μH	30 nF	0.236 Ω
Variable direction auxiliary coil L_j	18 μH	30 nF	0.236 Ω
Receiving coil L_R	170 nH	30 μF	0.15 Ω

The number of turns, radius and other parameters of each coil are consistent with those mentioned earlier.

With a distance d_{SR} of 8 cm between the sending coil and the receiving coil, the position of the codirectional

auxiliary coil is altered to measure the system's transfer power at different locations. The measurement results are shown in Fig. 10.
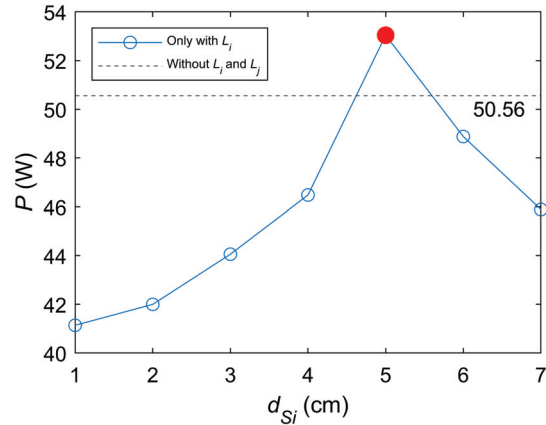
Fig. 10. The received power with codirectional auxiliary coil.

It can be seen that when d_{Si}=5 cm, the transfer power is highest, so the codirectional auxiliary coil is placed in this position. After the addition of the codirectional auxiliary coil, a frequency splitting phenomenon occurred, that is, when the distance between the codirectional auxiliary coil and the sending coil is too close, the power is lower than that without the addition of auxiliary coil [23].

After determining the position of the codirectional auxiliary coil, we studied the impact of the variable direction auxiliary coil. We rotated the axis parallel to the *x*-axis in the direction away from the sending coil, and measured the transfer power at different angles. The results are shown in Fig. 11.
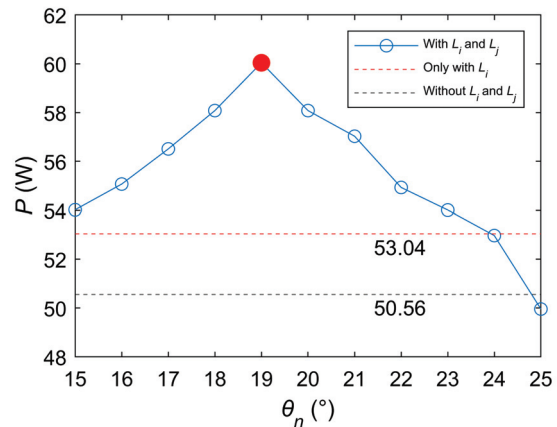
Fig. 11. The received power with two auxiliary coils.
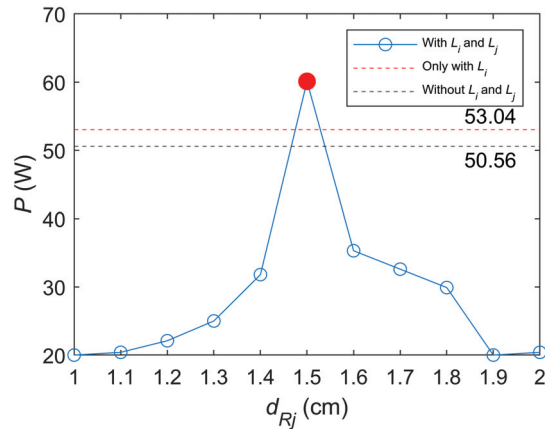
Fig. 12. The received power with two auxiliary coils when $\theta_n = 19°$.

When the angle between the variable direction auxiliary coil and the xy plane is 19°, the power is maximum and higher than when only the codirectional auxiliary coil is added. Therefore, the proposed design method can effectively improve transfer power and achieve variable direction transfer.

When θ_n is 19°, we varied d_{Rj} and measured the transfer power, as shown in Fig. 12. According to the proposed design method, the rotational center of the variable direction auxiliary coil is located at the center position of d_{Ri}, i.e., $d_{Rj} = d_{ij} = 1.5$ cm. Due to the precise requirements of coil positioning in WPT [22] and the existence of frequency splitting phenomena [23], the power rapidly decreases when the variable direction auxiliary coil is located at other positions.

The magnetic flux distribution of the system is shown in Fig. 13. The magnetic flux generated by the sending coil is guided towards the direction of the receiving coil through the auxiliary coils L_i and L_j, effectively improving the transfer power.
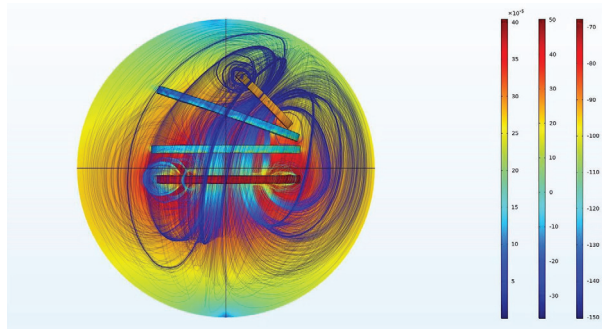
Fig. 13. Magnetic flux distribution.

IV. EXPERIMENTAL MEASUREMENTS AND RESULTS

Analysis from computational electromagnetics provided a basis for studying the placement of auxiliary coils. Validation of the analysis results will be conducted through experiment.
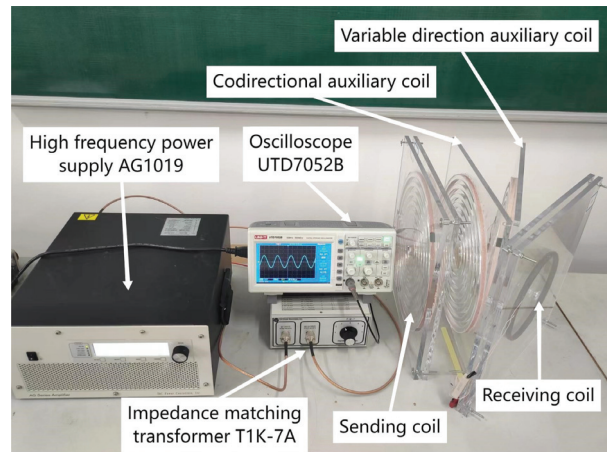
Fig. 14. Experimental prototype.

Figure 14 illustrates the experimental prototype for the variable direction WPT system. Power supply AG1019 is adopted to produce an HF voltage signal with a frequency of 70 kHz. The impedance matching transformer T1K-7A is employed to mitigate the influence of reflected power from the system on AG1019. The parameters of each coil are consistent with those used in the simulation. The experimental prototype adopts an SS topology with a load resistance of 5 Ω.

After fixing the sending and receiving coils, the distance between the codirectional auxiliary coil and the sending coil is varied, and the transfer power is measured at different positions. The results are depicted in Fig. 15.

The power peaks when the distance between the codirectional auxiliary coil and the sending coil is 5 cm. Due to the manual winding of the coil, a slight error in the design size leads to slightly lower experimental power than the simulated power. Specific values measured during the experiment are detailed in Table 3.

To further enhance received power, a variable direction auxiliary coil is added to the system. Following the method described earlier, the codirectional auxiliary coil is fixed at $d_{Si} = 5$ cm. The angle of the variable direction auxiliary coil is adjusted, and received power is measured at different positions, as illustrated in Fig. 16.

At $\theta_n = 19°$, the maximum received power is 58.07 W. Compared with the situation without the addition of the codirectional auxiliary coil, the received power has
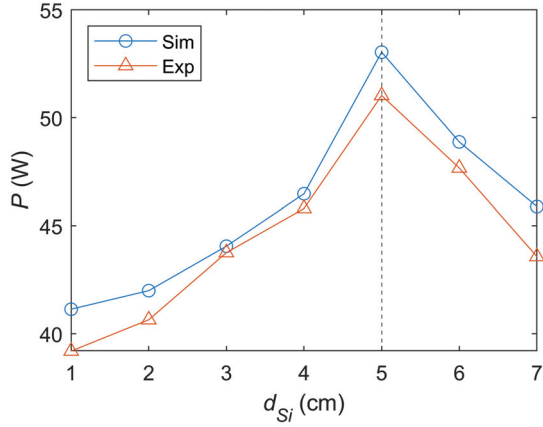
Fig. 15. The experiment results of received power with codirectional auxiliary coil.

Table 3: The experiment results of received power with codirectional auxiliary coil

d_{Si}	d_{Ri}	Received Power
1 cm	7 cm	39.2 W
2 cm	6 cm	40.65 W
3 cm	5 cm	43.76 W
4 cm	4 cm	45.8 W
5 cm	3 cm	51.03 W
6 cm	2 cm	47.67 W
7 cm	1 cm	43.58 W
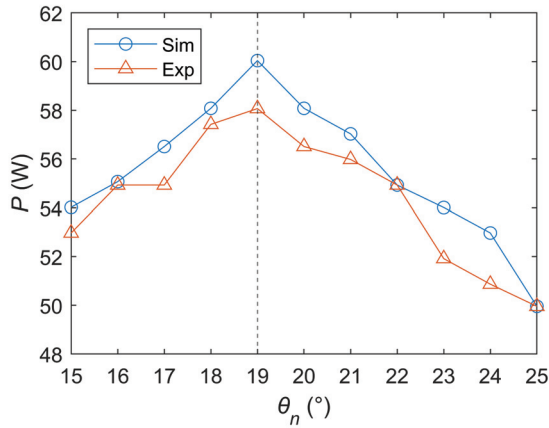
Fig. 16. The experiment results of received power with two auxiliary coils.

increased by 7.04 W. In comparison with the original two-coil system, the received power has increased by 14.92%.

When $\theta_n=19°$, the transfer power is measured by varying the distance between the variable direction auxiliary coil and the receiving coil, as shown in Fig. 17.

The power rapidly decreases when the variable direction auxiliary coil is located at other positions.
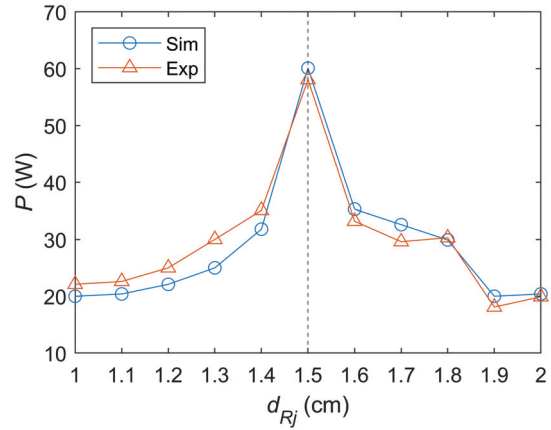
Fig. 17. The experiment results of received power with two auxiliary coils when $\theta_n=19°$.

When L_i and L_j are not placed according to the proposed design method, even when operating at the resonant frequency, the power is lower. As shown in Fig. 18, at different distances, the power is consistently below 35 W.
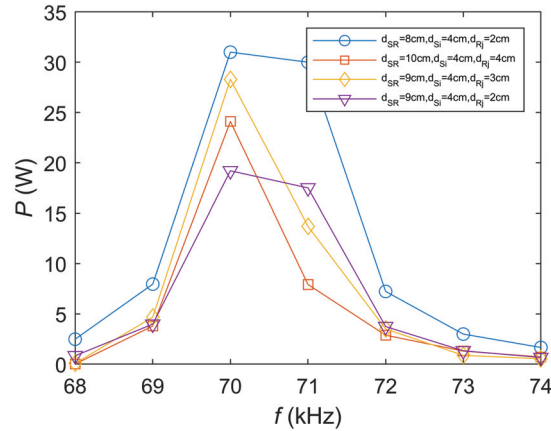
Fig. 18. Transfer power of coils at different positions.

The above experiment demonstrates that auxiliary coils can effectively enhance the received power of the system. The variable direction transfer method proposed in this paper proves effective in improving received power at specific positions. Consistency between the computational electromagnetics analysis and experimental results validated the feasibility of our design method.

V. CONCLUSION

In application scenarios, when the sending and receiving coils deviate from being parallel, the

performance of the WPT system deteriorates significantly. In traditional two-coil WPT systems, the received power experiences a considerable reduction when the receiving coil is rotated. Addressing this issue, this paper introduces a method for a variable direction WPT system based on two auxiliary coils.

Due to the lack of explicit formulas for calculating power in complex WPT systems, the mutual inductance and current related to transfer characteristics were analyzed. To validate the rationality of the design method, the magnetic flux distribution of the system was studied through simulations. Finally, the analysis results were verified through experiments, confirming the feasibility of the proposed approach.

Moreover, when altering the angle between the sending and receiving coils, the proposed variable direction transfer method also contributes to improved received power. Nonetheless, the transfer efficiency remains suboptimal, prompting further investigation into optimizing the coil structure and control modes as our next step. In other scenarios, adopting more coils and using intelligent algorithms to calculate parameters are also our future work.

ACKNOWLEDGMENT

REFERENCES

[1] B. Sami and T. Mauro, "Theoretical study of different access points in coupled wireless power transfer - powerline communication systems," *Appl. Comput. Electromagn. Soc. J.*, vol. 33, no. 10, pp. 1112-1116, 2018.

[2] X. Huang, Y. Dou, S. Lin, Y. Tian, and M. Andersen, "Synchronous push-pull class E rectifiers with load-independent operation for megahertz wireless power transfer," *IEEE Trans. Power Electron.*, vol. 36, no. 6, pp. 6351-6363, 2020.

[3] D. Kim, A. T. Sutinjo, and A. Abu-Siada, "Near-field analysis and design of inductively-coupled wireless power transfer system in FEKO," *Appl. Comput. Electromagn. Soc. J.*, vol. 35, no. 1, pp. 82-93, 2020.

[4] S. Li and C. Mi, "Wireless power transfer for electric vehicle applications," *IEEE J. Em. Sel. Top. P.*, vol. 3, no. 1, pp. 4-17, 2015.

[5] Y. Gao, C. Duan, A. A. Oliveira, A. Ginart, K. B. Farley, and T. Zion, "Three-dimensional coil positioning based on magnetic sensing for wireless EV charging," *IEEE Trans. Transp. Electrification*, vol. 3, no. 3, pp. 578-588, 2017.

[6] X. Wu, P. Sun, S. Yang, L. He, and J. Cai, "Review on underwater wireless power transfer technology and its application," *Trans. China Electrotech. Soc.*, vol. 34, no. 8, pp. 1559-1568, 2019.

[7] R. Sasaki, K. Koizumi, and S. Kiryu, "Wireless power transmission with a sown auxiliary coil to improve power efficiency for an implantable device," *Int. J. Appl. Electron.*, vol. 64, no. 1-4, pp. 843-851, 2020.

[8] D. H. Sadek, H. A. Shawkey, and A. A. Zekry, "Multiband triple L-Arms patch antenna with diamond slot ground for 5G applications," *Appl. Comput. Electromagn. Soc. J.*, vol. 36, no. 3, pp. 302-307, 2021.

[9] H. Sun, S. Hou, Y. Zhao, W. Yan, and Y. Wu, "Investigation of electromagnetic exposure of WPT coil to human body based on biological electromagnetic safety assessment," *Appl. Comput. Electromagn. Soc. J.*, vol. 36, no. 10, pp. 1355-1366, 2021.

[10] H. Zhang, Z. Zhong, and W. Wu, "Adaptive compensation loop control method for dynamic range wireless power transfer in endoscopic capsules applications," *Appl. Comput. Electromagn. Soc. J.*, vol. 33, no. 5, pp. 499-504, 2018.

[11] A. Kurs, A. Karalis, R. Moffatt, J. D. Joannopoulos, P. Fisher, and M. Soljacic, "Wireless power transfer via strongly coupled magnetic resonances," *Science*, vol. 317, no. 5834, pp. 83-86, 2007.

[12] Y. Guo, L. Wang, and C. Liao, "A general equivalent model for multi-coil wireless power transfer system analysis and its application on compensation network design," *Appl. Comput. Electromagn. Soc. J.*, vol. 33, no. 6, pp. 648-656, 2018.

[13] A. K. Ranaweera, C. A. Moscoso, and J. W. Lee, "Anisotropic metamaterial for efficiency enhancement of mid-range wireless power transfer under coil misalignment," *J. Phys. D.*, vol. 48, no. 45, Art no. 455104, 2015.

[14] S. Wang, C. Jiang, X. Tao, F. Chen, C. Rong, C. Lu, Y. Zeng, X. Liu, R. Liu, and B. Wei, "Enhancing the stability of medium range and misalignment wireless power transfer system by negative magnetic metamaterials," *Materials*, vol. 13, no. 24, Art no. 5695, 2020.

[15] P. Yadav and M. Veerachary, "Auxiliary coil based square coupler for wireless power transfer system," *IEEE Trans. Ind. Appl.*, vol. 58, no. 4, pp. 4980-4993, 2022.

[16] X. Wang, C. Yu, Y. Wu, and J. Wang, "Structure design of quadrilateral overlapped wireless power transmission coupling coil," *Sensors*, vol. 22, no. 16, Art no. 5955, 2022.

[17] J. H. Cho, S. H. Jung, and Y. J. Kim, "Wireless power transfer for variable load, distance, and power division ratio in a loosely-coupled

multiple-receiver relay system," *IEEE Trans. Ind. Appl.*, vol. 70, no. 7, pp. 6809-6818, 2023.

[18] W. Tang, Q. Zhu, J. Yang, D. Song, and R. Zou, "Simultaneous 3-D wireless power transfer to multiple moving devices with different power demands," *IEEE Trans. Power Electron.*, vol. 35, no. 5, pp. 4533-4546, 2019.

[19] C. Liu, K. T. Chau, C. Qiu, and F. Lin, "Investigation of energy harvesting for magnetic sensor arrays on Mars by wireless power transmission," *J. Appl. Phys.*, vol. 115, no. 17, Art no. 17E702, 2014.

[20] A. Ali, N. Yasin, A. Rambe, I. Adam, N. Ramli, H. Rahim, T. Sabapathy, M. Norizan, and S. Sobri, "Analysis of symmetric two and four-coil magnetic resonant coupling wireless power transfer," *Appl. Comput. Electromagn. Soc. J.*, vol. 37, no. 4, pp. 497-506, 2022.

[21] S. Liu, Y. Feng, W. Weng, J. Chen, J. Wu, and X. He, "Contactless measurement of current and mutual inductance in wireless power transfer system based on sandwich structure," *IEEE Trans. Emerg.*, vol. 10, no. 5, pp. 6345-6357, 2022.

[22] X. Zhang, C. Xue, and J. Lin, "Distance-insensitive wireless power transfer using mixed electric and magnetic coupling for frequency splitting suppression," *IEEE Trans. Microw. Theory Tech.*, vol. 65, no. 11, pp. 4307-4313, 2017.

[23] Z. Liao, S. Ma, Q. Feng, C. Xia, and D. Yu, "Frequency splitting elimination and utilization in magnetic coupling wireless power transfer systems," *IEEE Trans. Circuits Syst. I Regul. Pap.*, vol. 68, no. 2, pp. 929-939, 2021.

Feihang Xiao received the B.S. degree in electrical engineering and automation from Changzhou University, China, in 2022. He is currently pursuing the M.S. degree with the School of Mechanical Engineering and Rail Transit, Changzhou University, China. His research interests include wireless power transfer and metamaterials.

Hao Qiang received the B.S. and M.S. degrees in electrical engineering from the Nanjing University of Science and Technology, Nanjing, China, in 2000 and 2004, respectively, and the Ph.D. degree in electrical engineering from Southeast University, China, in 2015. He was the Deputy Director of the Department of Electrical Engineering and Automation. Since 2007, he has been engaged in the teaching of electrical engineering and automation. His research interests include wireless power transfer, metamaterials, image processing, and vehicles to grid.

Design of Wideband 8×8 Butler Matrix using Composite Right/Left-handed Transmission Line for Multi-mode OAM Generation

Yan Zhang[1,2], Haoran Ye[1], Jialin Zhang[1], Xurui Zhang[1], and Shanwei Lü[1]

[1]School of Electronic Information Engineering
Beihang University, Beijing, China
yanzhang@buaa.edu.cn, yehaoran@buaa.edu.cn, sy1902127@163.com,
zy2202328@buaa.edu.cn, lueshw@buaa.edu.cn

[2]Shenzhen Institute of Beihang University
Shenzhen, China

Abstract – In this paper, a wideband Butler matrix for the uniform circular array antenna (UCA) generating multi-mode orbital angular momentum (OAM) vortex wave is designed. Firstly, the novel network topology of a Butler matrix is proposed. For the purpose of design and optimization convenience, the 8×8 Butler matrix is separated into two different sub 4×4 Butler matrix modules and one connection-output module. Then several wideband microwave components used in a Butler matrix, such as 3 dB directional coupler and stable phase shifter with composite right/left-handed (CRLH) transmission line, are designed. To demonstrate the effectiveness of the design process, a Butler matrix working in 5-7 GHz is designed and fabricated. It is found that the simulation results are in good agreement with the measured data. The constant amplitude distribution and progressive phase differences of $\pm 45°$, $\pm 90°$ between the output ports are observed, hence the ± 1, ± 2 mode OAM waves can be generated by the proposed Butler matrix.

Index Terms – Butler matrix, CRLH transmission line, multi-mode OAM, wideband.

I. INTRODUCTION

Expected in the 2030s, 6-generation (6G) communication planning has begun. Compared with 5G, higher capacity, higher data rates, and lower latency are required by the 6G communication system. A possible way to increase data rate of wireless communication is to use orbital angular momentum (OAM) vortex waves instead of traditional plane waves [1–4]. This spatial reuse of different OAM modes could improve greatly the channel capacity [5–7].

Compared with other methods of generating OAM waves [8–12], uniform circular array antenna (UCA) support the generation of a variety of OAM modes [13–15], and its feed status can be adjusted to generate OAM of various modes flexibly. UCA can be fed by beamform-

ing network (BFN) which have economical and efficient advantages to generate OAM waves with connection to the UCA element. BFNs such as a Butler matrix [16–17] are usually composed of coupler, crossover, and phase shifter. In order to obtain a high quality OAM wave, the design of the microwave components of a Butler matrix is import and difficult to realize in wideband.

With a conventional Butler matrix with one layer transmission line it is difficult to realize a stable phase shift for wideband application [18]. In order to realize wideband performance, a multi-layer coupling structure is discussed [19, 20]. For the design of the phase shifter, a composite right/left-handed (CRLH) transmission line [21, 22] is applied to the phase shifter to obtain larger phase shift values with necessary compact structure. To simplify the topology of a Butler matrix, fewer phase shifters are desired for generating necessary OAM modes. A simplified Butler matrix topology is necessary but relevant research is rare.

In this paper, a wideband 8×8 Butler matrix for generating $\pm 1/\pm 2$ modes OAM waves is designed. For some key microwave components, 3 dB directional couplers and phase shifters with the phase value of $-45°$, $0°$, and $90°$ are designed by wideband structure with the CRLH transmission line in order to realize stable phase shift.

II. TOPOLOGY OF A BUTLER MATRIX

For OAM application, the UCA element is fed by BFN with equal amplitude and progressive phase difference [23]. In order to generate an OAM beam of $\pm 1/\pm 2$ mode by feeding eight-element antenna array, an equal amplitude distribution with phase differences of $\pm 45°$ and $\pm 90°$ are required.

Firstly, the sub Butler matrix module 1 and 2 is proposed to realize consistent phase difference between the four output ports. Then, the sub Butler matrix modules are connected by connection-output modules to obtain consistent phase difference of eight outputs. The sub

Butler matrix module 1 based on $0°/-45°$ phase shifter and sub Butler matrix module 2 based on $90°$ phase shifter are designed, as shown in Fig. 1.
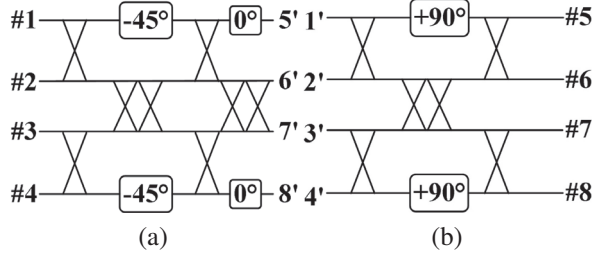

Fig. 1. Topology of sub Butler matrix module: (a) sub Butler matrix module 1 and (b) sub Butler matrix module 2.

As shown in Fig. 1, port #1-8 on the left side are input ports and port #1'-8' on the right side are output ports. The sub Butler matrix modules 1 and 2 can realize equal phase differences output of $-45°$, $45°$, $90°$, and $-90°$ by the excitation of port 1, 4, 5, and 8, respectively. The connection-output module is shown in Fig. 2.
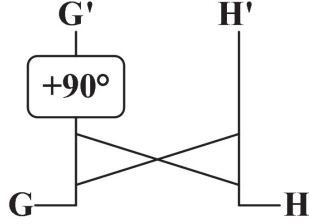
Fig. 2. Connection-output module.

As shown in Fig. 2, four outputs of a sub Butler matrix module are connected to the input of a connection-output module in sequence to obtain eight outputs which have $180°$ phase difference between those two outputs, ports G' and H'. The entire $8×8$ Butler matrix network is shown in Fig. 3.
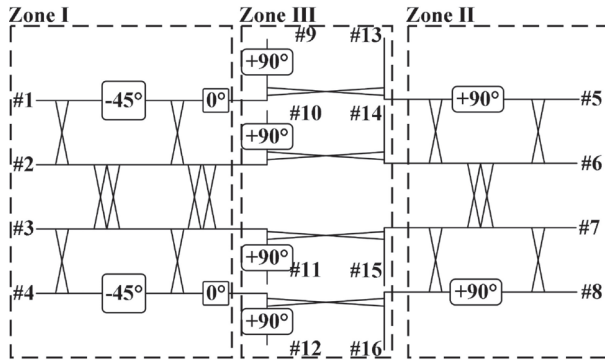
Fig. 3. Topology of an $8×8$ Butler matrix.

As shown in Fig. 3, the input ports are located on the outside and the transmission lines of the output ports do not overlap with each other. In this design, only $0°/-45°/90°$ phase shifters are needed, so the design complexity of the wideband phase shifter is reduced. For sub module 1 (Fig. 3 zone I), the $-45°$ phase shifter and cross coupler are used to realize $-45°$, $45°$ output phase differences by excitation of ports 1 and 4, respectively. For sub module 2 (Fig. 3 zone II), the $90°$ phase shifter and cross coupler are used to realize $90°$, $-90°$ output phase differences by excitation of ports 5 and 8, respectively. In order to generate $+1$ mode OAM, the excitation of port 4 could realize $45°$ phase difference distributions of $-90°$, $-45°$, $0°$ and $45°$. The phase distributions of $-90°$, $-45°$, $-0°$, $45°$, $90°$, $135°$, $180°$, and $225°$ can be generated by the connection-output module (Fig. 1 zone III) because of the $180°$ phase difference between the two output ports of the connection-output module. The phase distribution of -1 mode OAM can be realized by the excitation of port 1, and the excitation of ports 5 and 8 can realize the phase distribution of -2 mode and $+2$ mode, respectively.

The detailed phase distribution of the Butler matrix is listed in the Table 1 for ±1, ±2 mode with phase difference of $-45°$, $+45°$, $-90°$, and $+90°$. The phase of each input port is zero, which satisfies the condition of unequal phase differences with different excitations of input ports. Compared with the conventional $8×8$ Butler matrix exciting eight OAM modes, the proposed Butler matrix could provide the necessary modes with fewer phase shifters.

Table 1: Phase distribution of $8×8$ Butler matrix

Mode		-1	1	2	-2
Input Port		1	4	5	8
Output Port	P9	45	-90	90	-180
	P10	0	-45	0	-90
	P11	-45	0	-90	0
	P12	-90	45	-180	90
	P13	-135	90	-270	180
	P14	-180	135	0	270
	P15	-225	180	-90	0
	P16	-270	225	-180	90

III. DESIGN OF WIDEBAND COMPONENT

The performance of each component using an $8×8$ Butler matrix would affect the wideband stability of the whole network significantly. So, the accurate design and balance optimization of 3 dB directional coupler and $-45°/0°/90°$ phase shifter are necessary. Firstly, a wideband 3 dB coupler is designed. Then, a $-45°$ phase shifter is obtained by adding a rectangular patch into the 3 dB coupler structure. Also, a transverse slot line is

introduced into the rectangular patch to realize a $0°$ phase shifter. Finally, two $45°$ phase shifters based on CRLH transmission line are applied to the $0°$ phase shifter to realize a $90°$ phase shifter.

A. 3 dB directional coupler and $-45°/0°$ phase shifter

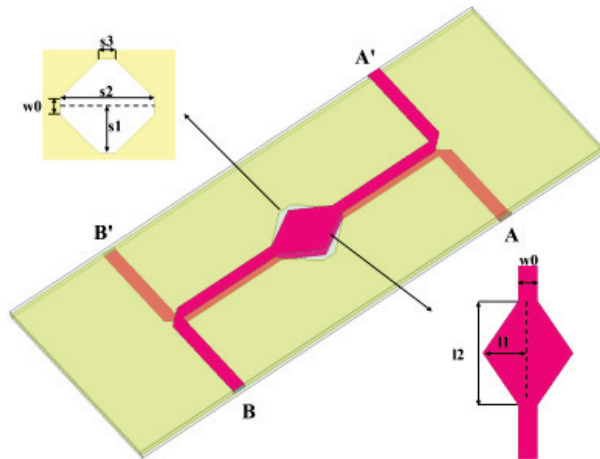The 3 dB directional coupler is designed, as shown in Fig. 4.

Fig. 4. 3 dB directional coupler (s1 = 4.78, s2 = 9.5, w0 = 1.61, s3 = 1.66, l1 = 3.8, l2 = 8.75 unit = mm).

As shown in Fig. 4, the 3 dB directional coupler consists of two pieces of substrate (h = 0.6 mm, ε_r=2.6). The top metal layer includes ports B and A'. The bottom metal layer is similar to the top layer, but the ports here are ports A and B'. The two coupling patches and the slot are given a diamond shape in order to avoid the discontinuity of the structure and reduce edge capacitance. The impedance of input and output ports is 50 Ω to connect with RF lines. The simulation results are shown in Fig. 5.

As shown in Fig. 5, the simulation results show that the amplitude balance is 3.25±0.15 dB and the phase balance is $90°±0.5°$ in the operating frequency
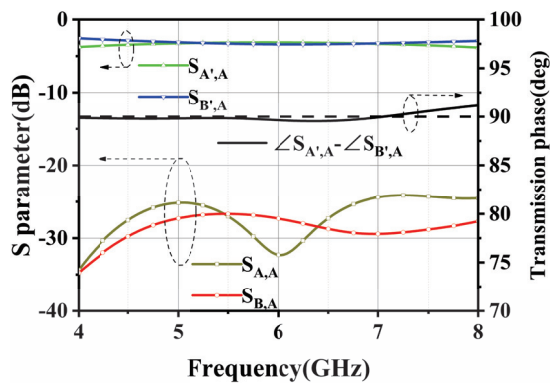
Fig. 5. Simulation results of 3 dB directional coupler.

range. The isolations of SA,A and SB,A are less than -24 dB which indicates that the coupling between the two input ports is low and has little effect with the situation of multi-ports excitation. The $-45°$ phase shifter is designed based on the structure of the 3 dB directional coupler. The structure of the $-45°$ phase shifter is shown in Fig. 6.
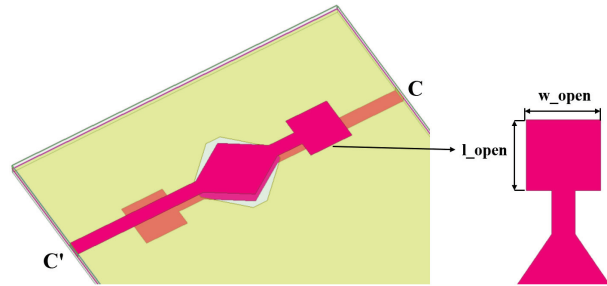
Fig. 6. $-45°$ phase shifter (l_open = 4.88, w_open = 5.1, unit = mm).

In order to obtain a wideband $-45°$ phase shifter, a rectangular patch is applied as an open-circuit structure. The effect of width and length of the rectangle patch on the phase shift is investigated. The simulation results are shown in Fig. 7.
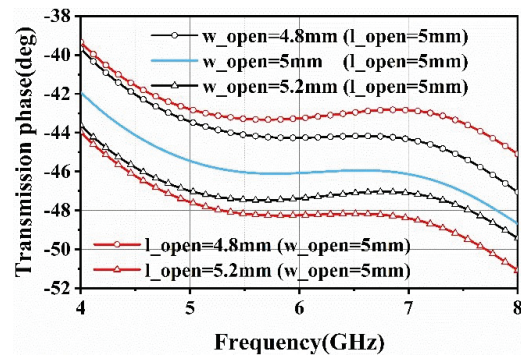
(a)
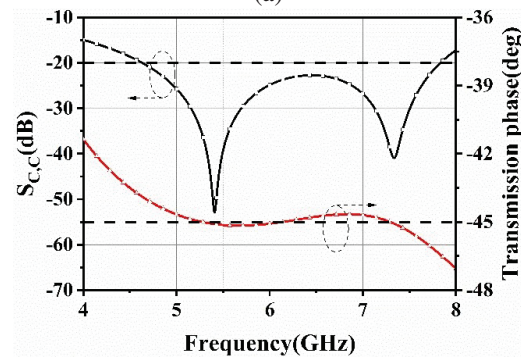
(b)

Fig. 7. Simulation results of $-45°$ phase shifter: (a) effect of w_open and l_open and (b) S parameter.

From Fig. 7, a stable phase shift of $-45\pm0.3°$ can be observed. The $0°$ phase shifter is designed based on the structure of the $-45°$ phase shifter, as shown in Fig. 8.
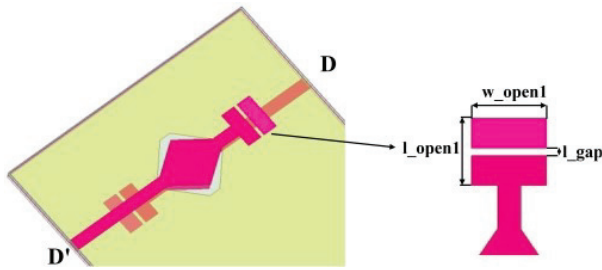
Fig. 8. $0°$ phase shifter (l_open1 = 4.64, w_open1 = 5.2, l_gap = 0.5, unit = mm).

Based on the $-45°$ phase shifter, a transverse slot line is introduced into the rectangle patch to realize the $0°$ phase shifter. The simulation results are shown in Fig. 9.
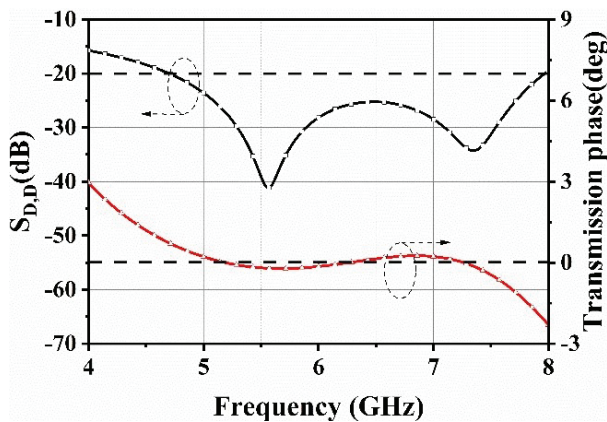
Fig. 9. Simulation results of $0°$ phase shifter.

It can be seen from Fig. 9 that the phase difference between port D and port D' is near to $0°$ and thus the $0°$ phase shifter is generated. The error of the $0°$ phase shifter is $\pm0.25°$ with the frequency range of 5-7 GHz.

B. 45/90° phase shifter

By cascading the $0°$ phase shifter to two $45°$ phase shifters with the CRLH transmission line, a $90°$ phase shifter could be realized. Firstly, the $45°$ phase shifter is designed, as shown in Fig. 10.

As shown in Fig. 10, the CRLH transmission composed of patch and microstrip line is simplified to the parallel inductors and series capacitors existing in the left-handed structure, so this shifter become miniaturized. The effect of the dimensions of CRLH transmission line structure on transmission parameter is investigated. The simulation results are shown in Fig. 11.

(a)

(b)
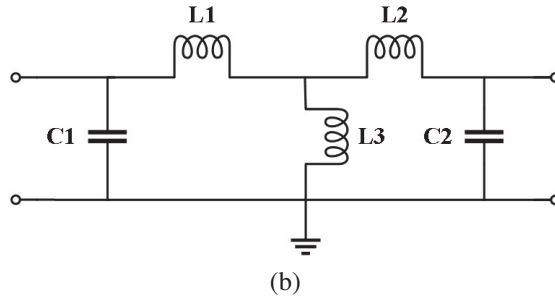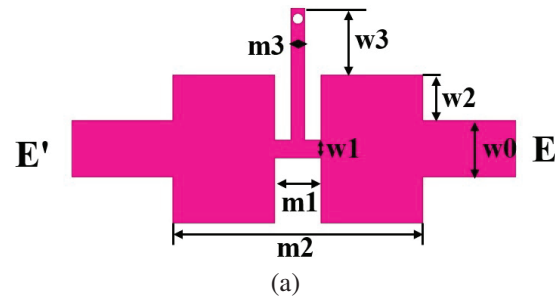
Fig. 10. $45°$ phase shifter (a) model and (b) equivalent circuit (m1 = 1.3, m2 = 7.1, m3 = 0.4, w0 = 1.61, w1 = 0.5, w2 = 1.3, w3 = 1.9, unit = mm).

(a)

(b)

Fig. 11. *Continued*.

(c)
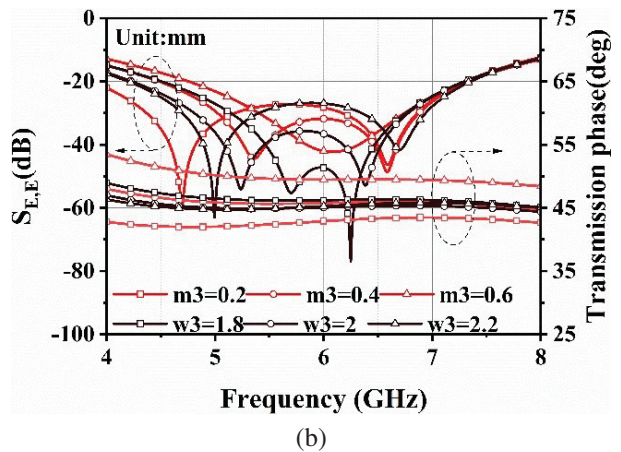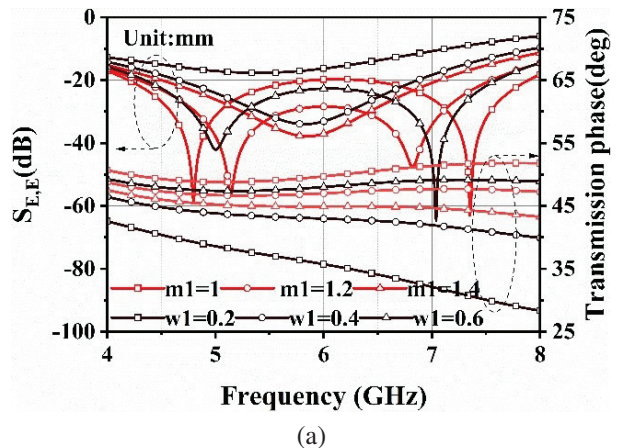
(d)
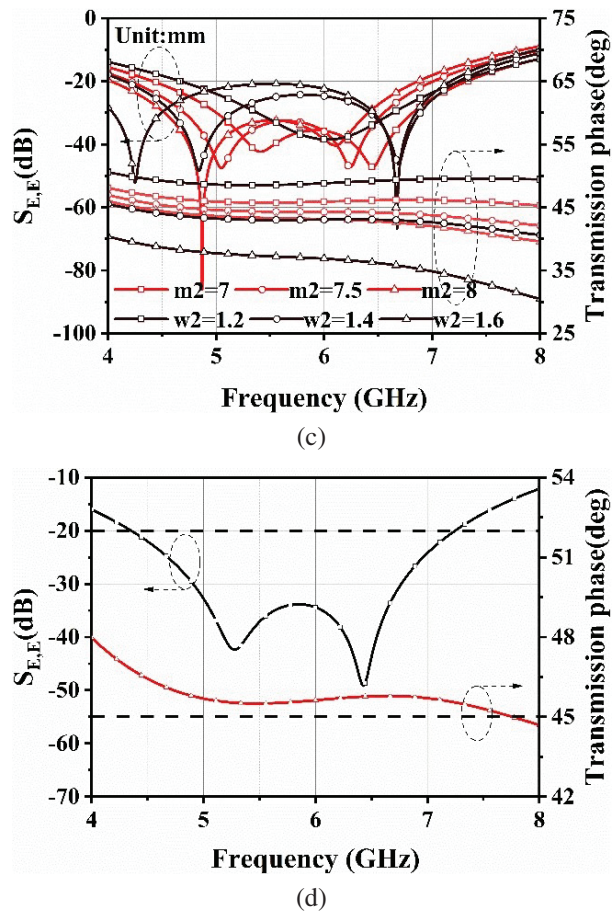
Fig. 11. Simulation results of 45° phase shifter: (a) effect of series inductance, (b) effect of parallel inductance, (c) effect of parallel capacitors, and (d) optimized simulation results.

The series inductance, parallel inductance, and parallel capacitors have effect on both low-frequency resonance points and high-frequency resonance points. Bandwidth can be changed by adjusting the structure parameters. The simulation results show that the phase imbalance does not exceed 0.8° at 5-7 GHz. Wideband stable phase shift characteristics can be observed. The 90° phase shifter is designed based on the 45° phase shifter as shown in Fig. 12.
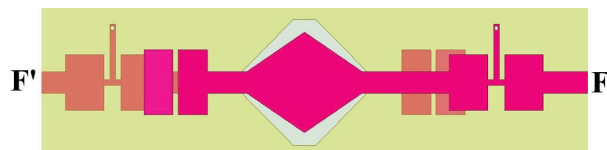
Fig. 12. 90° phase shifter.

On the basis of the 0° phase shifter, the CRLH transmission line is connected at the input port and output port

to obtain the 90° phase shifter structure. The simulation results are shown in Fig. 13.
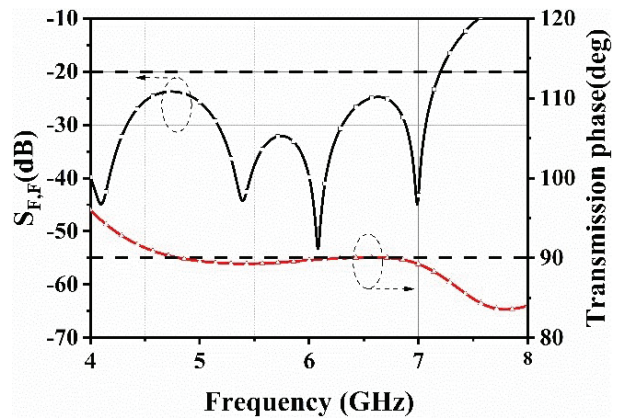
Fig. 13. Simulation results of 90° phase shifter.

As shown in Fig. 13, the simulation results indicate that the phase shift value is 89.6°±0.4°. Hence, large and stable phase shift values can be achieved in the wide band, compared with a conventional phase shifter.

In general, the 3 dB coupler and −45°/0°/90° phase shifter are designed in sequence. The imbalance of the amplitude and phase shift are quite small for this component.

IV. SUB BUTLER MATRIX AND CONNECTION-OUTPUT MODULE

Based on the wideband components, a sub Butler matrix module and connection-output module could be obtained. The sub Butler matrix module is shown in Fig. 14.
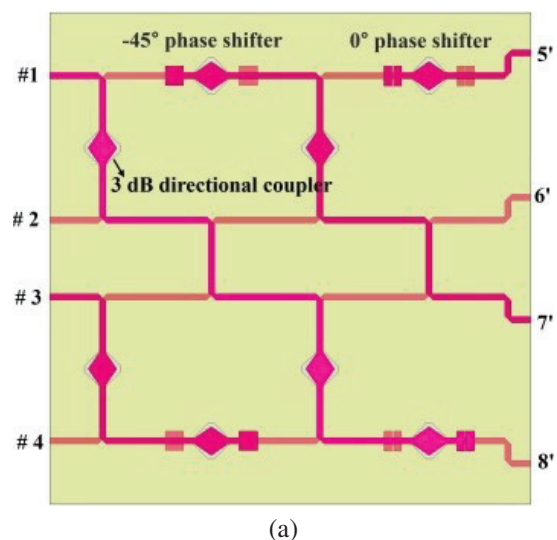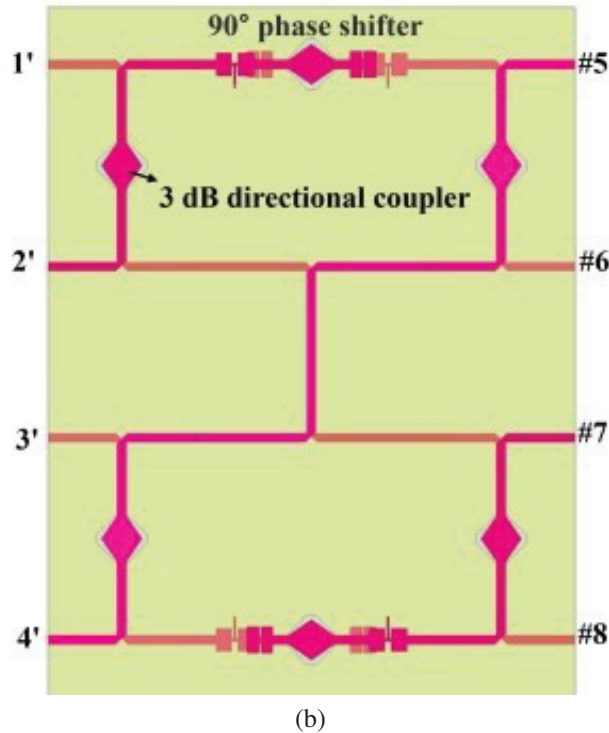

(a)

Fig. 14. *Continued*.

Fig. 14. Sub Butler matrix module: (a) sub module 1 and (b) sub module 2.

Using the phase shifter and 3 dB directional coupler designed above, the sub Butler matrix module is constructed by connecting these components with a microstrip line in Fig. 14 corresponding to zones I and II in Fig. 3. The simulation results are shown in Fig. 15.

It can be seen from Fig. 15 that the amplitude imbalance of the output of sub Butler matrix modules 1 and 2 do not exceed 0.8 dB and 1.0 dB, respectively. The $\pm 45°+1.6°$ and $\pm 90 \pm 1.5°$ phase differences can be
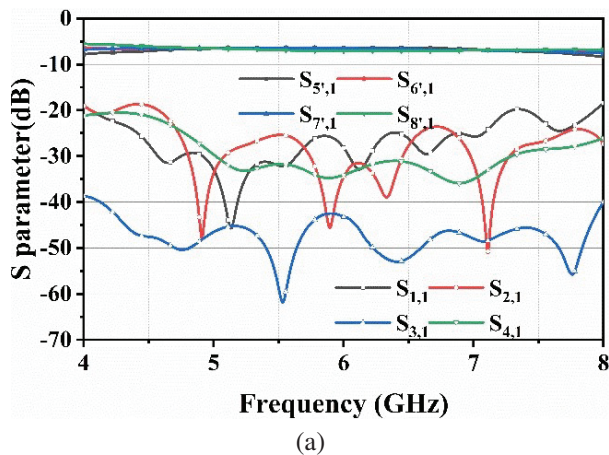
Fig. 15. *Continued*.
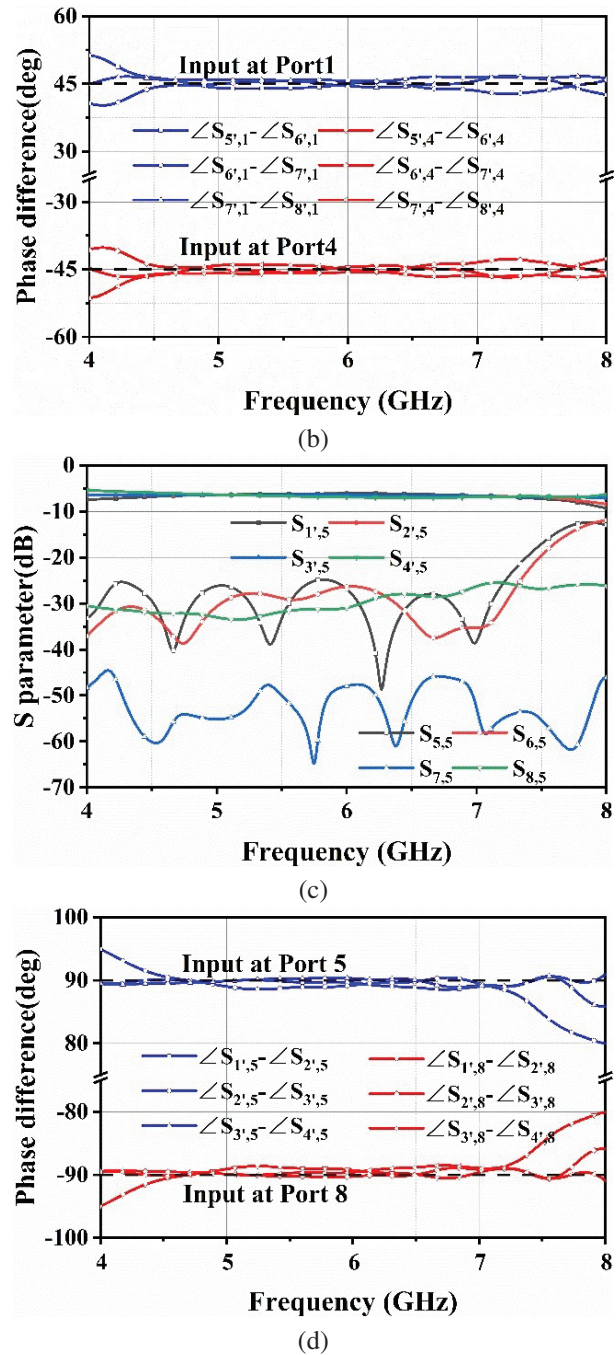
Fig. 15. Simulation results of a sub Butler matrix module: (a) $S_{x,1}$, (b) output phase of sub Butler matrix module 1, (c) $S_{x,5}$, and (d) output phase of sub Butler matrix module 2.

obtained by excitation ports 1, 4, 5, and 8. In order to combine two 4×4 sub Butler matrix modules and output ports, the connection-output module corresponding to zone III in Fig. 3 is designed. The connection-output module is shown in Fig. 16.
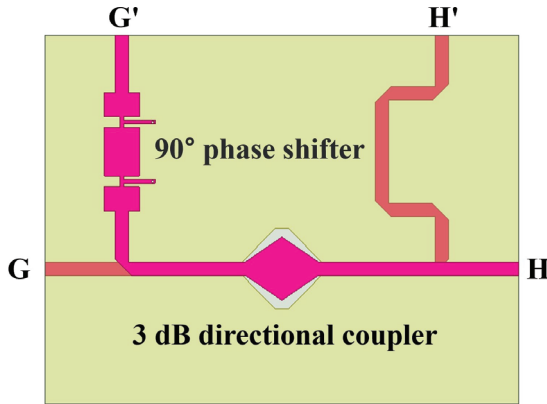
Fig. 16. Connection-output module composed of 90° phase shifter and 3 dB directional coupler.

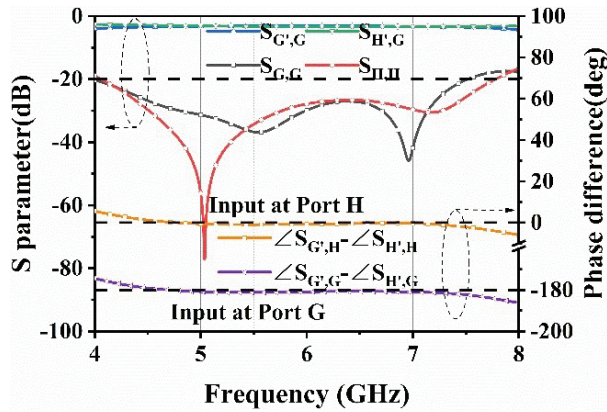The simulation results are shown in Fig. 17.

Fig. 17. Simulation results of connection-output module.

As shown in Fig. 17, the simulation results indicate the reflection coefficient and isolation are less than −25 dB at 5-7 GHz. The amplitude balance of the output ports is 3.2±0.3 dB. The 180±1.2° and 0±1.0° phase difference between ports G' and H' can be realized by the excitation of ports G and H, respectively.

V. RESULTS AND DISCUSSION

Based on the sub Butler matrix module and connection-output module, an 8×8 Butler matrix can be realized, as shown in Fig. 18.

Corresponding to the topology of Fig. 1, zone I and zone II are sub Butler matrix module 1 and module 2, respectively. These two sub Butler matrix modules are connected by the middle connection-output module, as shown in zone III. The phase distribution of ±1, ±2 OAM modes can be obtained from the 9-16 outputs by the excitation of ports 1, 4, 5, and 8, respectively. The simulation results are shown in Figs. 19 and 20.
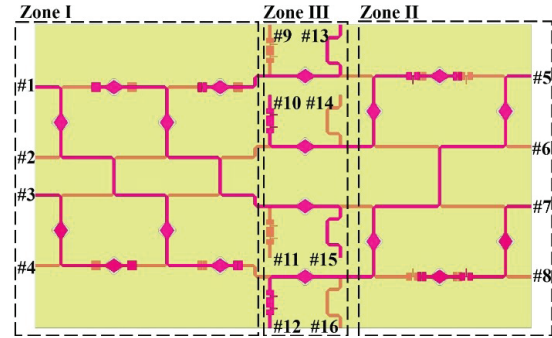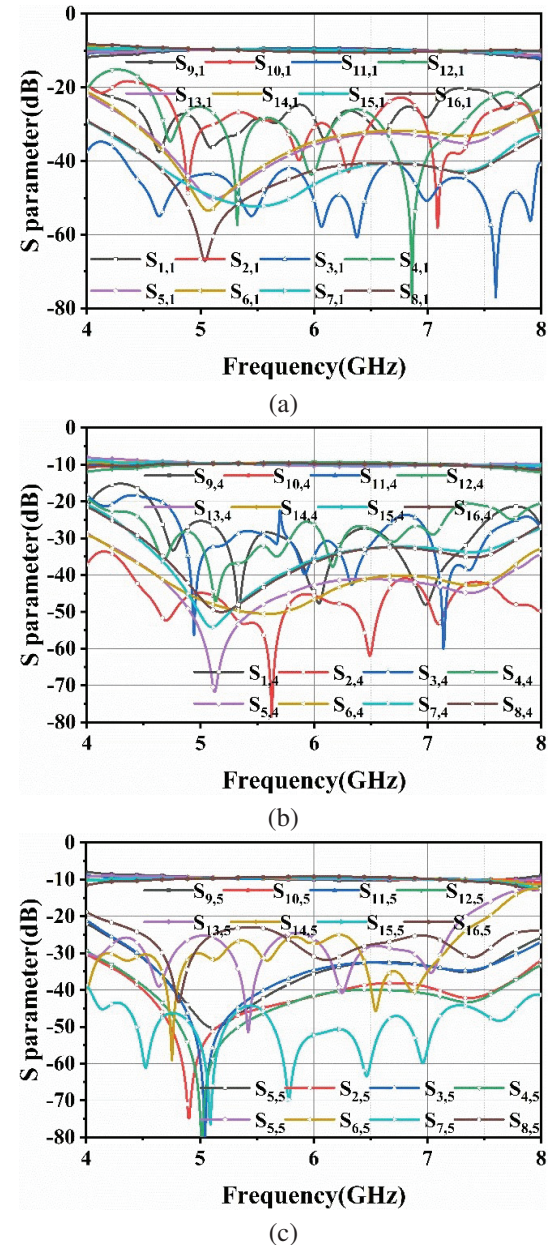

Fig. 18. 8×8 Butler matrix.

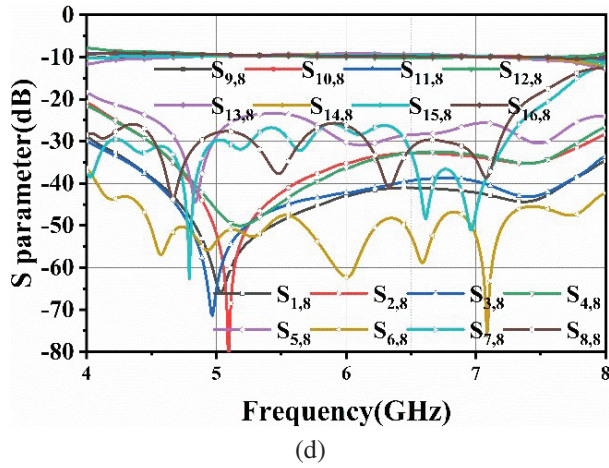(a)

(b)

(c)

Fig. 19. *Continued.*

(d)

Fig. 19. Simulation results of S parameters: (a) port 1, (b) port 4, (c) port 5, and (d) port 8.
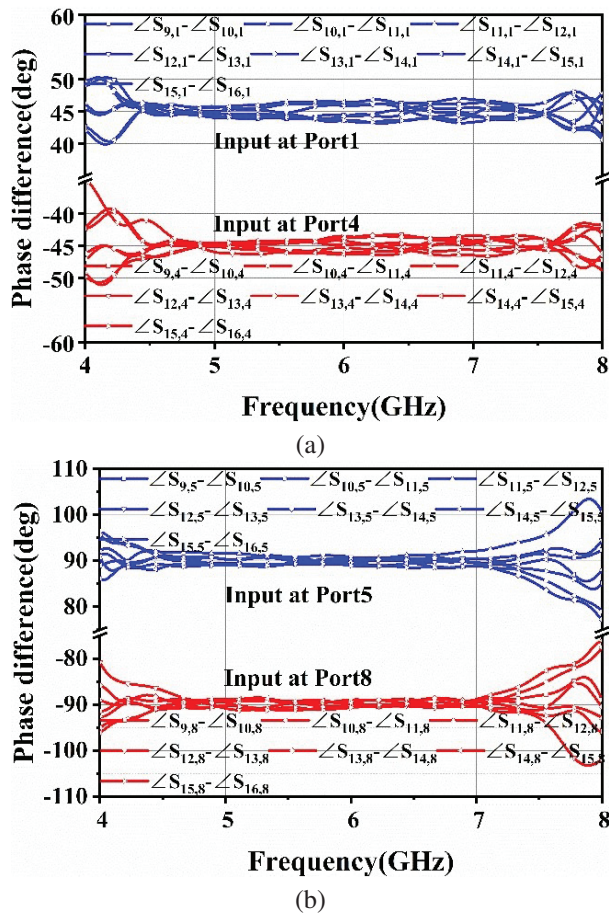

(a)

(b)

Fig. 20. Simulation results of phase difference: (a) input at port 1 and port 4 and (b) input at port 5 and port 8.

The simulation results indicate that there is a similarity between ports 1 and 4, as well as between ports 5 and 8, due to the symmetry of the Butler matrix structure.

It can be observed that the amplification is almost equal and phase distribution is consistent with theory results as shown in Table 1. The reflection coefficient of ports 1 and 5 and the isolations are less than −20 dB in 5-7 GHz. The transmission coefficients for input ports 1 and 5 is −9.9±0.6 dB and −9.7±0.5 dB, respectively. The phase balances by the excitation of ports 1 and 5 are 45°±2.1° and 90°±2.2°, respectively. Quite good amplitude and phase stability can be observed in wide band.

In order to demonstrate the design work, two sub Butler matrix modules and a connection-output module are fabricated, as shown in Fig. 21.

(a)

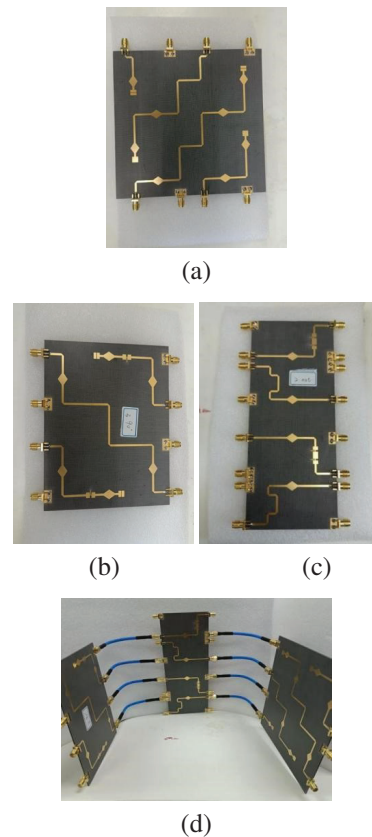(b)   (c)

(d)

Fig. 21. Photographs of the proposed Butler matrix: (a) sub Butler matrix module 1, (b) sub Butler matrix module 2, (c) connection-output module, and (d) whole Butler matrix.
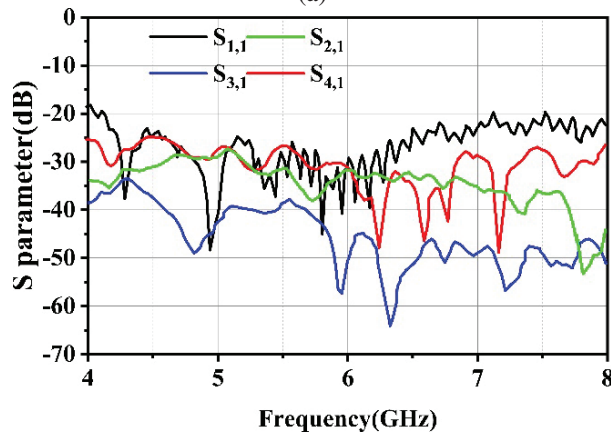
A complete 8×8 Butler matrix structure can be obtained by connecting the output port of the sub Butler matrix module with input port of the connection-output module. The S parameters of these three modules and the 8×8 Butler matrix are measured. The measured results of the sub Butler matrix module 1 are shown in Fig. 22.
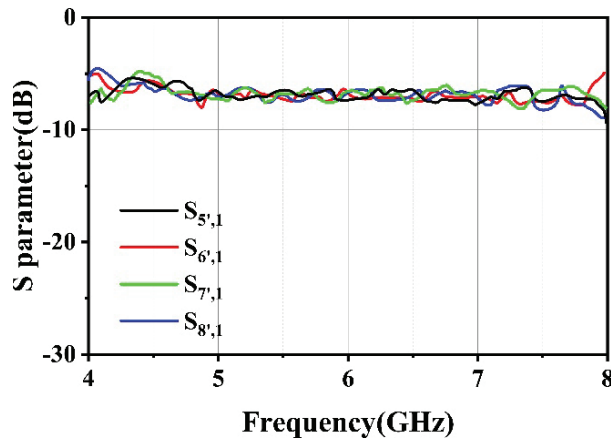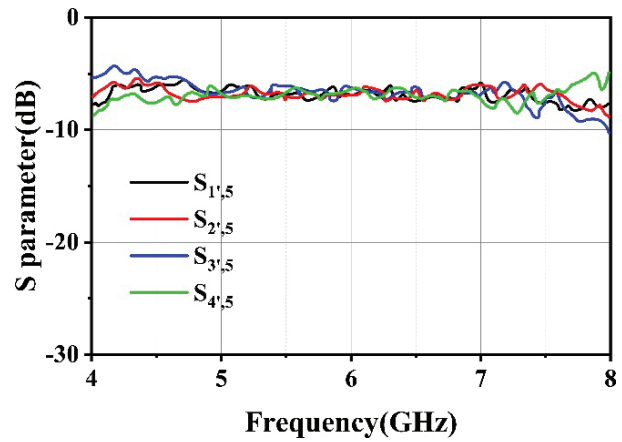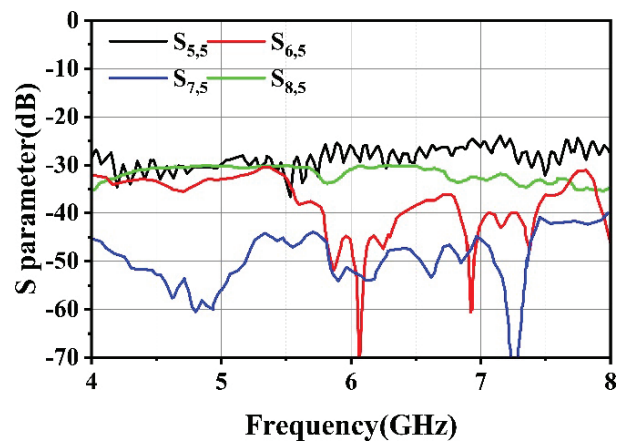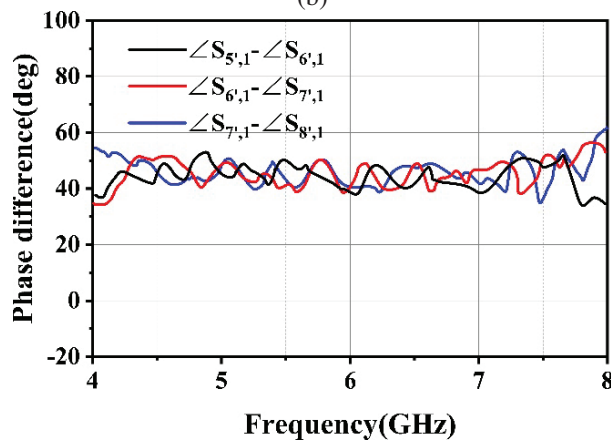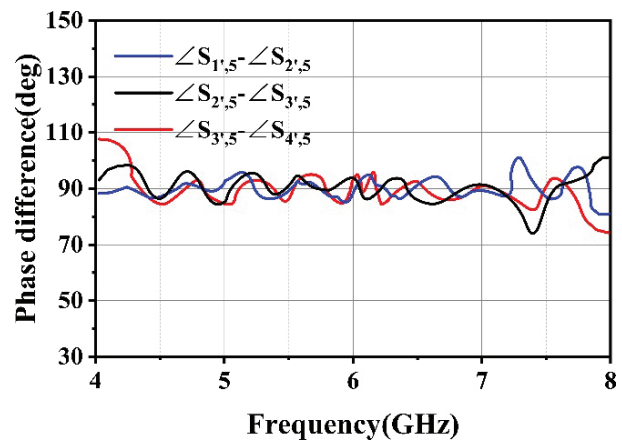
Fig. 22. Measured results of sub Butler matrix module 1: (a) transmission coefficient, (b) reflection coefficient and isolation, and (c) phase difference of output.

Fig. 23. Measured results of sub Butler matrix module 2: (a) transmission coefficient, (b) reflection coefficient and isolation, and (c) phase difference of output.

As shown in Fig. 22, the amplitude imbalance of output of sub Butler matrix module 1 does not exceed 1.2 dB. The $45°\pm5.6°$ phase difference can be obtained by excitation port 1. The measured results of sub Butler matrix module 2 are shown in Fig. 23.

As shown in Fig. 23, the amplitude imbalance of the output of sub Butler matrix module 2 does not exceed 1.4 dB. The $90°\pm5.5°$ phase difference can be obtained

by excitation port 5. The measured results of connection-output module are shown in Fig. 24.

As shown in Fig. 24, the amplitude and phase balance of connection-output module is -3.3 ± 0.5 dB and $180°\pm5.2°$ in the operating frequency range. The measured results of the 8×8 Butler matrix is shown in Figs. 25 and 26.

From Figs. 25 and 26, it can be seen that the measured results are in good agreement with the simulation results. The amplitude and phase balance in the operating frequency range are -10.3 ± 0.8 dB and -10.0 ± 0.7 dB, $45°\pm7.3°$ and $90°\pm7.2°$ for -1 mode and -2 mode, respectively. The amplified and phase error between measured and simulation results is less than 0.5 dB and 5° in most frequencies. Compared with the existing designs of the Butler matrix listed in Table 2, the number of beams for beamforming Butler matrix and the number of OAM wave modes for OAM generate Butler matrix is also listed. The proposed work has the advantages of low insertion loss, small phase error, and wide bandwidth, which is very attractive in wideband OAM generation. Also, the modified topology of the Butler matrix needed fewer phase shifters to generate necessary OAM modes.
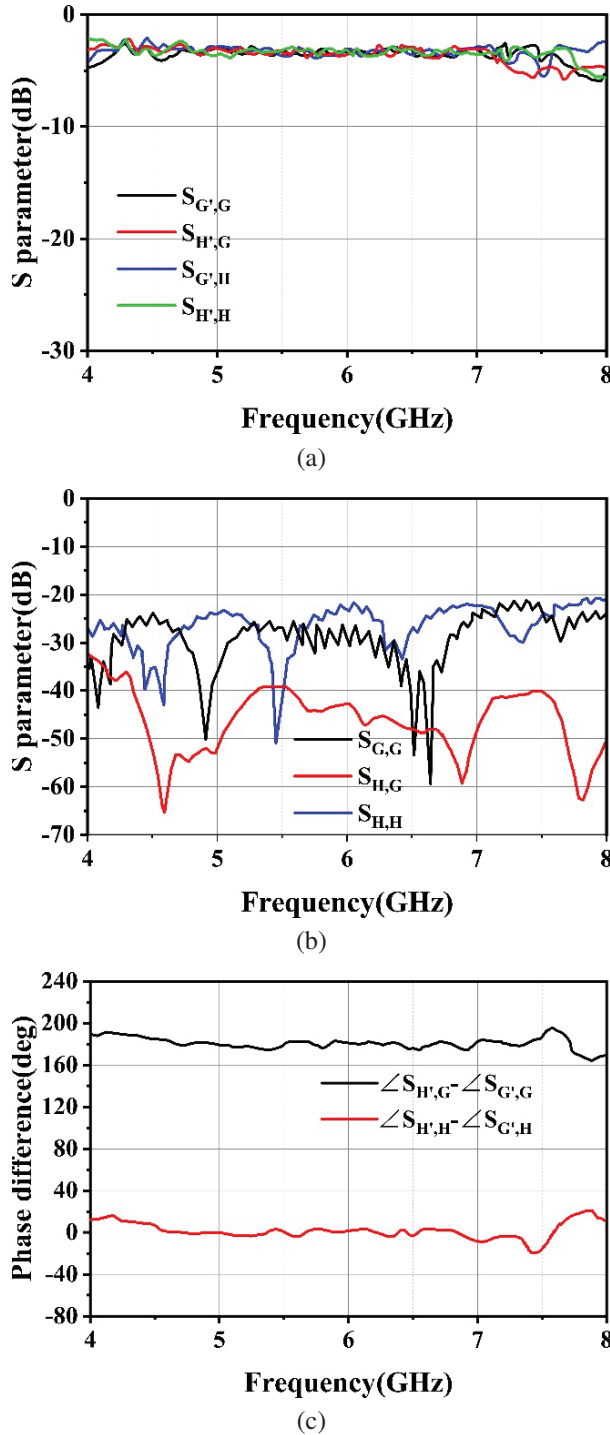

Fig. 24. Measured results of connection-output module: (a) transmission coefficient, (b) reflection coefficient and isolation, and (c) phase difference of output.
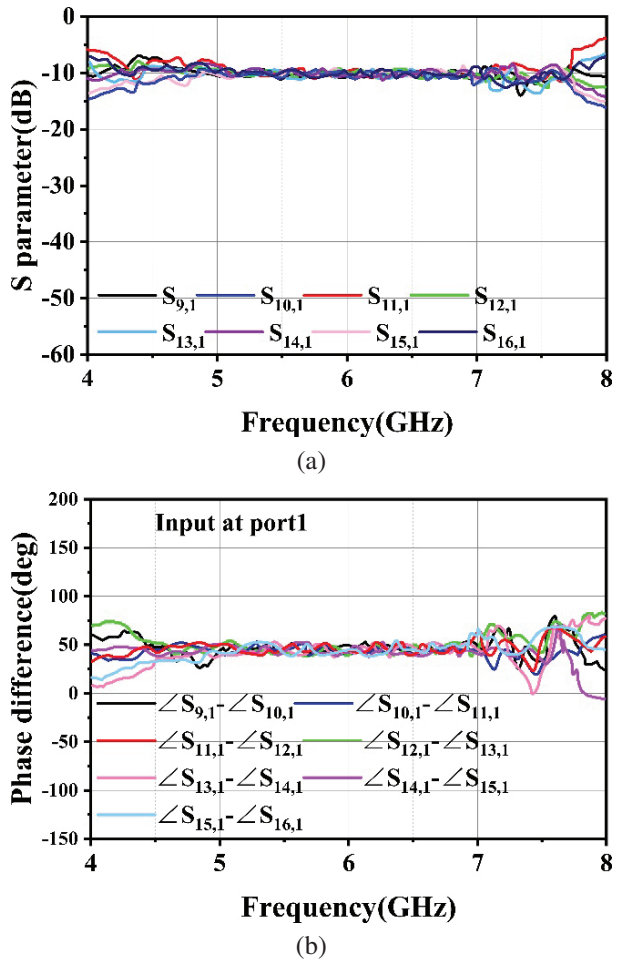

Fig. 25. Measurement results for -1 mode: (a) transmission coefficient and (b) phase difference of output.
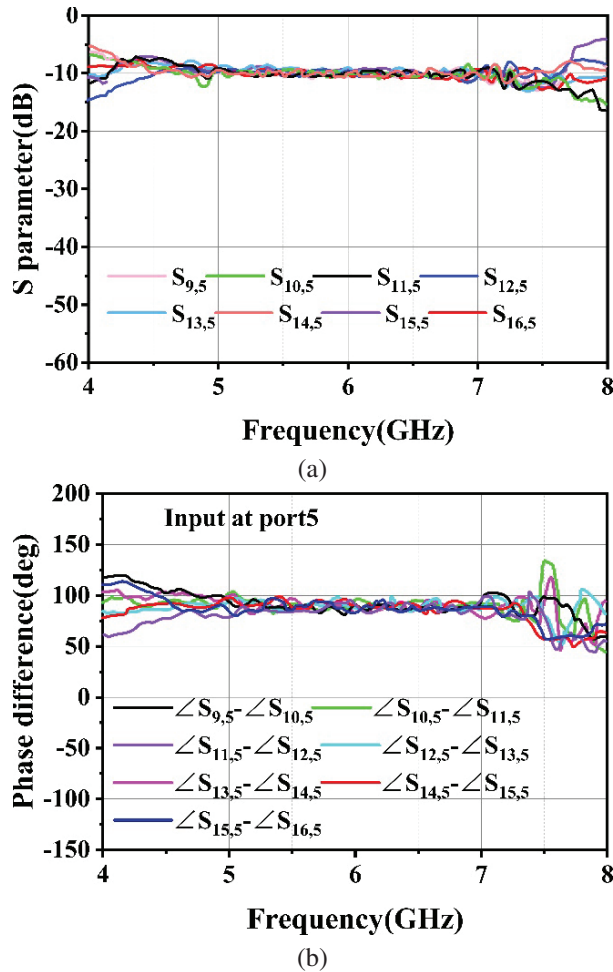
Fig. 26. Measurement results for −2 mode: (a) transmission coefficient and (b) phase difference of output.

Table 2: Comparison with previews work

Ref.	Freq. (GHz)	Insert Loss/ Phase Error	Band-width	Return Loss/ Isolation	Ports Num.	Beams/ Modes Num.
[24]	1.8	−7 ± 0.5 dB/4°	12%	<−25 dB/ <−20 dB	4×4	4 Beams
[25]	7.5	−7 ±1 dB /7°	10.7%	<−10 dB/ <−15 dB	4×4	3 Modes
[26]	2.2	−10.1±2.2 dB/ 20.7°	27%	<−10 dB/ <−10 dB	8×8	8 Beams
[27]	2.45	−10 ±1 dB/10°	8%	<−15 dB/ <−15 dB	8×8	4 Modes
This work	5-7	−10.3± 0.8 dB/7.3	33%	<−15 dB/ <−15 dB	8×8	4 Modes

VI. CONCLUSION

In this paper, a wideband 8×8 Butler matrix for generating ±1/±2 OAM modes is designed. Unlike the conventional 8×8 Butler matrix generating eight modes, this design requires fewer phase shifters to generate necessary modes OAM vortex wave. Wideband microwave components are designed, namely 3 dB directional cou-

pler and −45°/0°/90° phase shifters based on CRLH transmission line. Two sub Butler matrix modules and a connection-output module are designed to form the 8×8 Butler matrix. This provides a design for generating multi-mode OAM waves with the advantages of simplified Butler matrix structure and stable transmission performance in the wide band. It is found that the measured results are in good agreement with simulation results. The quite small imbalance of amplitude and phase shift can be realized for different OAM modes.

REFERENCES

[1] B. Thidé, H. Then, J. Sjöholm, K. Palmer, J. Bergman, T. D. Carozzi, Y. N. Istomin, N. H. Ibragimov, and R. Khamitova, "Utilization of photon orbital angular momentum in the low-frequency radio domain," *Physical Review Letters*, vol. 99, no. 8, p. 087701, 2007.

[2] S. M. Mohammadi, L. K. S. Daldorff, K. Forozesh, B. Thidé, J. E. S. Bergman, B. Isham, R. Karlsson, and T. D. Carozzi, "Orbital angular momentum in radio: measurement methods," *Radio Science*, vol. 45, no. 4, 2010.

[3] A. Papathanasopoulos and Y. Rahmat-Samii, "A review on orbital angular momentum (OAM) beams: Fundamental concepts, potential applications, and perspectives," in *2021 XXXIVth General Assembly and Scientific Symposium of the International Union of Radio Science (URSI GASS)*, Rome, Italy, pp. 1-4, 2021.

[4] F. Tamburini, E. Mari, A. Sponselli, B. Thidé, A. Bianchini, and F. Romanato, "Encoding many channels on the same frequency through radio vorticity: first experimental test," *New Journal of Physics*, vol. 14, no. 3, pp. 811-815, 2011.

[5] K. A. Opare, Y. Kuang, and J. J. Kponyo, "Mode combination in an ideal wireless OAM-MIMO multiplexing system," *IEEE Wireless Communications Letters*, vol. 4, no. 4, pp. 449-452, Aug. 2015.

[6] Y. Ren, L. Li, G. Xie, Y. Yan, Y. Cao, H. Huang, N. Ahmed, Z. Zhao, P. Liao, C. Zhang, G. Caire, A. F. Molisch, M. Tur, and A. E. Willner, "Line-of-sight millimeter-wave communications using orbital angular momentum multiplexing combined with conventional spatial multiplexing,"

IEEE Transactions on Wireless Communications, vol. 16, no. 5, pp. 3151-3161, May 2017.

[7] W. Cheng, H. Zhang, L. Liang, H. Jing, and Z. Li, "Orbital-angular-momentum embedded massive mimo: achieving multiplicative spectrum-efficiency for mmwave communications," *IEEE Access*, vol. 6, pp. 2732-2745, 2018.

[8] Y. Yan, G. Xie, M. P. J. Lavery, H. Huang, N. Ahmed, C. Bao, Y. Ren, Y. Cao, L. Li, Z. Zhao, A. F. Molisch, M. Tur, M. J. Padgett, and A. E. Willner, "High-capacity millimetre-wave communications with orbital angular momentum multiplexing," *Nature Commun*., vol. 5, pp. 1-9, Sep. 2014.

[9] F. Qin, J. Yi, W. Cheng, Y. Liu, H. Zhang, and S. Gao, "A high-gain shared aperture dual-band OAM antenna with parabolic reflector," in *Proc. 12th Eur. Conf. Antennas Propag. (EuCAP)*, London, pp. 8-11, 2018.

[10] L. Fang, H. Yao, and R. M. Henderson, "OAM antenna arrays at E-band," in *IEEE MTT-S Int. Microw. Symp. Dig.*, Honolulu, HI, pp. 658-661, June 2017.

[11] J. Liang and S. Zhang, "Orbital angular momentum (OAM) generation by cylinder dielectric resonator antenna for future wireless communications," *IEEE Access*, vol. 4, pp. 9570-9574, 2016.

[12] B. Xu, C. Wu, Z. Wei, Y. Fan, and H. Li, "Generating an orbital-angular momentum beam with a metasurface of gradient reflective phase," *Opt. Mater. Exp.*, vol. 6, no. 12, p. 3940, 2016.

[13] H. Sasaki, Y. Yagi, T. Yamada, T. Semoto, and D. Lee, "Hybrid OAM multiplexing using Butler matrices toward over 100 Gbit/s wireless transmission," *2020 IEEE Globecom Workshops*, Taipei, Taiwan, pp. 1-5, 2020.

[14] P.-Y. Feng, S.-W. Qu, and S. Yang, "OAM-generating transmitarray antenna with circular phased array antenna feed," *IEEE Transactions on Antennas and Propagation*, vol. 68, no. 6, pp. 4540-4548, June 2020.

[15] R. Chen, W.-X. Long, X. Wang, and L. Jiandong, "Multi-mode OAM radio waves: Generation, angle of arrival estimation and reception with UCAs," *IEEE Transactions on Wireless Communications*, vol. 19, no. 10, pp. 6932-6947, Oct. 2020.

[16] J. Butler and R. Lowe, "Beam-forming matrix simplifies design of electronically scanned antenna," *Electron. Des*., vol. 9, pp. 170-173, 1961.

[17] H. Moody, "The systematic design of the Butler matrix," *IEEE Trans. Antennas Propag*., vol. 12, no. 6, pp. 786-788, 1964.

[18] Q. Sun, Y.-L. Ban, J.-W. Lian, and X.-F. Li, "A new array formation method for millimeter-wave transverse slot scanning array antenna," in

2020 IEEE International Symposium on Antennas and Propagation and North American Radio Science Meeting, Montreal, QC, Canada, pp. 707-708, 2020.

[19] I. Messaoudene, H. Youssouf, M. Bilal, M. Belazzoug, and S. Aidel, "Performance improvement of multilayer Butler matrix for UWB beamforming antenna," *Proc. Seminar Detection Syst. Archit. Technol.(DAT)*, pp. 1-4, 2017.

[20] A. A. M. Ali, N. J. G. Fonseca, F. Coccetti, and H. Aubert, "Design and implementation of two-layer compact wideband Butler matrices in SIW technology for Ku-band applications," *IEEE Trans. Antennas Propag*., vol. 59, no. 2, pp. 503-512, Feb. 2011.

[21] S. Lim, C. Caloz, and T. Itoh, "Metamaterial-based electronically controlled transmission-line structure as a novel leaky-wave antenna with tunable radiation angle and beamwidth," *IEEE Transactions on Microwave Theory and Techniques*, vol. 52, no. 12, pp. 2678-2690, Dec. 2004.

[22] A. Karimbu Vallappil, M. K. A. Rahim, B. A. Khawaja, and M. N. Iqbal, "Compact metamaterial based 4×4 Butler matrix with improved bandwidth for 5G applications," *IEEE Access*, vol. 8, pp. 13573-13583, Jan. 2020.

[23] S. M. Mohammadi, L. K. S. Daldorff, J. E. S. Bergman, R. L. Karlsson, B. Thide, K. Forozesh, T. D. Carozzi, and B. Isham, "Orbital angular momentum in radio: A system study," *IEEE Transactions on Antennas and Propagation*, vol. 58, no. 2, pp. 565-572, Feb. 2010.

[24] H. X. Xu, G. M. Wang, and X. Wang, "Compact Butler matrix using composite right/left-handed transmission line," *Electron. Lett*., vol. 47, no. 19, pp. 1081-1083, Sep. 2011.

[25] J. Yang, J. Hu, T. Zhang, Q. Zhang, and W. Wu, "A three-mode OAM antenna with a Butler matrix feeding network," in *2021 IEEE International Conference on Power Electronics, Computer Applications (ICPECA)*, Shenyang, China, pp. 323-326, 2021.

[26] C.-C. Chang, R.-H. Lee, and T.-Y. Shih, "Design of a beam switching/steering Butler matrix for phased array system," *IEEE Transactions on Antennas and Propagation*, vol. 58, no. 2, pp. 367-374, Feb. 2010.

[27] B. Palacin, K. Sharshavina, K. Nguyen, and N. Capet, "An 8×8 Butler matrix for generation of waves carrying Orbital Angular Momentum (OAM)," in *The 8th European Conference on Antennas and Propagation (EuCAP 2014)*, The Hague, Netherlands, pp. 2814-2818, 2014.

Yan Zhang received the B.S. and Ph.D. degrees in electromagnetic field and microwave technology from the Beijing University of Aeronautics and Astronautics (BUAA), Beijing, China, in 2002 and 2006, respectively. From 2007 to 2008, he was a Post-Doctoral Researcher with the Communication, Navigation, Surveillance/Air Traffic Management(CNS/ATM) Laboratory, Civil Aviation Administration of China(CAAC), BUAA.

He is currently an Associate Professor of electronics and information engineering with BUAA. He has authored over 40 papers. His research interests include antenna, electromagnetic surface and antenna array.

Dr. Zhang was the recipient of the Outstanding Doctoral Dissertation Award and the Outstanding Post-Doctoral Researcher Award presented by BUAA in 2008.

Haoran Ye received the degree in Physics in 2021. He is currently pursuing the M.S. degree in Electronic Science and Technology, School of Electronic and Information Engineering, Beihang University. His research interests include antenna and electromagnetic metamaterial.

Jialin Zhang received the B.S. and M.S. degrees in electromagnetic field and microwave technology from the Beihang University, Beijing, China, in 2019 and 2021, respectively. His research interests include antenna, metamaterial and antenna array.

Xurui Zhang received the B.S. degree in communication engineering from Xiamen University, Xiamen, China, in 2022. He is currently working toward the M.S. degree in electronic science and technology with the School of Beihang University, Beijing, China. His research interests include electromagnetic metamaterials and vortex wave.

Shanwei Lü was born in Dalian, Liaoning Province, China, in 1937. He received the B.S. degree in electromagnetic field and microwave technology from the Beijing Institute of Aeronautics and Astronautics (BIAA), Beijing, China, in 1961. From 1961 to 1976, he was with the Microwave Technique Laboratory, BIAA. He is currently a Professor and Ph.D. Supervisor with the School of Electronics and Information Engineering, Beijing University of Aeronautics and Astronautics (BUAA), Beijing, China.

He has authored or coauthored five books and over 120 journal papers. His research interests include computational electromagnetics, radar antennas, navigation antennas, and antenna feeds.

Prof. Lü was the recipient of the 1991 Second Prize of Science and Technology Progress for leaky waveguide antennas, the 1992 Third Prize of National Invention for the conformal slotted antennas of sectoral waveguides, and the 1998 Third Prize of Science and Technology Progress for conformal slotted antennas of cam-rectangular waveguides.

Selective Microwave Wireless Power Transfer to Sensors Embedded in Concrete at Sub-wavelength Spacing using Electromagnetic Time-reversal Technique

Baidenger Agyekum Twumasi[1,2], Jia-Lin Li[1], Faith Kwaku Deynu[2], Ebenezer Tawiah Ashong[2], Christian Dzah[2], and Dustin Pomary[2]

[1]School of Resources and Environment
University of Electronic Science and Technology of China, Chengdu, China
btwumasi@htu.edu.gh, jialinli@uestc.edu.cn

[2]Dept. of Electrical and Electronic Engineering
Ho Technical University, Ho, Ghana
fdeynu@htu.edu.gh, eashong@htu.edu.gh, chdzah@htu.edu.gh, dpomary@htu.edu.gh

Abstract – Wireless power transfer has become a trending research area for remotely transferring power. This paper presents the numerical simulation study of selective wireless power transfer to closely spaced wireless sensors embedded in reinforced concrete. A selective microwave wireless power transfer is achieved at a 10 mm separation between tightly-coupled monopole antennas (wireless sensor antennas). Both tightly-coupled wireless sensors operate at 2.45 GHz, hence beating the diffraction limit at $\lambda/12$ with the incorporation of additional scatterers in the reinforced concrete environment. The main objective is to realize selective wireless power transfer to wireless sensors with sub-wavelength separation (closely spaced) to which one makes the power request. Here, the presence of meta-structures creates some randomness serving as scatterers in the use of the electromagnetic time-reversal technique which enhances the spatial refocusing beyond the diffraction limit. This implies that the focal spot is less than half of the carrier wavelength at the operating frequency. At any time that one of the tightly-coupled sensor antennas sends a power request, power will be transferred to it alone. Cases of dry concrete with and without reinforced bars have been studied with electromagnetic time-reversal techniques for the closely spaced sensors embedded in concrete.

Index Terms – electromagnetic time reversal, sensors, super-resolution, wireless power transfer.

I. INTRODUCTION

There is increasing demand for wireless devices for various applications such as wireless power transfer [1–4] and electronic toll collection systems [5]. Antennas play crucial roles in wireless power transfer hence the need for an optimum design. In [6], the authors proposed the design of a dipole antenna with matching network using genetic algorithm (GA) optimization. The antenna designed in [6] comprised of a loaded wire dipole and matching network, in which loads and matching network were optimized by the GA in order to enhance the antenna's performance. In [7], an orthogonally integrated hybrid antenna for intelligent transportation systems was proposed. The authors in [1] studied a near field wireless power transfer to sensors embedded in concrete under different scenarios. However, the action distance for this system is not large. Many wireless devices in the era of the internet of things need to be powered and kept on to perform their intended functions. Most of these devices run on batteries which need to be replaced after they run down or get trickle charged in their active service life. In the literature, numerous methods for charging such batteries to enable them to stay in active service over prolonged periods have been proposed.

Wireless power transfer has gained increasing attention in recent years due to the need to continuously power wireless sensors used for various critical monitoring applications. For example, in [3] the authors designed and optimized a robust concrete embedded antenna and minimized the influence of the background material on the energy transfer efficiency to monitor the health of civil structures. In [8], a proof of concept for near field communication for powering sensors in concrete is studied, where the sensors were deeply buried in the concrete. Here, the effect of re-enforcement bars was not considered. Wireless sensors for health monitoring of civil structures can be buried inside the concrete during the construction phase or after the construction to report the health of the civil structure [9]. In [9], power transmission to sensors embedded in reinforced

concrete structures is presented. The study considered a single antenna embedded in the concrete structure. Nevertheless, to obtain accurate and timely information on the health of civil structures, multiple sensors will be required.

With the need to monitor civil structures in space constrained environments, embedding closely spaced sensors will be necessary and a super resolution method for transmissions is much desired. This article presents a numerical simulation study which explores the realization of selective wireless power transfer to closely spaced wireless sensors embedded in reinforced concrete for structural health monitoring applications.

II. ELECTROMAGNETIC TIME-REVERSAL WIRELESS POWER TRANSFER

The electromagnetic time-reversal (EMTR) technique which has been widely applied in acoustic has found wide applications in electromagnetics as well. It has been used in medical imaging, target detection [10], wireless power transfer [11], wireless transmission using pulse shaping [12], power wave forming [13] and telecommunications [14] among others.

The EMTR technique is characterized by spatial and temporal focusing effects. In electromagnetic time reversal, the more complex the medium is with scatterers resulting in reverberation and reflections (multipath), the better the focusing effect. Such complex scattering medium helps to increase the aperture of the antenna time-reversal mirror (TRM). The TRM is enabled to collect the scattered fields, record, flip in time and then transmit back into the same medium from the TRM positioned outside the concrete. The time-reversed waves are found to converge back to the source where the initial transmission originated if the medium is reciprocal [15]. This is even more precise and can be exploited for selective focusing on closely spaced antennas. It is evident that the EMTR technique has been used in various applications in literature but not much research has been done on its application to wireless power transfer to tightly-coupled sensors embedded in concrete with reinforcement bars. In [11], a single-channel TRM is employed as a novel method of wireless power transfer to a moving target in a reverberant medium. EMTR wireless power transfer can surmount the challenges of inductive wireless power transfer such as increasing the action distance and may also reduce the risk of electrocution in its action path since the scattered waveform is not a beam of waves. However, to the best of our knowledge, EMTR wireless power transfer to tightly-coupled monopoles embedded in concrete at separation of 10 mm with reinforcement bars in conjunction with an electromagnetic scatterer plate has not been studied. This article aims to study the selective microwave wireless power transfer to

tightly-coupled antennas operating at 2.45 GHz in multiple scattering environments within reinforced concrete structures.

In EMTR wireless power transfer, the receiver transmits a signal to the transmitter, which is then time-reversed and re-transmitted back to the receiver. This process can be described mathematically as:

$$\mathbf{E}_{R(x,y,z,t)} \rightarrow \mathbf{E}_{T(x,y,z,t)} \rightarrow \mathbf{E}_{T(x,y,z,-t)} \rightarrow \mathbf{E}_{R(x,y,z,-t)}, \quad (1)$$

where $\mathbf{E}_{R(x,y,z,t)}$ is the electric field at the receiver at time t, $\mathbf{E}_{T(x,y,z,t)}$ is the electric field at the transmitter at time t, and $\mathbf{E}_{T(x,y,z,-t)}$ is the time-reversed electric field at the transmitter at time, $-t$.

Using time-reversal symmetry property, we can substitute E(-t) for E(t) in the electromagnetic wave equation to obtain:

$$\nabla^2\mathbf{E} - \mu_0\varepsilon_0\partial^2\mathbf{E}/\partial t^2 = 0, \quad (2)$$

$$\nabla^2\mathbf{E} - \mu_0\varepsilon_0\partial^2\mathbf{E}/\partial(-t)^2 = 0, \quad (3)$$

$$\nabla^2\mathbf{E} + \mu_0\varepsilon_0\partial^2\mathbf{E}/\partial t^2 = 0. \quad (4)$$

These equations describe the behavior of the time-reversed electric field in air medium during EMTR wireless power transfer. However, this equation alone is not sufficient to calculate the exact behavior of the electric field during EMTR wireless power transfer. A more detailed analysis, which considers the specific geometry of the transmitter and receiver, is needed to derive more accurate equations for this process. The electromagnetic wave equation in a concrete environment can be derived by modifying the wave equation in a vacuum to consider the presence of a medium with a non-zero permittivity and permeability. In general, the electromagnetic wave equation in a medium can be written as:

$$\nabla^2\mathbf{E} - \mu\partial^2\mathbf{E}/\partial t^2 - \mu\partial\left(\mu^{-1}\partial\mathbf{E}/\partial t\right)/\partial t = 0, \quad (5)$$

where $\mathbf{E}$ is the electric field, μ is the permeability of the medium, and ε is the permittivity of the medium. The second and third terms on the left-hand side of (5) consider the effect of the medium on the propagation of electromagnetic waves.

In a concrete environment, the permeability and permittivity of the medium can be different from those in a vacuum. In general, the permeability of concrete is close to that of free space (i.e., $\mu \approx \mu_0$), while the permittivity can be significantly higher (i.e., $\varepsilon > \varepsilon_0$). Therefore, the electromagnetic wave equation in a concrete environment can be written as:

$$\nabla^2\mathbf{E} - \mu_0\varepsilon\partial^2\mathbf{E}/\partial t^2 - \mu_0\partial\left(\varepsilon_r\varepsilon_0^{-1}\partial\mathbf{E}/\partial t\right)/\partial t = 0, \quad (6)$$

where ε_r is the relative permittivity (or dielectric constant) of the concrete, which describes how much the permittivity of the concrete differs from that of free space.

III. DESIGN OF ANTENNA TIME-REVERSAL MIRROR (ATRM)

For structural health monitoring of concrete structures, there will be the need for embedding wireless

sensors near some concrete structures due to space constraints for structural health monitoring and related applications. Due to this, the study of selective focusing of microwave wireless power transfer to embedded tightly-coupled sensors is necessary. Electromagnetic time reversal with spatial focusing properties promises to help realize such selective transfer of power to such tightly-coupled sensors embedded in concrete structures. Therefore, this study focuses on the study of selective wireless power transfer from antennas located outside the concrete structure to tightly-coupled antennas embedded in the concrete structure. The tightly-coupled sensors are denoted by two tightly-coupled monopoles both operating at 2.45 GHz with a separation of 10 mm.

Firstly, two tightly-coupled monopoles are designed to represent the antennas of the wireless sensors embedded in concrete. The two tightly-coupled wire monopole antennas have a separation distance of 10 mm and are positioned on the same ground plane with a radius of 150 mm. Both monopole antennas operate at 2.45 GHz. The optimized height of each monopole is 28 mm. Figure 1 shows the structure of the designed tightly-coupled monopole antennas. The optimum height of these monopole antennas was realized through parameter sweeping study.
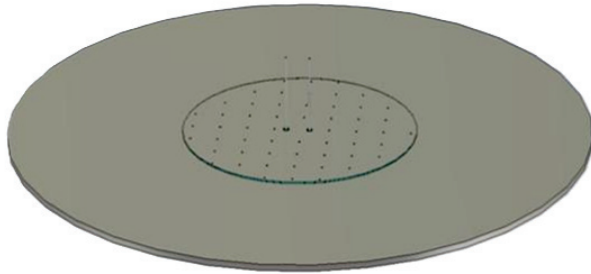

Fig. 1. Tightly-coupled monopole antennas on a large ground plane.

Secondly, we propose the design of a dual-band antenna TRM operating at 2.45 GHz and 5.2 GHz to be used in a wireless power transfer application as TRM to wireless sensors embedded in concrete at 2.45 GHz. It consists of a single-layer substrate ($\varepsilon_r = 2.65$, $\tan\delta = 0.003$) etched with round-end bowtie shaped patch made of copper placed at alternate sides of a 49 mm $\times$ 43 mm substrate having a thickness of 0.8 mm and fed by a coaxial feed line. The bowtie antenna evolved from the conventional microstrip bowtie antenna as discussed in [16]. The initial design of the bowtie antenna was based on the design equation in [16]. After the initial design, the antenna was modified to have a probe feed-line. The antenna design was then fine-tuned through numerical simulations. The rounded bowtie antenna is

closely related to the conventional one hence the resonance frequency of the patch bowtie antenna for its dominant mode can be derived following the equations in [16] as:

$$f_r = 1.152 \frac{c}{L^2 \sqrt{\varepsilon_{eff}}} \left(\frac{(W + 2\Delta L) + (S + 2\Delta L)}{(W + 2\Delta L) + (W_c + 2\Delta L)} \right), \quad (7)$$

$$\Delta L = \frac{0.412 h \left(\varepsilon_{eff} + 0.3 \right)}{\left(\varepsilon_{eff} - 0.258 \right)} \left(\frac{\frac{W + W_c}{2h} + 0.262}{\frac{W + W}{2h} + 0.813} \right), \quad (8)$$

$$e_{eff} = \left(\frac{e_r + 1}{2} \right) + \left(\frac{e_r - 1}{2} \right) \left(\frac{24h}{W + W_c} + 1 \right)^{-\frac{1}{2}}. \quad (9)$$

The guided wavelength of the bowtie antenna can be obtained as:

$$\lambda_g = \frac{\lambda_0}{\sqrt{\varepsilon_{eff}}}. \quad (10)$$

The effective side length is expressed as [16]:

$$a_{eff} = a + \frac{h}{\sqrt{e_{eff}}}. \quad (11)$$

The final dimensions of the antenna were optimized using HFSS. The optimum size of the substrate used is 30 mm $\times$ 30 mm and 0.8 mm thickness. The proposed antenna TRM has slots etched on the radiator and metallic scatterers at both sides of the substrate. The other parameters of the proposed antenna TRM are as follows: the flare angle is 130 degrees, the patch on the left-hand side has a radius of 18.768 mm, and the dimensions of the rectangular slot on the left patch is 1.5 mm by 18.678 mm. The patch on the right-side has a radius of 18.760 mm and its rectangular slot has dimensions of 1.5 mm by 19.00 mm. The microstructures (slots) etched on the patch have radii of 0.30 mm and 0.80 mm with a separation of 0.40 mm between them as shown in Fig. 2.
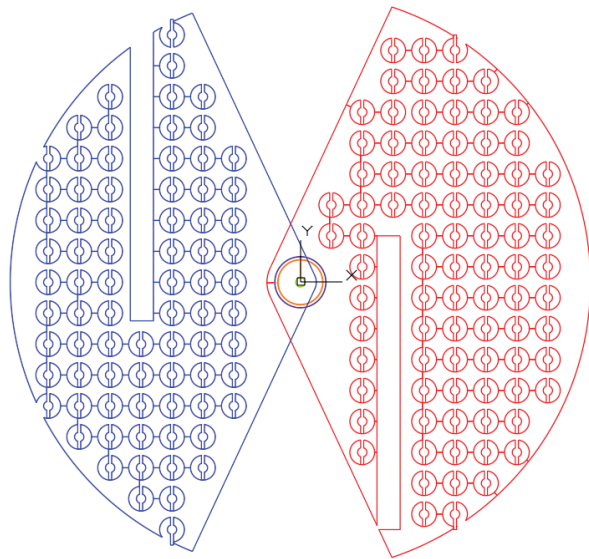

Fig. 2. Layout of the antenna time-reversal mirror.

IV. DISCUSSIONS OF ANTENNA TRM SIMULATION AND EXPERIMENTAL RESULTS

A prototype of the fabricated bowtie antenna is depicted in Fig. 3. The simulated and measured reflection coefficient of this demonstrator are shown in Fig. 4. The reflection coefficient of the dual-band bowtie antenna with scatterers on both radiators and substrate is below -10 dB from 2.295 GHz to 2.505 GHz resulting in 210 MHz measured bandwidth in the lower operating band (2.45 GHz). For the upper band (5.2 GHz), a measured -10 dB impedance bandwidth of 735 MHz was recorded for frequencies ranging from 4.71 GHz to 5.445 GHz. From Fig. 4, the simulated results for this antenna show that the reflection coefficient is below -10 dB from 2.34 GHz to 2.56 GHz resulting in 240 MHz bandwidth at the lower operating frequency (i.e. 2.45 GHz).

Again, the reflection coefficient is less than -10 dB from 4.75 GHz to 5.54 GHz resulting in 790 MHz band-
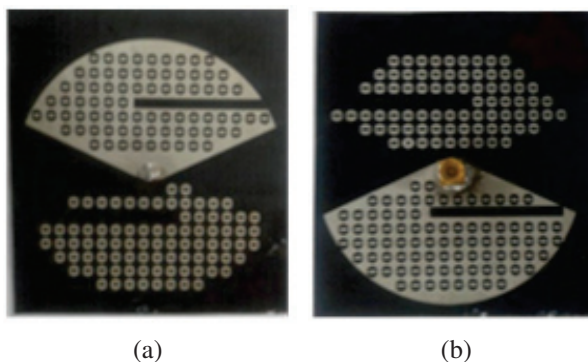
width with the return loss reaching 12.20 dB at 5.2 GHz. We observed that there are some discrepancies between the simulated and measured results. This can be attributed to losses of the coaxial feedline (cable) used for the measurement, the influence of the SMA connector and the unbalanced feed structure of the antenna TRM as well as non-ideal environmental conditions and fabrication uncertainties.

(a)   (b)

Fig. 3. Photograph of antenna TRM: (a) front and (b) back.
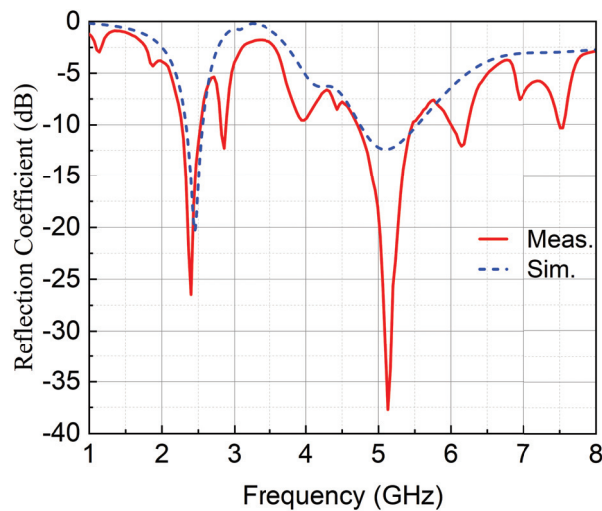
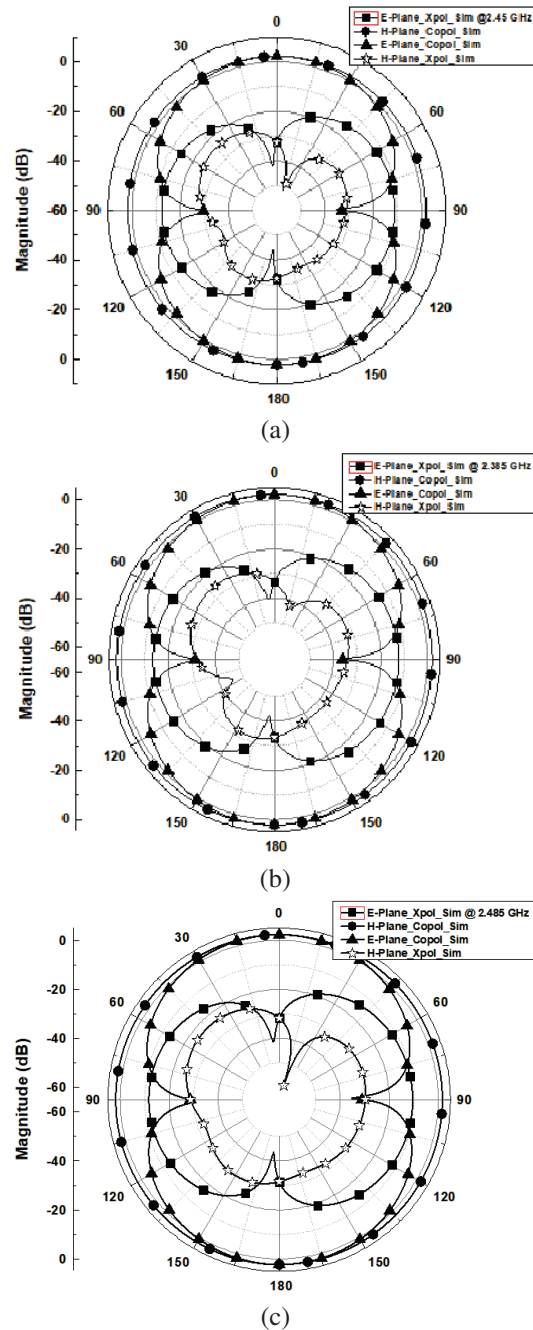Fig. 4. Simulated and measured S_{11} of the TRM.

(a)

(b)

(c)

Fig. 5. Simulated radiation patterns of antenna TRM at (a) 2.45 GHz, (b) 2.385 GHz, and (c) 2.485 GHz.

The simulated radiation performance of the proposed antenna at the lower band is shown in Figs. 5 (a-c). It shows simulated radiation performance at 2.385, 2.45 and 2.485 GHz, respectively, all showing typical dipole radiation patterns.

The antenna TRM was also characterized for radiation performance for the upper band resonating at 5.2 GHz and two other frequencies within its operating bandwidth. The radiation patterns are shown in Figs. 6 (a-c) at the frequencies indicated. The measurement setup of the bowtie antenna TRM is shown in Fig. 7.
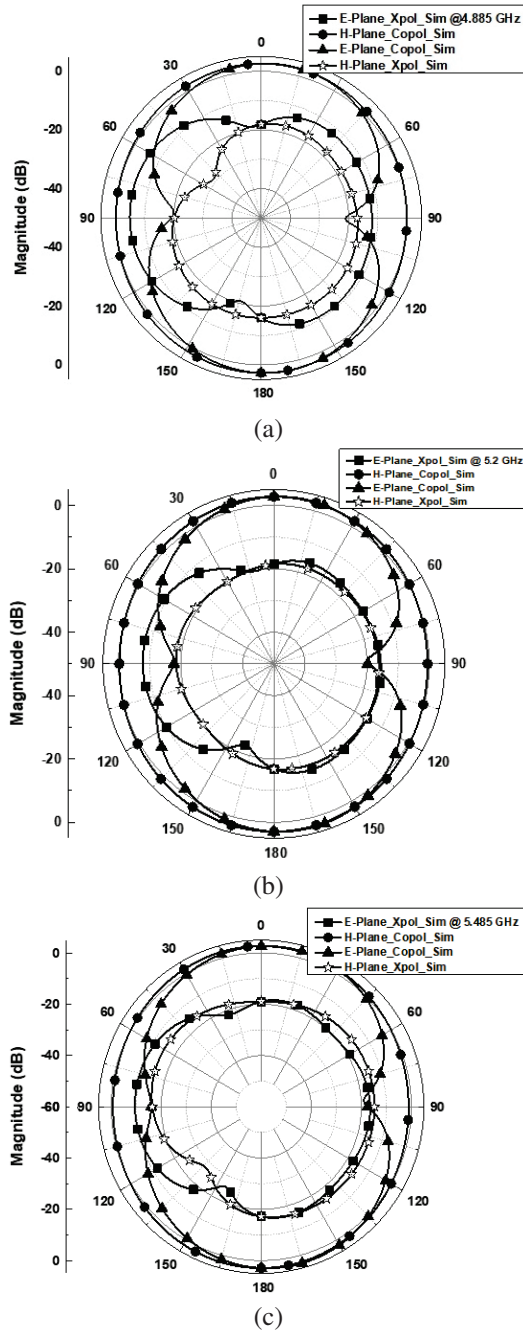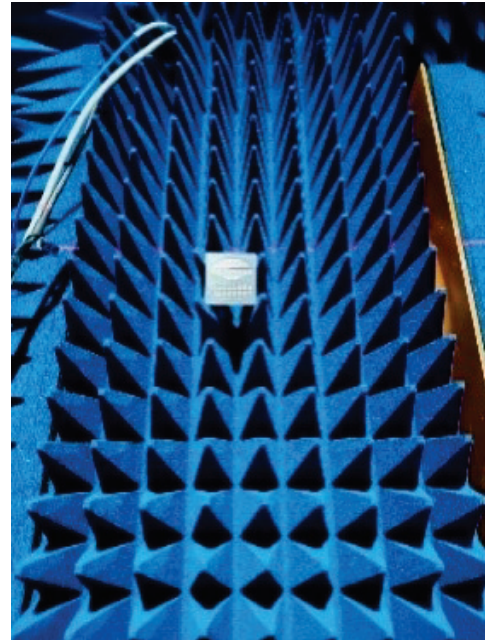

Fig. 7. Measurement setup of the bowtie antenna TRM.

The scatterers on the bowtie antenna distract the flow of shield current on the radiators serving as perturbation structures on the patch radiators which changes the direction of flow of these currents.

Hence a form of near-field scatterers on the bowtie antennas analogous to the near-field metal wire medium arranged at sub-wavelength scale. The size of these scatterers is much smaller than the size of the antenna radiator implying that these slots will resonate at a far higher frequency. From the observed radiation patterns, it shows that the microstructure scatterers have enhanced the radiation performance of the antenna TRM by decreasing the cross-polarization levels. The resulting high cross polarization discrimination decreases any unwanted field components which is a desired feature of an antenna TRM. This enhances the focusing properties based on the evanescent wave reciprocity principles resulting in super-resolution realizations when used with some wire medium/microstructure array of scatterers in the near field of the transmitting antenna since evanescent waves experience exponential decay. A method of enhancing its propagation to the far field is necessary, hence the techniques adopted.

The simulated reflection coefficient of the tightly-coupled monopole antenna is shown in Fig. 8. Opti-

(a)

(b)

(c)

Fig. 6. Radiation characterization (simulated) of bowtie antenna TRM at (a) 4.885 GHz, (b) 5.2 GHz, and (c) 5.485 GHz.

mum performance is realized when the length of the monopole antenna is 28 mm. The two tightly-coupled wire monopole antennas have separation of 10 mm with a ground plane of 150 mm in radius and both operate at 2.45 GHz. The optimized height of each monopole is 28 mm.
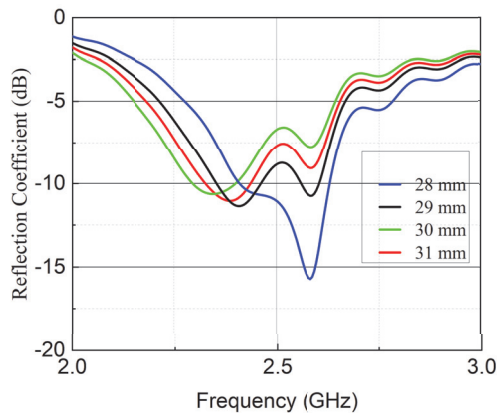

Fig. 8. Simulated reflection coefficient (S_{11}) of the tightly-coupled monopole antennas.

V. NUMERICAL SIMULATION OF SELECTIVE WIRELESS POWER TRANSFER TO SENSORS EMBEDDED IN CONCRETE

Figure 9 shows the setup of the tightly-coupled antennas embedded in concrete without re-enforcement bars. In this setup, the antenna TRMs with slots are positioned outside the concrete structure and the tightly-coupled monopole antennas/sensors requesting power are embedded in the concrete structure. The antenna TRM has a face-to-face separation distance of 300 mm.
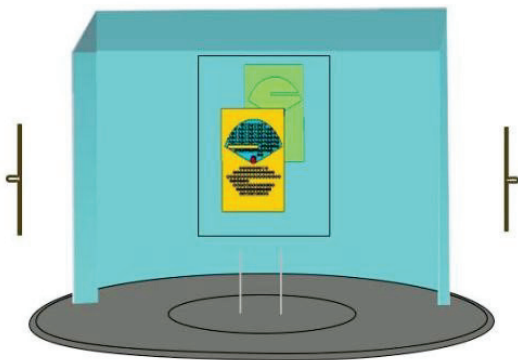
Four TRMs were used to provide power transfer to the embedded tightly-coupled antennas. Table 1 shows performance comparison between the proposed antenna and other studies. The proposed antenna compares favorably with other works. The concrete material has a dielectric constant of 4.5 with a loss tangent of 0.011. A block of concrete was modelled with dimensions of 200 mm by 200 mm and a height of 150 mm.

For this study, three setups have been considered and numerically studied. In Fig. 9, there are no re-enforcement bars and scatterers. In Fig. 10, re-enforcement bars (rebars) are embedded in the concrete. The re-enforcement bars are made of iron rods with the properties of a lossy metal. The iron rods' diameter is 16

Table 1: Performance comparison of the proposed antenna and other works

Ref	Dimension (mm)	Bandwidth (GHz)	Frequency (GHz)	Gain (dBi)
[17]	50×50 (etched on both copper layers)	NA	2.4, 3.5, 5.3	1.8, 1.5, 4.5
[16]	110×50 (etched on single copper layer)	NA	0.9 / 1.8 1.25, 2.1	3.5/ 4.4 3.9, 5.1
[18]	45 × 65 (edged on both copper layers)	4.0-6.8	4.2, 5.5, 6.6	11.08 at 5.5 GHz
This work	**49 × 43**	**2.295-2.505, 4.71-5.445**	**2.45, 5.2**	**3.7, 3.0**

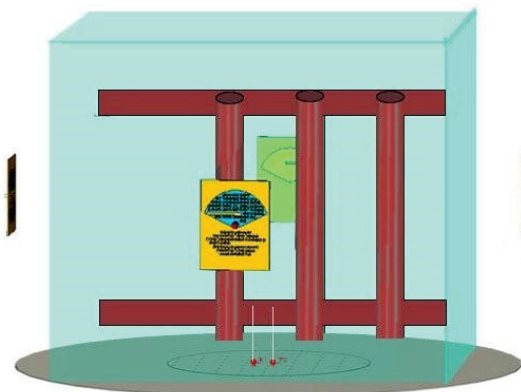Fig. 9. Setup for concrete without re-enforcement bars with embedded tightly-coupled monopoles.

Fig. 10. Re-enforced concrete structure with embedded monopole antennas and rebars and surrounding TRMs.

mm with a length of 200 mm and arranged as shown in Fig. 10.

Further, the concrete is embedded with rebars and additional two plates of electromagnetic scatterers close to the iron rods.

The electromagnetic scatterer plate is designed with a microwave substrate with copper strips of the length of a wavelength at the operating frequency and sub-wavelength separation arranged on one side of the microwave substrate. The dielectric constant of the microwave substrate used is 2.65.

Figure 11 shows the unit cell of the proposed scatterer embedded in the concrete structure. The corresponding dimensions are listed in Table 2. The complete 15×15 scatterer plate is shown in Fig. 12.
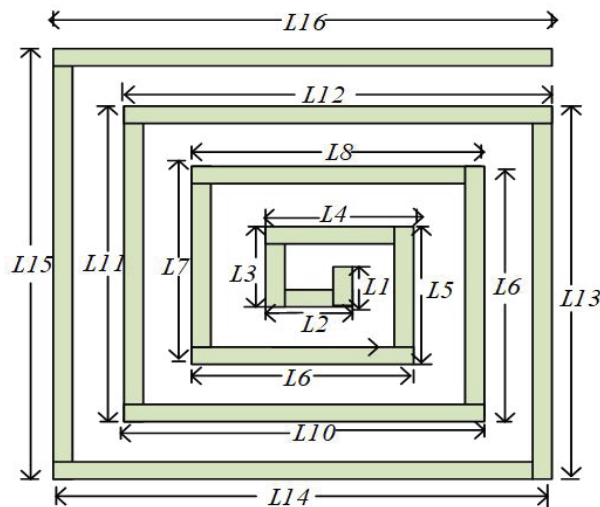

Fig. 11. Unit cell of the scatterer showing its respective dimensions.

Table 2: Dimensions of the scatterer

Parameter	Value (mm)	Parameter	Value (mm)
L1	3.00	L10	8.625
L2	3.625	L11	9.25
L3	4.25	L12	9.875
L4	4.875	L13	10.50
L5	5.5	L14	11.125
L6	6.125	L15	11.75
L7	6.75	L16	12.375
L8	7.375	Width of strip	1.00
L9	8.00		

All numerical simulations were carried out using Computer Simulation Technology (CST). MATLAB was used to reverse the signals for the time-reversal signal re-transmission. An initial channel-sounding pulse was
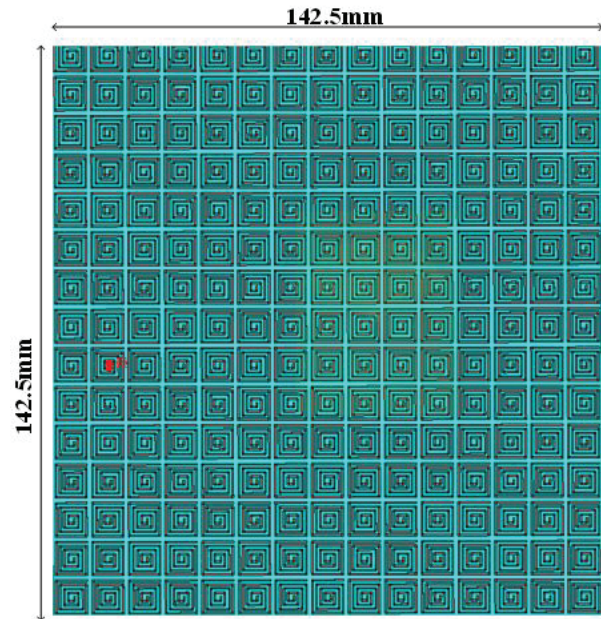

Fig. 12. The 15 × 15 array scatterer plate.

transmitted from the antenna/sensor making the power request. This signal (total field) is then received by four antennas (ATRM), flipped in time using the MATLAB program and then re-transmitted from the TRM into the concrete structure using CST. The complete setup including the additional electromagnetic scatterers in the form of a scatterer plate is shown in Fig. 13.

The objective is to improve the scattering of the electromagnetic waves to realize super-resolution wireless power transfer. This structure consists of an array of coiled copper strips with their unit cell as depicted in Fig. 11 and the scatterer plate as shown in Fig. 12. The
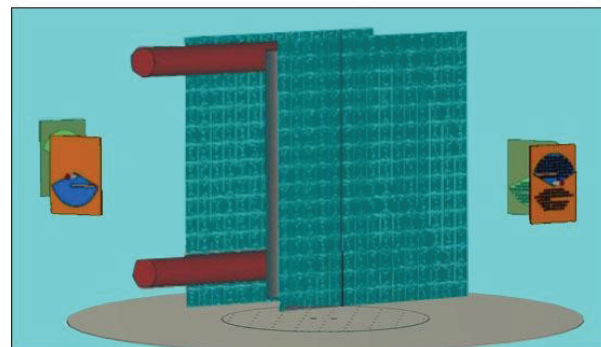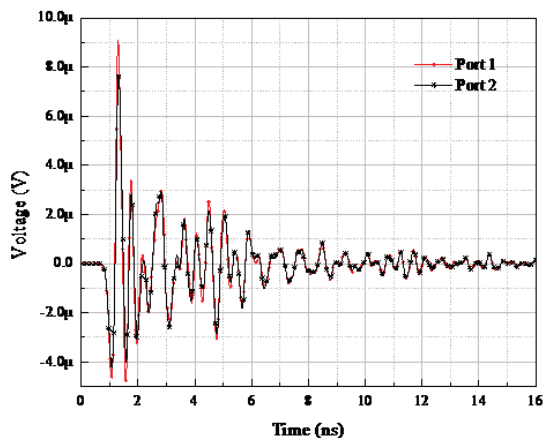

Fig. 13. Setup of re-enforced concrete with additional scatterers embedded in concrete.
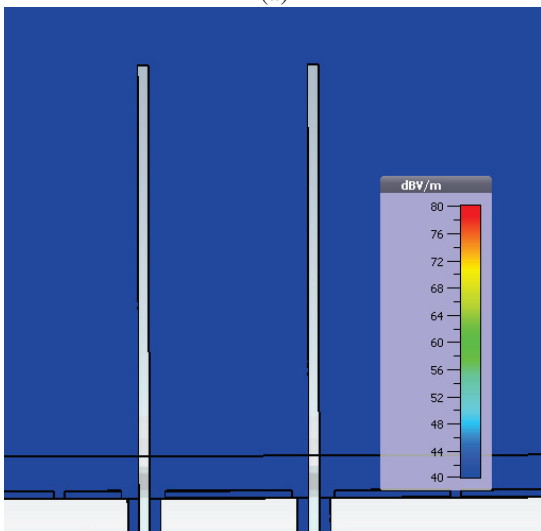
scatterers and the rebars embedded in the concrete have helped to enhance the effective aperture of the embedded monopole antennas hence yielding super-resolution performance using the time-reversal technique.

VI. NUMERICAL SIMULATION RESULTS AND DISCUSSIONS OF SUPER-RESOLUTION WIRELESS POWER TRANSFER IN CONCRETE

The numerical simulation results of the three cases studied are presented in this section. Figure 14 (a) shows the time signals plot of the setup of wireless power transfer into the concrete without rebars and the scatterer plates. The results in Fig. 14 (a) show that this setup failed to realize super-resolution wireless power transfer for the tightly-coupled monopoles as the magnitude of the voltage signal received by the two monopoles is

nearly the same in magnitude. There is no clear distinction showing the attainment of at least a 50% difference in the magnitude of the amplitude of the time signals received by the two tightly-coupled antennas [19]. Figure 14 (b) shows the electric field distribution for this case.

It can be observed from Fig. 14 (b) that the two monopole antennas have almost the same level of electric field distribution around them and no distinction as to which monopole transmitted the channel-sounding pulse. The two monopole antennas have been denoted on the time signal plots as Port 1 and Port 2, respectively, denoting monopole antenna 1 and monopole antenna 2. It can be observed from Fig. 15 (a) that the magnitude of the time signals between antenna 1 (Port 1) and antenna 2 (Port 2) shows at least a 50% difference in magnitude of the time signals between the time 2-4 ns, where the time from 0-2 ns can be regarded as
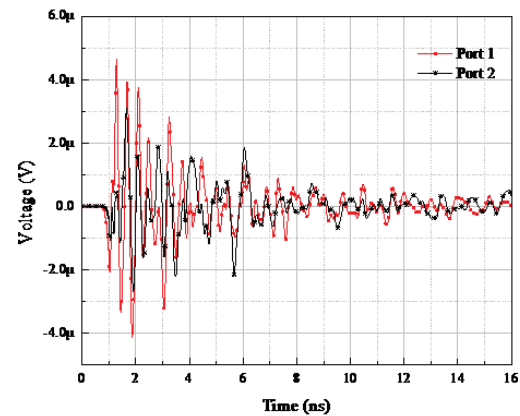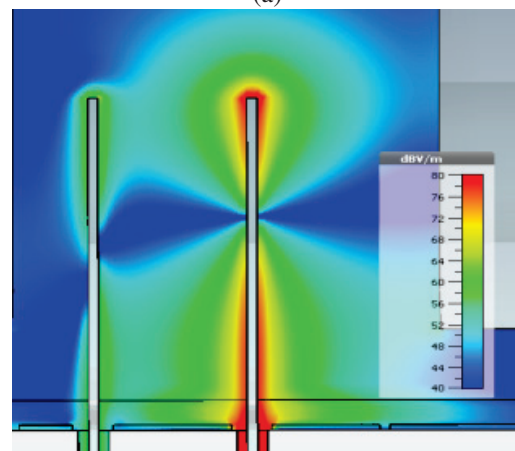

(a)

(b)

Fig. 14. Results for concrete without re-enforcement and additional scatterers: (a) time signal plot and (b) electric field distribution on the tightly-coupled antennas.

(a)

(b)

Fig. 15. Results for the two tightly-coupled monopoles embedded in concrete with enforcement bars: (a) time signal diagram of the two monopoles and (b) electric field distribution.

the early time response and also after 4-16 ns, regarded as the late time response hence not considered in the analysis. From the time signals plots and the electric field distribution shown in Fig. 15 (b), it is observed that this scenario has realized super-resolution wireless power transfer to the tightly-coupled monopole antennas. The monopole antenna that initially transmitted making the power request has a stronger electric field distribution on it as compared to the other that did not transmit. Figure 15 shows the time signals plot and the electric field distribution, where additional electromagnetic scatterers have been embedded close to the rebars. It can be seen from Fig. 15 that between 2 and 4 ns, this study has realized super-resolution wireless power transfer between the tightly-coupled monopoles with a separation distance of 10 mm. The electric field distribution shown in Fig. 15 (b) demonstrates a clear distinction between the tightly-coupled antennas with the receiving antenna (Port 1) showing a stronger field distribution than Port 2.

For the first time, to the best of our knowledge, we propose a figure of merit (FoM) for evaluating microwave wireless power transfer into concrete structures using the EMTR technique for tightly-coupled monopoles. This can be derived based on the efficiency of power transfer and the robustness of the technique to variations in the properties of the concrete medium.

The power transfer efficiency (η) is a key metric for evaluating the performance of wireless power transfer systems. It is defined as the ratio of the power received by the receiver (P_R) to the power transmitted by the transmitter (P_T), or $\eta = P_R/P_T$. In the context of microwave wireless power transfer into concrete structures using the EMTR technique, η can be calculated based on the power received by the receiver during the time-reversal process and the power transmitted by the receiver during the forward transmission. The properties of concrete, such as its relative permittivity (ε_r) and loss tangent ($\tan\delta$), can vary significantly depending on factors such as moisture content, temperature and the presence of reinforcing materials (rebars). To ensure reliable wireless power transfer using the EMTR technique, the system must be robust to such variations in concrete properties. One way to evaluate the robustness of the technique is to calculate the sensitivity of the power transfer efficiency to changes in the concrete properties. This can be expressed as a relative change in efficiency (η) per unit change in ε_r or $\tan\delta$.

Based on these considerations, a possible FoM for evaluating microwave wireless power transfer into concrete structures using the time-reversal technique can be defined as:

$$\text{FoM} = \eta / \left(s^2 \varepsilon_r + s_{\tan\delta}^2 \right), \qquad (12)$$

where s_{ε_r} and $s_{\tan\delta}$ are the sensitivities of the power transfer efficiency to changes in ε_r and $\tan\delta$, respectively. This FoM considers both the power transfer efficiency and the robustness of the system to variations in concrete properties.
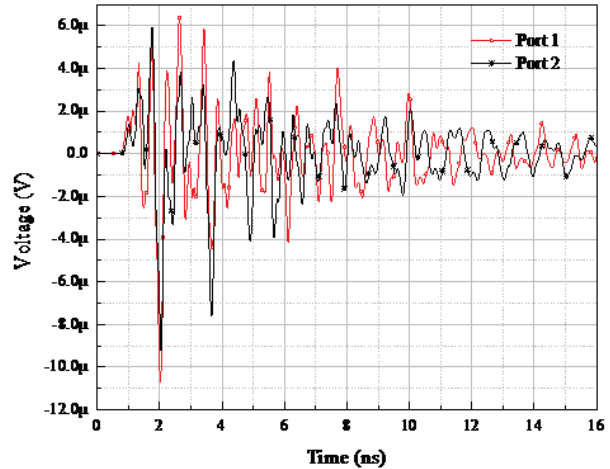
(a)
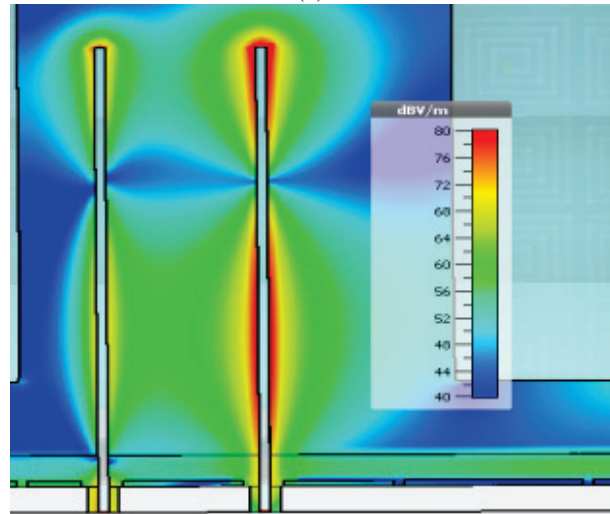
(b)

Fig. 16. Results for the two tightly-coupled monopoles embedded in concrete with enforcement bars and additional scatterers: (a) time signals plot and (b) electric field distribution of the tightly-coupled antennas embedded in the concrete.

A higher FoM indicates a more efficient and robust wireless power transfer system. For wireless power transfer of closely spaced monopole antennas, the following leads to the derivation of a FoM for the system.

The spacing between the closely spaced monopole antennas embedded into concrete can have a significant impact on the efficiency of wireless power transfer. In general, the spacing should be as small as possible to

maximize the coupling between the monopole antennas, while avoiding interference between them.

Based on these considerations, a possible FoM for evaluating microwave wireless power transfer into concrete structures using the electromagnetic time reversal technique for closely spaced monopoles embedded into concrete can be defined as:

$$FoM = \frac{\eta}{s_{\varepsilon_r}^2 + s_{tan\delta}^2 + \frac{\lambda}{\delta}}, \quad (13)$$

where λ is the wavelength of the transmitted signal and δ is the spacing between the monopole antennas. The last term in the equation considers the practical constraint on the spacing between the monopole antennas. A higher FoM indicates a more efficient and robust wireless power transfer system for a given spacing between the monopole antennas. Note that the specific values of the sensitivities and the practical constraint term may vary depending on the specific application and the design of the wireless power transfer system.

In many applications, it is desirable to limit the extent of power transfer to a localized region of the concrete structure. The degree of localization of power transfer can be evaluated using metrics such as the spatial distribution of the power density, or the ratio of the power density in the target region to the total power density received by the receiver.

Based on these considerations, a possible FoM for evaluating microwave wireless power transfer into concrete structures using the electromagnetic time reversal technique for closely spaced monopole antennas embedded into concrete can be defined as:

$$FoM = \frac{\eta}{s_{\varepsilon_r}^2 + s_{tan\delta}^2} \times \frac{(P_T, P_R)_{target}}{(P_T, P_R)_{total}}, \quad (14)$$

where $s_{\varepsilon r}$ and $s_{tan\delta}$ are the sensitivities of the power transfer efficiency to changes in ε_r and $tan\delta$, respectively, and $(P_T, P_R)_{target}$ and $(P_T, P_R)_{total}$ is the total transmitted and received power in the target region and the total transmitted and received power, respectively. This FoM considers the power transfer efficiency, robustness of the technique and degree of localization of power transfer. A higher FoM indicates a more efficient, robust and localized wireless power transfer system.

VII. CONCLUSION

In this paper, a super-resolution microwave wireless power transfer to antennas embedded in concrete has been studied. Furthermore, the operating environment of the tightly-coupled monopole antennas has been studied with its effect on the selective wireless power transfer realization. The case of receiving power by one tightly-coupled monopole antenna using electromagnetic time reversal coupled with scatterers has shown that the antennas' environment can affect it constructively or destructively depending on the technique used. With the EMTR

technique, the scatterers have constructively aided the realization of selective wireless power transfer of $1/12\lambda$ of the operating frequency at 2.45 GHz within the industrial, scientific and medical (ISM) band. This study has shown some promising potential in selective wireless power transfer with the electromagnetic time reversal, which will help transfer power to tightly-coupled antennas in space-constrained applications for wireless trickle charging of wireless sensors for civil health structural monitoring. In addition, a figure of merit (FoM) has been defined for the first time to characterize wireless power transfer into concrete structures using the electromagnetic time-reversal technique for tightly-coupled monopoles (sensors).

REFERENCES

[1] R. H. Bhuiyan, M. R. Islam, J. M. Caicedo, and M. Ali, "A study of 13.5-MHz coupled-loop wireless power transfer under concrete and near metal," *IEEE Sens. J.*, vol. 18, no. 23, pp. 9848-9856, 2018.

[2] Y. Peng, W. Qi, Y. Chen, R. Mai, and U. K. Madawala, "Wireless sensor power supply based on eddy currents for structural health monitoring," *IEEE Trans. Ind. Electron.*, vol. 71, no. 7, pp. 1-10, 2023.

[3] T. Bigler, G. Kovács, A. Treytl, and R. Windl, "NFC for powering sensors in concrete," in *IEEE Symposium on Emerging Technologies and Factory Automation, ETFA*, pp. 1355-1358, 2020.

[4] S. H. Lee, M. Y. Kim, B. S. Lee, and J. Lee, "Impact of rebar and concrete on power dissipation of wireless power transfer systems," *IEEE Trans. Ind. Electron.*, vol. 67, no. 1, pp. 276-287, 2020.

[5] L. T. Tran, C. D. Khuat, and L. V. Phi, "A wideband, high gain and low sidelobe array antenna for modern ETC systems," *Applied Computational Electromagnetics (ACES) Journal*, vol. 38, no. 5, pp. 333-342, 2023.

[6] K. Kayalvizhi and S. Ramesh, "Design and analysis of reactive load dipole antenna using genetic algorithm optimization," *Applied Computational Electromagnetics (ACES) Journal*, vol. 35, no. 3, pp. 279-287, 2020.

[7] S. Syedyusuff, R. Subramaniam, and R. Vijay, "Orthogonally integrated hybrid antenna for intelligent transportation systems," *Applied Computational Electromagnetics (ACES) Journal*, vol. 36, no. 5, pp. 519-525, 2021.

[8]   G. Castorina, L. Di Donato, A. F. Morabito, T. Isernia, and G. Sorbello, "Analysis and design of a concrete embedded antenna for wireless monitoring applications [antenna applications corner]," *IEEE Antennas Propag. Mag.*, vol. 58, no. 6, pp. 76-93, 2016.

[9]   J. R. Tenório Filho, J. Goethals, R. Aminzadeh, Y. Abbas, D. E. V. Madrid, V. Cnudde, G. Vermeeren, D. Plets, and S. Matthys, "An automated wireless system for monitoring concrete structures based on embedded electrical resistivity sensors: Data transmission and effects on concrete properties," *Sensors*, vol. 23, no. 21, p. 8775, 2023.

[10] B. A. Twumasi and J. L. Li, "Numerical simulation study on bowtie antenna-based time reversal mirror for super-resolution target detection," *J. Electr. Eng.*, vol. 70, no. 3, pp. 236-243, 2019.

[11] F. Cangialosi, T. Grover, P. Healey, T. Furman, A. Simon, and S. M. Anlage, "Time reversed electromagnetic wave propagation as a novel method of wireless power transfer," in *2016 IEEE Wireless Power Transfer Conference, WPTC 2016*, 2016.

[12] S. Ding, S. Gupta, R. Zang, L. Zou, B. Z. Wang, and C. Caloz, "Enhancement of time-reversal subwavelength wireless transmission using pulse shaping," *IEEE Trans. Antennas Propag.*, vol. 63, no. 9, pp. 4169-4174, 2015.

[13] M. Ku, Y. Han, H. Lai, Y. Chen, S. Member, and K. J. R. Liu, "Power waveforming: Wireless power transfer beyond time reversal," *IEEE Trans. Signal Processing*, vol. 64, no. 22, pp. 5819-5834.

[14] A. E. Fouda, F. L. Teixeira, and M. E. Yavuz, "Time-reversal techniques for MISO and MIMO wireless communication systems," *Radio Sci.*, vol. 47, no. 5, 2012.

[15] G. Lerosey, J. De Rosny, A. Tourin, A. Derode, G. Montaldo, and M. Fink, "Time reversal of electromagnetic waves," *Physical Review Letters*, vol. 92, no. 19, p. 193904.

[16] O. W. Ata and M. I. Jawadeh, "Design of a novel split-bowtie slotted multi-resonant antenna," *International Journal of Electrical and Electronic Engineering & Telecommunications*, pp. 1-8, 2022.

[17] Y. Tawk, K. Y. Kabalan, A. El-Hajj, C. G. Christodoulou, and J. Costantine, "A simple multiband printed bowtie antenna," *IEEE Antennas Wirel. Propag. Lett.*, vol. 7, pp. 557-560, 2008.

[18] P. Dhanaraj and S. Uma Maheswari, "Performance analysis of electrically coupled SRR bowtie antenna for wireless broadband communications," *Wireless Networks*, vol. 26, no. 7, pp. 5271-5283, 2020.

[19] H. Tu, S. Xiao, D. Lesselier, and M. Serhir, "Super-resolution characteristics based on time-reversed single-frequency electromagnetic wave," *J. Electromagn. Waves Appl.*, vol. 30, no. 13, pp. 1670-1680, 2016.

Baidenger Agyekum Twumasi was born in Nsawam, E/R-Ghana in 1981. He received an H.N.D. in Electrical/Electronic Engineering from Ho Technical University (Ho Polytechnic), Ghana, in 2004, the Master of Engineering degree (MEng.) in Telecommunication Management from the HAN University of Applied Sciences, Arnhem, the Netherlands in 2011, and the Ph.D. degree in Electronic Science and Technology from the University of Electronic Science and Technology of China, Chengdu, China in 2020. He is with the University of Electronic Science and Technology of China (UESTC), China, as a post-doctoral researcher. He has been with the Electrical & Electronic Engineering Department of Ho Technical University (HTU), Ho, in Ghana since February 2008 where he is currently a Senior Lecturer. His current research interests include antennas and propagation, electromagnetic time-reversal applications, wireless power transfer, flexible (wearable) electronics, circuits and systems.

Jia-Lin Li was born in October 1972 in Sichuan, China. He received the M.S. degree from the University of Electronic Science and Technology of China (UESTC), Chengdu, China, in 2004, and the Ph.D. degree from the City University of Hong Kong, Hong Kong, in 2009, both in electronic engineering. From September 2005 to August 2006, he was a Research Associate with the Wireless Communication Research Center, City University of Hong Kong, Hong Kong. From September 2009 to April 2021, he was with the School of Physical Electronics, UESTC and initially served as a Lecturer and then a professor. Since May 2021, he has been with the School of Resources and Environment, UESTC. His research interests include microwave/millimeter-wave antennas and arrays, circuits and systems, electromagnetic-wave detection, and imaging.

Faith Kwaku Deynu received his MSc. degree in Telecommunication Engineering at HAN University of Applied Sciences, Netherlands in 2011 and his Ph.D. degree in Information and Communication Engineering at University of Electronic Science and Technology of China (UESTC), Chengdu, China. He is currently a Senior Lecturer at Electrical/Electronic Engineering Department of Ho Technical University, Ho, Ghana. His research interests include internet protocol (IP) multimedia subsystems, optical fiber, and power line communication systems.

Ebenezer Tawiah Ashong received a B.Sc. degree in Telecommunication Engineering from Kwame Nkrumah University of Science and Technology, Kumasi, Ghana in 2015 and an MEng degree in Electronic Engineering from Hanbat National University, Daejeon, Korea, in 2019. He is currently pursuing a PhD in Electrical and Information Engineering at Seoul National University of Science and Technology, Seoul, Korea. He is currently a Lecturer in the Department of Electrical & Electronic Engineering at Ho Technical University, Ho. His current research interests include antennas and arrays, wireless power transfer, electromagnetic compatibility, measurement and instrumentation, and telecom policy and regulation.

Christian Dzah was born in Ho, Volta Region of Ghana in 1977. He obtained his Higher National Diploma (HND) Certificate in Electrical/Electronic Engineering from Ho Polytechnic, Ghana in 2009. He obtained his Bachelor of Science Degree in Electrical/Electronic Engineering from Regional Maritime University, Accra-Ghana, in 2015. In 2019, he obtained his Master of Philosophy Degree in Electrical and Electronic Engineering from the University of Mines and Technology, Tarkwa, Ghana. Currently, he is an Assistant Lecturer in the Department of Electrical/Electronic Engineering, at Ho Technical University, Ghana.

Dustin Pomary received his Bachelor of Engineering in Biomedical Engineering from All Nations University, Koforidua, Ghana, in 2017 and his MPhil in Biomedical Engineering at the University of Ghana, Legon, in 2021. His thematic area of study is implants sciences and regenerative engineering. He is currently an Assistant Lecturer in the Department of Electrical & Electronic Engineering at Ho Technical University, Ho, Ghana. His current research interests include implant sciences, regenerative engineering, drug delivery, computational simulation, and biomaterials.